Particle Dynamics in Monolithic Catalysts

Heiredal, Michael Lykke

Publication date:
2010

Document Version
Publisher's PDF, also known as Version of record

Particle Dynamics in Monolithic Catalysts

Ph.D. Thesis

Michael Lykke Heiredal

Department of Chemical and Biochemical Engineering
Technical University of Denmark
Building 229
DK-2800 Kgs. Lyngby
Denmark

2010

ISBN 978-87-92481-15-3
Printed by Frydenberg a/s, Copenhagen, Denmark

Preface

The present Ph.D. thesis is written in accordance with the partial requirements of the Ph.D. degree at the Technical University of Denmark. The Ph.D. project was carried out between September 2006 and August 2009 at the Department of Chemical and Biochemical Engineering, Technical University of Denmark, within the CHEC (Combustion and Harmful Emission Control) research centre in cooperation with Haldor Topsøe A/S and the Danish Agency for Science, Technology and Innovation which is an institution under the Danish Ministry of Science, Technology and Innovation.

The author would like to thank his main supervisor Professor Anker Degn Jensen, Department of Chemical and Biochemical Engineering, DTU, for his guidance and supervision during the project and for always being willing to discuss the experiments, theoretical aspects and developed models and all other questions. The author is very grateful for all the support from Professor Anker Degn Jensen during the whole Ph.D. study. Without all his support and encouragement when things were difficult, this Ph.D. study would not have been possible.

The author would also like to thank Dr. Joakim Reimer Thøgersen, Haldor Topsøe A/S and Associate Professor Flemming Frandsen, Department of Chemical and Biochemical Engineering, DTU, for their guidance and supervision during the project.

The author would like to thank technician Carsten Nørby from CHEC for all his help with the experiments and the technicians from the workshop at the department for helping in building the experimental setup.

The author would also like to thank (now retired) Associate Professor Hans Livbjerg for very inspiring discussions and guidance during the design and build up of the experimental setup.

Preface

The author had the pleasure of staying four weeks at the ANSYS Fluent office in Göteborg, Sweden in August/September 2008 and again two weeks in March/April 2009, during his Ph.D. study. The author is very grateful to his friend, senior CFD engineer Jens-Uwe Friemann from Ansys Fluent in Göteborg, for his help with programming and implementing the UDFs for electrostatic dispersion of submicrometer particles both in the Eulerian and the Lagrangian reference frame and particle-wall interactions and grow-up velocity for the deposit of particles on the wall in the Lagrangian reference frame. The author is also very grateful for fruitful discussions in general about electrostatic forces on particles and other physical mechanisms involved in this Ph.D. study. Without the help and cooperation from Jens-Uwe the implementation of the different models in Fluent would not have been possible within this Ph.D. Study. Finally the author is very grateful for having met Jens-Uwe and for his friendship.

The author is also grateful to Chyar Somo, ANSYS Fluent, Göteborg for providing the licenses for the commercial Computational Fluid Dynamic solver ANSYS-Fluent® used in the present work.

The author would also like to thank all his colleagues in the Stationary DeNOx group at Haldor Topsøe A/S for their support during the three years and for creating a nice and inspiring working environment.

Finally the author would like to thank Chunyan Wang Stenberg for all her love, patience and support and for holding on during this Ph.D. study. Without this the author would not have been able to carry through this Ph.D. Study

Michael Lykke Heiredal

Kgs. Lyngby, Denmark
May 2010

Summary

The present Ph.D. study describes an experimental and Computational Fluid Dynamics (CFD) investigation of particle dynamics in monolithic catalysts. A review of the current knowledge of particle deposition mechanisms is presented. This review also gives a short overview of plugging and deposition in monolithic catalysts and a short overview of ash formation.

In the experimental part of the work deposition of submicrometer KCl aerosol particles due to Brownian diffusion and electrostatic dispersion in laminar tube flow have been investigated. The experimental investigations were conducted on both a straight and a bent pipe. The results showed that electrostatic forces were an important deposition mechanism in laminar pipe flow with the same order of magnitude as deposition due to Brownian motion. The electrostatic forces were due to space charging because of charged particles. Measurements of the average number of elementary charges on the aerosol particles were also carried out. These results showed that in average the KCl aerosol particles were negatively charged. Investigations showed that particles neutralized to approximately Boltzmann charge equilibrium compared to particles with the same initial particle number concentration carrying an average charge, due to the process of generation, had lower deposition efficiency. The experimental investigations also showed that the space charging more or less could be suppressed by lowering the particle number concentration. Investigations of aerosol particle deposition in a bent and a straight pipe, respectively showed that secondary flow has an impact on the deposition efficiency for submicrometer particles for Stokes numbers below one. In the experimental investigations the enhancement was about 15% point. In general good agreement was found between the experimental results and CFD simulations. However, CFD simulations with particles carrying an average charge underestimated the deposition efficiency compared to the experimental results. For the monodispersed particles it was shown that the electrostatic effects

could be totally suppressed using very low particle concentrations by selecting the particles with the NDMA.

Experiments were also conducted on micrometer particles in laminar flow in a bend in connection with a straight vertical pipe in order to investigate the influence of Saffman lift on particle deposition using monodisperse micrometer cross-linked PMMA particles with diameters of 10, 20, 30 and 40 μm, respectively. The experimental investigations showed a maximum for the total deposition efficiency of about 80% (Saffman and inertial impact) and about 70% for the Saffman lift force for 30 μm particles. The deposition efficiency due to inertial impact in the bend showed a maximum of about 40% for 20 μm particles. The particle-wall interaction model implemented in CFD was validated against the experimental results and good agreement was found for the individual particle diameters against the total deposition efficiency. The experiments also showed that the deposition efficiency for the bend due to inertial impact and the deposition efficiency for the straight pipe due to Saffman lift force showed some differences between the experimental results and the CFD results. This was believed to be due to differences between the CFD model of the bend (which was modelled as a perfect 90-degree bend and a straight part) and the bend in the experiments. Comparison between the experimental results for the deposition efficiency due to Saffman lift in a vertical deposition pipe, CFD simulations and a pseudo steady-state model was also carried out. The CFD simulations were based on developing flow in the same vertical deposition pipe assuming perfect adhering walls and the pseudo steady-state model was based on an analytical expression for Saffman lift. The agreement between the experimental results of deposition due to Saffman lift and the simulations of developing flow and particle concentration profile were good and comparison with the analytical expression for deposition due to Saffman lift also gave good agreement. It was also observed that due to the assumption of perfect adhering walls the CFD simulations and the simple model did not capture the experimental observed maximum in deposition efficiency for 30 μm particles. It was also observed that for particles above 30 μm the deviation between the CFD simulation and the analytical expression becomes larger because acceleration of the particles becomes important.

Pilot scale experiments were conducted in order to investigate plugging in SCR $DeNO_x$ monolithic catalysts using commercial corrugated-type SCR monolithic catalysts obtained from Haldor Topsøe A/S. The monolithic catalysts used in the tests were DNX x30 and DNX x80, respectively. DNX x30 SCR monolithic catalysts with a hydraulic diameter of 3.4 mm were exposed to potassium chloride, KCl, particles over time for 24, 48, 78, 120 and 158 hours. The total

deposition efficiency of the DNX x30 SCR monolithic catalysts in the pilot scale experiments was about 30%. The deposition pattern observed was a “volcano type” of deposition pattern which was also seen in full-scale low-dust applications. The average number of elementary charges was measured on the KCl aerosol particles in the pilot scale experiments and showed that the particles were positively charged and carried an average number of elementary charges equal to 0.001 elementary charges per particle. A SCR DNX x80 monolithic catalyst (dummy) with a hydraulic diameter of 8 mm was exposed to KCl particles over about 240 hours and severe deposition was identified.

A general CFD model for prediction of particle deposition and deposit build-up in SCR $DeNO_x$ monoliths has been implemented. CFD simulations assuming laminar and turbulent flow through the monolith, respectively have confirmed that turbulent diffusion in about the first half of the axial length of the monolith channels and inertial impact and gravitational settling on the top of the monolith are the dominating mechanisms for particle deposition leading to plugging of the catalyst. It was observed that for laminar flow the CFD model underpredicted the accumulated mass compared to the experimental results with a factor of about 17 and for turbulent flow the CFD model overpredicted the experimental results with a factor of about 2.4. The results have demonstrated that CFD is a powerful tool to explain experimental results and to gain an increased understanding of the particle deposition and plugging in monolithic catalysts.

Summary

Resumé

Nærværende Ph.D. afhandling beskriver et eksperimentelt og ”Computational Fluid Dynamics” (CFD) studie af partikeldynamik in monolit katalysatorer. Et litteraturstudie dækkende den nuværende viden om partikelafsætningsmekanismer præsenteres. Litteraturstudiet dækker også tilstopning og afsætning i monolit katalysatorer samt giver et kort overblik over askedannelsesmekanismer.

Afsætning af submikrometer KCl aerosolpartikler på grund af Brownske bevægelser og elektrostatisk spredning er undersøgt i laminare rørstrømninger. Undersøgelserne blev udført på både et bøjet og et lige rør. Resultaterne viste at elektrostatiske kræfter er en vigtig afsætningsmekanisme i laminare rørstrømninger på lige fod med Brownsk diffusion. Påvirkningen fra de elektrostatiske kræfter skyldtes ”space charging” fra de ladede aerosolpartikler. Målinger af det gennemsnitlige antal elementarladninger som partiklerne bar viste at gennemsnitligt var KCl submikrometer partiklerne i eksperimenterne negativt ladede. Undersøgelserne viste, at partikler afladt til Boltzmann ladningsligevægt har lavere afsætningseffektivitet end partikler som bærer en gennemsnitsladning hidrørende fra deres generering ved samme initiale partikelantalskoncentration. De eksperimentelle undersøgelser viste også, at ”space charging” mere eller mindre kunne undertrykkes ved at sænke den initielle koncentration af partiklerne. Undersøgelser af partikelafsætningen i et bøjet og et lige rør viste, at sekundære strømninger har en indvirkning på afsætningseffektiviteten for submikrometer partikler, som har et Stokes tal mindre end én. Forøgelsen af afsætningen var på omkring 15% point. Generelt blev der fundet god overensstemmelse mellem eksperimenterne og CFD simuleringerne. Dog underestimerede CFD simuleringer afsætningseffektiviteten i forhold til de eksperimentelle resultater i de tilfælde, hvor partiklerne bar en gennemsnitsladning. For monodisperse partikler blev det vist, at de elektrostatiske effekter kunne undertrykkes helt ved at udvælge dem ved lave koncentrationer fra NDMA’en.

Afsætningseksperimenter blev også udført på mikrometer partikler i laminare strømninger i et bøjet rør i forlængelse med et lige rør med henblik på at undersøge indflydelsen af Saffman "lift" kraften på partikelafsætningen. Der blev anvendt "monodisperse" mikrometer "cross-linked" PMMA partikler med diametre på henholdsvis 10, 20, 30 and 40 μm. Eksperimenterne viste et maksimum for den totale afsætningseffektivitet på omkring 80% ("Saffman and inertial impact") og omkring 70% for Saffman "lift" kraften for 30 μm partikler. Afsætningseffektiviteten hidrørende fra "inertial impact" i bøjningen viste et maksimum på omkring 40% for 20 μm partikler. Partikel-væg interaktionsmodellen implementeret i CFD blev valideret med de eksperimentelle resultater og viste god overensstemmelse med den totale afsætningseffektivitet. Eksperimenterne viste også, at afsætningseffektiviteten for bøjningen hidrørende fra "inertial impact" og afsætningseffektiviteten for det lige rør pga. Saffman "lift" kraften viste nogen afvigelse i forhold til CFD simuleringerne. Årsagen hertil menes at skyldes forskelle mellem CFD modellen af bøjningen (som blev modelleret som en perfekt 90 graders bøjning i forlængelse med et lige stykke) og bøjningen i eksperimenterne. Sammenligning mellem de eksperimentelle resultater for Saffman "lift" kraften i et lige rør, CFD simuleringer og en pseudo stationær model blev også foretaget. CFD simuleringerne var baseret på en udviklende strømning med perfekt adhæsion af partiklerne på væggen i det samme vertikale rør, og den pseudo stationære model var baseret på et analytisk udtryk for afsætningseffektiviteten pga. Saffman "lift" kraften. Overensstemmelsen mellem de eksperimentelle resultater og afsætningseffektiviteten pga. Saffman "lift" kraften i en udviklende strømning med udviklende partikel koncentrationsprofil var god. Det blev også observeret, at pga. antagelsen med perfekt adhæsion af partiklerne på væggen fangede, hverken CFD simuleringerne eller den simple model, det i eksperimenterne observerede maksimum i afsætningseffektiviteten for 30 μm partikler. Yderligere blev det også observeret, at for partikler større end 30 μm blev afvigelsen mellem CFD simuleringerne og det analytiske udtryk for afsætningseffektiviteten større pga. at accelerationen af partiklerne begynder at blive betydende.

Pilotskala eksperimenter blev udført med henblik på at undersøge tilstopning i SCR $DeNO_x$ monolit katalysatorer. Kommercielle korrugerede SCR monolit katalysatorer fra Haldor Topsøe A/S blev benyttet. Katalysatorerne var henholdsvis DNX x30 og DNX x80 katalysatorer.

DNX x30 SCR $DeNO_x$ monolit katalysatorer med en hydraulisk diameter på 3,4 mm blev eksponeret for KCl partikler i tidsintervaller på 24, 48, 78, 120 og 158 timer. Den totale afsætningseffektivitet for en DNX x30 SCR $DeNO_x$ monolit

katalysator var omkring 30%. Tilstopningsmønstret, som blev observeret, var en slags "vulkan type", som også observeres i fuldskala "low-dust" installationer. Det gennemsnitlige antal elementarladninger på KCl partiklerne i pilotskala eksperimenterne blev også målt, og viste at gennemsnitsantallet var 0.001 elementarladninger. En SCR DNX x80 monolit katalysator med en hydraulisk diameter på 8 mm blev eksponeret for KCl partikler i ca. 240 timer, og kraftig tilstopning blev observeret.

En general model til simulering af afsætning og tilstopning i SCR $DeNO_x$ monolitter er blevet implementeret i CFD. Simuleringer af henholdsvis laminare og turbulente strømninger har bekræftet at turbulent diffusion i ca. den første halvdel af monolitkanalernes længde samt "inertial impact" og "gravitational settling" på toppen af katalysatoren er de dominerende partikelafsætningsmekanismer, som skaber tilstopning i katalysatorerne. Det blev også observeret, at CFD simuleringer af laminare strømninger igennem monolit katalysatorerne underestimerede den afsatte masse med ca. en factor 17 i forhold til eksperimenterne. For CFD simuleringer af turbulente strømninger igennem monolit katalysatorerne overestimerede CFD simuleringerne den afsatte masse med ca. en factor 2.4. Generelt har resultaterne vist, at CFD er et kraftfuldt værktøj til at forklare eksperimentelle resultater og opnå forøget indsigt i partikelafsætning og tilstopning i monolit katalysatorer.

Contents

Nomenclature

Latin letters

a_0	Radius of deformed area at contact point	[m]
A_{deform}	Deformed area at contact point	[m^2]
A_{inlet}	Inlet area of pipe	[m^2]
$\vec{A}_{wall}$	Face area vector	[m^2]
B	Mechanical mobility	[m/N·s]
$B(\xi)$	Non-dimensional skin friction	[-]
c	Total molar concentration	[mol/m^3]
c_f	Skin friction	[-]
C_c	Cunningham slip correction factor	[-]
C_D	Drag coefficient	[-]
C_{NI+}	Ion concentration	[$\#/m^3$]
C_{NI-}	Ion concentration	[$\#/m^3$]
C_0	Aerosol cocentration	[$\#/m^3$]
d	Characteristic dimension of the channel	[m]
d_{ij}	Deformation tensor	[1/s]
d_{lk}	Deformation tensor	[1/s]
D^+	Non-dimensional particle diameter	[-]
D	Particle diffusion coefficient / Brownian diffusivity	[m^2/s]
D_{AB}	Mass diffusivity	[m^2/s]
D_p	Particle diameter	[m]
D_T	Coefficient of diffusion due to a temperature gradient	[m^2/s]
e	Elementary charge	[C]
e	Exponential function	[-]
$\vec{e}$	Molar energy flux vector	[J/m^2-s]
$\vec{E}$	Electrostatic field strength vector	[N/C]
$E_{el,1}$	Electrostatic energy before collision	[J]
$E_{el,2}$	Electrostatic energy after collision	[J]
$E_{kin,1}$	Kinetic energy before collision	[J]

$E_{kin,2}$	Kinetic energy after collision	[J]
E_{deform}	Energy loss due to wall collision	[J]
E_L	Surface field strength	[V/m]
f	Friction factor	[-]
f_n	Fraction of particles carrying *i* number of elementary Charges	[-]
$\vec{F}_B$	Force due to Brownian motion	[N]
F_{drag}	Drag force	[N]
$\vec{F}_E$	Electrostatic force vector	[N]
$F_{gravitation}$	Force due to fravity	[N]
$\vec{F}_i$	Time-averaged body force vector	[N]
$\vec{F}_L$	Saffman lift force	[N]
F_n	Form drag	[N]
$\vec{F}_q$	Coulomb force	[N]
F_t	Skin friction	[N]
g	Gravitational acceleration	[m/s^2]
g^+	Non-dimensional gravitational acceleration	[-]
G_k	Generation of turbulent kinetic energy	[kg/m-s^3]
h_m	Mean heat transfer coefficient	[W/m^2 K]
$h\varpi$	Liffschitz-van der Walls constant	[Nm]
H	Strength of the pipe wall	[N/m^2]
i	Number of elementary charges	[#]
$\bar{i}$	Average number of elementary charges	[#]
i_L	Limit number of elementary charges	[#]
I	Current	[A]
J	Particle flux	[#/m^2-s]
J_i	Flux vector	[kg/m^2-s]
J_w	Wall particle flux	[#/m^2-s]
k	Roughness height	[m]
k	Turbulent kinetic energy	[m^2/s^2]
k	Coefficient of restitution	[-]
k	Thermal conductivity	[W/K-m]
k_s^+	Non-dimensional roughness height	[-]
k_B	Boltzmann constant	[J K^{-1}]
K	Brownian agglomeration coefficient	[#/m^3-s]
K	Saffman integration constant	[-]
K	Empirical proportionality constant	[kg/m^3]
K_E	Electrostatic constant of proportionality	[Nm^2/C^2]
Kn	Knudsen number	[-]
K°_{vdW}	van der Waals adhesion force	[N]
l_x	Width of injection surface	[m]

l_y	Height of injection surface	[m]
L	Heigth of duct	[m]
L	Tube length	[m]
L_1^+	Non-dimensional coefficient for Saffman lift force	[-]
m	Total mass of aerosol	[kg]
$m_{deposit,\ bend}$	Mass of aerosol deposit in a bend	[kg]
$m_{deposit,\ pipe}$	Mass of aerosol deposit in a pipe	[kg]
m_{in}	Accumulated mass of aerosols into a bend and pipe	[kg]
$m_{in,\ pipe}$	Accumulated mass of aerosols into a pipe	[kg]
$M_{H2O,liq}$	Mass of liquid water	[kg]
m_p	Particle mass	[kg]
$\dot{m}$	Aerosol mass flow rate	[kg/s]
$\dot{m}_{parcel}$	Mass flow of particles	[kg/s]
M	Molecular weight	[kg/mol]
n	Particle number concentration	[#/m^3]
n_0	Initial particle number concentration	[#/m^3]
n_{out}	Particle number concentration at otlet of tube	[#/m^3]
n_{bulk}	Bulk particle number concentration	[#/m^3]
n_{parcel}	Number of parcels injected	[#]
$\vec{n}_p$	Unit vector	[m]
N	Aerosol concentration	[#/cm^3]
N	Particle flow	[#/s]
N	Molar flox	[mol/m^2-s]
N_0	Total initial number concentration of particles	[#/cm^3]
$N(t)$	Arbitrary number concentration of particles	[#/cm^3]
O	Order of magnitude	[-]
$\underline{p}$	Static pressure	[Pa]
$\overline{p}$	Time-averaged thermodynamic pressure	[Pa]
$p_{A,vap}$	Water vapour pressure	[Pa]
p_{tot}	Total pressure	[Pa]
P	Penetration efficiency	[-]
P_{image}	Deposition efficiency due to image force	[-]
P_d	Penetration efficiency due to Saffman	[-]
P_D	Diffusional penetration efficiency	[-]
Pe	Peclet number	[-]
q	Total charge on a particle	[C]
$\underline{q}$	Rate of formation of aerosol per unit volume	[#/s/m^3]
$\overline{q}$	Absolute average charge on a particle	[C]
q_1	Charge on particle before wall collision	[C]
q_2	Charge on particle before wall collision	[C]
q_0	Impact charge after collision	[C]

q_e	Particle charge where no displacement occurs during a collision	[C]
Q	Charge on a particle	[N]
Q	Volume flow	[m^3/s]
r_c	Critical radius	[m]
R	Universal gas constant	[J/mol K]
R	Inner radius of pipe	[m]
R_p	Radius of particle	[m]
R_{tube}	Radius of pipe	[m]
R_{pipe}	Radius of pipe	[m]
Re	Reynolds number	[-]
Re_V	Reynolds number based on velocity	[-]
Re_κ	Reynolds number based on velocity gradient	[-]
Re_Ω	Reynolds number based on particle rotation	[-]
S	Density ratio between particle and fluid	[-]
S	Stopping distance	[m]
S^+	Dimensionless stopping distance	[m]
Sc	Schmidt number	[-]
$S_{n.ij}$	Spectral intensity	[-]
Stk	Particle Stokes number	[-]
S_{ϕ_k}	Source term	[kg/m^3-s]
t	Time	[s]
T	Temperature	[K]
u	Characteristic velocity of the fluid	[m/s]
$\vec{u}$	Velocity vector of flow field	[m/s]
$\underline{u_i}$	Instantaneous velocity vector	[m/s]
$\underline{u}_i$	Average velocity vector	[m/s]
$\underline{u}_i'$	Fluctuating velocity vector	[m/s]
$\vec{u}_p$	Particle velocity vector	[m/s]
u^*	Friction velocity / shear velocity	[-]
u_{avg}	Average velocity of fluid	[m/s]
U_0	Mean axial velocity / average velocity in the pipe	[m/s]
u_{fluid}	Fluid velocity	[m/s]
u_i	Fluid velocity tensor	[m/s]
u_r	Radial velocity	[m/s]
$V_{grow\text{-}up}$	Grow-up velocity	[m/s]
v_p	Particle velocity	[m/s]
v_{p0}	Root-mean-square radial velocity	[m/s]
v_t	Terminal settling velocity	[m/s]
v_z	Axial velocity	[m/s]
v_ξ	Velocity in non-dimensional radial direction	[m/s]

v_η	Velocity in non-dimensional axial direction	[m/s]
$\vec{v}_m$	Particle migration velocity due to an external force field	[m/s]
$\vec{v}_{el}$	Electrical migration velocity	[m/s]
V	Relative velocity of the particle to the fluid	[m/s]
V_{avg}	Average gas velocity	[m/s]
V_{dep}^+	Dimensionless deposition velocity	[-]
V_s	Space-charge parameter	[-]
$w_{p,1}$	Particle before particle-wall collision	[m/s]
$w_{p,crit}$	Critical particle velocity for particle-wall adhesion	[m/s]
W	Width of duct	[m]
W_{AR}	Molar flow	[mol/s]
$W_{vdW,1}$	Energy due to adhesion before collision	[J]
$W_{vdW,2}$	Energy due to adhesion after collision	[J]
x_A	Mol fraction of component A	[-]
x_i	Cartesian tensor	[m]
y	Physical distance from wall	[m]
y^+	Dimensionless distance from wall	[-]
z_0	Distance at contact	[m]
Z	Electrical mobility	[m^2/V·s]
Z_{I+}	Ion mobility	[m^2/V·s]
Z_{I-}	Ion mobility	[m^2/V·s]

Greek letters

ρ	Density of fluid	[kg/m^3]
ρ_c	Space charge density	[C/m^3]
ρ_f	Density of fluid	[kg/m^3]
ρ_p	Density of particle	[kg/m^3]
κ	Velocity gradient	[1/s]
κ	Dielectric constant	[-]
λ	Mean free path of the fluid	[m]
δ_{ij}	Kronecker's delta	[-]
$\prod$	Dimensionless deposition parameter	[-]
Δ	Dimensional diffusion parameter	[-]
ν	Kinematic viscosity of fluid	[m^2/s]
μ	Dynamic viscosity of fluid	[Pa·s]
μ_t	Turbulent viscosity	[Pa·s]
γ	Packing efficency	[-]

τ	Dimensionless residence time	[-]
τ	Characteristic time for coagulation	[s]
τ_p	Particle relaxation time	[s]
τ_p^+	Dimensionless particle relaxation time	[-]
τ_w	Wall shear stress	[N/m^2]
$\eta_{overall}$	Overall deposition efficiency in a bend and a pipe	[-]
η_{bend}	Deposition efficiency in a bend	[-]
η_{pipe}	Deposition efficiency in a pipe	[-]
η_{tube}	Penetration efficiency	[-]
λ	Mean free path of the fluid	[m]
λ	Thermal conductivity	[W/K·m]
λ_p	Particle thermal conductivity	[W/K·m]
λ_r	Ratio of thermal conductivity	[-]
Γ_k	General diffusion coefficient	[-]
ε	Eddy viscosity of fluid	[m^2/s]
ε	Rate of dissipation of turbulence kineticenergy	[m^2/s^3]
ε_0	Permittivity of free space	[AsV^{-1}m^{-1}]
ε_p	Particle turbulent diffusivity / particle eddy diffusion coefficient	[m^2/s]
ω	Angular velocity of particle	[rad/s]
ω_z	vorticity	[1/s]
Ω	Rotation speed of particle	[1/s]
$\vec{\nabla}^2$	Laplacian operator	[-]
ϕ	Particle sphericity	[-]
ϕ_k	Arbitrary skalar	[-]
Φ	Electrostatic potential	[V]
ξ	Dimensionless axial length	[-]
ξ_0	Limiting trajectory	[-]
ψ	Random number between 0 and 1	[-]

Chapter 1

Introduction

The conversion of energy to supply the industrialized world with heat and power has created major environmental problems such as emission of sulphur and nitrogen oxides, as well as fly ash and submicrometer particles.

The major sources of nitrogen oxides are fossil fuel combustion and burning of biomass in stationary power stations and vehicles [Bosch and Janssen (1988); Sloss (1991)]. The nitrogen oxides from combustion of fossil fuel mainly consist of NO and NO_2, and is the largest source identified with respect to emission of nitrogen oxides, especially in the industrialized regions in the Northern Hemisphere [Delmas et al. (1997)]. NO and NO_2 are commonly referred to as NO_x, where NO is representing about 90 to 95% of the NO_x [Bosch and Janssen (1988)]. Another potential product of combustion is nitrous oxide (N_2O), which is not a major product but since it can be converted into NO in the stratosphere, it is often considered along with NO_x [Bosch and Janssen (1988)]. Most of the emission of N_2O comes from Fluidized bed combustion of coal and is in the range of 100-150 ppm which is much higher than the emission from conventional pulverized fuel combustion [Jensen (1996)].

1.1 Pollution from Nitrogen Oxides

The two most important nitrogen oxides with respect to pollution are nitric oxide (NO) and nitrogen dioxide (NO_2) [Sloss (1991)]. These oxides of nitrogen are atmospheric pollutants because reactions of the nitrogen gases in the atmosphere have several effects on the environment, where they contribute to formation of acidic rain, photochemical smog, destruction of the ozone layer, the greenhouse effect and are toxic for humans. Figure 1.1 shows a schematic illustration of the cycling of nitrogen in the atmosphere.

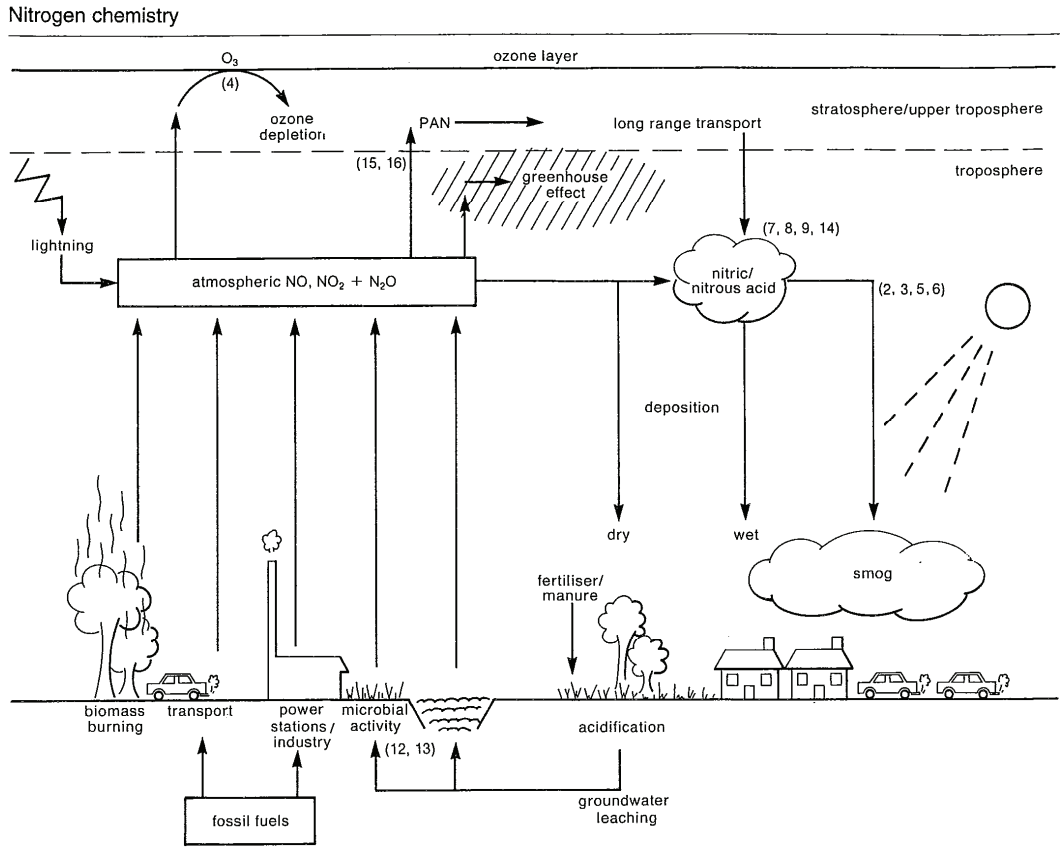

Figure 1.1: Schematic illustration of the cycling of nitrogen in the environment [Bosch and Janssen (1988)].

1.2 Stationary Coal Fired Power Stations

A major contributor to the emission of nitrogen oxides is combustion of coal in stationary power stations. There are various available coal combustion technologies, among which pulverized coal combustion is preferred compared to other combustion technologies in Denmark. In this technology coal particles are suspended in air and burned as a gas, which makes ignition and control easier [Frandsen and Østberg (1995)]. Another advantage of pulverized coal combustion is that, it can in principle be used for combustion of any type of coal, because of high thermal effect in a small area, effective burning and few problems with ash [Singer (1991)]. Combustion of coal in pulverized form has been developed over several decades with continuous improvement in design and performance and it is most commonly used in either large scale utility or industrial boilers or in process equipment such as cement kilns. Today it accounts for around 40% of the total

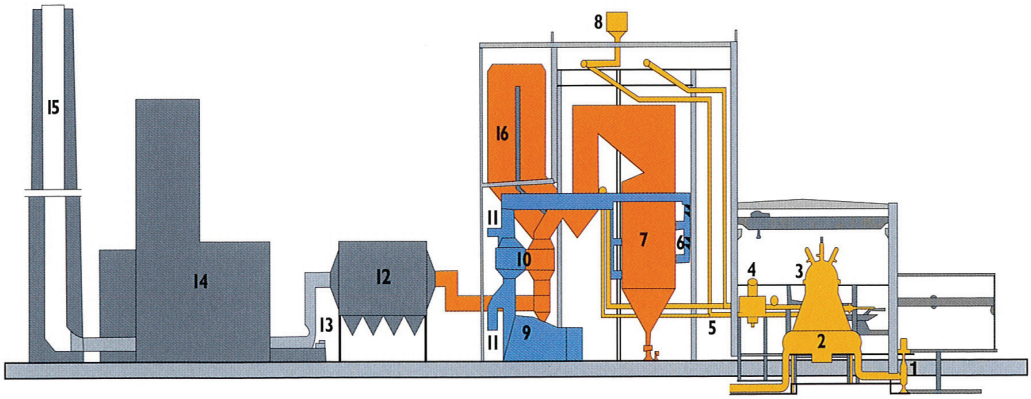

Figure 1.2: Illustration of a coal fired power station at Amager, Denmark. 1) Main cooling pump 2) Condensator district heating heat exchange 3) Turbine 4) Feed pump unit 5) Steam pipe 6) Burner 7) Boiler 8) Silencer for safety valve 9) Fresh air channel for burner 10) Air preheater 11) Primary air channel for coal mill 12) Ash removal 13) Suction blower 14) Desulphurization plant 15) Stack 16) DeNO$_x$ system [Energi E2].

electricity produced worldwide [Wu (2005)]. *Figure 1.2* illustrates the principle of a pulverized coal fired power station. In a pulverized coal fired power station, coal is first transported to the coal mill, where it is pulverized to a fine powder and dried giving particles in the size range between about 5-400 μm with a mass mean diameter typically between 40-80 μm [Wu (2005)]. These coal particles are subsequently mixed with primary air and blown into the furnace for combustion. In the furnace the coal/air mixture is ignited and burns suspended in air. During the combustion there are three different mechanisms involved in the formation of NO_x [Bosch and Janssen (1988); Glarborg et al. (2003)]:

- **Thermal NO_x** formed by reaction of nitrogen with molecular oxygen in the combustion air, which occurs at temperatures exceeding 1400°C.
- **Fuel NO_x** formed by oxidation of nitrogen containing compounds bound in the fuel.
- **Prompt NO_x** formed by the reaction between nitrogen, N_2, and hydrocarbon radicals, CH_i, forming intermediate, HCN. The intermediate, HCN, is then partly oxidized to NO.

The major source of NO_x from fossil fuel combustion systems, e.g. coal fired power stations, is generally fuel NO_x with some contribution from thermal NO_x. A thorough review of the fuel nitrogen conversion in solid fuel fired systems has recently been given by Glarborg et al. (2003).

1.3 Emission Control

Today, significant expertise in reducing emission of nitrogen oxides from combustion of pulverized coal has been achieved either by primary means, i.e. by in-furnace measures such as low-NO_x burners and air-staging or by secondary means, i.e. by post-combustion flue gas cleaning. Emission control by secondary means is systems that are installed downstream of the furnace and can be divided into the following categories:

- Reburning
- Selective Catalytic Reduction of NO_x (SCR)
- Selective Non-Catalytic Reduction of NO_x (SNCR)
- Hybrid SCR/SNCR
- Simultaneous SO_2 and NO_x removal techniques

These technologies commonly involve injection of ammonia, urea or other chemical reagents which react with the NO_x in the flue gas converting it to molecular nitrogen or nitrates.

1.4 Background

1.4.1 The SCR DeNO_x Process

The most efficient and widely used process for post-combustion cleaning for NO_x is the so called Selective Catalytic Reduction of NO_x (SCR). In this process ammonia or urea is injected in the flue gas allowing for reactions between NO_x and NH_3 into harmless water and nitrogen over a catalyst which generally follows the reactions shown in Equation (1.1).

$$
\begin{aligned}
a) \quad & 4NO + 4NH_3 + O_2 \rightarrow 4N_2 + 6H_2O \\
b) \quad & 6NO_2 + 8NH_3 \rightarrow 7N_2 + 12H_2O \\
c) \quad & NO + NO_2 + 2NH_3 \rightarrow 2N_2 + 3H_2O \\
d) \quad & 4NH_3 + 3O_2 \rightarrow 2N_2 + 6H_2O
\end{aligned}
\qquad (1.1)
$$

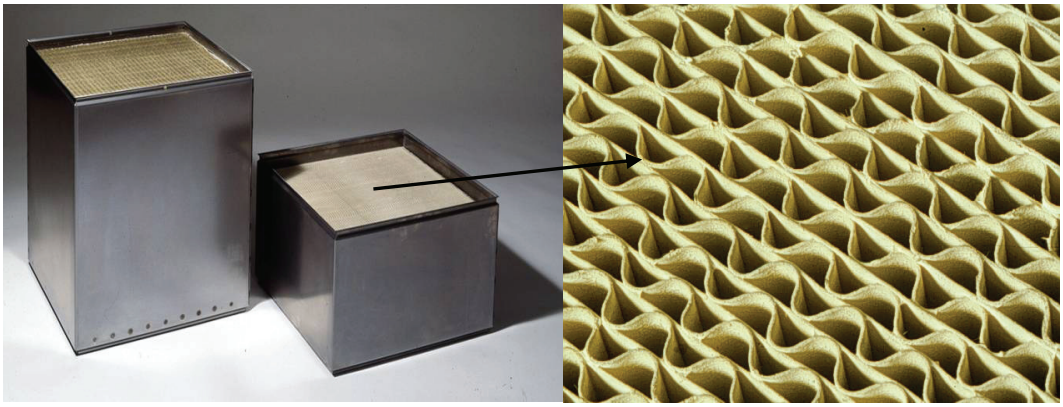

Figure 1.3: Picture of Topsøe $DeNO_x$ SCR catalysts with corrugated monolith [Slabiak (2005)].

- Reaction (a) is the standard SCR $DeNO_x$ reaction for NO and takes place in the temperature range between 150-550°C.
- Reaction (b) is the reduction of NO_2 and takes place in the temperature range between 150-550°C.
- Reaction (c) is a fast SCR reaction and is only significant in the low temperature range between 150-350°C.
- Reaction (d) is the oxidation of ammonia and takes place only in the high temperature range above 450°C.

Reaction (a) in Equation (1.1) is the most favoured reaction and accounts for the overall stoichiometry of the SCR $DeNO_x$ process. The "selective" part of the SCR $DeNO_x$ process refers to the ability of ammonia to react selectively with NO_x instead of being oxidized by oxygen [Forzatti and Lietti (1996)].

Figure 1.3 shows a picture of a Topsøe SCR $DeNO_x$ catalyst based on a corrugated, fibre-reinforced titanium dioxide (TiO_2) carrier impregnated with the active divanadium pentaoxide (V_2O_5) and tungsten trioxide (WO_3). The Topsøe SCR $DeNO_x$ catalyst has a cross-sectional area of 466 × 466 mm and exists in two different lengths of respectively 250 and 500 mm. For coal fired power stations, the high dust position is the most used position for the SCR $DeNO_x$ configuration where it is placed between the economizer and the air preheater. The reason for this is that the temperature of the flue gas between the economizer and the air preheater is in the range of 300-400°C which is optimal for catalytic activity [Soud and Fukasawa (1996); Forzatti and Lietti (1996); Beeckman and Hegedus (1991)].

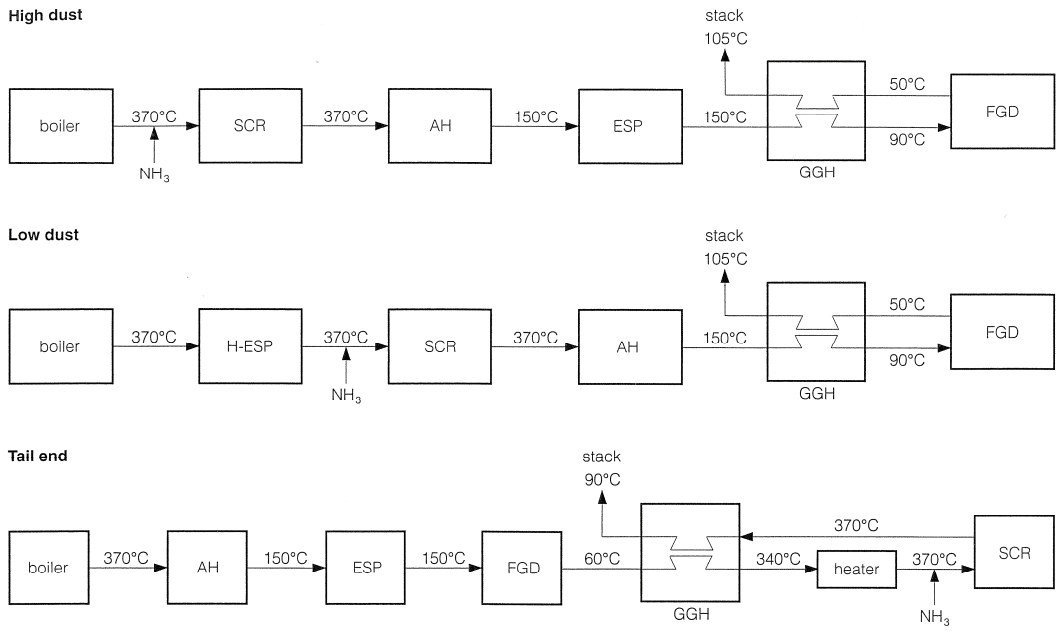

Figure 1.4: Schematic illustration of high dust and tail end/low dust configuration for coal fired boilers [Wu (2002)].

A schematic illustration of the high-dust, low-dust and tail-end configurations of the SCR $DeNO_x$ system applied to coal fired power stations is shown in Figure 1.4. The high-dust position typically ensures 80-90% NO_x reduction [Forzatti (2001)]. The low-dust configuration is generally considered if the electrical resistance of the fly ash and particles permits the use of a hot electrostatic filter. Another advantage of the low-dust configuration is the low catalyst degradation due to fly ash plugging, erosion and attrition. Because of cost issues due to gas reheating, the tail-end configuration is used only when the flue gas contains high amounts of catalyst poison, e.g. arsenic, alkali, phosphorous or $CaSO_4$ to avoid catalyst degradation, or where the conditions around the boiler do not allow build-in of a high-dust SCR reactor.

1.4.2 Operating Issues with SCR $DeNO_x$ Technology

Loss of catalytic activity (deactivation) is a major problem related to operating heterogeneous catalysis. The deactivation process is both chemical and physical by nature and occurs simultaneously with the main reactions and is an inevitable process. However, it can be slowed down and some of its consequences can be avoided [Forzatti and Lietti (1999)].

1.4.2.1 Deactivation

Deactivation of catalysts can occur due to a number of different mechanisms which are both chemical and physical by nature. The five main categories are the following [Jensen 2004; Zheng et al. (2005); Bartholomew (2007)]:

- Chemical poisoning
- Plugging and fouling/blinding
- Sintering
- Loss of active component
- Inhibition

The loss of activity due to chemical poisoning is caused by chemisorption of components on the active sites, like e.g. arsenic, alkali or phosphorous components. Fouling or blinding is a physical blockage of the pore systems where the deposited aerosol particles form a surface fouling layer, like e.g. a $CaSO_4$ fouling layer. Plugging is catalytic deactivation due to physical blocking of macro pores or the channels in the catalyst caused by fly ash and particles in the flue gas. Sintering is the loss of activity due to loss of (active) surface area at high temperatures. Loss of active components (vanadium depletion) may occur due to vaporization of vanadium from the catalyst. Inhibition is a reversible condensation of liquid/solid in the catalyst structure, e.g. ammonium bisulphate condensation.

1.4.2.2 Plugging and Deposition

The high-dust zone in the stationary power stations is usually preferred for placing the SCR reactor. Therefore, a major operating problem using the SCR $DeNO_x$ process under high-dust conditions is the risk of deposition in the channels or totally plugging the channels in the monolithic catalyst due to the high content of fly ash and particles in the flue gas.

The content of fly ash and particles formed by the combustion processes is usually around 10 g/Nm^3 [Raask (1985), p. 373]. Monolithic catalysts are generally designed as a collection of catalytic channels (see Figure 1.3) where the flue gas flows parallel to the wall to minimize the risk of plugging. Despite regular soot blowing it is observed that a major part of the channels in the catalysts are generally being deactivated due to plugging (see Figure 1.5). Plugging can be minimized, e.g. by using larger channel diameters but the latter requires a larger catalyst volume in order to obtain the same conversion which makes the reactor more expensive. Figure 1.5 illustrates plugging of channels in a monolithic

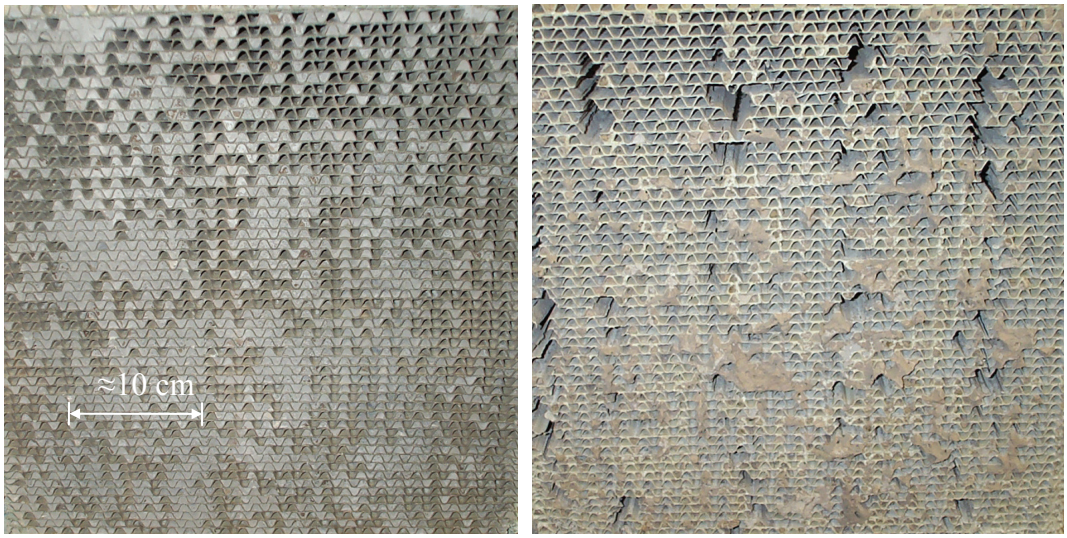

Figure 1.5: Plugging of channels in a monolithic catalyst from Nordjyllandsværket. The left picture is from the top of the catalyst and the right picture from the bottom. Hydraulic diameter about 6.4 mm [Jørgensen (2001)].

catalyst due to fly ash particles from the Power Station, Nordjyllandsværket. The left picture of Figure 1.5 shows the catalyst from the top and the right picture shows the catalyst from the bottom. The picture clearly shows that many of the channels have been blocked due to plugging and it also shows severe erosion at the bottom of the catalyst.

In low-dust applications the SCR reactor is placed after the electrostatic filter and before the air preheater. The content of fly ash particles in the flue gas after the electrostatic filter is typically between 10-20 mg/Nm^3. Figure 1.6 shows severe plugging ("volcano type") in a low-dust application. This type of installation has to be vacuum cleaned every 2-3 month because of plugging.

1.5 Scope of this Thesis

The main objective of the present study has been to develop a general CFD model for prediction of particle deposition and deposit build-up in SCR DeNO$_x$ monoliths. Focus has been put on investigating deposition mechanisms for deposition of nanometer, submicrometer and micrometer particles in laminar flow, and the main topics are:

Figure 1.6: Low dust application. Example of "volcano type" of deposition in a waste incineration plant from Brussels after 15,000 to 20,000 hours of operation. Hydraulic diameter about 3.4 mm. Courtesy Topsøe.

- Experimental investigations of particle deposition due to Brownian diffusion
- Experimental investigation of particle deposition due to shear-induced lift
- Pilot scale plugging experiments of SCR $DeNO_x$ monoliths
- CFD modelling of particle deposition

Emphasis has been put on obtaining experimental results used for validating the fundamental deposition mechanisms implemented in a general CFD model and obtaining results from pilot scale experiments in order to validate this model for prediction of particle deposition and deposit build-up in SCR $DeNO_x$ monoliths.

The present thesis consists of six chapters. In chapter 2 the present knowledge of particle deposition mechanisms are reviewed. This chapter also gives a short overview of plugging and deposition in monolithic catalysts and a short overview of ash formation. The experimental methods for investigating particle deposition and plugging in laminar and turbulent flow are presented in chapter 3. The

computational fluid dynamics method including particle transport and deposition mechanisms due to convection, diffusion, electrostatic dispersion, shear-induced lift, particle-wall interaction and a simple model for particle-wall adhesion and deposit build-up are presented in chapter 4. Chapter 5 gives the results and discussion of the experimental investigations of particle deposition and comparison with CFD simulations. Finally, conclusions and suggestions for further work are given in chapter 6.

Chapter 2

Literature Review

The present chapter reviews the current knowledge of particle deposition mechanisms in laminar and turbulent flow and also shortly describes operating issues with the SCR $DeNO_x$ technology and fundamental fly ash formation mechanisms.

2.1 Plugging and Deposition

Plugging of the SCR $DeNO_x$ monolith by fly ash particles can be a severe operating problem both in the high-dust zone as illustrated in Figure 1.5 and in low-dust applications as illustrated in Figure 1.6. Besides fly ash, plugging can also be due to deposition of ammonium sulphates on the catalyst which would also cause deactivation. Plugging of the monolith will make the pressure loss across the monolith increase which is another undesired effect. Sometimes it is observed that the fly ash found in the plugged channels has been hardened, and often a crust of hardened fly ash is found especially at the top and bottom of the plugged channels.

Figure 2.1a illustrates plugging of the catalyst initiated by top plugging, which e.g. can occur if a pile of fly ash falls down on the catalyst or if stalactites on the catalyst front edge tip over or by inertial impact. The tendency towards this kind of plugging will primarily depend on the void fraction and hydraulic diameter of the catalyst. Figure 2.1b illustrates plugging of the catalyst initiated by inlet plugging because of the angle of incidence of the gas flow to the monolith. This type of plugging is often seen in SCR $DeNO_x$ catalysts [Jørgensen (2001); Thorhauge (2004)]. The effect is probably due to separation of the flow at the front edge of the catalyst where submicrometer particles will probably deposit due to Brownian and turbulent diffusion. At the same time, the deposit will be

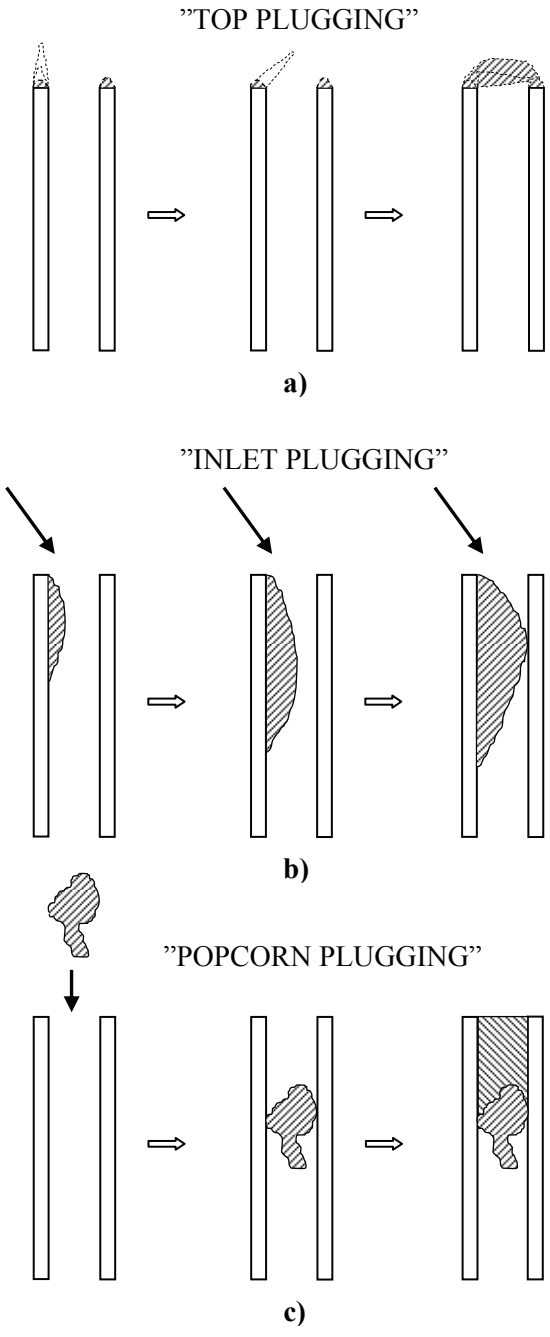

Figure 2.1: Schematic illustration of plugging of the monolithic catalyst. a) Initiated by top plugging. b) Initiated by inlet plugging. c) Initiated by popcorn plugging.

protected from inertial impaction from larger particles because of the angle of incident of the gas flow, which would probably otherwise have eroded the deposit.

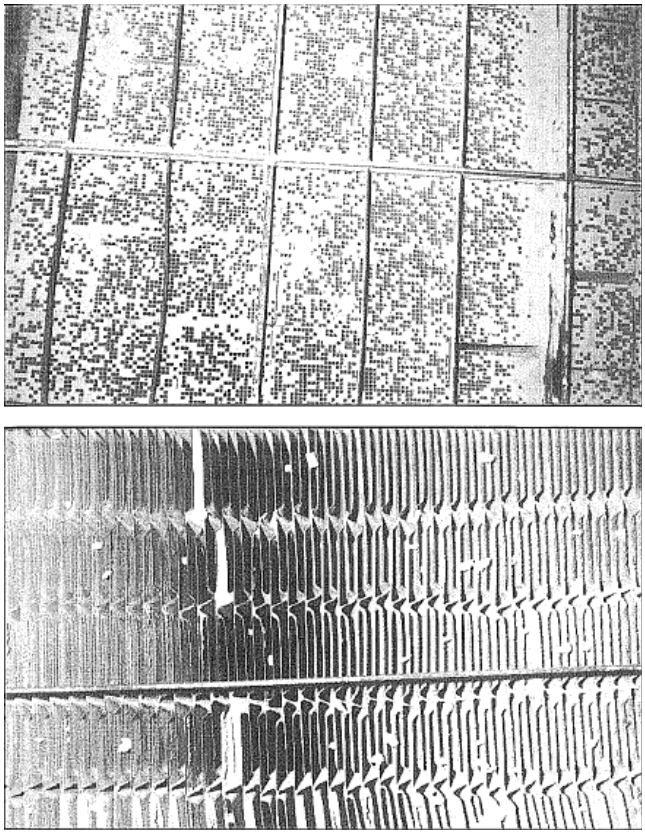

Figure 2.2: Comparison of plugging in honeycomb and a plate-type catalyst after approximately 10,000 hours of operation [Spitznagel et al. (1994)].

According to Thorhauge (2004), the hydraulic diameter of the channels in the monolithic catalyst will probably not have any effect on this type of plugging. Figure 2.1c shows an illustration of plugging due to fly ash agglomerates ("popcorn") with a size comparable to the hydraulic diameter of the channels in the monolithic catalyst. Fly ash particles usually deposit on heat transfer surfaces, such as the furnace water wall of a boiler, to form sintered masses of fly ash particles. When these agglomerates are dislodged they often break into small pieces. These pieces are about 1 to 30 mm and are often called "popcorn ash" due to the resemblance to popcorn in size and low apparent density [Cherkaduvasala et al. (2007)]. According to Thorhauge (2004) the catalyst resistance against "popcorn" is probably determined by the surface roughness and hydraulic diameter.

There has not been much work reported in the open literature on pilot plant test of fly ash plugging of SCR monolithic catalysts. Benson et al. (2005) investigated the potential for fly ash plugging and catalyst blinding for Selective Catalytic

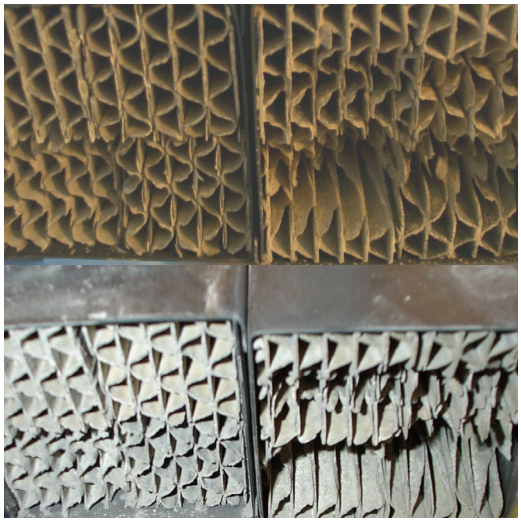

Figure 2.3: Erosion and attrition of the fronts of monolithic catalysts [Jensen (2002)].

Reduction of NO_x control using a slipstream reactor at power plants firing subbituminous and lignite coals. These types of coal produce ash that plugs and blinds catalysts and the problems are related to the formation of sulphate- and phosphate-based blinding materials on the surface of the catalysts and the carrying of deposit fragments, or "popcorn ash", from other parts of the boiler and depositing them on the top of the SCR catalysts. Formation of low-melting-point sodium-calcium-magnesium sulphates, phosphates, and possibly carbonates is therefore the most significant problem that limits a successful application of SCR catalysts to lignite coal. The reason for this is because it will form on the surface of the catalysts and it will carry over deposits that will plug the catalyst openings resulting in increased pressure drop and decreased efficiency. But the degree of ash-related impacts on SCR catalyst performance depends on the composition of the coal, the type of firing systems, flue gas temperature and catalyst design.

Another example of plugging in SCR catalysts is given by Spitznagel et al. (1994) in Figure 2.2 which shows a comparison of the blockage frequency for a honeycomb and a plate-type catalyst after approximately 10000 hours of operation. The catalysts have been operated downstream of a boiler with two $DeNO_x$ reactors in the high-dust configuration so that one contained the honeycomb-type catalyst and the other one the plate-type catalyst. Therefore both catalysts have been exposed to identical operating conditions. It can be seen that a larger number of channels have been blocked in the honeycomb-type catalyst compared to the plate-type where only a few channels are blocked.

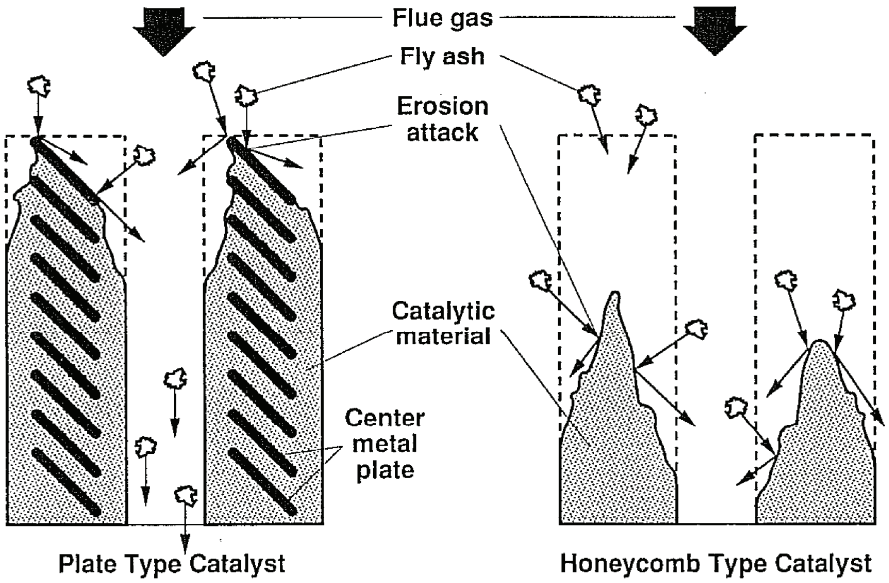

Figure 2.4: Principle of erosion of plate and honeycomb type catalysts [Spitznagel et al. (1994)].

2.2 Erosion and Attrition

There has not been much work reported in the open literature on erosion/attrition of monolithic catalysts due to the high contents of fly ash and particles in the flue gas. However, there has been reported general literature on erosion caused by solid particles and fly ash, e.g. Goodwin et al. (1969), Evans et al. (1978), Hilgraf and Cohrs (1992)].

Kotwal and Tabakoff (1981) have reported an approach for erosion prediction due to fly ash in combustion gases. Figure 2.3 shows an example of erosion due to fly ash particles in the flue gas. The effect of fly ash content on erosion is significant when particles larger than 30 μm are present, and the effect of fly ash composition on erosion is more significant in the case of high velocity particles impinging the surface [Kotwal and Tabakoff (1981)].

Jensen (2002) has investigated the propensity of fly ash erosion and observed erosion of $DeNO_x$ monoliths in the high-dust positions due to fly ash related to abrasion wear. Jensen (2002), stated that the erosion propensity of fly ash was mainly dependent upon particle size distribution and the content of mineral species, and that the erosion propensity tended to increase with increasing particle

size and increasing content of hard minerals such as quartz. This is also in accordance with observations done by Kotwal and Tabakoff (1981).

2.3 Fly Ash Formation

Ash formation involves various processes including coalescence, fragmentation, fusion vaporization and condensation that can occur sequentially or simultaneously. As inorganic matters are associated with the coal in different forms, they may experience different temperature-time histories during combustion. This may result in different physical-chemical transformations, thus generating ash particles of different sizes and chemistry.

2.3.1 Basic Mechanisms of Fly Ash Formation

A number of complex processes are involved in the ash formation, which takes place at the same time as the rapid oxidation of the organic carbon in the coal. In the coal combustion processes in most power plants, crushed coal from the mine is pulverised into particles (fine powder) between about 5 and 400 μm (less than 2% is over 300 μm and 70-75% is below 75 μm, for a bituminous coal [Wu (2005)]) with a mass mean diameter typically between 40-80 μm. The coal particles are then blown into the furnace with the carrier air, where the combustion takes place at temperatures from 1300-1700ºC. When the coal particles are injected into the furnace, the coal particles enter a zone of high turbulence and high temperature and are rapidly heated up to over 1300ºC by radiation and conduction from the hot gasses. The heating rate is extremely rapid and is in the order of 10^4 to 10^6 ºC/s. The coal particle may then mechanically break up into fragments during heating because of thermal stresses, and the particle may then burst open from the internal evolution of the vaporization of the volatile fractions originally present in the coal or formed by pyrolysis. The heated coal particle may also swell and become more porous. During combustion of the particle, pores in its structure open and the porosity increases further. In the end the particle becomes so porous that it disintegrates into a number of fragments in which each may contain a fraction of the mineral matter that was present in the parent coal particle.

Flagan and Friedlander (1978) identified two major mechanisms of particle formation in pulverized coal combustion. The first mechanism they identified was an ash residual which is left over after the carbon is consumed, and because the temperature of the pulverized coal combustion is high enough for the ash to melt,

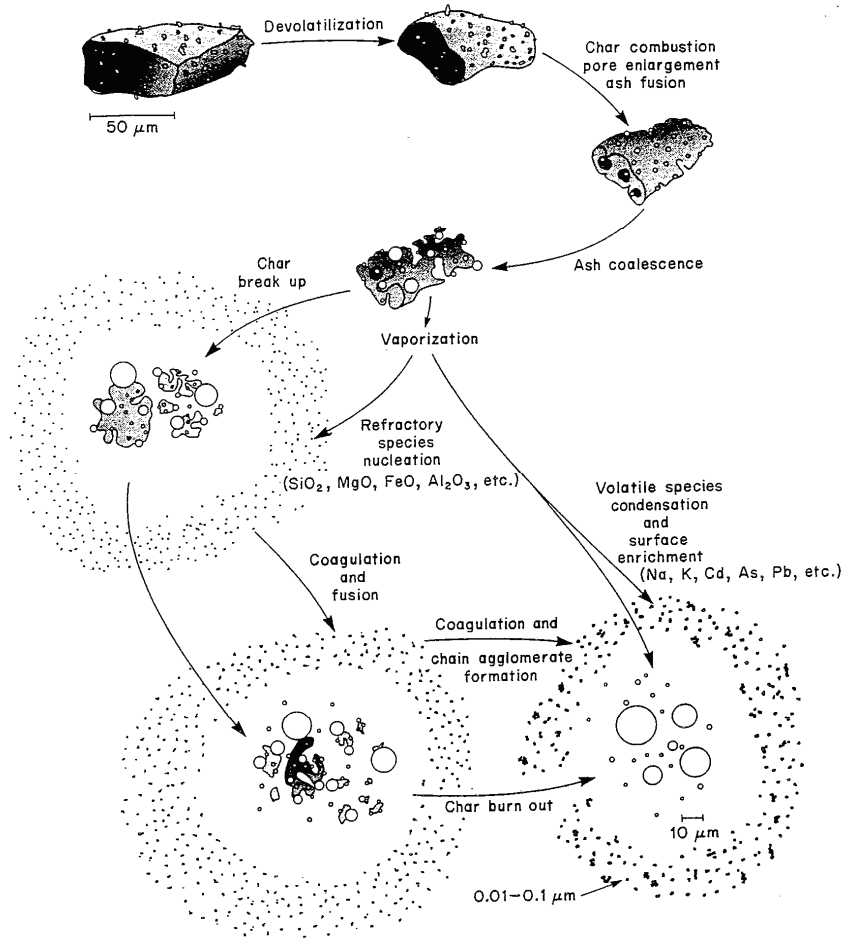

Figure 2.5: Schematic illustration of the mechanisms involved in formation of ash particles from coal combustion (from Flagan and Seinfeld (1988)).

this will form droplets where the size is related to the size of the burning coal particle. These particles have a mass mean diameter of 10 to 20 μm and account for most of the aerosol mass but probably not for the very large numbers of submicron particles observed in the flue gases of coal fired boilers [Flagan (1979)].

The other mechanism Flagan and Friedlander (1978) identified was that small fractions of the ash (about 1%) vaporized due to high combustion temperatures. Then part of the volatilized ash homogeneously nucleates to form very small particles which then grow by coagulation and condensation of additional vaporized ash. When the combustion products cool down these vapours condense either homogeneously forming new small particles or heterogeneously on the

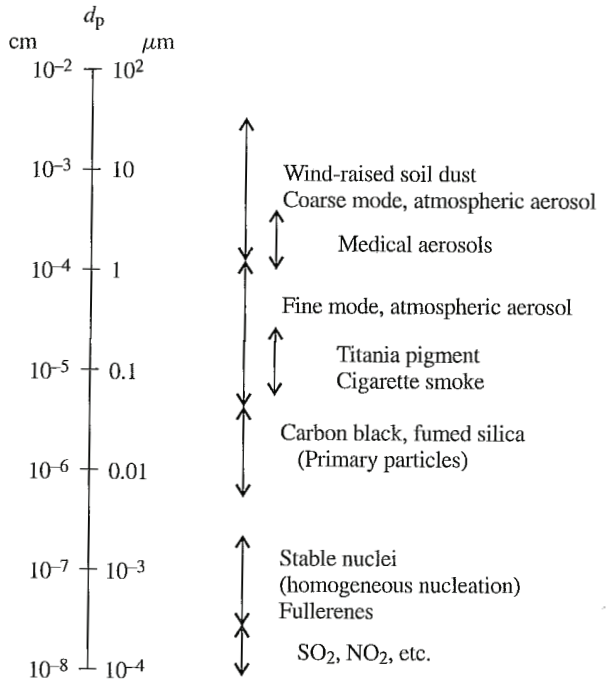

Figure 2.6: Example of aerosol particle size range [Friedlander (2000), p. 5].

surfaces of existing particles. Growth of particles by coagulation then leads to a predicted narrow mode in the particle size distribution in the size range of 0.01 to 0.1 μm, which is much smaller than the mineral inclusions originally present in the coal. The mechanism involved in the formation of coal fly ash is shown in a schematic representation in Figure 2.5.

Flagan and Seinfeld (1988) reported that measured particulate size distribution in the flue gases of pulverized coal combustion systems tends to support the two ash particle formation mechanisms identified by Flagan and Friedlander (1978) with a fine mode and a coarse mode of the particle sizes. The coarse mode which is generally above 1 μm in size with a broad peak at 3 to 50 μm diameter consists of most of the mass of the fly ash. The fine mode has a narrow peak around 0.1 μm and consists of less than 2% of the total fly ash mass.

2.4 Particle Dispersion and Deposition Mechanisms

Aerosols are small particles that are suspended in gases. They are formed by the conversion of gases to particles or by the disintegration of liquids or solids. They could also be created by re-suspension of powdered material or break-up of

agglomerates. In general, formation from the gas phase has a tendency to produce much finer particles than particles from disintegration processes (except in the case of condensation directly on existing particles). Particles that are formed directly from gases are usually smaller than 1 μm in diameter. Disintegration of solid particles tends to produce larger particles, e.g. fly ash that is formed by disintegration of solid particles typically contains aerosol particles with a size distribution between submicrometer particles up to about 200 μm. Smoke, dust, haze, fume, mist and soot are all commonly used terms in describing particulate systems. Dust usually refers to solid particles produced by disintegration processes, while smoke and fume particles are generally smaller and formed from gas phase. Mists are composed of liquid droplets and soot usually refers to small carbon particles generated in fuel combustion but are now frequently used to describe very fine solid particles of silica and other inorganic oxides generated intentionally in industrial processes [Friedlander (2000), p. 1]. Figure 2.6 illustrates an example of aerosol particle size ranges.

Aerosol transport mechanisms depend on the characteristics of the particles (size, shape, density and charge) and different mechanisms will be dominating for transporting submicrometer particles compared to larger particles. In the case of fly ash, these typically contain particles with a size distribution between submicrometer particles up to about 200 micrometers. In general, aerosol transport processes takes place at two different scales, where the scales are interacting and the transport processes include heat, mass, momentum and charge transfer. Looking at the individual particle scale, the exchange of heat, mass, momentum and charge may take place between the particle and the surrounding gas. At larger scales, looking at clouds of particles, they move due to gradients in concentration, temperature and electric fields at rates depending on particle size and properties. Understanding of particle transport mechanisms and deposition is basic to design of gas cleaning equipment, like for example SCR $DeNO_x$ monolithic catalysts. The different transport mechanisms that are potentially present in a monolithic catalyst are the following:

- Brownian diffusion
- Turbulent diffusion
- Turbophoresis
- Inertial transport
- Thermophoresis
- Shear-induced lift
- Electrostatic forces
- Drag forces
- Gravitational forces

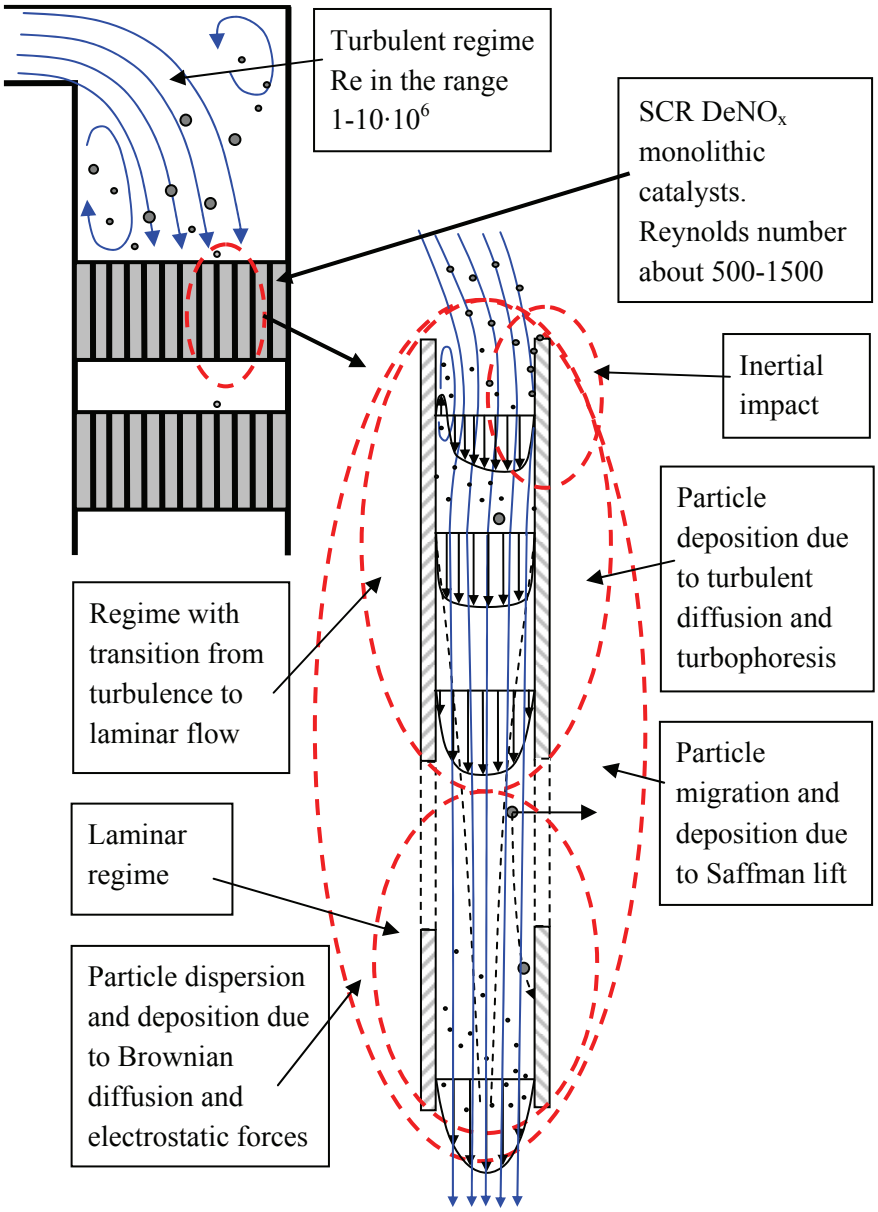

Figure 2.7: Schematic illustration of different particle deposition mechanisms that are potentially present in a monolithic catalyst.

These different transport mechanisms are discussed in the following sections of this chapter. Figure 2.7 illustrates these potentially present mechanisms in a monolithic catalyst. Upstream of the catalysts the flue gas flow is fully turbulent with a Reynolds number in the order of $1 \cdot 10^6$ depending on the operating conditions of the power plant. When the flue gas flow enters the channels of the monolithic catalysts, the flow will go into transition from turbulent to laminar

flow. The Reynolds number in the channels of the catalyst based on the hydraulic diameter of the channels is typically in the order of 500 to 1500 depending on the flow conditions and size of the channels. The turbulence will therefore decay in the channels, and the transition length from turbulence to laminar flow is in order of half the channel length based on calculations form Langhaar (1942). Turbulent diffusion and turbophoresis are therefore important transport and deposition mechanisms in the top part of the monolithic catalysts (about half the channel length) due to large gradients in the turbulent kinetic energy. Inertial impact on the top of the monolithic catalysts is also an important mechanism for deposition of particles. In the channels turbulent deposition will dominate the first part of the channels but in the part of the channels, where turbulence have died out and laminar flow is occurring, Saffman lift and Brownian diffusion will be the dominating deposition mechanisms. When the particles are charged they can induce an electrostatic field which disperses the particles and increases deposition. Because the monolithic catalyst is made of non-conducting/poorly-conducting materials the particles are not discharged when they deposit on the catalyst surface. This again induces an electrostatic field at the surface which will affect the particle deposition by attracting or repelling particles depending on whether they are positively or negatively charged. Due to flow separation at the outlet of the monolithic catalyst, submicrometer particles can be caught in the recirculation zone due to both Brownian and turbulent diffusion. These particles can also erode the catalyst surface at the outlet. Large micrometer particles (fly ash particles larger than 20 μm) with high inertia can also have a positive influence on the deposition because they can have a cleaning effect on the monolithic catalyst by detachment and re-suspension of already deposited particles [Thorhauge (2004)]. The reason for this is that the impact of particles with high inertia can contain a very high level of kinetic energy where some of the energy in the impact is also used to overcome the attractive forces of already deposited particles. These large particles can also erode the catalyst surface at the inlet. Large agglomerates of fly ash particles (so called “popcorn”) can block a channel in the monolithic catalysts and thereby initiate a plugging of the channel.

Thermophoresis, which is a physical phenomenon in which aerosol particles, when subjected to a thermal gradient, move against the direction of decreasing temperature, is not an important transport and deposition mechanism in a monolithic catalyst because the $DeNO_x$ process is very close to isothermal conditions. Gravitational forces (gravitational settling) are not an important deposition mechanism, except in the flow stagnation areas on top of the monolithic catalyst, because the monolithic channels are usually vertical with down flow. Thermophoretic and gravitational forces will therefore not be reviewed in the following.

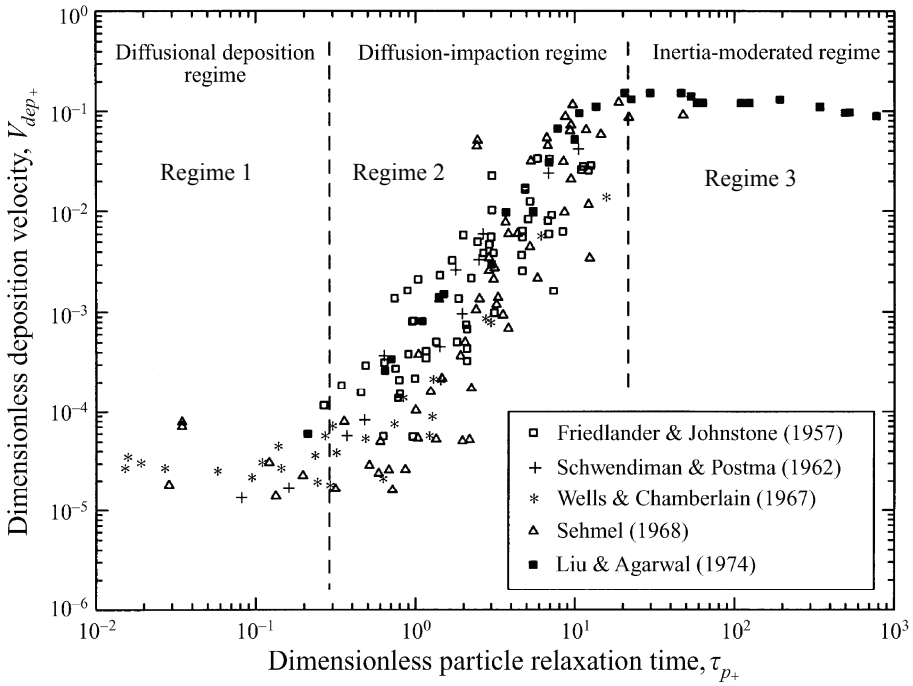

Figure 2.8: Summary of experimental data on dimensionless particle deposition velocity versus dimensionless particle relaxation time from fully developed turbulent pipe flow. Illustrate the three regimes in particle deposition. Regime 1, turbulent diffusion. Regime 2, turbulent diffusion-eddy impaction. Regime 3, particle inertia moderated [Young and Leeming (1997)].

The dimensionless deposition velocity, V_{dep}^{+}, is the effective velocity (dimensionless) with which particles migrate to a surface and is defined as follows

$$V_{dep}^{+} = \frac{J_w}{n_{bulk} u^*} \tag{2.1}$$

where J_w is the flux of particles to the wall per unit area, n_{bulk} is the bulk particle number concentration and u^* is the shear velocity (or friction velocity), which is derived based on dimensional analysis and can be calculated as follows

$$u^* = \sqrt{\frac{\tau_w}{\rho_f}} \tag{2.2}$$

where τ_w is the shear stress at the wall. The dimensionless particle relaxation time, τ_p^{+}, is defined as

$$\tau_p^{+} = \frac{\tau_p u^{*2}}{\nu} = \frac{S D_p^2 u^{*2} C_c}{18\nu^2}; \quad \tau_p = \frac{m_p C_c}{3\pi\mu D_p} = \frac{D_p^2 \rho_p C_c}{18\mu} \tag{2.3}$$

where S is the density ratio between the particle and the fluid, D_p is the particle diameter, m_p is the mass of the particle and μ is the dynamic viscosity of the fluid. In Equation (2.3), C_c is the Cunningham correction factor (or slip correction factor) calculated as follows

$$C_c = 1 + Kn\left[1.257 + 0.40\exp\left(-\frac{1.10}{Kn}\right)\right] \tag{2.4}$$

where Kn is the Knudsen number defined as

$$Kn = \frac{2\lambda}{D_p} \tag{2.5}$$

in which λ is the mean free path of the fluid. The Cunningham correction factor is introduced because Stokes' law is based on the solution of equations of continuum fluid mechanics (macroscopic scale) and is applicable to the limit of the *Knudsen number (Kn)* $\rightarrow 0$ [Seinfeld and Pandis (2006), p. 406].

Figure 2.8 shows the dimensionless deposition velocity, V_{dep}^{+}, versus the dimensionless particle relaxation time, τ_p^{+}, which is the characteristic time associated with the motion of the particle. Based on the experimental data in Figure 2.8, Young and Leeming (1997) showed, that the particle deposition is normally divided into three regimes - a diffusional deposition regime, a diffusion-impact regime and an inertia-moderated regime. The division into these three regimes has also been confirmed by Guha (1997), Guha (2008a) and Guha (2008b). In the diffusional deposition regime, particle transport to the walls in turbulent flows is well represented by a gradient diffusion model consisting of turbulent diffusion in the core of the pipe and Brownian diffusion in a very thin region directly adjacent to the wall. In the diffusion-impaction regime the deposition is a result of interaction between particles having significant inertia and the fluid turbulent eddies. In the inertia-moderated regime diffusion is assumed to have little or no influence on the deposition because the very large particles acquire sufficient momentum from large eddies in the turbulent core to reach the wall. The reduction in deposition rate with increasing particle size is explained by the increasing particle inertia causing a decreasing response to the turbulence. Young and Leeming (1997) also concluded that turbophoresis dominated the particle behaviour in the diffusion-impaction and inertia-moderated regimes.

2.4.1 Brownian Diffusion

Brownian motion, which is the stochastic movement of particles suspended in a fluid, is named in honour of the botanist Robert Brown, who in 1827, while he

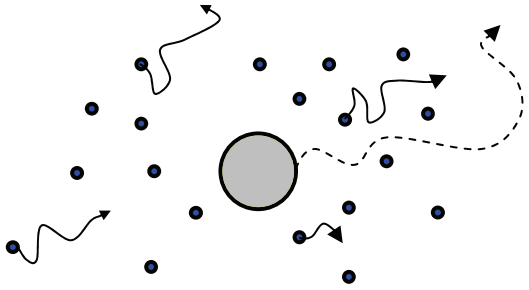

Figure 2.9: Schematic illustration of the Brownian motion process.

was examining pollen grains suspended in water, observed that particles in vacuoles in the pollen were showing continuous jittery motion. The first investigators to formulate the theory of Brownian diffusion were Einstein (1905) and Uhlenbeck (1930). The first to study the concept of the transport and deposition of particles from a fluid flow was Albrecht (1931) and his work was concerned with the collection of water drops and ice crystals suspended in an air flow.

Small particles suspended in a fluid will be continuously bombarded by the surrounding fluid molecules and result in a random motion of the particles known as *Brownian motion* – as illustrated in Figure 2.9. A way to quantitatively understand the Brownian motion is to consider a particle that is settling in a fluid due to the action of gravity. The particle will eventually reach its terminal velocity depending on its particle size and the viscosity of the fluid. Depending on the velocity of the particle a drag force is generated that acts in the direction opposite to the direction of the particle's motion. If the particle is large, e.g. larger than 1 μm, then the individual bombardment by the microscopic molecules of the fluid will have little or no effect on the motion of the particle. In that case, the motion of the particle will entirely be determined by the continuum fluid drag force and gravity. However, if the particle is small (a submicrometer particle), e.g. few nanometers, then the particle motion will exhibit fluctuations from the random collisions by the fluid molecules. The Brownian diffusivity of particles (or the coefficient of diffusion), D, is one of the important transport properties of aerosol particles. An expression for D can be defined as a function of particle size and the properties of the gas as follows

$$D = \frac{k_B T}{3\pi\mu D_p} C_c \tag{2.6}$$

where k_B is the Boltzmann constant, T is the temperature, C_c is the Cunningham correction factor, μ is the fluid viscosity and D_p is the particle diameter. Equation

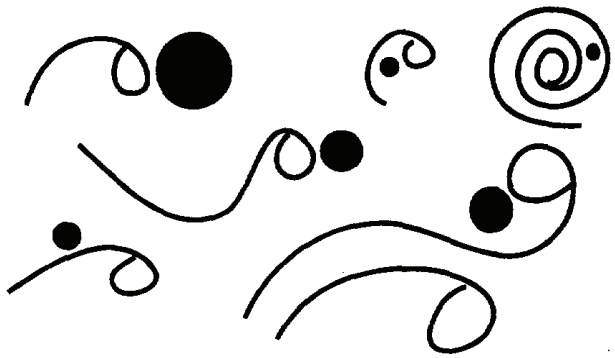

Figure 2.10: Schematic illustration of eddy-particle interaction in turbulent flow [Shirolkar et al. (1996)].

(2.6) is called the Stokes-Einstein equation. The spread of particles with time due to pure diffusion (no convection) can be determined by solving the equation of diffusion which can be stated as follows

$$\frac{\partial n}{\partial t} = D\vec{\nabla}^2 n \tag{2.7}$$

where n is the particle number concentration and D is the Brownian diffusivity of the particles as given in Equation (2.6).

2.4.2 Turbulent Diffusion

In general, the effect of turbulent eddies on particle motion and dispersion in a turbulent flow field is significant except for very large particles ($\tau_p^+ > 20$), which are non-responsive to the turbulent velocity fluctuations. For e.g. a particle with at density of 2000 kg/m^3 and a dynamic viscosity, $\mu = 3.11 \cdot 10^{-5}$ Pa·s (air at 623 K) in laminar pipe flow with a velocity of 6.9 m/s, $\tau_p^+ > 20$ corresponds to a particle diameter, $D_p > 27$ μm (u^* is the shear velocity calculated from the Blasius law $u^* = 0.2 u_{avg} \Big/ \mathrm{Re}^{\frac{1}{8}}$ [Blasius (1913)]). Turbulent diffusion which is particle dispersion in a turbulent flow field due to fluctuating fluid forces is a phenomenon similar to Brownian motion. Figure 2.10 shows an illustration of the eddy-particle interaction in turbulent flow. A qualitative understanding of the effect of a concentration gradient in homogeneous turbulence can be seen from Figure 2.11. Here, small particles closely follow the fluid eddies and at any location, the probability of a particle being transported by a fluid eddy to the left is the same as being transported to the right. But due to the higher number of particles further away from the wall, the flux through any imaginary cross-sectional plane from the right exceeds the flux from the left. Therefore, there is a net flux of particles from

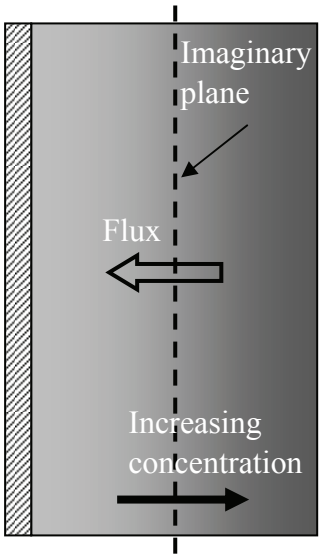

Figure 2.11: Schematic diagram showing flux of particles driven by concentration gradient and homogeneous turbulence intensity, obtained from [Guha (1997)].

the right to the left (towards the wall) along the concentration gradient. The same explanation is valid for particle flux due to Brownian motion [Guha (1997)].

Deposition of small particles in a turbulent boundary layer can be calculated by integrating a Fick's law type of diffusion as follows

$$J = -\left(D + \varepsilon_p\right)\frac{dn}{dy} \tag{2.8}$$

where D is the Brownian diffusivity, ε_p is the turbulent diffusivity (eddy diffusion coefficient), which varies with the position, y is the perpendicular distance from the wall and dn/dy is the particle concentration gradient. In Equation (2.8) it is assumed that the turbulent diffusivity, ε_p, of the particles due to turbulence is of the same order as the eddy viscosity, ε, of the fluid. The turbulent diffusivity, ε_p, can be estimated by the eddy viscosity, ε, given in Equation (2.9).

Davies (1966a) and Davies (1966c, p. 428), studied deposition due to turbulent diffusion of aerosol particles from turbulent flow in pipes and deduced an empirical expression for the eddy diffusion coefficient (turbulent diffusivity), ε_p, for aerosol particles. The empirical expression for the eddy diffusion coefficient relates it to the distance from the wall, y^+, between the centre of the pipe and the wall over a 10^6 fold range of y^+ and is given as follows

$$\frac{\varepsilon_p}{\nu} = \frac{\left(y^+\right)^{\left(4-\left(y^+\right)^{0.08}\right)}}{1000\left(\frac{2.5\cdot 10^7}{\mathrm{Re}}\right)^{\frac{y^+}{400+y^+}}} \tag{2.9}$$

where y^+ is a dimensionless distance from the wall and is a type of Reynolds number (immediately adjacent to the wall there will be an extremely thin viscous sub-layer followed by the buffer layer and the turbulent core) and is defined as

$$y^+ \equiv \frac{\rho y u^*}{\mu} \equiv \frac{y u^*}{\nu} \tag{2.10}$$

where y is the physical distance from the wall and u^* is friction velocity. For $y^+ \leq 1$ the viscous forces are dominating. Equation (2.9) is valid between

$$\begin{aligned} 10^{-7} \leq \frac{\varepsilon_p}{\nu} \leq 1000 \\ 0.05 < y^+ < 50000 \qquad \left(\mathrm{Re} = 10^6\right) \\ 0.05 < y^+ < 500 \qquad \left(\mathrm{Re} = 10^4\right) \end{aligned} \tag{2.11}$$

Davies (1966b) later extended his work to include small particles which were transported due to Brownian diffusion.

2.4.3 Turbophoresis

The Fick's law of diffusion given in Equation (2.8) does not capture the whole physics of deposition and neglects a mechanism that is operative in inhomogeneous turbulent flow that assumes dominance for large particle relaxation times. This mechanism is called Turbophoresis and Reeks (1983) was the first to use this name.

Turbophoresis causes particle transport due to gradients in the fluctuating velocities in a turbulent flow field and is a different mechanism compared to turbulent diffusion which causes particle transport due to gradients in the particle concentration. Figure 2.12 illustrates a uniform concentration of particles in an inhomogeneous turbulent flow, with a gradient of turbulence intensity perpendicular to the wall. The particles are assumed to be large so that they are in the inertia-moderated regime as shown in Figure 2.8 where they have considerable inertia to slip through the containing fluid eddy. Therefore, at any particular

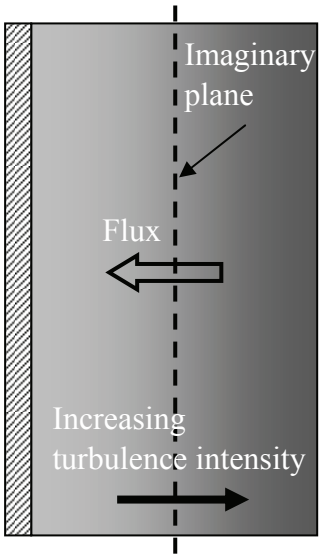

Figure 2.12: Schematic diagram showing flux of particles driven by a gradient in turbulence intensity and uniform particle concentration, obtained from [Guha (1997)].

location, the probability of a fluid eddy throwing the particle towards the right is the same as that of a fluid eddy throwing a particle towards the left. But however, the probability of a particle being thrown rightward from a region of low turbulence intensity so that it reaches the imaginary plane is less than that of a particle being thrown leftward from a region of high turbulence intensity. Consequently, there is a net flux of particles from a region of high turbulence intensity to a region of low turbulence intensity [Guha (1997)].

Guha (1997) and Guha (2008a) has stated that it is important to note that turbophoresis depends on the particle root-mean-square (RMS) velocity and therefore may be different from the fluid RMS velocity if the particle inertia is large. The contribution from turbophoresis in dispersion and deposition is therefore negligible for small particles and Fick's law in Equation (2.8) is therefore an adequate description for deposition of small particles. When the particles are very small they will follow the fluid eddies effectively because the particle RMS velocity and the fluid RMS velocity are essentially the same, and turbophoresis is therefore negligible for small particles even if there is a gradient in the fluid turbulence intensity. For larger particles with larger particle relaxation time, τ_p, the turbophoresis becomes dominating and thereby increases the deposition rate by a few orders of magnitude. But for even larger particles (larger particle relaxation time, τ_p) the particles are less able to follow fluid fluctuations and the particle RMS velocity becomes progressively smaller as compared to the

fluid RMS velocity, which is one of the factors responsible for the eventual decrease in deposition velocity with increasing particle size – see Figure 2.8, regime 3. The application of the models will be illustrated in section 2.4.10.

2.4.4 Inertial Transport

Particles suspended in a gas may not be able to follow the motion of an accelerating gas because of their inertia and may lead to particle deposition on surfaces and is known as inertia deposition. This deposition mechanism is most important for particles larger than 1 μm and is, unlike Brownian diffusion, a deterministic process in the inertial range, except for the very important case of turbulent transport. An aerosol stream with large particles of high inertia in e.g. a bend, when forced to change direction, is unable to follow the streamlines. This can be evaluated by the Stokes number, *Stk*, which is a dimensionless number defined as

$$Stk = \frac{C_c \rho_p D_p^2 U_{avg}}{18 \mu R_{tube}} \tag{2.12}$$

where U_{avg} is the average velocity in the pipe and R_{tube} is the radius of the pipe. The Stokes number in Equation (2.12) gives information about whether the particles will be able to follow the streamlines in curved flow or they will deviate from the streamlines due to their inertia. If the Stokes number, $Stk << 1$, the particles will follow the streamlines perfectly and if $Stk >> 1$, they will continue moving in straight lines and deviate from the streamlines when these are curved. Depending on the initial particle position at the bend inlet and parameters such as the Stokes number, *Stk*, and the flow Reynolds number, Re, large particles (or particles with $Stk >> 1$) can collide with the walls and be removed from the suspending gas. Small particles with low inertia (or particles with $Stk << 1$) on the other hand can follow the streamlines closely and penetrate the bend.

2.4.5 Shear-Induced Lift

Lift forces on a spherical particle are e.g. due to rotation of the particle (Magnus lift) and may be caused either by a velocity gradient (shear field) or may be imposed by some other source such as contact or rebound from a surface or due to shear-induced lift (Saffman lift).

The Magnus lift force develops due to rotation of a particle as shown in Figure 2.13. If a sphere is immersed in a uniform Stokes flow, then the flow around the

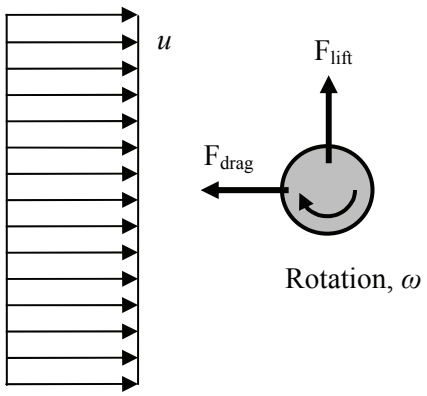

Figure 2.13: Schematic illustration of the Magnus effect.

sphere will be symmetric and there will be no lift on the sphere. If the sphere now rotates with a clockwise angular velocity, ω, the fluid at and near the top speeds up, whereas the flow at and near the bottom slows down. The flow then has a circulation and there will be a lift force on the sphere. Because of the circulation there will be a pressure difference from top to bottom of the sphere which then gives rise to a lift force. This effect was shown by Rubinow and Keller (1961).

Saffman (1965) and Saffman (1968) studied lift on particles in an unbound linear shear flow. He showed that a sphere moving through a very viscous fluid with a velocity relative to a uniform simple shear, where it also were allowed to rotate with an angular velocity and a translation velocity parallel to the streamlines of the flow, would experience a lift force as illustrated on Figure 2.14. This lift force plays an important role in the motion of particles in pipe flow, boundary layers, and other shear fields, where it creates a migration velocity perpendicular to the flow direction. Saffman (1965) and Saffman (1968) stated the lift force as follows

$$F_L = \mu \frac{KVR_p^2 \kappa^{\frac{1}{2}}}{\nu^{\frac{1}{2}}} + O\left(\nu^{-\frac{1}{2}}\right) \tag{2.13}$$

where K=6.46, V is the relative velocity of the particle to the gas flow, R_p is the radius of the particle, ν is the kinematic viscosity of the fluid, κ is the velocity gradient and the $O(\nu^{-1/2})$ is terms of order $\nu^{-1/2}$ or smaller. The direction of the lift force depended on the sign of the velocity gradient, κ. Saffman (1965) and Saffman (1968) defined the sufficient conditions for validity of equation (2.13), based on three Reynolds numbers, as

$$\mathrm{Re}_V << \mathrm{Re}_\kappa^{\frac{1}{2}}; \quad \mathrm{Re}_\kappa << 1; \quad \mathrm{Re}_\Omega << 1 \tag{2.14}$$

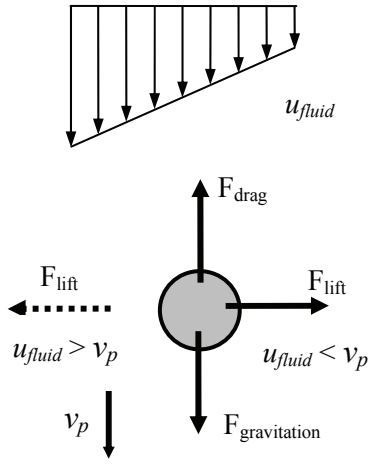

Figure 2.14: Schematic illustration of a particle under the influence of gravitation in an unbounded linear shear field.

The three Reynolds numbers were defined as follows

$$\mathrm{Re}_V = \frac{VR_p}{\nu}; \quad \mathrm{Re}_\kappa = \frac{\kappa R_p^2}{\nu}; \quad \mathrm{Re}_\Omega = \frac{\Omega R_p^2}{\nu} \tag{2.15}$$

As it can be seen from equation (2.13) for small Reynolds numbers (one can think of that as being due to large viscosity) the term $O(v^{-1/2})$ can be neglected and it can also be seen that to the order $O(v^{-1/2})$, the lift force is independent of the rotation of the particle [Saffman (1965); Saffman (1968)]. Saffman (1965) and Saffman (1968) therefore concluded, when the Reynolds number was small, that unless the rotation speed of the particle was very much greater than the rate of the shear, and for a freely rotating particle $\Omega = \kappa/2$, the lift force due to particle rotation was less by an order of magnitude than that due to shear.

Figure 2.15 shows a case where the relative velocity is positive and therefore there is a lift force in the direction of higher velocity of the fluid (the continuous phase). On the other hand, as shown in Figure 2.16, if the relative velocity is negative there is a lift force in the direction of lower velocity of the fluid. A physical explanation of the Saffman lift force (shear-induced lift force) is the following: Due to the shear field a velocity gradient will be present across the particle and the higher velocity at one side of the particle creates a lower pressure at this side and the lower velocity at the opposite side of the particle creates a higher pressure at that side. The pressure difference over the particle then creates a lift force from the high pressure side to the low pressure side. Depending on the relative velocity of the particle and the gas flow, the lift force can either be against the wall or away from the wall in a bounded channel flow.

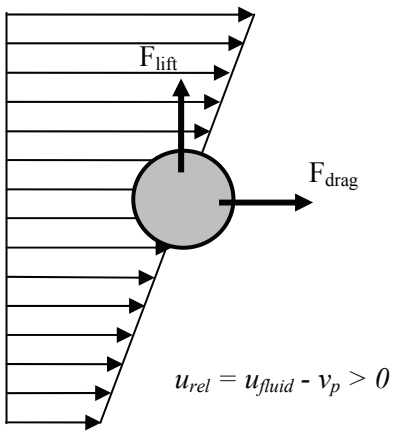

Figure 2.15: Schematic illustration of shear induced lift.

Other investigators have extended the work of Saffman (1965) and Saffman (1968) for unbounded linear shear flow. McLaughlin (1991) extended the work to situations in which the Reynolds number, Re_V, based on the velocity difference (slip velocity) was not small compared to the square root of the shear Reynolds number, Re_κ, but both Reynolds numbers were assumed to be small compared to unity. McLaughlin (1991) showed that the magnitude of the inertial migration velocity rapidly decreased to very small values when the Reynolds number based on the velocity difference became larger than the Reynolds number based on the square root of the shear Reynolds number. He also showed that, in general, Saffman's formula overestimated the magnitude of the migration velocity compared to the slip velocity.

Li and Ahmadi (1992) gave an expression for the Saffman lift force per unit mass due to shear flow as follows

$$\overrightarrow{F_L} = \frac{2K\nu^{1/2}\rho_f d_{ij}}{\rho_p D_p \left(d_{lk}d_{kl}\right)^{1/4}}\left(\vec{u}-\vec{u}_p\right) \tag{2.16}$$

where K=2.594 is the constant coefficient of Saffman's lift force, d_{ij} is the deformation tensor which is defined as follows

$$d_{ij} = \frac{1}{2}\left(\frac{\partial u_i}{\partial x_j}+\frac{\partial u_j}{\partial x_i}\right) \tag{2.17}$$

Equation (2.16) is a generalization of the two-dimensional expression given by Saffman (1965) and Saffman (1968) to a three-dimensional shear field and is valid for small particle Reynolds numbers. McLaughlin (1993) investigated the lift on a small sphere in a wall bound linear shear flow and thereby filled in the gap

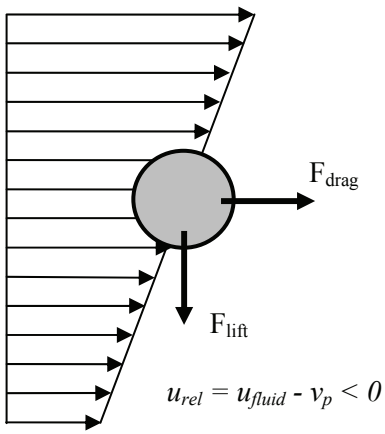

Figure 2.16: Schematic illustration of shear induced lift.

between the results earlier published by Saffman (1965) and Saffman (1968) and McLaughlin (1991) for unbounded linear shear flow. McLaughlin (1993) derived an expression for the lift force by superposition of the disturbance flow created by the wall and the migration velocity due to an unbounded shear field.

The lift force stated by Saffman (1965) and Saffman (1968) is only valid when the particle is far away from the wall and the shear rate is very strong and the expression for the lift force predicts that it points against the wall when the particle leads the fluid in the flow direction. The expression by McLaughlin (1993) predicts that the direction of the lift force depends not only on the slip velocity but also on the distance from the wall and the shear rate. Cherukat and McLaughlin (1994) derived an expression for predicting the inertial lift on a sphere moving in a linear shear flow field near a flat infinite wall, when the distance between the sphere, the wall and the radius of the sphere was comparable. In addition to the translation, the sphere also was allowed to rotate with the angular speed about an axis parallel to the wall and normal to the direction of the translation. They stated that the effect of rotation became only important when the shear was large and the sphere was close to the wall. In the present work the expression by Li and Ahmadi (1992) for unbounded flow is used for predicting the lift force in the CFD simulations.

2.4.6 Electrostatic Forces

Most aerosol particles carry some electric charge and some may be highly charged and their dispersion and deposition are strongly affected by the presence of an

electrostatic field. For highly charged particles the electrostatic force can be thousands of times greater than the force of gravity.

2.4.6.1 Particle Charging

Particles are charged by a number of different processes and among the important charging mechanisms are *flame charging*, *static electrification*, *tribo-electrification*, *diffusion charging* and *field charging* [Hinds (1999) p. 323].

Flame charging is due to particles formed in a flame or when particles pass through a flame because direct ionization of gas molecules at the high temperature of the flame creates high concentrations of positive and negative ions and thermionic emissions of electrons or ions from particles. The net charge of the particles depends on the material of the particle and is usually symmetric with respect to polarity giving an equal number of positively and negatively charged particles [Hinds (1999) p. 323]. *Static electrification* charges particles by mechanical action as they are separated from the bulk material or other surfaces and can produce highly charged particles under the right circumstances. Particles are usually charged during their formation, re-suspension, or high-velocity transport and the three primary mechanisms of static electrification that can charge particles while they are generated are *electrolytic charging*, *spray electrification*, and *contact charging* [Hinds (1999) p. 324]. *Electrolytic charging* occurs when liquids with a high-dielectric constant are separated from solid surfaces. An example is during atomization where these liquids strip off charge from the surface of the atomizer and produce slightly up to moderately charged droplets as the liquid separates from the surfaces. E.g. pure water is a high dielectric liquid that can become charged during atomization [Hinds (1999) p. 324]. *Spray electrification* is caused by the disruption of charged liquid surfaces, which produce charged droplets, when surfaces are disrupted during the formation of droplets by atomization or bubbling. The reason for this is that some liquids have a charged surface layer due to surface effects [Hinds (1999) p. 324]. *Contact charging* or triboelectrification (triboelectric effect) is caused during separation of dry, non-metallic particles from solid surfaces. Charge is transferred between a particle and a surface when a particle adheres to it causing the particle to acquire a net positive or negative charge when the particle separates from the surface. The polarity of the particle and the amount of charge of the particle depend on the material involved and their relative positions in the triboelectric series [Hinds (1999) p. 324]. The triboelectric series is a list that ranks various materials according to their tendency to gain or lose electrons. It usually lists materials in order of decreasing tendency to charge positively (lose electrons), and increasing

tendency to charge negatively (gain electrons). *Diffusion charging* is due to random collision of ions and particles due to Brownian motion and is the main charging mechanism for particles less than 1 μm and do not require an external electric field to charge the particles. Interaction between the charged particles induces an electrical field that also migrate ions. But as the charge accumulates on the particles it produces a field that tends to repel additional ions reducing the charging rate on the particle. *Field charging* is caused by unipolar ions in the presence of a strong electric field which charges the particles. The effect of field charging is more significant for particles larger than 1 μm and increases with the square of the particle size [Hinds (1999) p. 325].

2.4.6.2 Charge Limits

Hinds (1999) have stated that there are fundamental limits on the maximum amount of charge that can be acquired by an aerosol particle of a given size. In cases where there is no strong external electrostatic field a very high charge can be achieved before a limit of spontaneous charge loss is reached due to spontaneous emission of electrons from the particle surface. When this limit is exceeded electrons on the surface will be ejected from the particle by the force of mutual repulsion due to crowding of electrons. For negatively charged spherical solid particles this limit for maximum charge is reached when the self-generated field at the surface of the particle reaches the necessary value for spontaneous emission of electrons from the particle surface. For spherical solid particles this limit, i_L, is given by

$$i_L = \frac{D_p^2 E_L}{4 K_E e} \tag{2.18}$$

where D_p is the particle diameter, E_L is the surface field strength, K_E is the electrostatic constant of proportionality ($K_E = 1/(4\pi\varepsilon_0) = 9.0 \cdot 10^9$ Nm^2/C^2) and e is the elementary charge. The surface field strength, E_L, required for spontaneous emission of electrons is given as $E_L = 9.0 \cdot 10^8$ V/m. For positively charged particles similar limits exist, with the difference that a positive ion must be emitted instead of an electron. However, since emitting a positive ion is more difficult than an electron higher surface field strength is required. For positive charged particles the surface field strength, E_L, required for spontaneous emission of positive ions is therefore given as $E_L = 2.1 \cdot 10^{10}$ V/m. Figure 2.17 shows the charge limit for negatively and positively charged particles respectively versus particle diameter.

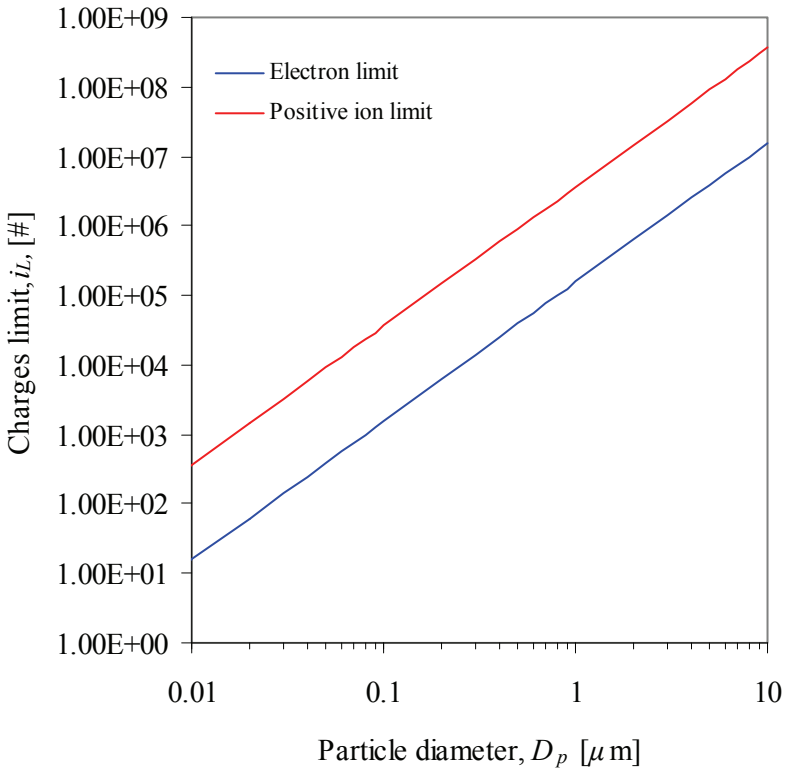

Figure 2.17: Particle charge limits, i_L, versus particle diameter, D_p, for positive and negative charged solid spherical particles, respectively.

2.4.6.3 Equilibrium Charge Distribution

In principle the minimum charge on an aerosol particle is zero, but this condition is rarely achieved because of random collisions between air ions and the aerosol particles. As an example the concentration of ions in ambient air is about 10^3 cm^{-3}, with approximately equal numbers of positive and negative ions. These pairs of positive and negative ions are produced by collision of cosmic rays and energetic nuclear particles produced by radioactive decay with the gas molecules [Byron and Willeke (2005) p. 542]. Therefore aerosol particles that are initially neutral will be charged due to random collisions between ions, and aerosol particles that are initially charged will lose their charge slowly as the charged particles attract oppositely charged ions. In this bipolar ion mixture these competing processes will eventually lead to an equilibrium charge state with the ionic atmosphere. This charge equilibrium is called the Boltzmann equilibrium charge distribution, but even though this minimum amount of charge is very small with a statistical

probability that some particles carry no charge, then a small fraction of the aerosol particles still carries more than one elementary charge. In this equilibrium state, the fraction of particles with diameter, D_p, that carries i charges is given as follows [Hinds (1999) p. 335; Byron and Willeke (2005) p. 542]

$$f_n = \frac{\exp\left(-\frac{i^2}{2\sigma^2}\right)}{\sum_{k=-\infty}^{\infty} \exp\left(-\frac{k^2}{2\sigma^2}\right)}; \qquad \sigma^2 = \frac{D_p k_B T}{2e^2} \tag{2.19}$$

For aerosol particles larger than 0.05 μm, Equation (2.19) becomes equal to the normal distribution and can be written as [Kasper (1981); Hinds (1999), p. 335]

$$f_v = \left(2\pi\sigma^2\right)^{-1/2} \exp\left(\frac{-i^2}{2\sigma^2}\right); \quad \sigma^2 = \frac{D_p k_B T}{2e^2} \tag{2.20}$$

Equation (2.20) agrees with Equation (2.19) within 7% for particles larger than 0.02 μm and within 0.04% for particles larger than 0.05 μm [Hinds (1999), p. 335]. For particles larger than 0.2 μm an empirical approximation for the average number of charges, $\bar{i}$, that is accurate within $\pm$ 5% can be defined as [Hinds (1999), p. 335]

$$\bar{i} \approx 2.37\sqrt{D_p} \tag{2.21}$$

2.4.6.4 Bipolar Charge Distribution

There have been an increased number of investigations of the charging of particles in the submicrometer regime because the measurement of aerosol particle size distributions are frequently obtained using a differential mobility analyser (DMA). The reason for this is that aerosol particles can be classified due to their electric mobility if the bipolar charge distribution for the aerosol is known.

Wiedensohler (1988) studied the bipolar charge distribution on aerosols and presented an empirical expression in order to approximate the bipolar size distribution in the size range from 1-1000 nm calculated from the Fuchs (1963) model. The approximation for the charge distribution which is valid for the particle size ranges between 1 nm $\leq D_p \leq$ 1000 nm for N = -1, 0, 1 and 20 nm $\leq D_p \leq$ 1000 nm for N = -2,-1, 0, 1, 2 elementary charges are given as follows [Wiedensohler (1988)]

$$f(N) = 10^{\left[\sum_{i=0}^{5} a_i(N)\cdot\left(\log D_p\right)^i\right]} \tag{2.22}$$

where $a_i(N)$ is the approximation coefficient [Wiedensohler (1988)], N is the number of elementary charges and D_p is the particle diameter. Wiedensohler (1988) also stated that the fraction of particles carrying three or more elementary charges could be calculated using the following expression originally derived by Gunn (1956) as follows

$$f(N) = \frac{e}{\sqrt{\left(4\pi^2\varepsilon_0 D_p k_B T\right)}} \exp\left(\frac{-\left[N - \frac{2\pi\varepsilon_0 D_p kT}{e^2} \ln\left(\frac{c_{NI+} Z_{I+}}{c_{NI-} Z_{I-}} \right) \right]^2}{2\frac{2\pi\varepsilon_0 D_p k_B T}{e^2}} \right) \tag{2.23}$$

where e is the elementary unit charge, ε_0 is the dielectric constant, $C_{NI\pm}$ is the ion concentration, $Z_{I\pm}$ is the ion mobility and k_B is the Boltzmann constant. Wiedensohler (1988) stated that aerosol particles smaller than approximately 70 nm carry at most two elementary charges. In order to calculate the bipolar charge distribution for submicrometer aerosols calculated based on Fuchs (1963) theory detailed computations are required.

The calculated bipolar charge distribution on submicrometer aerosol particles based on the approximation by Wiedensohler (1988), given in Equation (2.22), is shown in Table 1. It also shows the average charge on the submicrometer aerosol particles based on the bipolar charge distribution. It can be seen from Table 1 that the average charge, on the submicrometer aerosol particles, for a bipolar charge distribution is negative. The reason for this is that the molecular weight of positive and negative ions differs and they therefore have different electric mobility. Gunn (1956) has stated that all ion-producing processes simultaneously generate a positive and a negative ion and therefore except for the influence of combination processes and transport due to electric fields there is a marked tendency to establishment of equal ionic population densities. However, since the electrical mobility of the negative ion is some 40 % larger than that of the positive ion, there is a parallel tendency for the negative ion conductivity to exceed that due to the positive ion. Tsai et al. (2005) has stated that the mobility of an electron is greater than that of a positive ion and therefore the fraction of particles carrying N negative charges is greater than that of particles carrying N positive charges.

Table 1: Calculated bipolar charge distribution based on Equation (2.22) from Wiedensohler (1988). The charge distribution is given in per cent.

D_p (nm)	$f(N)$ -2	-1	0	1	2	*Average charge*
1	-	0.48	99.93	0.45	-	-0.000306
1.3	-	0.57	98.10	0.53	-	-0.000406
2	-	0.83	97.42	0.75	-	-0.000773
3	-	1.25	97.65	1.10	-	-0.00152
5	-	2.25	96.93	1.89	-	-0.003546
7	-	3.36	94.98	2.76	-	-0.0060343
10	-	5.14	91.24	4.12	-	-0.010216
13	-	6.95	87.39	5.49	-	-0.014591
20	0.02	10.96	79.31	8.52	0.01	-0.02461
30	0.17	15.79	70.28	12.19	0.10	-0.037407
50	1.14	22.29	58.14	17.25	0.68	-0.059633
70	2.80	25.79	50.32	20.13	1.66	-0.079326
100	5.61	27.93	42.59	22.10	3.41	-0.102203
130	8.13	28.21	37.40	22.60	5.14	-0.11598
200	12.11	26.41	29.91	21.65	8.34	-0.123127
300	14.50	22.98	24.06	19.27	10.88	-0.109329
500	14.90	18.16	18.18	15.66	12.39	-0.075131
700	13.97	15.58	15.08	13.65	12.60	-0.046693
1000	12.61	13.85	12.35	12.29	13.19	-0.003988

Li and Ahmadi (1993a) and Soltani et al. (1998) also stated that the real charge distribution in the atmosphere may be different from the Boltzmann charge distribution for particles less than 0.1 μm and that one reason for this is that negative ions tend to have higher mobility (and diffusivity) when compared with the positive ions. As a result of that, small particles tend to carry more negative charges (roughly twice as much) than positive ones, which skew the distribution.

2.4.6.5 Electrostatic Forces

Electrostatic deposition can take place because of the image (polarization) force between charged particles and a conductive wall, or because of electrostatic repulsion between particles charged with the same polarity (space-charge) [Alonso and Alguacil (2007)]. Coulomb forces lead to attraction or repulsion at long distances and image forces lead to attractive forces at small separations

[Byron and Willeke (2005), p. 542]. Shah et al. (2007) stated the electrostatic force due to an electrostatic field in vector notation as follows

$$\vec{F}_E = q\vec{E} - \frac{q^2}{16\pi\varepsilon_0 y^2}\vec{n}_p \tag{2.24}$$

where $q=ie$ is the total charge carried by the particle and i is the number of elementary charges, $e=1.6\cdot10^{-19}$C, $\vec{E}$ is the electric field strength, y is the distance to the wall, $\vec{n}_p$ is the unit vector from the location of the particle to the point of the wall where the distance is smallest and $\varepsilon_0=8.859\cdot10^{-12}\mathrm{AsV^{-1}m^{-1}}$ is the permittivity of the gas. In (2.24) the first term on the right hand side is the Coulomb force and the second term is the image force. Shah et al. (2007) stated that the image force only has a significant contribution to the electrostatic force in the vicinity of the wall. Li and Ahmadi (1993a), He and Ahmadi (1999) and Soltani and Ahmadi (1999) have stated the electrostatic force including two additional terms due to the dielectrophoretic force and the dipole-dipole force. In the present work only the electrostatic force due to the Coulomb force and the image force is used.

2.4.6.6 Image Force

An image force is present between a charged particle and a conducting surface. This corresponds to the force exerted by an image charge of $-q$ at position $-y$ from the surface, when the particle is at position $+y$ from the surface [Chen and Lai (2004)].

Vauge (2002) and Mayya et al. (2002) discussed the image force in detail. Vauge (2002) concluded that the image force did not contribute to the capture of charged aerosol particles by a conducting wall when treating the aerosol charges distributed as a continuum. Mayya et al. (2002) critized his conclusion, and by an analysis of the forces when the particles were considered discrete he obtain the collective influence of image forces on charged particles either confined to a cavity or present outside an electrically insulated sphere.

2.4.6.7 Space Charge

The concentration of a cloud of unipolarly charged aerosol particles will decrease as a result of the mutual electrostatic repulsion among the charged aerosol particles. Because of that, the total number of charged aerosol particles in a system will decrease with time due to migration of the charged particles to the boundaries of the system created by space charge [Davies (1966c)]. This

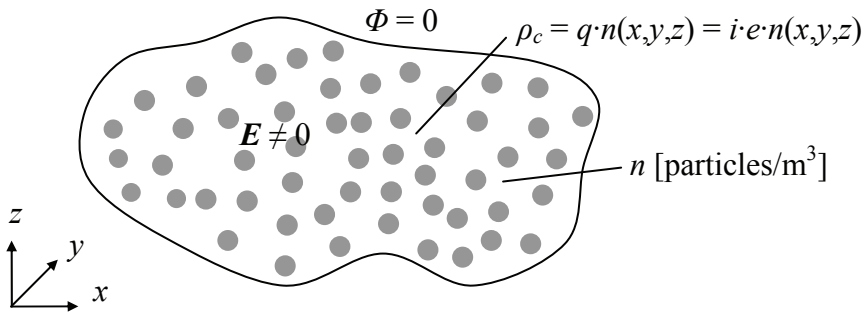

Figure 2.18: Schematic Illustration of space charging due to a cloud of unipolar charged particles or a cloud of particles carrying a positive or negative average charge in an enclosure with zero potential on the walls.

mechanism of aerosol decay is important when there is a high concentration of charged aerosol particles or when a strong source of ions is present, for example a radioactive source like a Krypton-85 source in an aerosol neutralizer. Figure 2.18 illustrates the concept of space charging due to a cloud of particles in an enclosure with zero potential on the walls. In general small particles carry few charges but their electrical mobility is high and therefore their contribution to the deposition process can be high even at moderately aerosol concentrations. Particle deposition by electrostatic repulsion has been studied for more than a century and a brief history can be found in Kasper (1981).

The electric field can be related to the charge density through the divergence of the electrical field strength, $\vec{E}$, as follows

$$\vec{\nabla} \cdot \vec{E} = \frac{\rho_c}{\varepsilon_0 \kappa} \approx \frac{\rho_c}{\varepsilon_0} \tag{2.25}$$

where ρ_c is the charge density and ε_0 is the permittivity of the free space (i.e. vacuum) and κ is the dielectric constant of the medium. Since the dielectric constant, κ, is essential unity for gases under all realistic conditions, only the permittivity, ε_0 is used in Equation (2.25). The charge density is the amount of charge per volume. The electric field strength is related to the electric potential, Φ, as follows

$$\vec{E} = -\vec{\nabla}\Phi \tag{2.26}$$

where Φ is the electric potential. The potential can be related to the charge density by substituting equation (2.26) into equation (2.25) as follows

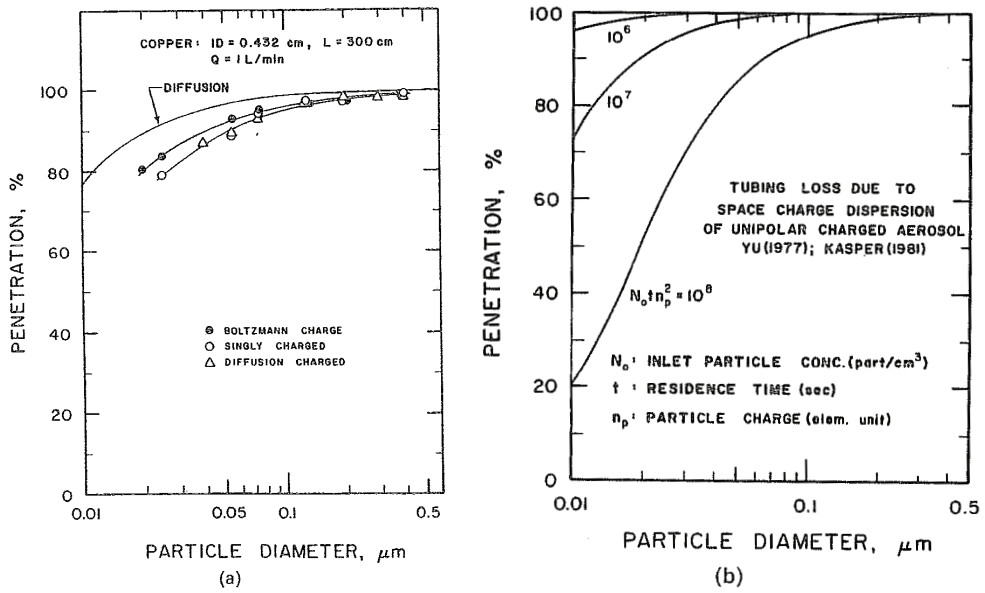

Figure 2.19: (a) Aerosol penetration of a charged aerosol through a conductive copper tube with a diameter of 0.432 cm, a length of 300 cm and a flow rate of 1 l/min. (b) Aerosol penetration of a charged aerosol through a conductive copper tube with a diameter of 0.965 cm, a length of 300 cm and a flow rate of 1 l/min [Liu et al. (1985)].

$$\vec{\nabla}\cdot\left(-\vec{\nabla}\Phi\right)=\frac{\rho_c}{\varepsilon_0}\Leftrightarrow\vec{\nabla}^2\Phi=-\frac{\rho_c}{\varepsilon_0} \tag{2.27}$$

Equation (2.27) is the Poisson equation, which in a charge-free region of space will become the Laplace equation

$$\vec{\nabla}^2\Phi=0 \tag{2.28}$$

For discrete charges, where the charge in a region consists of a number of discrete point-like charge carriers, like unipolar charged aerosol particles all carrying the same number of electrical unit charges. The charge density can be expressed as follows [Kasper (1981)]

$$\rho_c\left(\vec{r}\right)=q\,n\left(\vec{r}\right) \tag{2.29}$$

where q is the number of electrical unit charge, $n(\vec{r})$ is the aerosol particle number concentration and $\vec{r}$ is the position vector to the aerosol particle. The space charge of aerosol particles each carrying a charge, q, creates a non-zero potential within the system and if the particle number concentration, n, of the

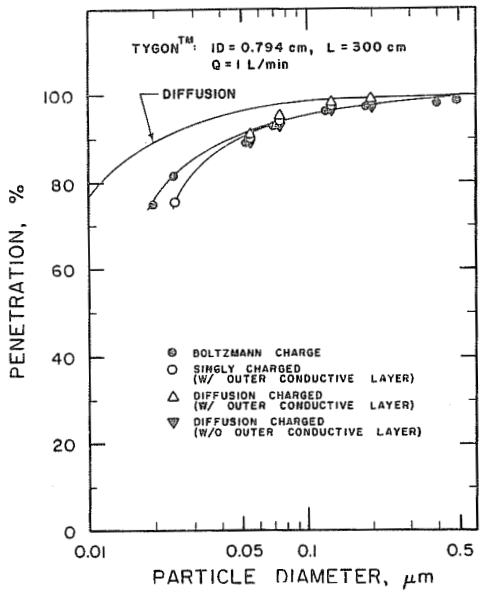

Figure 2.20: Aerosol penetration of a charged aerosol through a non-conductive Tygon (polyvinylchloride) tube with a diameter of 0.794 cm, a length of 300 cm and a flow rate of 1 l/min [Liu et al. (1985)].

aerosol particles are large, their space charge forms a continuum where the electrostatic potential, Φ, is a smooth function given by Poisson's equation as

$$\vec{\nabla}^2 \Phi = -\frac{q\,n}{\varepsilon_0} = -\frac{ie\,n}{\varepsilon_0} \tag{2.30}$$

where $q=ie$ is the total charge carried by a particle and n is the particle number concentration.

2.4.6.8 Electrostatic Field inside Tubes

Liu et al. (1985) carried out series of experiments in order to investigate the deposition of charged NaCl aerosol particles (0.01-0.5 μm) through a variety of coiled tubes of a length of 3 m, made respectively of conducting copper and insulating plastic. The experiments were carried out for various flow rates and tube diameters, but unfortunately Liu et al. (1985) did not specify the aerosol particle concentration in their experiments. Figure 2.19 shows the aerosol penetration measured through a conductive copper tubing with an internal diameter of 0.432 cm, a length of 3 m and a flow rate of 1.0 l/min for a singly charged aerosol, a diffusion charged aerosol, an aerosol with Boltzmann charge equilibrium and for a neutral aerosol (with zero charge) calculated based on

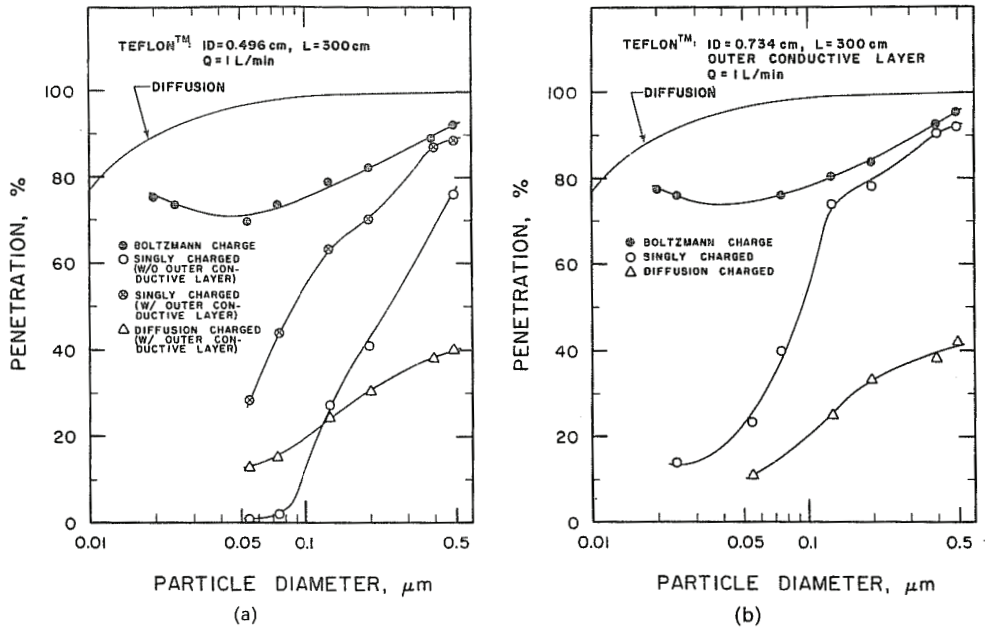

Figure 2.21: Measured aerosol penetration of a charged aerosol through a Teflon (polytetrafluoroethylene) tube with: (a) a diameter of 0.496 cm, a length of 300 cm and a flow rate of 1 l/min. (b) a diameter of 0.734 cm, a length of 300 cm and a flow rate of 1 l/min. Both tubing had an outer conductive surface [Liu et al. (1985)].

Gormley and Kennedy (1949), Equation (2.39). Liu et al. (1985) calculated the parameters governing image force (Equation (2.53), Yu and Chandra (1978)) and space charge deposition [Yu (1977)] and concluded that both image force and space charge were relatively unimportant and should not contribute significantly to particle deposition in the tube. It has to be said that this conclusion is only valid if the aerosol concentration is low or, regarding the image force, if the aerosols are only carrying a few charges.

Liu et al. (1985) also concluded that the difference between the observed penetration and that calculated by means of Gormley and Kennedy (1949), Equation (2.39) had to be explained by some mechanical effect (secondary flow). Figure 2.20 shows the aerosol penetration measured through a non-conductive Tygon (polyvinylchloride) tubing with an internal diameter of 0.794 cm, a length of 3 m and a flow rate of 1.0 l/min. The static electric charge on the tubing was generated by bending and flexing it a number of times. Liu et al. (1985) concluded that the measured penetration was nearly indistinguishable from that of conductive copper tubing under similar conditions i.e. electrostatic forces did not affect the result.

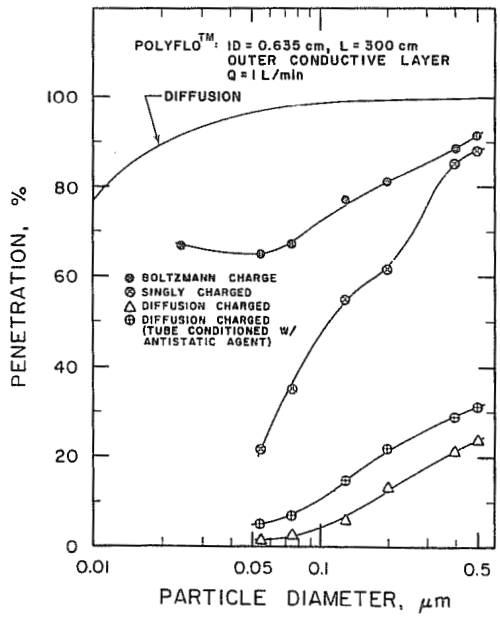

Figure 2.22: Measured aerosol penetration of a charged aerosol through a Polyflo (polyethylene) tube with a diameter of 0.635 cm, a length of 300 cm and a flow rate of 1 l/min. The tubing had an outer conductive surface [Liu et al. (1985)].

Liu et al. (1985) made quantitative measurements of the magnitude of the electric field in a plastic tube, by carrying out experiments in which the external surface of the plastic tubing was wrapped with a grounded aluminium foil. They stated that this conductive wrapping would cause some of the electric field lines originating from the electric charge on the plastic tubing surface to pass through the plastic tubing walls and terminate on the outer conductive layer. They also stated that without this outer conductive layer, the electric field lines would pass through the space inside the tube and terminate on the charge of an opposite polarity on the tubing surface. Liu et al. (1985) concluded that the conductive layer would be expected to reduce the effect of electric charge on the deposition of charged aerosol particles. Figure 2.21 and Figure 2.22 respectively show the results of the measured penetration of a charged aerosol through a Teflon tubing (polytetrafluoroethylene) with an internal diameter of 0.496 cm and 0.734 cm, a length of 3 m and a flow rate of 1.0 l/min and a Polyflo tubing (polyethylene) with an internal diameter of 0.635 cm, a length of 3 m and a flow rate of 1.0 l/min. All tubing had an outer conductive surface.

Liu et al. (1985) observed that instead of nearly complete deposition of charged particles a finite penetration value could be measured and that the penetration was considerably lower than that calculated for pure diffusion. They concluded that

the additional deposition was due to the effect of electric charge on the surface of the plastic tubing.

2.4.7 Drag Forces

There are two sources from which drag arises: pressure and shear stresses. Drag from pressure is called form drag because it depends on the shape or form of the body. Drag from shear stress is called skin friction drag or friction drag. For flow past a sphere (or the motion of a particle through a fluid) the Reynolds number can be defined based on the diameter or radius of the sphere. For a sphere in creeping flow, where the Reynolds number Re < 1, the viscous forces dominate the inertial forces. In this case the drag force is given by the Stokes' law and is based on the solution of the Navier-Stokes equations around the sphere. The total drag force is then given by

$$F_{drag} = F_n + F_t = 6\pi\mu R_p V = 3\pi\mu D_p V \tag{2.31}$$

in which F_n is the form drag, F_t is the skin friction, μ is the viscosity of the fluid, R_p and D_p respectively the particle radius and diameter and V is the relative velocity of the particle to the gas flow. To account for non-continuum effects the Cunningham correction factor is introduced in the Stokes' law in Equation (2.31) giving

$$F_{drag} = \frac{3\pi\mu D_p V}{C_c} \tag{2.32}$$

The Cunningham correction factor was defined in Equation (2.4). Therefore the Stokes' law holds for a rigid sphere that moves at constant velocity with a Reynolds number less than unity. When the inertia effects on the flow surrounding a particle increase with increasing particle Reynolds number, the Stokes' law cannot apply to the flow field. To account for the drag over the entire range of Reynolds numbers as illustrated in Figure 2.23, the drag force can be expressed in terms of an empirical drag coefficient, C_D, as follows

$$F_{drag} = \frac{1}{2} C_D A_p \rho_f V^2 \tag{2.33}$$

where A_p is the projected area of the particle normal to the main flow and ρ is the density of the fluid. For a spherical particle with a particle diameter, D_p, the drag force is given as

$$F_{drag} = \frac{\pi}{8} C_D \rho_f D_p^2 V^2 \tag{2.34}$$

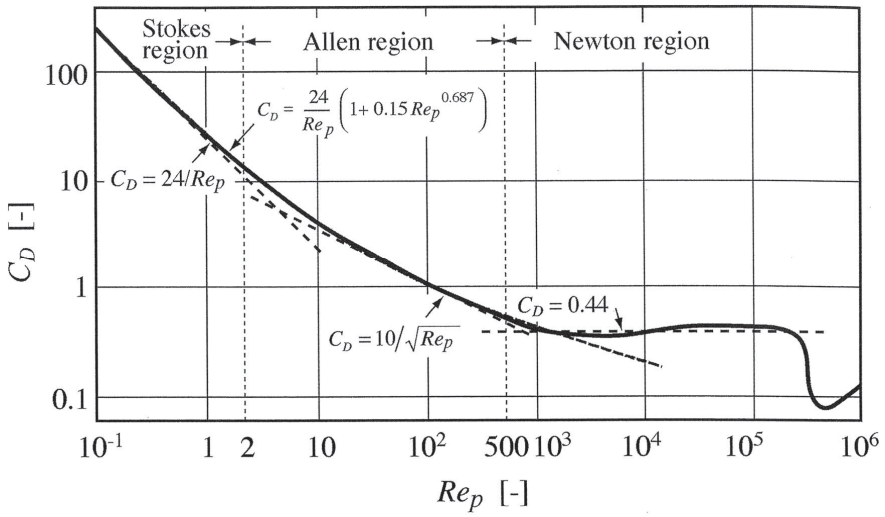

Figure 2.23: Resistance coefficient versus particle Reynolds number [Masuda et al. (2006), page 128].

The drag coefficient, C_D, for a spherical particle can be calculated as a function of the particle Reynolds number from the following correlations given by Haider and Levenspiel (1989)

$$C_D = \frac{24}{\mathrm{Re}}\left(1+0.1806\,\mathrm{Re}^{0.6459}\right)+\frac{0.4251}{1+\dfrac{6880.95}{\mathrm{Re}}} \tag{2.35}$$

For non-spherical particles the drag coefficient can be calculated as [Haider and Levenspiel (1989)]

$$\begin{aligned} C_D \;=\; & \frac{24}{\mathrm{Re}}\left(1+\exp\left(2.3288-6.4581\phi+2.4486\phi^2\right)\mathrm{Re}^{(0.0964+0.5565\phi)}\right) \\ & +\frac{\mathrm{Re}\times\exp\left(4.905-13.8944\phi+18.4222\phi^2-10.2599\phi^3\right)}{\mathrm{Re}+\exp\left(1.4681+12.2584\phi-20.7322\phi^2+15.8855\phi^3\right)} \end{aligned} \tag{2.36}$$

where ϕ is the particle sphericity which accounts for the particle shape as follows

$$\phi = \frac{s}{S} \tag{2.37}$$

In Equation (2.37), s is the surface of a sphere having the same volume as the particle and S is the actual surface. Equation (2.36) is a fit of the drag coefficient, C_D, over a wide range of particle Reynolds numbers from Stokes' region and in to the Newtonian region as shown in Figure 2.23

The terminal settling velocity, v_t, of a particle is the velocity for which the gravity force is just balanced by the drag force (neglecting buoyancy). Substituting the drag force given in Equation (2.34) for a spherical particle and the drag coefficient, C_D, for Stokes flow (24/Re) (correcting for non-continuum effects) and expressing the relative velocity of the particle to the gas flow, V, as the terminal settling velocity, v_t, gives

$$\begin{gathered} F_{drag} = mg \\ \Downarrow \\ \frac{\pi}{8} C_D \rho_f D_p^2 v_t^2 C_c = \rho_p \frac{\pi}{6} D_p^3 g \\ \Updownarrow \\ v_t = \frac{D_p^2 \rho_p g C_c}{18\mu} = \tau_p g \end{gathered} \tag{2.38}$$

where τ_p is the particle relaxation time (characteristic time) given in Equation (2.3). Because of the characteristically small value of the characteristic time, $\tau = v_t/g$ (relaxation time) for a particle to approach steady motion relative to the time scales over which other effects are changing, the velocity of a particle in a fluid very quickly adjusts to a steady state at which the drag force is balanced by the sum of other forces acting on the particle. In turbulent flows this means that particles with small values of the relaxation time will be able to follow the turbulent fluctuations immediately and thereby be dispersed (spread) due to turbulent diffusion. For gas-solid flow, particles with small values of the relaxation time correspond to small particles which are in the turbulent diffusion regime or the turbulent diffusion-eddy impaction regime (regimes 1 and 2 as shown in Figure 2.8). For particles with large values of the relaxation time in turbulent gas-solid flow this means that the particles are not really able to quickly adjust to the turbulent fluctuations and, therefore, a particle that has gained momentum from the turbulent eddies in a region of high turbulence will continue the motion and is not likely to respond to the changes in the turbulence intensity when entering a region of low turbulence intensity. Therefore particles transported this way are in the particle inertia moderated regime (regime 3 as shown in Figure 2.8) and the mechanism causing the particles to be transported due to gradients in the fluctuating velocities is turbophoresis.

2.4.8 Laminar Deposition Models

2.4.8.1 Brownian Diffusion

Gormley and Kennedy (1949) studied diffusion of particles due to Brownian motion from a laminar flow in a cylindrical tube. They assumed fully developed axisymmetrical flow and neglected axial diffusion and found the transport efficiency (penetration) for diffusional deposition from laminar tube flow at a distance, L, to be the following

$$\eta_{tube} = \frac{n}{n_0} = 1 - 4.07\Pi^{2/3} + 2.4\Pi + 0.446\Pi^{4/3} + \ldots$$

$$\Pi = \frac{\pi DL}{2Q} < 0.0156$$

$$\eta_{tube} = \frac{n}{n_0} = 0.8191e^{-7.314\Pi} + 0.0975e^{-44.6\Pi} + 0.0325e^{-114\Pi} + \ldots \tag{2.39}$$

$$\Pi = \frac{\pi DL}{2Q} > 0.0156$$

where n_0 is the initial concentration, n is the concentration at a distance, L, and the dimensionless tube deposition parameter, Π. Gormley and Kennedy (1949) showed that the deposition increased with decreasing particle size, decreasing tube diameter and increasing residence time of the particles. Figure 2.24 shows an example of the deposition efficiency in laminar tube flow calculated from Equation (2.39) based on a volume flow of $4.7 \cdot 10^{-6}$ m^3/s, a mean velocity of about 0.17 m/s, a tube length of 3 m with a diameter of 6 mm giving a residence time of about 18 seconds. Davies (1973) reviewed diffusion and deposition of aerosol particles from laminar flow in pipes for expressions derived by solving the convection-diffusion equation for an aerosol concentration. Ingham (1975) studied the steady-state mass diffusion equation governing the concentration, n, of aerosol particles suspended in a laminar flow in a circular tube. The convection-diffusion equation was given as

$$u_r \frac{\partial n}{\partial r} + v_z \frac{\partial n}{\partial z} = D\left[\frac{1}{r}\frac{\partial}{\partial r}\left(r\frac{\partial n}{\partial r}\right) + \frac{\partial^2 n}{\partial z^2}\right] + q \tag{2.40}$$

where u_r and v_z are the radial and axial velocity of the fluid, D is the aerosol particle diffusion coefficient and q is the rate of formation of aerosols per unit volume. Ingham (1975) obtained an analytical solution for the aerosol particle concentration, n, for small diffusion parameter, $\Delta = DL/4U_0R^2 = \Pi/2$ assuming

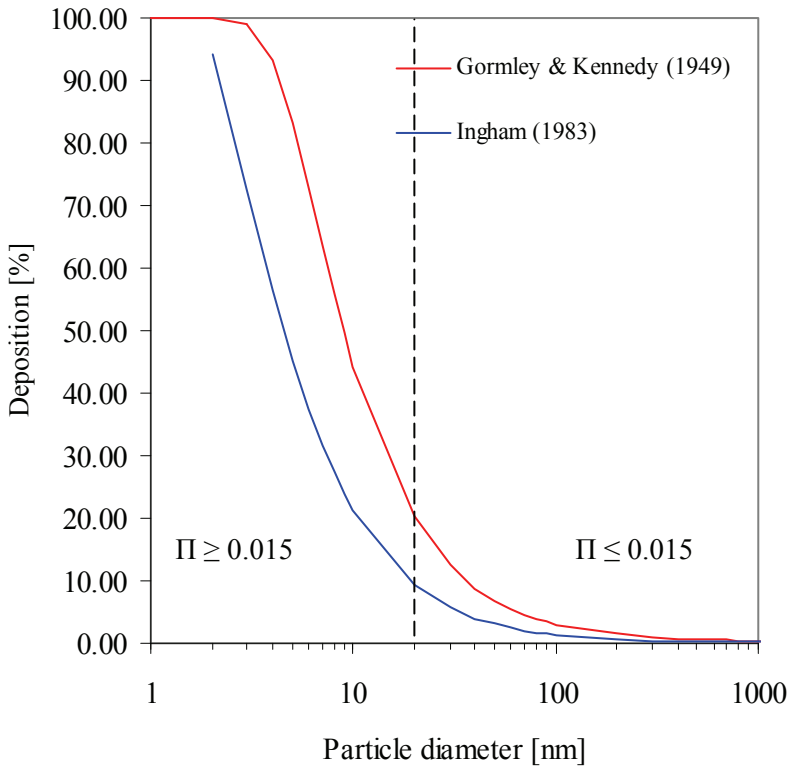

Figure 2.24: Example of the deposition efficiency in laminar tube flow. Fluid = air, volume flow, $Q=4.7\cdot10^{-6}$ m^3/s, average gas velocity = 0.17 m/s, tube length, L=3 m, tube diameter = 6 mm, residence time ≈ 18 s, temperature T=300 K and viscosity $\mu=1.85\cdot10^{-5}$ kg/(m-s) based on Equation (2.39) [Gormley and Kennedy (1949)]. The square channel based on Equation (2.44) [Ingham (1983)], the channel sides were 5.3 mm giving the conditions as the tube flow.

cylindrical symmetry, no formation of aerosols, neglecting axial diffusion and matched the solution for large Δ as given by Gormley and Kennedy (1949) in Equation (2.39) for Π > 0.0156. Ingham (1975) obtained an empirical solution for the complete range of values of the diffusion parameter, Δ, as follows

$$\frac{n}{n_0} = 0.819e^{-14.63\Delta} + 0.0976e^{-89.22\Delta} + 0.0325e^{-228\Delta} + ae^{-b\Delta^{2/3}}$$
$$\Delta = \frac{DL}{4U_0R^2} = \frac{\Pi}{2} \qquad (2.41)$$

where D is the aerosol particle diffusion coefficient, L is the length of the tube, U_0 is the mean axial velocity of the fluid, R is the inner radius of the tube and a and b are two constants which much be chosen such $n/n_0 \approx 1\text{-}6.41\Delta^{2/3}$ for small values

of Δ. Ingham (1983) analytically studied the problem of aerosol particle deposition from laminar flow in rectangular channels with varying aspect ratios. He assumed that instantaneously at the entry the flow was fully developed Poiseuille flow and that axial diffusion could be neglected by assuming a large Peclet number, *Pe*, where the Peclet number equals the Schmidt number, *Sc*, multiplied with the Reynolds number, Re, as follows

$$Pe = Sc\,\mathrm{Re}; \qquad Sc = \frac{\nu}{D} = \frac{\mu}{\rho_f D}; \qquad \mathrm{Re} = \frac{ud}{\nu} \tag{2.42}$$

where ν is the kinematic viscosity of the fluid, μ is the dynamic viscosity of the fluid, ρ_f is the density of the fluid, D is the Brownian diffusivity of the particles, u is some characteristic velocity of the flow and d is some characteristic dimension of the channel, e.g. the hydraulic diameter of the rectangular channel. Ingham (1983) also assumed the Peclet number was much larger than the Reynolds number so that the diffusion boundary layer was much thinner than the viscous boundary layer at the entry of the pipe. He gave the solution for the mean concentration, n, of aerosols for a channel with walls bounded by the planes $x = \pm a$, $y = \pm b$ for the limiting case $a/b \to 0$ as follows

$$\begin{gathered} \frac{n}{n_0} = 1 - 1.168 z_1^{2/3} + 0.1 z_1 + O\left(z_1^{4/3}\right) \\ z_1 = \frac{zD}{b^2 U_0} \end{gathered} \tag{2.43}$$

where z is the axial coordinate of the channel, D is the particle diffusivity and U is the mean velocity in the channel. For $a/b = 1$, the solution for the mean concentration, n, of aerosols was given as

$$\begin{gathered} \frac{n}{n_0} = 1 - 2.466 z_1^{2/3} + 1.496 z_1 + O\left(z_1^{4/3}\right) \\ z_1 = \frac{zD}{b^2 U_0} \end{gathered} \tag{2.44}$$

Figure 2.24 shows an example of the deposition efficiency in laminar tube flow calculated from Equation (2.44) based on a volume flow of $4.7 \cdot 10^{-6}$ m^3/s, a mean velocity of about 0.17 m/s, a tube length of 3 meter and $a = b = 5.3$ mm giving a residence time of about 18 seconds. The cross-sectional area is the same as for a circular tube with a diameter of 6 mm. As it can be seen from Figure 2.24 the deposition efficiency in the square channel having the same cross-sectional area as the circular tube with a diameter of 6 mm with the same volume flow and mean velocity is significant less than the deposition efficiency in the circular tube. The reason for this is probably because for the same residence time in the square and

circular tube the aerosol particles have to diffuse different radial distances to the tube walls for the different tube types.

Ingham (1984) studied the diffusion of aerosols from a laminar stream flowing through a short cylindrical pipe where he took the fluid flow entrance effects in the pipe into account. It was assumed that the fluid flow developed independently but simultaneously with the aerosol diffusion field. The solution for the mean concentration, n, of aerosols leaving the pipe at the dimensionless axial length, ξ, is as follows for $\xi \leq 0.02$

$$\frac{n}{n_0} = 1 - \frac{6}{\Gamma\left(\frac{1}{3}\right)}\left(\frac{4}{9}\right)^{\frac{1}{3}} I \left(\frac{Pe}{\mathrm{Re}}\right)^{\frac{-2}{3}}; \qquad I = \int_0^{\xi} \frac{\sqrt{B}d\xi}{\left(\int_0^{\xi}\sqrt{B}d\xi\right)^{\frac{1}{3}}} \tag{2.45}$$

$$\xi = \frac{z}{R\,\mathrm{Re}};\ Pe = \frac{2U_0 R}{D};\ \mathrm{Re} = \frac{2U_0 R}{\nu}$$

where $B(\xi)$ is the non-dimensional skin friction near the surface of the pipe (the non-dimensional skin friction was given as $B(\xi)=c_f$ Re/4, where c_f is the skin friction), Pe is the Peclet number, Re is the Reynolds number, z is the axial coordinate of the pipe, U_0 is the uniform velocity of the fluid at the inlet of the pipe, R is the inner radius of the pipe, D is the particle diffusion coefficient and ν is the kinematic viscosity of the fluid. If $0.02 \leq \xi \leq 0.5$, then I in Equation (2.45) is given as

$$I \approx 2.3811\left(\xi + b\right)^{2/3} \tag{2.46}$$

where b is a constant, $b \approx 0.00663$. For $\xi \geq 0.5$, then the solution by Gormley and Kennedy (1949) and Ingham (1975) can be used.

2.4.8.2 Saffman Lift

Lipatov et al. (1989) and Lipatov et al. (1990) studied aerosol crosswise migration and deposition in vertical ducts due to Saffman lift using the methods of limiting trajectory – see Figure 2.25. The principle of the limiting particle trajectory is that a particle starting at a critical radial position, ξ_0, at the entrance of a tube, will deposit exactly at the end of a tube with the length, L. Lipatov et al. (1989) derived an expression by assuming fully developed laminar flow, where flow and gravity were in the same direction. Based on this, they set up a force balance on a particle in quasi-equilibrium (zero acceleration and only a balance between drag

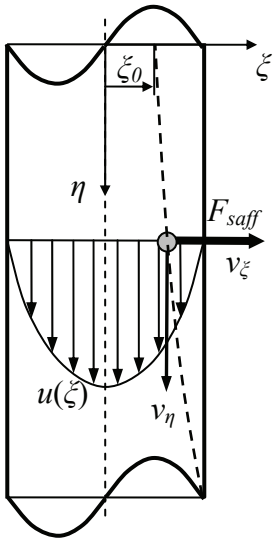

Figure 2.25: Schematic illustration of a fully developed axisymmetrical tube flow with gravity in the positive η-direction (vertical direction). The red dotted line illustrates the limiting trajectory. With the particle velocity faster than the fluid flow the Saffman lift force is in the positive ξ-direction as illustrated.

and lift perpendicular to the flow and drag and gravity in the flow direction) as follows

$$\begin{aligned} \frac{d\xi}{d\eta} &= \frac{v_\xi}{v_\eta} \\ v_\eta &= u\left(\xi\right) + v_s \\ u\left(\xi_0\right) &= 2U_0\left(1-\xi^2\right) \end{aligned} \tag{2.47}$$

The full derivation of Equation (2.48) and Equation (2.50) can be found in Appendix I. For slip velocities much less than the mean gas velocity, $v_t << U_0$, they stated the fraction of particle deposition for down flow as a function of the dimensionless cross coordinate of the limiting particle trajectory, ξ_0, as follows

$$\begin{aligned} 6.46 &= 11.8\chi^{-1}\left(\xi_0^{1.5} - 5\xi_0^{0.5} + 4\right) \\ \chi &= \frac{l}{d} A\,\mathrm{Re}^{-0.5},\ A = \frac{g\rho_p R_p^3}{\rho_f \nu^2},\quad \mathrm{Re} = \frac{U_0 d}{\nu} \end{aligned} \tag{2.48}$$

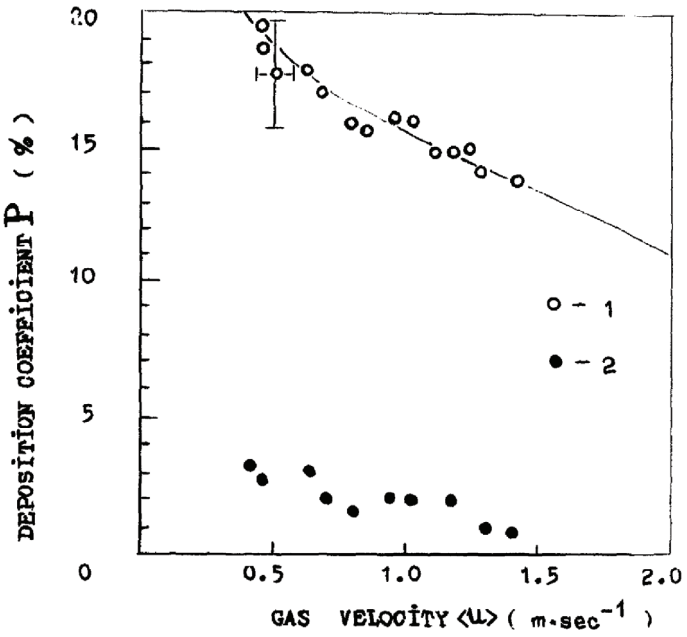

Figure 2.26: Deposition of particles in laminar flow through a vertical cylindrical tube due to Saffman lift force. The non-filled dots are for downwards flow and the filled dots are for upward flow. Tube length, L=0.18 m and a diameter of 5.6 mm [Lipatov et al. (1989)].

where U_0 is the average aerosol particle longitudinal velocity and d is the diameter of the tube. Figure 2.25 gives a schematic illustration of a fully developed axisymmetrical flow with gravity in the positive η-direction (vertical direction). The red dotted line illustrates the limiting trajectory. With the particle velocity faster than the fluid flow the Saffman lift force is in the positive ξ-direction as illustrated and particles between the limiting particle trajectory, ξ_0, and the tube wall will deposit on the wall. The limiting particle trajectory, ξ_0, is calculated from Equation (2.48) and the penetration from Equation (2.49) as follows

$$P_{Saffman} = \left(1 - \xi_0^2\right)^2 \tag{2.49}$$

In that way all particles starting at a radial position greater than the limiting particle trajectory in the inlet will deposit in the tube. To the best knowledge of the author, Lipatov et al. (1989) made a typing error in their expression for the limiting trajectory, ξ_0, (Equation (2.48)) where the exponent should have been 2.5 and not 1.5 and the constant 11.8 should be 11.996. The equation for the limiting trajectory, ξ_0, should then be stated as follows

$$6.46 = 11.996\chi^{-1}\left(\xi_0^{2.5} - 5\xi_0^{0.5} + 4\right) \tag{2.50}$$

Lipatov et al. (1989) carried out experiments in order to investigate particle deposition in upward and downward laminar flow through a vertical cylindrical tube due to Saffman lift force. The particles they used were Lycopodium spores with an aerodynamic diameter of 30 μm, a density of 1200 kg/m^3 (Živcová et al. (2007)) and they measured the deposition efficiency for tubes with a length varying from 0.1 to 0.25 m and a diameter varying from 3 to 10 mm. The average gas velocity in the tube varied from 0.4 to 1.5 m/s. Figure 2.26 shows the result of the deposition efficiency in upward and downward flows as a function of the gas velocity in the tube for a tube with a length of 0.18 m and a diameter of 5.6 mm. As it can be seen from Figure 2.26 the deposition efficiency was significantly greater for the downward flow than for the upwards flow. Lipatov et al. (1989) showed with their results that under certain conditions, the Saffman lift force could play a significant role in particle deposition (particle losses) during transport in laminar tube flow. It could be argued that the deposition efficiency in the upward flow theoretically should have been zero because the relative velocity of the particles to the gas flow was negative and the Saffman lift force on the particles therefore were pointing towards the centre of the tube. Other effects such as electrostatic forces, Brownian diffusion, developing flow or transition to turbulence could have affected the experimental result. A similar study was made by Gutfinger et al. (2003) who extended the analysis to include particle acceleration and thereby removed the pseudo steady-state assumption.

2.4.8.3 Electrostatic Forces

Alonso and Alguacil (2007) stated a very simple expression for the particle penetration, P, in terms of the diffusional penetration, P_D, (i.e. from Brownian motion) and the space-charge parameter, V_s, based on phenomenological considerations as follows

$$P = \frac{P_D}{1 - 0.49V_s\left(1 - P_D\right)/\ln P_D} \tag{2.51}$$

where P_D is the diffusional penetration and V_s is the space-charge parameter given as follows

$$V_s = \frac{v_s}{a} = \frac{ieZn_0L}{U_0\varepsilon_0} \tag{2.52}$$

where i is the number of elementary charges, e is the elementary charge, n_0 is the particle number concentration at the tube inlet, L is the length of the tube, U_0 is

the mean fluid velocity, $a=R/L$ and ε_0 is the dielectric constant of a vacuum. Equation (2.52) is valid for small values of i and inasmuch as image force effect can be neglected. Alonso and Alguacil (2007) compared detailed numerical calculation of simultaneous diffusion and space-charge penetration against the simple expression given in Equation (2.51) and found very good agreement.

Yu and Chandra (1978) theoretically investigated deposition of charged particles by image force from laminar flows in rectangular and cylindrical channels, neglecting gravity, inertial and Brownian motion of particles. They stated that the deposition efficiency in a circular tube due to the image force could be defined as

$$P_{image} = 1 - \left(\frac{r_c}{R}\right)^2 \tag{2.53}$$

where R is the tube radius and r_c is the critical radius vector outside which all particles were deposited. The critical radius, r_c, is related to the dimensionless residence time, τ, as follows

$$\tau = 4\left(\frac{R}{r_c} + 2\ln\frac{r_c}{R} - \frac{r_c}{R}\right) \tag{2.54}$$

The dimensionless residence time, τ, is defined as

$$\tau = \frac{Bq^2 L}{4\pi\varepsilon_0 R^3 U_0} \tag{2.55}$$

where q is the charge on the particle, L is the length of the channel, ε is the permittivity and B is the mechanical mobility of the particle defined as

$$B = \frac{C_c}{3\pi\mu D_p} \tag{2.56}$$

Yu and Chandra (1978) concluded that the effect of the image force on particle deposition was likely negligible for particles carrying less than 10 elementary charges. But they also concluded that in this range the electrostatic force could still play a significant role if the particle number concentration is sufficiently high, e.g. 10^8-10^9 #/cm^3, so that space charge effects would become important because of electrostatic repulsion due to the Coulomb force.

2.4.9 Empirical Models for Turbulent Flow

Empirical models based on correlations of experimental data for particle deposition are normally divided into the three deposition regimes (the diffusional

deposition regime, the diffusion-impact regime and an inertia-moderated regime as seen in Figure 2.8.) as follows [Papavergos and Hedley (1984)]

$$V_{dep}^{+} = k_1 \left(Sc\right)^{-2/3}; \qquad \tau_p^{+} < 0.2 \qquad \left(Diffusional\ Regime\right)$$

$$V_{dep}^{+} = k_2 \left(\tau_p^{+}\right)^2; \qquad 0.2 < \tau_p^{+} < 20 \quad \left(Diffusional - Impact\ Regime\right) \quad (2.57)$$

$$V_{dep}^{+} = k_3; \qquad \tau_p^{+} > 20 \qquad \left(Inertia - Moderated\ Regime\right)$$

where Sc is the particle Schmidt number and τ_p^{+} is the dimensionless particle relaxation time. Papavergos and Hedley (1984) stated that the typical values of the constants in Equation (2.57) are $k_1 = 0.07$, $k_2 = 3.5 \cdot 10^{-4}$ and $k_3 = 0.18$.

2.4.9.1 Turbulent Diffusion Regime

Cleaver and Yates (1975), examined deposition of particles from a turbulent flow based on the structure of the turbulent boundary layers which had shown turbulent down sweep on to the wall as illustrated in Figure 2.27. In turbulent flow fluid is continually being swept towards the wall and ejected away again in a turbulent burst (the bursting process consists of a form of quasi-cyclic process in flow near the wall) and it was then expected that once a particle was entrained in a "down sweep" it would continue in it with little interruption. They calculated the deposition rates of the particles based on the assumption that particles were transported by convection to the wall due to the down sweep. Cleaver and Yates (1975) developed an empirical expression for the diffusional particle deposition rate as follows

$$V_{dep}^{+} = 0.084 Sc^{-2/3} \qquad (2.58)$$

where V_{dep}^{+} is the non-dimensional particle flux defined in Equation (2.1). Wood (1981a) made an extensive study of mass transfer of particles and acid vapour to cooled surfaces. He presented simple equations for the calculation of turbulent deposition of both H_2SO_4 and alkaline particles in straight channels. For turbulent diffusion onto smooth surfaces in the turbulent diffusion regime Wood (1981a) and Wood (1981b) gave the following simple expression

$$V_{dep}^{+} = 0.057 Sc^{-2/3} \qquad (2.59)$$

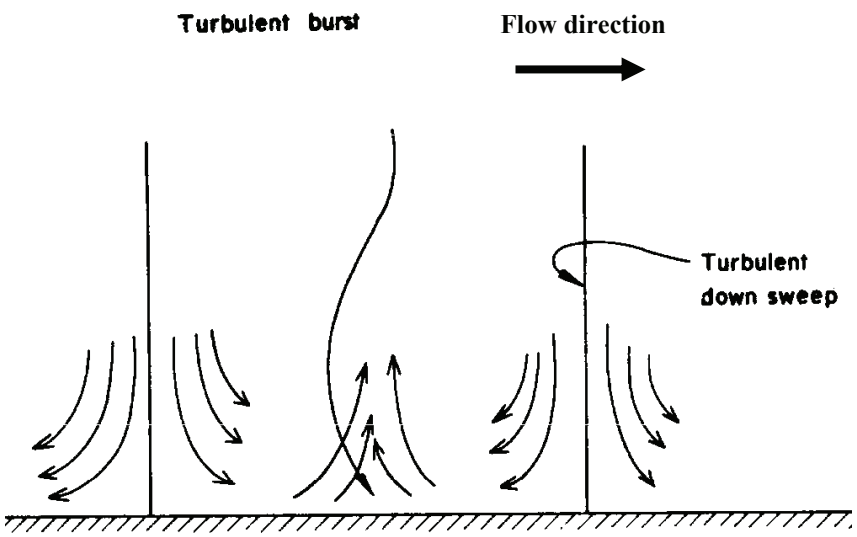

Figure 2.27: Illustration of turbulent down sweep in the sub-layer, which is related to the turbulent bursting process [Cleaver and Yates (1975)].

where D is the particle diffusivity and v is the kinematic viscosity of the fluid. The expression in Equation (2.59) gives the deposition rate for very small particles (order 10^{-3} μm). For particles larger than about 0.1 μm, where the eddy diffusion-impaction mechanism begins to take effect, it falls to very low values.

2.4.9.2 Turbulent Diffusion-Eddy Impaction Regime

In the eddy diffusion-impaction regime (regime 2) deposition may be calculated by considering the turbulent eddy diffusion of the eddy impaction process, where the particles that acquire a transverse velocity from the turbulent eddies are projected across the viscous sublayer to make contact with the wall.

Friedlander and Johnstone (1957) were among the first to develop a general theory on the subject of turbulent particle deposition. They proposed a projective mechanism for particle deposition which was based on the idea that turbulence eddies carried particles in the radial direction of a pipe under turbulent flow. The particles were transported from the turbulent core to the near wall region until one stopping distance of the wall (the stopping distance is the effective radius of the particles due to their inertia) by turbulent diffusion and were subsequently projected, due to the inertial effects from the momentum imparted by the turbulence eddies, through the boundary layer. The stopping distance, which a

particle with a given initial velocity move through a stagnant gas, is given for a spherical particle as follows

$$S = \frac{mv_{po}}{3\pi\mu D_p} = \tau_p v_{po}; \quad S^+ = \frac{Su^*}{\nu} \tag{2.60}$$

where v_{p0} is equal to the root-mean-square of the radial component of the fluctuating gas velocity in tube flows. Friedlander and Johnstone (1957) integrated Equation (2.8) down to one stopping distance to the wall (because the particle only needs to diffuse by turbulent diffusion to one stopping distance from the wall) and assumed that the concentration was zero at $y^+ = S^+$. Immediately adjacent to the wall there is an extremely thin viscous sub-layer followed by the buffer layer and the turbulent core. y^+ is the dimensionless distance from the wall and is a type of Reynolds number, defined as

$$y^+ = \frac{yu^*}{\nu} \tag{2.61}$$

Friedlander and Johnstone (1957) obtained the following expression for the deposition velocity for the non-dimensional stopping distance, $S^+ < 5$

$$V_{dep} = \frac{V_{avg}\dfrac{f}{2}}{1+\sqrt{\dfrac{f}{2}}\left(\dfrac{1525}{\left(S^+\right)^2 - 50.6}\right)} \tag{2.62}$$

where V_{avg} is the average gas velocity and f is the friction factor. For $5 \le S^+ \le 30$ Friedlander and Johnstone (1957) obtained

$$V_{dep} = \frac{V_{avg}\dfrac{f}{2}}{1+\sqrt{\dfrac{f}{2}}\left(5\ln\left[\dfrac{5.04}{S^+/5 - 0.959}\right] - 13.73\right)} \tag{2.63}$$

and for $S^+ > 30$ they obtained the following expression

$$V_{dep} = V_{avg}\frac{f}{2} \tag{2.64}$$

The "free-flight" model predicts a monotonic increase in deposition velocity with increasing dimensionless particle relaxation time, τ_p^+, and is not able to predict the

decrease in deposition velocity which has been observed from experiments in the particle inertia-moderated regime (regime 3 - Figure 2.8) [Guha (2008a)].

Wood (1981a) gave the following expression for the turbulent eddy diffusion-impaction regime for straight tube flow as follows

$$V_{dep}^{+} = 0.057Sc^{-2/3} + 4.5\cdot 10^{-4}\left(\tau_p^{+}\right)^2$$

$$\tau_p^{+} = \frac{\left(u^{*}\right)^2 \tau_p}{\nu};\ \tau_p = \frac{\rho_p D_p^2}{18\mu} \tag{2.65}$$

where u^* is the friction velocity.

2.4.9.3 Inertia-Moderated Regime

For relatively large particles, the particle inertia becomes so large that the particle cannot attain the eddy velocity during the time they are caught up by an eddy and deposition has been observed to nearly be independent of particle size or slightly decreasing. Papavergos and Hedley (1984) stated that

$$V_{dep}^{+} = k_3 \tag{2.66}$$

where k_3 = 0.18. Wood (1981a) gave a correlation that was constant for τ_p^{+} between 17 and 200 and slightly decreasing for τ_p^{+} above 265. The correlation is stated in Equation (2.67) as follows

$$V_{dep}^{+} = 0.13; \qquad 17 \le \tau_p^{+} \le 200$$

$$V_{dep}^{+} = \frac{2.6}{\sqrt{\tau_p^{+}}}\left(1 - \frac{50}{\tau_p^{+}}\right); \quad \tau_p^{+} \ge 265 \tag{2.67}$$

2.4.9.4 Models for Rough Walls

Wood (1981b) presented a simple analytical method to both smooth and rough surfaces in straight tube flow and derived approximations to these equations with accuracy adequate for most purposes. For rough surfaces (k_s^{+}>1 for typical

particle diameters) and for $\phi >> 1$, Wood (1981b) gave the approximate solution as

$$V_{dep}^{+} \cong \left[\frac{1524}{0.45k_s^{+}\left(0.9k_s^{+} - 5/\phi\right)} - 6.3 \right]^{-1} \tag{2.68}$$

where ϕ =1/[2.9 $Sc^{-1/3}$] and the particle diffusion coefficient in the Schmidt number is depending on the particle diameter. For $\phi << 1$ it was given as follows

$$V_{dep}^{+} \cong \left[24.2 + \frac{14.5}{Sc^{-2/3}} \left(\frac{2}{3\sqrt{3}} - \frac{k_s^{+}}{27.6\ Sc^{-1/3}} \right) \right]^{-1} \tag{2.69}$$

In Equation (2.68) and Equation (2.69), k_s^{+} is the non-dimensional roughness height and is defined as follows

$$k_s^{+} = \frac{ku^{*}}{\nu} \tag{2.70}$$

and is the equivalent sand grain roughness height, and the regimes are defined as [Schlichting and Gersten (2000), p. 529]

$$\begin{gathered} \textit{Hydraulically smooth}: \\ 0 \le k_s^{+} \le 5 \\ \\ \textit{Transient regime}: \\ 5 \le k_s^{+} \le 70 \\ \\ \textit{Completely rough regime}: \\ k_s^{+} \ge 70 \end{gathered} \tag{2.71}$$

Fan and Ahmadi (1993) developed a simplified empirical model for turbulent deposition of spherical particles in vertical ducts with smooth and rough surfaces based on a perturbation method. They observed that the deposition rate was dominated by the inertia eddy impaction and interception processes (regime 2) for particles of larger size or for rough walls, while it was controlled by the diffusion process (regime 1) for submicrometer particles under smooth wall condition. They also observed that a minimum deposition rate existed for smooth walls at the transition range where both mechanisms were insignificant. The simplified empirical model for the total deposition rate was for V_{dep}^{+}<0.14 proposed as follows

$$V_{dep}^{+}=\begin{cases}0.084Sc^{-2/3}+\dfrac{1}{2}\left[\dfrac{\left(0.64k^{+}+\frac{1}{2}d^{+}\right)^{2}+\dfrac{\tau_p^{+2}g^{+}L_1^{+}}{0.01085\left(1+\tau_p^{+2}L_1^{+}\right)}}{3.42+\left(1+\tau_p^{+2}g^{+}L_1^{+}\right)\Big/\left(0.01085\left(1+\tau_p^{+2}L_1^{+}\right)\right)}\right]^{1/\left(1+\tau_p^{+2}L_1^{+}\right)} \\ \times\left[1+8e^{-\left(\tau_p^{+}-10\right)^{2}/32}\right]\dfrac{0.037}{1-\tau_p^{+2}L_1^{+}\left(1+\left(g^{+}/0.037\right)\right)}\end{cases} \tag{2.72}$$

where d^+ is the non-dimensional particle diameter, g^+ is the non-dimensional acceleration of gravity and L_1^+ is the non-dimensional coefficient for Saffman lift force. Otherwise in the inertia-moderated regime (regime 3) the total deposition rate was given as

$$V_{dep}^{+}=0.14 \tag{2.73}$$

Fan and Ahmadi (2000) generalized the model of Fan and Ahmadi (1993) for application to deposition of elongated particles, but it will not be repeated here.

2.4.9.5 Electrostatic Forces

Li and Ahmadi (1993a) gave an empirical expression based on the expression of Wood (1981a) for turbulent diffusion and turbulent eddy diffusion-impaction onto smooth surfaces and corrected it for the effect of Coulomb force as follows

$$V_{dep}^{+}=0.057Sc^{-2/3}+4.5\times10^{4}\left(\tau_p^{+}\right)^{2}+\frac{\bar{q}ED}{2k_BTu^{*}} \tag{2.74}$$

where $\bar{q}=\left|\bar{n}\right|e$ is the absolute average charge, E is the electric field strength, D is the particle diffusivity coefficient, k_B is the Boltzmann constant and T is the temperature. Soltani et al. (1998) modified the expression of Cleaver and Yates (1975) for the diffusional deposition and obtained a similar expression as given in Equation (2.74).

2.4.10 Eulerian Models

In the Eulerian-Eulerian models the different phases are all treated as continuous phases and momentum and continuity equations are solved for each phase. The gradient diffusion models given in Equation (2.8) are an example of an Eulerian-

Eulerian model and are an integration of the modified Fick's law of diffusion where the particles are assumed to diffuse all the way to the wall. The gradient diffusion models can be considered as a conceptual simplification of the free-flight models where the only particle deposition mechanisms are Brownian and turbulent diffusion. These models predict that the deposition velocity decreases continuously with increasing particles size and are only valid for small particles in a turbulent boundary layer in the turbulent diffusion regime (regime 1 in Figure 2.8). Guha (1997), Guha (2008a) and Guha (2008b) developed a unified Eulerian-Eulerian advection-diffusion theory for dispersion and deposition of dilute suspended particles of any sizes in a fluid. Particles were therefore assumed not to interact with each other and only to have one-way coupling so that the motion of the particles only depended on the flow field. The theory was derived from the fundamental Eulerian conservation equations of mass and momentum for particles and the theory included molecular and turbulent diffusion, turbophoresis, thermophoresis, shear-induced lift force, surface roughness, electrical forces and gravitational settling. They stated that the framework was general, and that the theory could be integrated efficiently with established multidimensional CFD codes for single-phase flow. The theory reduced to Fick's law of diffusion in the limit of small particles and thereby linked Fick's law to a broader scheme of particle transport. Guha (2008a) concluded that the prediction of deposition velocity from this Eulerian theory was at least as accurate as those from the state-of-the-art Lagrangian calculations, but was much faster than the Lagrangian calculation. For fully developed vertical flow the flux, J, of particles in the y-direction (perpendicular to the wall) has been stated as [Guha (1997); Guha (2008a); Guha (2008b)]

$$J = -\left(D + \varepsilon_p\right)\frac{\partial \bar{n}}{\partial y} - D_T \bar{n}\frac{\partial \ln T}{\partial y} + \bar{\rho}_p \bar{V}_{py}^{c} \tag{2.75}$$

where D_T is the coefficient of diffusion due to temperature gradients, T is the temperature, $\bar{n}$ is the particle number concentration and $\bar{V}_{py}^{c}$ is the convective velocity of the particle in the y-direction. The overbar in Equation (2.75) denotes time-mean values. The coefficient of diffusion due to a temperature gradient, D_T, is given as follows

$$D_T = D\left(1 + \frac{\eta}{kT}\right) \tag{2.76}$$

where η is the thermophorectic force coefficient, given as follows from Talbot (1981)

$$\eta = \frac{2.34\left(6\pi\mu v r\right)\left(\lambda_r + 4.36Kn\right)}{\left(1 + 6.84Kn\right)\left(1 + 8.72Kn + 2\lambda_r\right)} \tag{2.77}$$

In Equation (2.77) λ_r is the ratio of the thermal conductivity of the fluid, λ, and that of the particles, λ_p ($\lambda_r = \lambda / \lambda_p$), and Kn is the Knudsen number. In Equation (2.75) for the generalized particle flux, the convective velocity of the particle, $\overline{V}^c_{py}$, in the y-direction has to be calculate from the particle momentum equation for downward flow as follows

$$\begin{aligned} y-momentum: \qquad & \overline{V}^c_{py}\frac{\partial \overline{V}^c_{py}}{\partial y}+\frac{\overline{V}^c_{py}}{\tau_I}=\frac{\partial \overline{V'^2_{py}}}{\partial y}+F_{Sy}+F_{E_y} \\ x-momentum: \qquad & \overline{V}^c_{py}\frac{\partial \overline{V}_{px}}{\partial y}=\frac{1}{\tau_I}\left(\overline{V}_{fx}-\overline{V}_{px}\right)+\left(1-\frac{\rho_f}{\rho_p^0}\right)g \end{aligned} \tag{2.78}$$

In Equation (2.78) the acceleration term is given by $\overline{V}^c_{py}\,\partial \overline{V}^c_{py}/\partial y$, the steady-state viscous drag is given by $\overline{V}^c_{py}\,\overline{V}^c_{py}/\tau_1$, the turbophoresis is given by $\partial \overline{V'^2_{py}}/\partial y$, the shear-induced lift force is given by F_{Sy} and the electrical force is given by F_{Ey}. The equation for the y-momentum in Equation (2.78) is almost de-coupled and depend only on $\overline{V}_{px}$ through the shear-induced lift force, F_{Sy}. Guha (2008a) has stated that calculations show that the shear-induced lift force in particular increases the deposition rate in the eddy diffusion-impaction regime (regime 2). He also stated that, the turbophoretic term depended on the particle RMS velocity which might be different from the fluid RMS velocity if the particle inertia was large. Chen and Lai (2004) proposed an Eulerian model for particle deposition under the influence of electrostatic forces for turbulent flow conditions based on a modified Fick's law equation as

$$V^+_{dep}=\left(\frac{D+\varepsilon_p}{\nu}\right)\frac{\partial n^+}{\partial y^+}+v^+n^++\frac{v^+_{i.1}}{\left(y^+\right)^2}n^+ \tag{2.79}$$

where the first term on the right-hand side is the Brownian and turbulent diffusion. The second term on the right-hand side is the migration velocity due to the Coulomb force and the third term is the drift velocity due to the image force. Chen and Lai (2004) concluded that the Coulomb force played an important role in particle deposition, where particles at extremely high charge level and in the presence of a strong electric field contributes significantly by enhancing deposition. They also concluded that the image force was important when the particle charge level is high and the electric field strength is weak.

2.4.11 Lagrangian Models

In the Eulerian-Lagrangian approach the fluid phase is treated as a continuum by solving the Navier-Stokes equations, while the dispersed phase is solved by

tracking a large number of particles through the calculated flow field. The dispersed phase can exchange momentum, mass and energy with the fluid phase. Since the particle trajectories are computed for each particle (or parcel of particles) the approach is limited to systems with a low volume fraction (below 10%) of the dispersed phase.

Ebert (1992) stated his opinion to the question of which approach (the Eulerian or the Lagrangian) is most suitable for predicting turbulent diluted suspension and concluded that it could not be answered uniquely. He argued that the Lagrangian approach is more expensive than the Eulerian with regard to computer costs but on the other hand the Lagrangian methods e.g. allows one to describe the history of a particle undergoing heat and mass transfer and heterogeneous chemical reactions in a straightforward way. He also argued that especially the Lagrangian approach combined with Large Eddy Simulation (LES) in order to predict accurately the turbulence of the carrier flow gives realistic result with independence of model assumptions for the large vortices. The Eulerian approach gives satisfactory results for well adjusted numerical parameters.

Numerous investigators have studied particle deposition in turbulent tube flow using an Eulerian-Lagrangian approach. They all showed that in general the curves of the particle deposition velocity, V_{dep}^{+} versus the dimensionless particle relaxation time, τ_p^{+}, were V-shaped.

Abuzeid et al. (1991) studied the dispersion of small particles between 0.05 to 5.0 μm suspended in a turbulent channel flow using a two-equation, *k-ε,* turbulence model for simulating the mean flow field. The motion of the suspended particles was given by a Lagrangian reference frame. The studies of Abuzeid et al. (1991) showed that turbulence fluctuations and Brownian motion had significant effects on the particle deposition process and they also showed that the turbulence fluctuations remained significant regardless of particle diameter, whereas Brownian effects became negligible as the particle diameter became greater than 1 μm. Abuzeid et al. (1991) also studied the effect of the Reynolds number on the wall deposition. They found that an increasing Reynolds number increased the deposition rate and they explained this to be caused by an increasing fluctuating kinetic energy in the flow as a result of the increasing Reynolds number. What they also observed from their simulations was that, at a high Reynolds number, the minimum deposition rate occurred at a particle diameter, $d_p \approx 0.5$ μm, and at a low Reynolds number the minimum deposition rate occurred at a particle diameter $d_p \approx 1$ μm. They explained that this shift in minimum deposition rate could be due to the relative significance of Brownian effects, turbulence and drag which tended to vary as the mean velocity increased.

Zhang and Ahmadi (2000a) and Zhang and Ahmadi (2000b) studied aerosol particle transport, deposition and re-entrainment in vertical turbulent channel flows by Direct Numerical Simulation (DNS) using an Eulerian-Lagrangian approach for different particle diameters under the conditions that the shear velocity was 0.2 m/s and the density ratio, S=1000. In general Zhang and Ahmadi (2000a) showed that the shear velocity, density ratio, the shear-induced lift force (Saffman lift) and the flow direction affected the particle deposition rate. One of the things they concluded from their studies was that the coherent vortex structure of the near wall turbulent flow played an important role in the particle deposition rate, which was also in agreement with their earlier studies.

Tian and Ahmadi (2007) have shown based on experimental data, semi-empirical equations and simulations using the code PARTICLE and FLUENT respectively in an Eulerian-Lagrangian reference frame that the deposition velocity has a "V-shaped" variation for aerosol particles in the size range between 0.01-50 μm for particle-to-fluid density ratio, S, kept fixed at S=2000. This size range includes both the diffusional deposition regime and the diffusional-impaction regime (see Figure 2.8 for the different deposition regimes), where the diffusional deposition regime is for ultra fine particles on the left side of the "V-shaped" curve for the deposition velocity and the diffusional-impaction regime (inertial range) is for particles larger than 10 μm. In the diffusional deposition regime deposition due to Brownian diffusion is the dominant mechanism for particle deposition and the deposition rate decreases with increasing particle size. In the diffusional-impaction regime turbulent diffusion is the dominant mechanism for particle deposition and increases with increasing particle size. It reaches a constant value for very large particles. The region between the diffusional deposition regime and the diffusional-impaction regime is called transition and corresponds to where the "V-shaped" curve for the deposition velocity has a minimum because both the molecular and turbulent diffusion and the inertial effects are small.

Figure 2.28 shows the comparison of deposition velocities predicted by the PARTICLE code [Tian and Ahmadi (2007)], experimental data [Papavergos and Hedley (1984)] and semi-empirical model predictions [Wood (1981a), Fan and Ahmadi (1993),] in a vertical duct with gravity in the flow direction. The Reynolds number based on the average velocity and channel width was 6667. Near wall turbulence was treated using a two-layer model (it uses a one-equation model to account for the near wall effect and beyond the "buffer layer" and part of the log layer the traditional RANS turbulence models are used). As it can be seen the RSM model with the two-layer model boundary conditions and a quadratic variation for the near-wall turbulence fluctuation normal to the wall (it is specified as RSM, "STW" & Eq.(23) in Figure 2.28) gives the best predictions of the

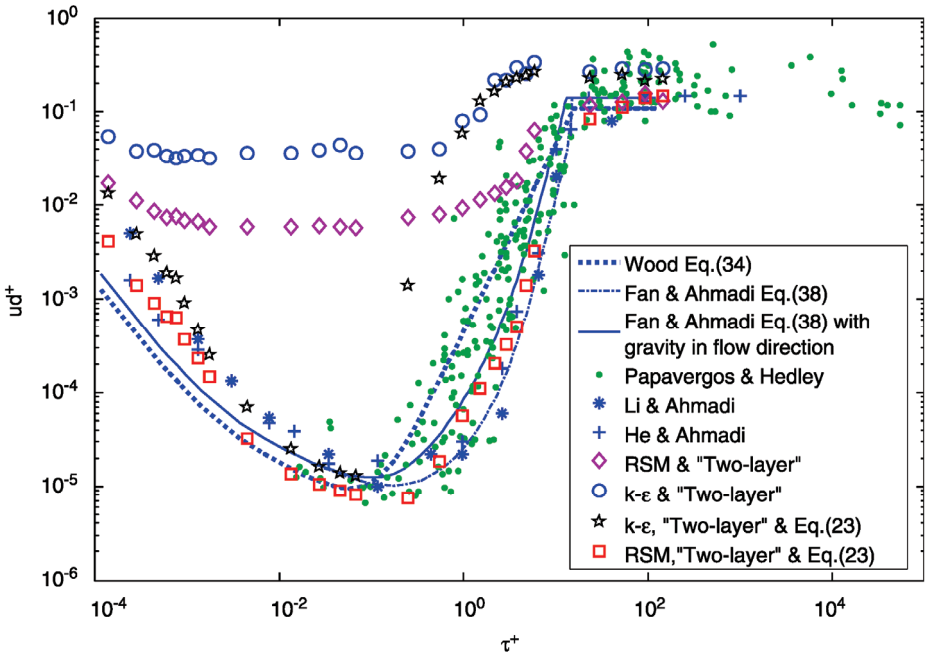

Figure 2.28: Comparison of deposition velocities predicted by the PARTICLE code, experimental data and semi-empirical model predictions in a vertical duct with gravity in the flow direction. Turbulence models use near wall treatment using two-layer models and a quadratic variations for the near-wall turbulence fluctuation normal to the wall. The Reynolds number based on the average velocity and channel width was 6667 [Tian and Ahmadi (2007)].

deposition velocities compared to experimental data and semi-empirical models. The simulation results also indicate that even with a two-layer model, boundary conditions and a quadratic variation for the near-wall turbulence fluctuation normal to the wall, the *k-ε* model is not able to predict the particle deposition in the transition and inertial regions. The reason for this is the effect of turbulence anisotropy in the near-wall region which is not captured by the *k-ε* model because it assumes isotropic turbulence.

Tian and Ahmadi (2007) also observed that only using standard wall functions both the *k-ε* model and the RSM model overpredicted the particles deposition velocities over the entire size range. They also concluded that the particle deposition velocities predicted with the code PARTICLE and FLUENT agreed well with the trend.

2.4.12 Overview of Deposition Mechanisms versus Particle Size

A short overview of the dominating deposition and dispersion mechanisms versus particle size for aerosol particle deposition in fluid flow is given in Table 2.

Table 2: Overview of deposition mechanisms versus aerosol particle size.

Aerosol particle deposition	
Deposition mechanisms	Significant particle size
Brownian diffusion	Significant for particles < 0.1-1 μm
Saffman lift	Significant for particles > 5-10 μm
Inertial impact	Significant for particles > 1 μm
Turbulent diffusion	Significant for particles < 5 μm
Turbophoresis	Significant for particle > 10-20 μm
Turbulent eddy-impaction (connected to turbophoresis)	Significant for particles > 5-20 μm
Gravitational settling - horizontal	Significant for particles > 1 μm
Thermophoresis	Significant for particles < 5 μm
Electrostatic forces: Coulomb forces	Significant for charged particles < 0.1-1 μm For micrometer particle they have to be highly charged
Electrostatic forces: Image forces	Significant for conducting surfaces, highly charged submicrometer particles with high electric mobility and very close to the surface

2.5 Particle Plugging Models

Several investigators have reported deposition of particles in laminar and turbulent pipe flow in the literature, but there are not many that have reported models for plugging of pipes due to deposition of aerosols and particles. Vaughan

(1978) developed a simple model for plugging of flow in cylindrical pipes by deposits of aerosol materials. He modelled the highly irregular and dendritic deposits assigning a mean density to the porous deposit and simplifying the geometry to a single growing plug that retained a fixed shape with rotational symmetry about the axis of a cylindrical pipe. The model correlated the integral mass of aerosol that flows through a pipe up to the point of plugging of the pipe with the diameter of the pipe as follows

$$m = Kd^3 \tag{2.80}$$

where m is the total mass of aerosols that flowed through the pipe before plugging, K is an empirically determined proportionality constant between 10000 and 50000 kg/m^3 and d is the diameter of the pipe. Equation (2.80) is a very general correlation that does not depend on aerosol concentration, particle size or flow rate and has been referred to as the "Morewitz criterion for aerosol plugging". For a rectangular duct Equation (2.80) becomes [Novick (1994)]

$$m = KW^2L \tag{2.81}$$

where W is the width of the duct and L is the height of the duct. Situations in which the "Morewitz criterion for aerosol plugging" was met but no plugging occurred was observed by Novick (1994). He therefore proposed an initial test condition that must first be met before the "Morewitz criterion for aerosol plugging" is considered valid. Kane (1986) studied the comparison of two models for aerosol deposition and plugging of pipes in which the comparison was done based on the amount of mass that could pass through the pipe before the pipe was effectively plugged. One model was the simple model given by Vaughan (1978) and the other model was based on turbulent deposition velocity. Based on the dimensionless turbulent deposition velocity, V_{dep}^{+}, the integral mass of aerosol that flows through a pipe up to a point of plugging of the pipe from the turbulent model is given as follows

$$m = \dot{m}\bar{t} = \frac{\dot{m}\rho_{p1}D^2L}{4R_d} = \frac{\dot{m}\rho_{p1}D}{4V_{dep}^{+}u^{*}C_0} \tag{2.82}$$

where m is the total mass of aerosol that flowed through the pipe before plugging, $\dot{m}$ is the aerosol mass flow rate in the pipe, $\bar{t}$ is the time from beginning of deposition to completion of plug, ρ_{p1} is the density of plug, D is the pipe diameter, L is the pipe length, R_d is the deposition rate, u^* is the friction velocity and C_0 is the aerosol concentration in the gas. In the case with the turbulent transport model, plugging was assumed to occur when the incremental calculations produced an open pipe diameter of less than half of the original open diameter.

The turbulent deposition velocity can be determined from the models given in Section 2.4.9. Kane (1986) concluded that the simple model given by Vaughan (1978) overpredicted the amount of aerosol particles that can be passed prior to plugging for small diameter pipes and underpredicts the amount that can be passed for large diameter pipes. He also concluded that the simple model by Vaughan (1978) was a limiting form of the more general model which was based on turbulent deposition velocity for a range of pipe diameters and flow conditions.

2.6 Adhesion of Particles

The impact of particles on the wall leads both to deposition but also to erosion/attrition which is an important consideration in the design of e.g. monolithic catalysts. One of the characteristics that distinguish aerosol particles from gas molecules and from millimetre-sized particles are that they attach firmly to any surface they contact and whenever aerosol particles contact one another they adhere and form agglomerates. The adhesive forces are very important in connection with deposition because they exceed other common forces by orders of magnitude and despite its importance particle adhesion is poorly understood and its description is partly qualitative [Hinds (1999) p. 141]. Extensive reviews of the particle adhesion mechanism have been provided by Corn (1966), Krupp (1967) and Bowling (1985). When a solid particle hits a surface at low velocity (less than a few m/s) the particle loses its kinetic energy by deforming itself and the surface and the greater the velocity, the greater the deformation and the better the adhesion. At high velocities, part of the kinetic energy is dissipated in the deformation process (plastic deformation), and part of it is converted elastically to kinetic energy of rebound. If the rebound energy exceeds the adhesion energy (the energy required to overcome the adhesive forces) the particle will bounce away from the surface [Hinds (1999), p. 146].

2.6.1 The Adhesive Forces

The main adhesive forces are the van der Waals force, the electrostatic force and forces arising from surface tension of adsorbed liquid films (capillary forces) or solid bridges. Van der Waals forces are known to cause adhesion onto a wall or onto another particle and come from interaction between solid surfaces on the molecular level and become apparent when smooth surfaces are brought into contact. The van der Waals forces are caused by electrically neutral atoms (or molecules) developing instantaneous dipoles caused by fluctuations in the electron clouds surrounding the nuclei. After two surfaces have made contact with

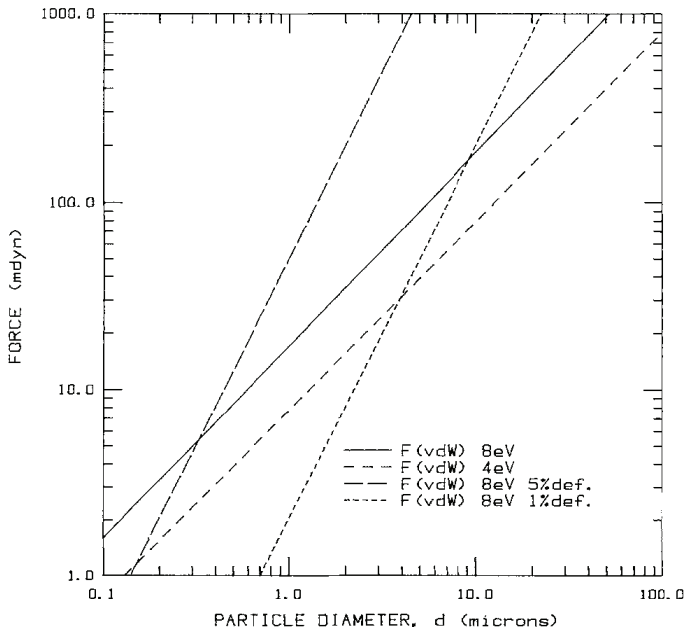

Figure 2.29: van der Waals force and deformation force as a function of particle diameter [Bowling (1985)].

each other by either van der Waals forces or electrostatic forces, the surface, may deform with time, thereby increasing the contact area and decreasing the separation distance and thus increasing the force of adhesion [Byron and Willeke (2005), p. 57-58]. Figure 2.29 shows the van der Waals force and the deformation force as a function of particle diameter and illustrates that deformation can add tremendously to the total force of adhesion. The deformation force is the increase in the adhesion force over time due to increase in the contact area caused by deformation of the particle and/or the surface.

The electrostatic forces are caused by particles carrying a charge which induces an equal and opposite charge in the surface which gives an attractive electrostatic force. Ranade (1987) has stated that there are two types of electrostatic interactions which may cause increased particle adhesion. The first type arises from difference in the work functions of two different materials resulting in a contact potential. The other electrostatic interaction occurs due to electric charge on the particle or the substrate surface. Adhesion due to capillary condensation can take place due to condensation of water vapour in the gap between bodies on contact because of air humidity. The bodies are therefore drawn together due to surface tension and reduced pressure of the liquid – these two effects cause an attractive force. Tabor (1977) discussed some of the theoretical problems in relation to surfaces. He concluded that surface roughness can greatly reduce the

adhesion between solids because the high surface asperities can prize the surface apart and break the adhesions occurring at the lower asperities. Therefore adhesion between solids depends not only on surface forces but also on surface roughness and the degree of ductility of the solid themselves. Li and Ahmadi (1992) reported that at low velocities the particles that strike a wall will adhere to it, however, as the velocity increased the particles may rebound from it. They also stated that bounce occurred when the kinetic energy of the particle was sufficiently large to escape the attractive forces on the surface. Heinl and Bohnet (2005) have proposed a model for particle-wall adhesion based on a suggestion from Löffler and Muhr (1972) which consists of an energy balance around the particle-wall collision including electrostatic forces as follows

$$E_{kin,1} + E_{el,1} = W_{vdW} + E_{kin,2} + E_{el,2} + E_{deform} \tag{2.83}$$

where E_{kin} is the kinetic energy, W_{vdW} is the energy due to adhesion with van der Waals, E_{el} is the electrostatic energy, E_{deform} is energy loss from the particle due to the wall collision and (1) and (2) are before and after the wall collision. Solving Equation (2.83) for the critical particle velocity with the prerequisite of adhesion where $E_{kin,2} = 0$ gives

$$w_{p,crit} = \sqrt{\left(\frac{\hbar\varpi}{eD_p 4\pi^2 z_0^2}\right)^2 \frac{3}{4H\rho_p} + \frac{3}{D_p^3\pi^2 e^2}\frac{1}{\varepsilon_0\rho_p}\left(\frac{2q_2^2}{2z_0 + D_p} - \frac{q_1^2}{l}\right)} \tag{2.84}$$

where the critical particle velocity substantially depends on the Liffschitz-van der Waals constant $\hbar\varpi$ (must be determined either by experiments or from the literature), the material combination of the pipe wall and the particle, the particle diameter, D_p, the distance at contact, z_0, the strength of the pipe wall, H, and the particle charge, q_i, before and after the wall collision. The particle charge after the collision can be calculated as proposed by Matsuyama and Yamamoto (1995)

$$q_2 = \frac{q_0}{q_e}\left(q_e - q_1\right) \tag{2.85}$$

where q_0 is the impact charge after collision from an initial neutral particle and q_e is the charge where no charge displacement occurs during a collision and is estimated by the potential difference at contact as follows

$$q_e = 9\pi\varepsilon_0 D_p \tag{2.86}$$

If the particle charge before the collision is known, Equation (2.84) can give the condition for adhesion if the particle velocity is smaller than the critical particle velocity as follows

$$\left|\vec{w}_{p,1}\right| \leq w_{p,crit} \tag{2.87}$$

As it can be seen from Equation (2.87), adhesion is only dependent on the particle velocity and not the particle concentration. Zhang et al. (2005) have stated a more simple model for the normal collision between a charged particle and the collecting plate of an electrostatic precipitator than the model by Heinl and Bohnet (2005). When comparing the model of Zhang et al. (2005) with the model from Heinl and Bohnet (2005) based on the suggestion from Löffler and Muhr (1972) the model of Zhang et al. (2005) only has fully elastic collision (no loss of kinetic energy due to non-elastic deformation during the collision) and does not take van der Waals forces into account. The reason for this is because electrostatic forces are the dominating adhesive forces in an electrostatic precipitator.

2.6.2 Detachment of Particles

A particle may detach from a surface when the applied forces overcome the adhesion forces. Therefore, a particle may lift-off from the surface, slide over it, or roll on the surface. Adhesive forces are proportional to the particle diameter, D_p, while removal forces are proportional to D_p^3 for gravitational, vibrational and centrifugal forces and D_p^2 for air flows [Hinds (1999), p.144]. These relationships suggest that as the particle size decreases, it becomes more difficult to remove the particle from the surface. This fact also agrees with our intuition that large, visible particles, such as grains of sand, can be removed by shaking or by air flow, but smaller ones, such as soot particles, cannot. The important point is that for a particle less than approximately 10 μm, the adhesive force is much greater than other forces, whereas a thick layer of particles less than 10 μm may be easily dislodged in large 0.1-10 mm chunks. The reason for this is that the particles adhere tightly to each other, to form large agglomerate that can easily be blown or shaken from the surface [Hinds (1999), p. 144]. Soltani and Ahmadi (1998) studied particle removal mechanisms in a turbulent flow and described two models based on the structure of turbulence in the near wall flow using the rolling detachment and sliding removal of particles. They concluded that rolling detachment was the dominant re-suspension mechanism of spherical particles in turbulent flows and that hydrodynamic torque acting on a particle attached to a wall is significant and had to be included in the re-suspension analysis. They also concluded that Saffman lift force on particle re-suspension was negligible and the

coherent wall eddies have a small effect on the particle detachment process, but the sublayer vortical motion and turbulence burst/inrush phenomenon were important for the detachment of particles. Soltani and Ahmadi (1998) compared their model predictions with experimental results and found qualitative agreement and argued that surface roughness might be the cause of the observed quantitative discrepancy between the model predictions and the experimental results. Zhang and Ahmadi (2000b) performed direct numerical simulation on aerosol particle removal and re-entrainment in turbulent channel flows and showed that the hydrodynamics drag and torque acting on the particle were the dominant mechanisms for particle detachment.

2.6.3 Re-Suspension

Re-suspension is the detachment of a particle from a surface and its transport away from the surface. Re-suspension may occur as a result of air jets, mechanical forces, the impact of other particles, or electrostatic forces. Soltani and Ahmadi (1995) studied particle entrainment in turbulent flow and found that particles captured in the relatively high speed streams moving away from the wall were the main mechanism for particle entrainment. Ahmadi and Guo (2007) studied the effect of electrostatic and capillary forces on non-spherical particle adhesion and removal in turbulent flows using the JKR (Johnson, Kendall, Roberts) theory and accounting for the increased adhesion by capillary forces. They also included the effect of electrostatic forces and nonlinear hydrodynamic drag in their analyses. They observed that for non-spherical particles larger than 30 μm the electrical forces (the particles carrying a charge of 20 μC/gm) provided the dominant contribution to the adhesion force. Ahmadi and Guo (2007) found that rolling was the dominant detachment mode for spherical and non-spherical particles and for particles that had a smaller number of large bumps that the critical shear velocity increased.

2.7 Concluding Remarks

The SCR DeNO$_x$ technology was first introduced by the Japanese at the end of the seventies, whereas the first commercial SCR DeNO$_x$ system in Europe was installed in 1986. Today SCR DeNO$_x$ technology with ammonia as reducing agent is the most effective NO$_x$ reduction process and a reduction of NO$_x$ emission of 80 to 90 per cent can be achieved. The SCR DeNO$_x$ technology can be applied both at the high-dust, low-dust and tail-end configuration in e.g. a coal fired power station in which the high-dust position is the most common. Today, most

monolithic catalysts used in coal fired power stations consist of vanadium as active catalyst dispersed on a monolithic titanium carrier. The optimal temperature operating conditions for the SCR process is 300 to 400°C. A disadvantage of the high-dust position is the risk of catalyst degradation due to plugging, erosion and attrition because of the high contents of fly ash and particles in the flue gas. Severe plugging can also be observed in low-dust applications with a "volcano type" of deposition pattern. In general, a good SCR catalyst can be characterized by high NO_x reduction activity, high tolerance against fly ash particles, SO_x and other flue gas components. It should also have high thermal stability, high resistance against thermal shock, long life time, low pressure drop and low SO_2 oxidation. A major problem operating the SCR catalyst is loss of catalytic activity. The deactivation of the catalyst can occur due to a number of different mechanisms which are both chemical and physical by nature. The five main categories are chemical poisoning, plugging and fouling, sintering, loss of active component and inhibition.

During the combustion of coal particles in a coal fired power station fly ash particles are formed. Two major mechanisms of particle formation in pulverized coal combustion are identified. For SCR $DeNO_x$ monolithic catalysts in the high-dust position they are exposed to fly ash particles in the size range from about 0.01-200 μm with a mass mean diameter of 10 to 20 μm.

Over the last several decades, a tremendous amount of work has been carried out in understanding transport and deposition of aerosol particles in laminar and turbulent pipe flow, both by experimental, analytic and numerical investigations. Submicrometer particles can be transported e.g. by turbulent diffusion, Brownian diffusion, thermophoretic or electrostatic forces. Larger particles of the size of micrometers can be transported e.g. by turbulent diffusion, turbophoresis, inertia, shear-induced lift, electrostatic forces (in the case of very strong electrostatic fields and very highly charged particles or due to space charge for high concentrations of charged particles) and gravitation. A particle in a viscous fluid will always experience a drag force but a lift force will only be present if there is an asymmetry in the flow either due to asymmetry of the body or due to rotation of the body in the flow. Lift forces on a spherical particle are either due to rotation induced by a velocity gradient across the particle or due to shear flow (shear-induced lift - Saffman lift). Lift forces can also be imposed by some other source such as contact or rebound from a surface. In laminar flow Brownian diffusion is an important deposition mechanism for uncharged submicrometer particles and for larger micrometer particles Saffman lift force is significant. In turbulent flow, turbulent diffusion is significant for both submicrometer particles and larger particles. For larger particles above about 10 μm turbophoresis becomes

significant. In case of turbulence the Saffman lift has only some effect in the viscous sub-layer, where the turbulence has died out. The reason for this is that the Saffman lift force migrate the particles to the wall in the viscous sub-layer where only Brownian diffusion dominates by imparting momentum to the particles. The deposition rate is proportional to the turbulence intensity and the deposition rate increases as the flow Reynolds number increases. The deposition rate for submicrometer particles increases rapidly with decreasing particle diameter by Brownian and turbulent diffusion. In general particle deposition rates are extremely sensitive to roughness and depend on the size of the particles, intensity of turbulence and roughness. When the particle deposition is dominated by Brownian diffusion, the influence of roughness is very little. But for increasing particle size and for increasing turbulence intensity during increasing turbulent diffusion, the influence of roughness becomes significant. The impact of particles on a wall leads to deposition but also erosion/attrition of the surface. The main adhesive forces are the van der Waals force, the electrostatic force and forces arising from surface tension of adsorbed liquid films. Van der Walls forces are known to cause adhesion onto a wall or onto another particle. Most aerosol particles carry some electric charge and some may be highly charged and therefore the most important electrostatic effect is the force exerted on a charged particle in an electrostatic field. For highly charged particles it is the case that the electrostatic force can be thousands of times greater than the force of gravity. When particles are charged and without an imposed external electrostatic field, electrostatic dispersion and deposition still exist due to space charging where the particles induces an electrostatic field.

In the open literature numerous models describing deposition of aerosol particles in laminar and turbulent pipe flows have been proposed during the last several decades but there is not much reported on general particle plugging models in pipe flow.

Chapter 3

Experimental Methods

The following chapter respectively describes the experimental setup used for Scanning Mobility Particle Sizer™ (SMPS™) Spectrometer measurements of nanometer and submicrometer potassium chloride (KCl) aerosol particle deposition due to Brownian diffusion and electrostatic dispersion. It also describes deposition of micrometer cross-linked Polymethyl Methacrylate (PMMA) particles due to shear-induced lift and KCl aerosol particle plugging experiments of SCR monolithic catalysts in a SCR pilot plant.

3.1 Setup for Polydisperse Submicrometer Aerosol Measurements

An experimental setup has been built for measuring deposition of nanometer and submicrometer polydisperse aerosol particles in a tube. Figure 3.1 shows a schematic illustration of the experimental setup. The experimental setup consisted of a Six-Jet Atomizer Model 9306A *TSI Incorporated* (see Appendix A for a detailed description), a Scanning Mobility Particle Sizer™ (SMPS™) Spectrometer Model 3936 *TSI Incorporated* (a detailed description is given in Appendix B), an Electrometer Model 3068B *TSI Incorporated* (see Appendix C), a Diffusion Dryer Model 3062 *TSI Incorporated* (see Appendix D), an Aerosol Neutralizer Model 3054 *TSI Incorporated* (see Appendix E), a three-meter long aerosol deposition pipe for measuring the deposition of aerosol particles and two sampling lines for respectively Scanning Mobility Particle Sizer™ (SMPS™) Spectrometer measurements and for total average charge measurements using an Electrometer. The flow rate in the aerosol deposition pipe was about 300 ml/min, giving an average velocity of around 0.17 m/s corresponding to a Reynolds number of about 63, to ensure enough residence time for deposition of nanometer and submicrometer particles. All fittings in the setup were Swagelok® and tubes

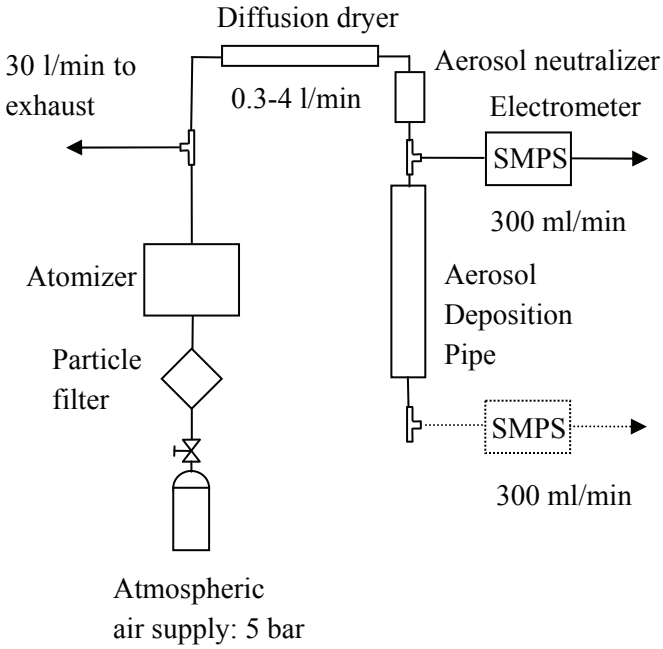

Figure 3.1: Schematic illustration of the experimental setup for measuring deposition of polydisperse submicrometer particles in a three-meter long electro polished aerosol deposition pipe with a diameter of 6 mm.

were made of carbonized silicon material to minimize deposition due to electrostatic forces. Dimensions of the fittings and tubes in the setup were ¼" inch except for connections to the atomizer, where ½" fittings and tubes were used. The aerosol deposition pipe consisted of an electro polished stainless steel tube with a diameter of 6 mm and the pipe was 3 meter long and bent in four sections of about 0.75 meter due to space requirements as seen in Figure 3.2. Further in order to investigate the effect of secondary flow on the aerosol particle deposition efficiency the electro polished pipe also consisted of a three-meter long straight pipe for comparison. The electro polished aerosol deposition pipe had an average surface roughness of 130 nm.

The principle of the setup was as follows: Particle free pressurized atmospheric air up to 5 bar controlled by a valve was fed to the atomizer through a particle filter. The atomizer was set to a pressure of up to 5 bar giving a flow rate up to about 10 l/min per nozzle which was connected to the exhaust system. Because the SMPS Spectrometer was set to a flow rate of 300 ml/min controlled by an internal vacuum pump in the Condensation Particle Counter (CPC), a side stream of about 300 ml/min was drawn from the atomizer main aerosol stream through the diffusion dryer and Aerosol Neutralizer (discharging the aerosol particles to a

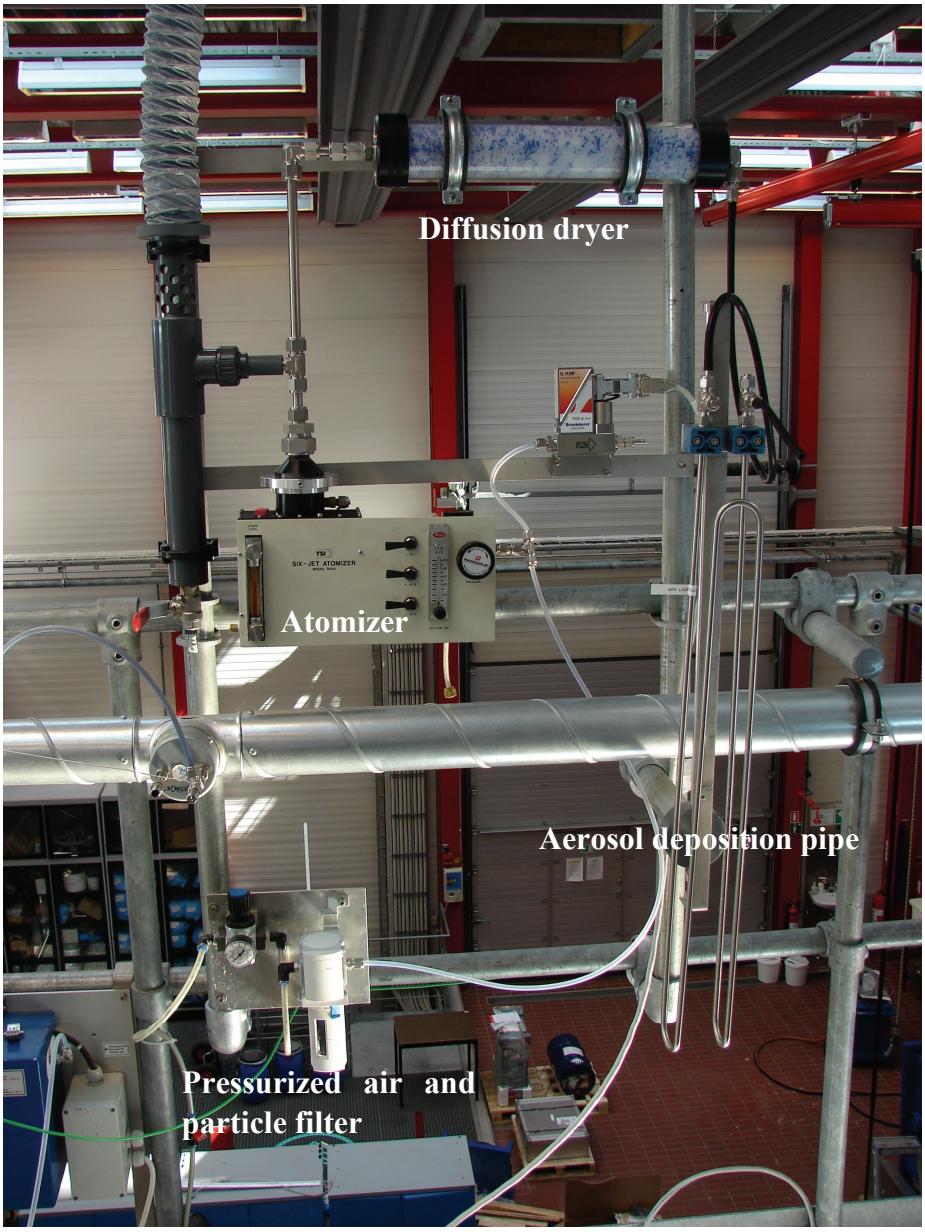

Figure 3.2: Aerosol deposition setup.

bipolar charge equilibrium – approximately Boltzmann charge equilibrium) and through the aerosol deposition pipe. The surplus of the aerosol stream from the atomizer was led to the exhaust system.

To minimize deposition losses through the sampling lines, these were made as short as possible giving a maximum length of about 10 cm. To minimize deposition in the system due to electrostatic forces the setup was grounded using

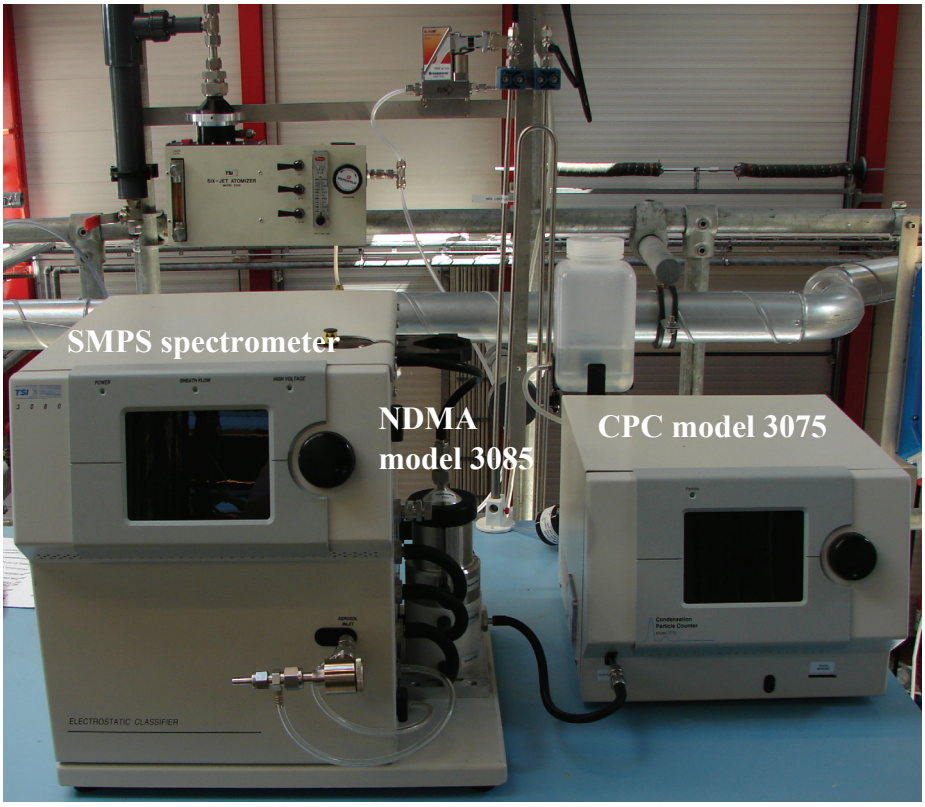

Figure 3.3: TSI SMPS spectrometer with a model 3085 NDMA and a model 3075 CPC.

stainless steel and carbonized tubes and explicitly grounded using electrical wires connected to the electrical installations.

The Scanning Mobility Particle Sizer™ (SMPS) Spectrometer consisted of an Electrostatic Classifier model 3080 *TSI Incorporated* used with either a Long Differential Mobility Analyser (LDMA) model 3081 *TSI Incorporated* or a Nano Differential Mobility Analyser (NDMA) model 3085 *TSI Incorporated* (depending on the aerosol size distribution and the system settings) and a Condensation Particle Counter (CPC) model 3775 *TSI Incorporated*. The SMPS spectrometer measured the size distribution of a polydisperse aerosol in the size range between 4.4-833 nm using the NDMA for particles in the size range between 4.4-168 nm and the LDMA for particles in the size range between 13-833 nm. The Condensation Particle Counter (CPC) model 3775 *TSI Incorporated* counted the different classes of particles classified by respectively the NDMA and LDMA.

Aerosol particles were generated by the Six-Jet Atomizer Model 9306A *TSI Incorporated*, using a liquid solution consisting of potassium chloride, KCl. The

KCl aerosol particles were generated from a liquid solution of KCl between 0.0002-0.002 wt% KCl. The number concentration and size distribution of the aerosol particles were controlled by the pressure in the atomizer and the concentration of the solution. The droplets were dried to solid particles through the diffusion dryer. Calculations show that for particles as large as 800 nm the evaporation time is only about 5 seconds and with a flow rate of 300 ml/min through the diffusion dryer (length about 50 cm and channel diameter about 12.5 cm) with a residence time of about 12 seconds the particles escaping the diffusion dryer can be assumed dry. The calculations can be seen in Appendix D.

Aerosol particle size distributions were measured at the top and at the bottom of the aerosol deposition pipe as illustrated in Figure 3.1. Respectively 5 or 10 size distributions were measured at the top and the bottom and repeated twice. The Scan Up time (the period during which the classifier centre rod voltage is exponentially increased in magnitude) and Scan Retrace time (the time the classifier voltage is reset to its initial voltage) of the SMPS Spectrometer was respectively 300 s and 15 s. Based on the 10 or 20 size distributions, an average size distribution was determined as well as the standard deviation. The aerosol particle deposition efficiency was then determined by subtracting the size distribution at the bottom of the aerosol deposition pipe from the size distribution at the top. The total aerosol particle number concentration at the top of the aerosol deposition pipe was measured by averaging the particle number concentration counted by the CPC each second over a period of 10 to 30 minutes. The average number of elementary charges per particle, i, was measured by averaging the current measured each second by the Electrometer over a period of 15 minutes and determined as follows

$$i = \frac{I}{NeQ} \tag{3.1}$$

where I (A) is the current measured by the Electrometer, N (particles/cm^3) is the aerosol concentration at the top of the aerosol deposition pipe, e is the elementary unit charge ($e = 1.6 \cdot 10^{-19}$ C) and Q (cm^3/s) is the volume flow through the aerosol deposition pipe.

Figure 3.2 shows a picture of the aerosol deposition setup as illustrated in Figure 3.1 without the Aerosol Neutralizer, and Figure 3.3 shows a picture of the SMPS spectrometer used in measuring the aerosol particle size distribution and number concentration.

In order to prevent errors in the aerosol particle deposition measurements, due to agglomeration, calculation of the characteristic time for agglomeration (the time

for the initial particle number concentration of particles to decrease one per cent) was carried out. This was done to ensure that the changes in particle size distribution measured before and after the three-meter long aerosol deposition pipe was only due to particle deposition and not due to agglomeration of particles which otherwise would give growth in particle sizes. These calculations showed that the characteristic time for agglomeration for e.g. an initial particle number concentration, $n_0 = 2 \cdot 10^{12}$ #/m^3 of monodisperse 100 nm particles in the inlet of the aerosol deposition pipe was about 2 seconds (worst case). The residence time in the three-meter long aerosol deposition pipe was about 18 seconds. So based on a rough approximation the size distribution would decrease 9% due to agglomeration. This was under the assumption that the size distribution was monodisperse with an initial particle number concentration, $n_0 = 2 \cdot 10^{12}$ #/m^3. In the experiments the maximum total particle number concentrations was about $2 \cdot 10^{12}$ #/m^3 for a polydisperse aerosol particle size distribution so the characteristic time for agglomeration would be higher and the effect of agglomeration has therefore been neglected. Comparison between top and bottom of the aerosol deposition pipe of aerosol particle size distributions based on particle number concentration and mass concentration also confirms that agglomeration can be neglected. The calculations can be seen in Appendix H.

3.2 Setup for Monodisperse Submicrometer Aerosol Measurements

In order to measure deposition of nanometer and submicrometer monodisperse aerosol particles with a known bipolar charge distribution in a pipe, the experimental setup shown in Figure 3.1 was redesigned as shown in Figure 3.4. In that way the influence of electrostatic forces on the deposition efficiency could be quantified by using the DMA to select a certain particle size, because the aerosol particles were discharged in the DMA by an aerosol neutralizer to a bipolar charge distribution (approximately Boltzmann charge equilibrium).

The experimental setup consisted of the same components as for the experiments with polydisperse particles, but the NDMA was now used to select a certain particle size as seen in Figure 3.4. The same condition for the setup was used for the monodisperse measurements as described in Section 3.1 for the polydisperse aerosol measurements. The NDMA was set to select particle sizes equal to 10 to 15 nm with intervals of 1 nm and 15 to 30 nm with intervals of 5 nm and 30 to 100 nm with interval of 10 nm. The total aerosol particle number concentration of the monodisperse aerosol particles respectively at the top and the bottom of the aerosol deposition pipe, selected by the NDMA, was measured by averaging the

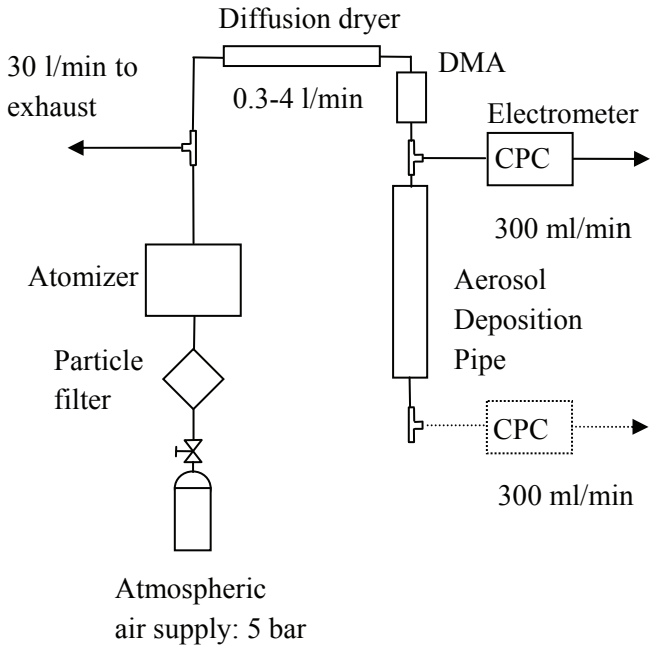

Figure 3.4: Schematic illustration of the experimental setup for measuring deposition of monodisperse submicrometer particles in a three-meter long electro polished pipe with a diameter of 6 mm.

particle number concentration counted by the CPC each second over a period of 900 to 1800 seconds. The aerosol particle deposition efficiency was then determined by subtracting the total aerosol particle number concentration at the bottom of the aerosol deposition pipe from the total aerosol particle number concentration at the top.

In order to validate the effect of secondary flow on the deposition of particles in the three-meter bent aerosol deposition pipe a three-meter long straight electro polished pipe was also used in the two setups illustrated in Figure 3.1 and Figure 3.4.

3.3 Setup for Monodisperse Micrometer Particle Measurements

An experimental setup has been built for measuring deposition of monodisperse micrometer cross-linked Polymethyl Methacrylate (PMMA) particles in a 1.0 meter straight pipe. Figure 3.5 shows a schematic illustration of the experimental setup and Figure 3.6 shows a picture of the setup.

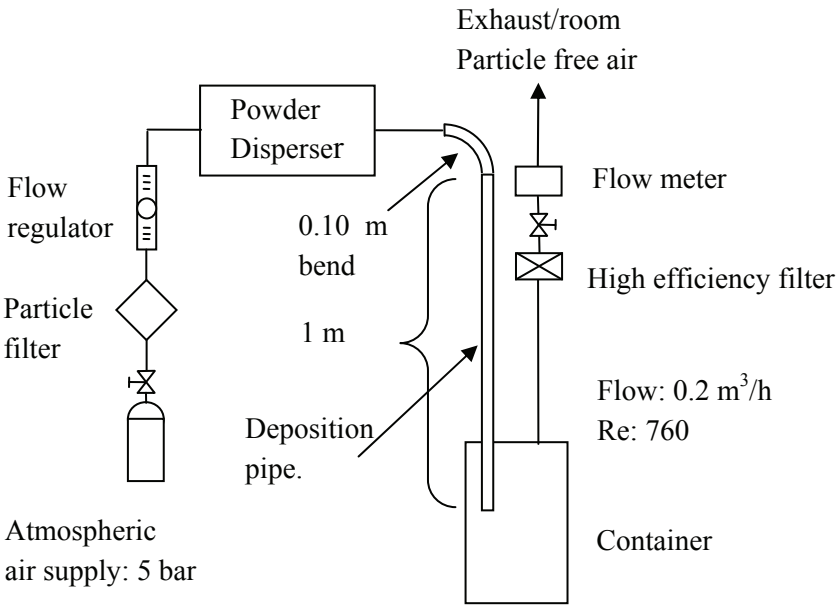

Figure 3.5: Schematic illustration of the experimental setup for measuring deposition of monodisperse micrometer particles in a 1.0 meter straight pipe with a diameter of 6 mm.

The experimental setup consisted of a particle filter, a flow regulator, a Palas RBG-2000 Powder Disperser (see Appendix F for a detailed description of the Palas RBG-2000 Powder Disperser), a 0.10 meter bend, a one-meter deposition pipe, a container, a high efficiency filter, a valve and a flow meter.

The operating principle was a follows: Pressurized air was led to the powder disperser, which contained the monodisperse particles (10, 20, 30 and 40 μm, respectively) as compacted powder in a cylindrical container. The flow rate of the pressurized air could be adjusted by means of a flow meter. The flow rate was set to 3.4 l/min corresponding to a Reynolds number of about 760 and a velocity of 2 m/s. The deposition pipe consisted of a 1.0 meter long electro polished stainless steel pipe with a diameter of 6 mm. The compacted powder was then fed onto a rotating brush by a piston and the powder loosened by the brush was blown away by the pressurized air. The speed of the rotating brush was 1200 rpm and the speed of the piston was 80 mm/h. The particles penetrating the deposition pipe were collected in a container and the mass of the container and particles were determined by weighing them. The particles that were deposited in the bend and in the pipe were collected by washing separately the bend and the pipe with demineralised water and collecting the particulate water in bottles. The particles were then filtered from the water and weighed in order to determine the mass of

the deposited particles. Each experiment was carried out for a period of time of 2 minutes for all four particle diameters. The mass entering the bend was determined based on the weight of the particles deposited in the bend and in the pipe and the penetrating particles collected at the outlet of the pipe. The mass entering the pipe was determined in a similar manner.

The overall deposition efficiency, the deposition efficiency of the bend and the pipe were then determined as follows

$$\eta_{overall} = \frac{m_{deposit,bend} + m_{deposit,pipe}}{m_{in}}$$
$$\eta_{bend} = \frac{m_{deposit,bend}}{m_{in}} \tag{3.2}$$
$$\eta_{pipe} = \frac{m_{deposit,pipe}}{m_{in,pipe}}$$

Monodisperse micrometer cross-linked PMMA particles with sizes 10 μm, 20 μm, 30 μm and 40 μm were used in the experiments.

3.4 SCR Pilot Plant

Commercial corrugated-type SCR monolithic catalysts obtained from Haldor Topsøe A/S were used in the KCl aerosol particle plugging experiments. The monolithic catalysts used in the test were respectively DNX x30 and DNX x80, and the monoliths were dummies in the sense that they consisted only of a corrugated, fibre-reinforced titanium dioxide (TiO_2) carrier and were not impregnated by divanadium pentaoxide (V_2O_5) and tungsten trioxide (WO_3). The sizes of the monolithic catalysts were 7.5×7.5×50 cm. An example is shown in Figure 3.8

Figure 3.7 shows a schematic illustration of the SCR pilot plant used for plugging test of full-length monolithic catalysts. The pilot plant consisted of a 50 kW natural gas burner, a water cooled lance consisting of a two fluid (pressurized air and the liquid solution) nozzle at the outlet for injecting liquid solutions, a square duct (SCR reactor) hosting a full length commercial monolithic catalyst, a soot blowing system two different heat exchangers and two 100 l containers for the liquid solution. The liquid solution was salt (7.4 g/l KCl) in distilled water.

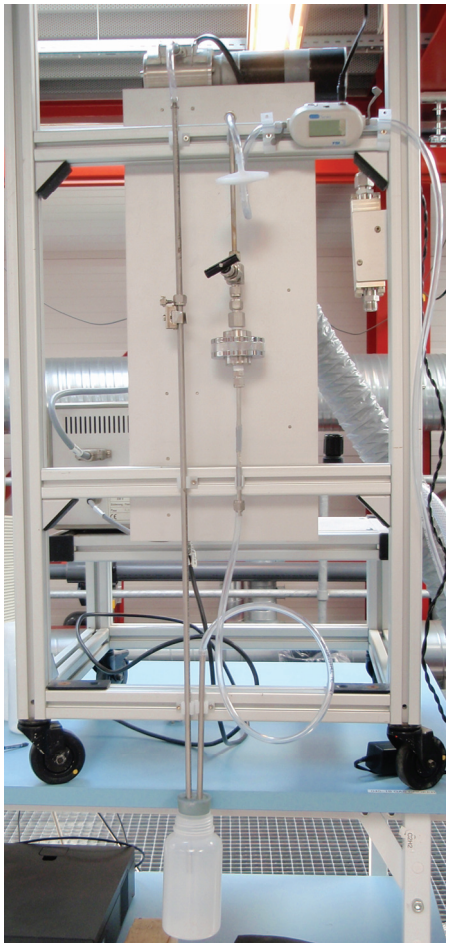

Figure 3.6: Micrometer particle deposition setup.

The principle of the setup was as follows: The setup ran slightly below atmospheric pressure (0-20 mbar) for safety reasons and natural gas was burned in order to generate flue gas. The flue gas exiting the burner at about 1000-1100°C was then led to a high-temperature pipe where the KCl solution was injected from the two 100 l containers through the water-cooled lance into the high-temperature pipe at a temperature above the melting point of KCl, and an aerosol of the KCl salt was generated. The pump injecting the salt solution from the two 100 l containers was set to a flow of 400 ml/h giving a mass flow of $8.22 \cdot 10^{-7}$ kg/s.

A bayonet heat exchanger was inserted into the main duct (high-temperature pipe) downstream of the formation of the desired aerosol particles to cool down the flue gas before the un-lined steel tube to avoid accelerated corrosion caused by the potassium compounds. The temperature of the flue gas at the inlet of the SCR reactor was kept at about 350°C. Three soot blowers were placed just above the

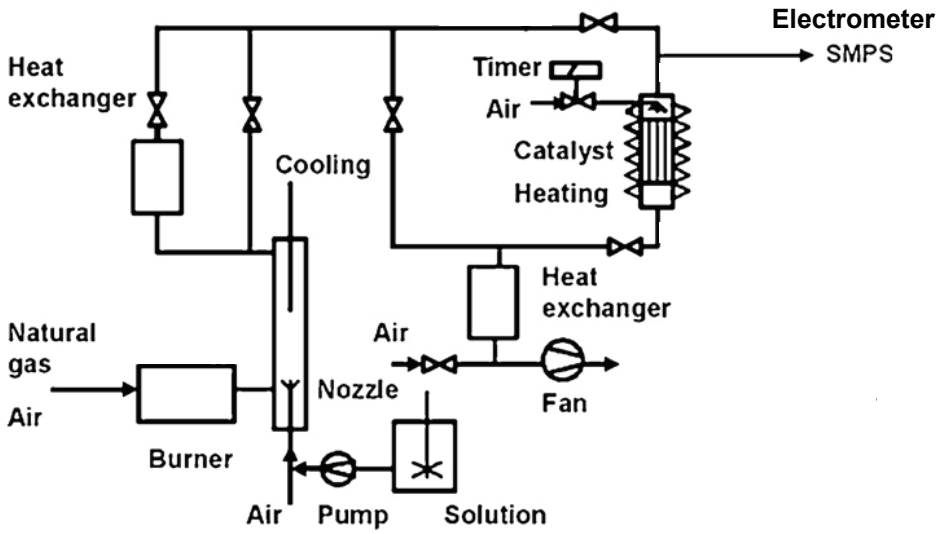

Figure 3.7: Schematic illustration of pilot-scale setup for monolithic catalysts plugging test.

monolithic catalyst to blow away any fragments of old deposit from the pipes upstream of the monolithic catalyst during start up in order to reduce deposition on the top of the monolithic catalyst induced by these fragments and to ensure a clean monolith at the beginning of the plugging experiments. The soot blowing was carried out by 3-5 s of blowing with compressed air at an interval of 30 minutes. The total flow rate at the outlet of the burner was about 60 Nm^3/h and the flow rate through the catalyst was kept at 40 Nm^3/h, by adjusting a bypass valve, which corresponded to a channel velocity of 4.5 m/s upstream of the catalyst.

The deposited mass of KCl aerosol particles in the monolithic catalysts was determined by washing the monolith after each experiment in ultra-pure water. In order to determine the axial deposition profile the monoliths were also cut in six pieces (0-1 cm, 1-10 cm, 10-20 cm, 20-30 cm, 30-40 cm and 40-50 cm). Each piece was washed in 4 or 5 l ultra-pure water and 50 ml samples were taken and sent to analysis for detecting the weight per cent of potassium, K, in the samples. The total amount of KCl aerosol particles deposited in the monolithic catalysts was then estimated based on the equimolar ratio of K and Cl in the KCl molecule.

Scanning Mobility Particle Sizer measurements just above the SCR reactor were carried out in order to measure the particle size distribution and number concentration at the inlet of the monolithic catalyst. Particle sampling was carried out at the inlet of the monolithic catalyst by an ejector sampler running with dry,

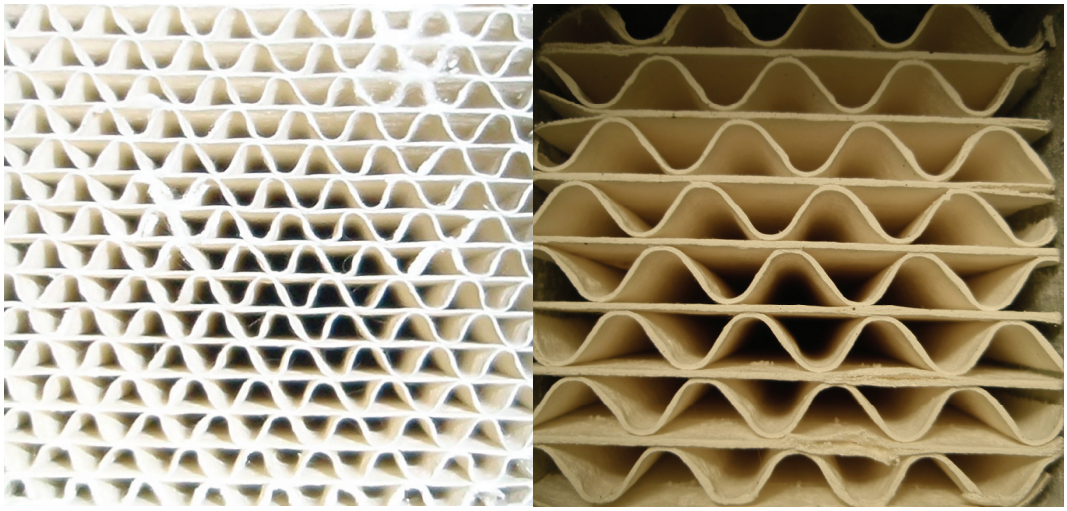

Figure 3.8:Illustration of a Topsøe DNX x30 and a DNX x80 monolithic catalyst which are used in the experimental investigation. The left picture shows the DNX x30 monolithic catalyst with a hydraulic diameter of 3.4mm. The right picture shows a DNX x80 monoltihic catalyst with a hydraulic diameter of 8 mm.

particle-free air. The flue gas in the ejector was cooled and diluted several orders of magnitude in order to prevent water condensation and particle agglomeration in the sampling line. The dilution ratio was obtained by measuring the CO_2 concentration both in the flue gas and in the diluted sample. The aerosol particle size distributions were measured 20 times. The scan up time and retrace time of the SMPS Spectrometer was respectively 300 s and 15 s. Based on the 20 size distributions an average size distribution and the standard deviation was determined. The total aerosol particle number concentration of the aerosol deposition pipe was measured by averaging the particle number concentration counted by the CPC each second over a period of 15 minutes. The average number of elementary charges per particle, *i*, was measured by averaging the current measured each second by the Electrometer over a period of 10 minutes.

Chapter 4

Computational Fluid Dynamics Methods

The following chapter describes the theory used to implement Brownian diffusion, electrostatic dispersion and shear-induced lift in an Eulerian-Eulerian and an Eulerian-Lagrangian (shear-induced lift only in an Eulerian-Lagrangian frame of reference) frame of reference in Computational Fluid Dynamics (CFD), respectively. It also describes the theory used to implement particle-wall interactions and accumulation of particle mass at surfaces, such as the wall of an SCR catalyst in a CFD model that takes deposit build-up into account. Finally it describes a simple empirical deposition model based on turbulent diffusion in a tube.

Particle diffusion, convection and deposition, due to Brownian motion and electrostatic forces in laminar flow, in an aerosol deposition pipe with a diameter of 6 mm and a length of 3 meter, bent in four sections of about 0.75 meter and a straight 3 meter long aerosol deposition pipe with a diameter of 6 mm, respectively has been numerically investigated using potassium chloride, KCl, particles in the particle size range between 1-1000 nm. The volume fraction calculated based on the measured size distributions has been in the range between about $1 \cdot 10^{-11}$ to $1 \cdot 10^{-10}$. The flow is therefore highly diluted and the influence of the particulate phase on the gas phase and agglomeration has been neglected in the simulations. Calculations of the characteristic time for agglomeration also confirm that agglomeration can be neglected, as shown in Appendix H. Because the particles are submicrometer the influence of gravity on the particles has been neglected. Particle dispersion and deposition due to shear-induced lift in laminar flow in a deposition pipe with a diameter of 6 mm and a length of 1.0 meter has been numerically investigated using cross-linked PMMA, particles in the particle

size range between 1-40 μm. The volume fraction calculated based on the measured concentrations has been in the range between about $5 \cdot 10^{-5}$ to $2 \cdot 10^{-4}$ and the effect of particle-particle interaction has therefore been neglected and a one-way coupling has been used in the simulations. Particle deposition in laminar and turbulent flow, respectively, in monolithic catalysts (Topsøe "sinus" geometry) has been numerically investigated using a particle-wall interaction model that takes deposit build-up into account. KCl, particles in the particle size range between 0.039-10 μm based on impactor measurements [Zheng et al. (2008)] were used in the simulations. The volume fraction calculated based on the measured concentrations was about $4.2 \cdot 10^{-9}$ so the effect of particle-particle interaction has been neglected. Two-way coupling has been used in the simulations because of the coupling between electrostatic potential, charge density and particle distribution and dynamic mesh. All the numerical investigations have been carried out using the commercial Computational Fluid Dynamics solver ANSYS-Fluent® version 6.23 and ANSYS-Fluent® version 12.0.1 respectively.

4.1 Computational Fluid Dynamics

The well-established general purpose finite volume methods have been used as discretization methods to approximate the governing equations describing fluid motion by a system of algebraic equations using the commercial Computational Fluid Dynamics (CFD) solver ANSYS-Fluent® version 6.23 and ANSYS-Fluent® version 12.0.1 respectively. The approximations are applied to small domains (control volumes) in space and/or time so the numerical solution provides results at discrete locations in space and/or time based on the flow geometry, the physical properties of the fluid and the boundary and initial conditions of the flow field. Because the underlying physical phenomena are complex and non-linear an iterative solution approach is required. The numerical prediction generally concerns sets of values of the flow variables, e.g. velocity, pressure, temperature, species, etc.

4.2 Numerical Modelling of Fluid Flow and Particles

Steady-state and transient laminar and turbulent CFD simulations have been carried out in three-dimensional Cartesian coordinates using both an Eulerian-Lagrangian reference frame and an Eulerian-Eulerian (only steady-state and laminar) reference frame. The effect of the dispersed secondary particle phase have been modelled using a Discrete Particle Model (DPM) or as a continuum (Eulerian reference frame) using User Defined Scalar transport equations,

respectively. In the turbulent cases using the Discrete Particle Model the stochastic Random Walk Model (RWM) has been used to model the dispersion of the particles. The fluid flow has been modelled using the Reynolds-averaged Navier-Stokes equations (RANS) which govern the transport of averaged flow quantities with the whole scales of turbulence being modelled. In the Reynolds averaging the solution variables to the Navier-Stokes equations are decomposed into a mean and a fluctuating component, which e.g. for the velocity is given as

$$u_i = \overline{u}_i + u_i' \tag{4.1}$$

These decomposed variables are substituted into the instantaneous continuity and momentum equations and time averaged, which then gives the Reynolds-averaged Navier-Stokes equations (RANS). The RANS equations have the same general form as the instantaneous continuity and Navier-Stokes equations (which are used for steady-state and transient laminar flow), with the velocities and other flow quantities now representing the time averaged values.

The equation for conservation of mass (continuity equation) for incompressible steady-state and transient flow can be stated as follows using tensor notation [Hughes and Brighton (1999), p. 248]

$$\frac{\partial \overline{u}_i}{\partial x_i} = 0 \tag{4.2}$$

where ρ is the density of the fluid and $\overline{u}_i$ is the time-averaged velocity. For a 3-dimensional incompressible transient flow the Reynolds-averaged Navier-Stokes equation for an inertial (non-accelerating) reference frame can be stated as [Hughes and Brighton (1999), p. 248]

$$\frac{\partial \rho \overline{u}_i}{\partial t} + \frac{\partial}{\partial x_j}\left(\rho \overline{u}_i \overline{u}_j\right) = -\frac{\partial \overline{p}}{\partial x_i} + \frac{\partial}{\partial x_j}\left[\mu\left(\frac{\partial \overline{u}_i}{\partial x_j} + \frac{\partial \overline{u}_j}{\partial x_i}\right)\right] + \overline{F}_i + \frac{\partial}{\partial x_j}\left(-\rho \overline{u_i' u_j'}\right) \tag{4.3}$$

where ρ is the density of the fluid, $\overline{p}$ is the time-averaged thermodynamic pressure and $\overline{F}_i$ are time-averaged body forces (e.g. that arise from interaction with a dispersed phase or gravity). The first term on the left-hand side of Equation (4.3) is the acceleration term and the second term is the convective acceleration term. The first term on the right-hand side is the pressure forces, the second term is the viscous forces (diffusion term), and the third term are body forces. For the RANS equations compared to the instantaneous Navier-Stokes equations an additional term appears on the right-hand side representing the effect of turbulence (called the Reynolds stresses).

For an arbitrary scalar, ϕ_k, the transport equation can be written as follows using tensor notation [Fluent (2006), p. 9-5]

$$\begin{gathered}\frac{\partial \rho \phi_k}{\partial t}+\frac{\partial}{\partial x_i}\left(\rho u_i \phi_k+J_i\right)=S_{\phi_k} \quad k=1..m \\ \Downarrow \\ \frac{\partial \rho \phi_k}{\partial t}+\frac{\partial}{\partial x_i}\left(\rho u_i \phi_k-\Gamma_k \frac{\partial \phi_k}{\partial x_i}\right)=S_{\phi_k} \qquad k=1..m\end{gathered} \tag{4.4}$$

where J_i is the flux tensor, Γ_k is the diffusion coefficient and S_{ϕ_k} is the source term for each of the k scalar transport equation and u_i is the velocity component of the velocity vector. For a steady-state incompressible flow, where the acceleration term is zero and the continuity equation is equal to zero as from Equation (4.2), a monodisperse aerosol with particle number concentration, n, neglecting gravity and constant particles diffusion coefficient, $\Gamma_k = \rho D$, Equation (4.4) would be

$$\begin{gathered}u_i \frac{\partial n}{\partial x_i}+n \frac{\partial u_i}{\partial x_i}=D \frac{\partial^2 n}{\partial x_i \partial x_i} \\ \Downarrow \\ u_i \frac{\partial n}{\partial x_i}=D \frac{\partial^2 n}{\partial x_i \partial x_i}\end{gathered} \tag{4.5}$$

For a polydisperse aerosol with n_k representing the particle number concentration of the k different particle sizes, there would just be k different scalar transport equation of Equation (4.5). In the case of turbulent flow, using Equation (4.4) or Equation (4.5), the transport equation for an arbitrary scalar, ϕ_k, then the velocity, u_i, is the time-averaged velocity and the arbitrary scalar, ϕ_k, is the time-averaged value of this scalar. In this case fluctuation in the arbitrary scalar, ϕ_k, has been neglected. The particle diffusion coefficients used in the CFD simulations have been calculated using the Stokes-Einstein equation

$$D=\frac{k_B T C_c}{3 \pi \mu D_p} \tag{2.6}$$

where C_c is the Cunningham correction factor, k_B is the Boltzmann constant, T is the temperature, μ is the dynamic viscosity of the fluid and D_p is the aerosol particle diameter. The Cunningham correction factor, C_c, is defined as

$$C_c=1+Kn\left[1.257+0.40 \exp\left(-\frac{1.10}{Kn}\right)\right] \tag{2.4}$$

where Kn is the Knudsen number and is defined as follows

$$Kn = \frac{2\lambda}{D_p} = \frac{\lambda}{R_p} \tag{2.5}$$

in which λ is the mean free path of the fluid and R_p is the particle radius. The particle mass flux vector, $\vec{J}$, per unit volume resulting from simultaneous diffusion and migration in an external force field can be obtained by summing the two effects [Friedlander (2000), p. 39]

$$\vec{J} = -\rho D\vec{\nabla}n + \rho\vec{v}_m n \tag{4.6}$$

where $\vec{v}_m$ is the particle migration velocity due to an external force field. For incompressible flow the general equation for conservation of the particle number concentration, n, for a monodisperse aerosol in the presence of an external force field [Friedlander (2000), p. 39], can be obtained, by substituting the particle mass flux vector, $\vec{J}$, given in Equation (4.6) into Equation (4.4) for k=1 and setting the source term, $S_{\phi_k} = 0$, as follows

$$\begin{gathered} \frac{\partial \rho\phi}{\partial t} + \frac{\partial}{\partial x_i}\left(\rho u_i \phi + J_i\right) = 0 \\ \Downarrow \\ \frac{\partial n}{\partial t} + \vec{\nabla}\cdot\left(n\vec{v} + \vec{v}_m n\right) = \vec{\nabla}\cdot\left(D\vec{\nabla}n\right) \end{gathered} \tag{4.7}$$

The particle force balance written in a Lagrangian reference frame is given as follows [Fluent (2006), p. 22-5]

$$m_p \frac{d\vec{u}_p}{dt} = \vec{F}_{drag} + m_p\left(1 - \frac{\rho_f}{\rho_p}\right)\vec{g} + \vec{F_L} + \vec{F_B} + \vec{F_E} \tag{4.8}$$

where $\vec{u}_p$ is the particle velocity at position $\vec{x}$, t is the time, ρ_f is the fluid density, ρ_p is the particle density and $\vec{g}$ is the gravitational acceleration vector. The first term on the right-hand side of Equation (4.8) is the drag force, $\vec{F}_{drag}$, the second term on the right-hand side is the Buoyancy, the third term on the right-hand side is the Saffman lift force, $\vec{F}_L$, the fourth term on the right-hand side is the force due to Brownian motion (Brownian force), $\vec{F}_B$, and the fifth term on the right-hand side is the electrostatic forces, $\vec{F}_E$.

The three-dimensional version of the Saffman lift force which is valid for small particle Reynolds numbers is given as follows

$$\vec{F_L} = m_p \frac{2K\nu^{1/2}\rho_f d_{ij}}{\rho_p D_p \left(d_{lk}d_{kl}\right)^{1/4}}\left(\vec{u} - \vec{u}_p\right) \tag{2.16}$$

where d_{ij} is the deformation tensor and is defined as

$$d_{ij} = \frac{1}{2}\left(\frac{\partial u_i}{\partial x_k} + \frac{\partial u_k}{\partial x_i} \right) \tag{4.9}$$

Equation (2.16) is a generalization of the two-dimensional expression given by Saffman (2.13) to a three-dimensional shear field and is valid for small particle Reynolds numbers.

Brownian motion effects are significant for submicrometer particles. The components of the Brownian force, F_{Bi}, is modelled as a Gaussian white noise process with spectral intensity, $S_{n,ij}$, given as [Li and Ahmadi (1992)]

$$S_{n,ij} = S_0 \delta_{ij} \tag{4.10}$$

In Equation (4.10), δ_{ij} is Kronecker's delta function and S_0 is given as follows

$$S_0 = \frac{216 \nu k_B T}{\pi^2 \rho_f d_p^5 \left(\frac{\rho_p}{\rho_f} \right)^2 C_c} \tag{4.11}$$

where ν is the kinematic viscosity of the fluid, k_B is the Boltzmann constant, T is the absolute temperature of the fluid. The amplitudes of the Brownian force components is given as

$$F_{B_i} = \zeta_i \sqrt{\frac{\pi S_{n,ij}}{\Delta t}} \tag{4.12}$$

where ζ_i in Equation (4.12) are zero-mean, unit-variance-independent Gaussian random numbers (three independent numbers are numerically generated for each time step). Δt is an integration time step during the particle tacking and Abuzeid et al. (1991) emphasize that Δt should be much larger than the molecular time scale and much smaller than the particle relaxation time.

The drag force, $\vec{F}_{drag}$, is calculated as [Fluent (2006), p. 22-5]

$$\vec{F}_{drag} = m_p \frac{18\mu}{\rho_p D_p^2 C_c} \frac{C_D \,\mathrm{Re}}{24} \left(\vec{u} - \vec{u}_p \right) \tag{4.13}$$

where $\vec{u}$ is the fluid velocity vector. The drag coefficient, C_D, for a spherical particle can be calculated as a function of the particle Reynolds number from the following correlation given by Haider and Levenspiel (1989)

$$C_D = \frac{24}{\mathrm{Re}} \left(1 + 0.1806\,\mathrm{Re}^{0.6459} \right) + 0.4251 \Big/ \left(1 + \frac{6880.95}{\mathrm{Re}} \right) \tag{2.35}$$

For submicrometer particles the drag force, $\vec{F}_{drag}$, is modelled based on Stokes' law as follows [Fluent (2006), p. 22-7]

$$\vec{F}_{drag} = m_p \frac{18\mu}{\rho_p D_p^2 C_c}\left(\vec{u} - \vec{u}_p\right) \tag{4.14}$$

4.3 Turbulent Flow

The whole scales of turbulence (the effect of turbulence) is represented through the Reynolds stresses in the Reynolds-averaged Navier-Stokes equations (RANS) given in Equation (4.3). The Reynolds stresses is modelled using the Boussinesq hypothesis to relate the Reynolds stresses to the mean velocity gradients as follows [Fluent (2006), p. 12-5]

$$-\rho\overline{u_i' u_j'} = \mu_t\left(\frac{\partial \bar{u}_i}{\partial x_j} + \frac{\partial \bar{u}_j}{\partial x_i}\right) - \frac{2}{3}\left(\rho k + \mu_t \frac{\partial \bar{u}_k}{\partial x_k}\right)\delta_{ij} \tag{4.15}$$

where k is the turbulent kinetic energy and μ_t is the turbulent viscosity. In the present work the k-ε model was chosen for its simplicity and robustness, computational economy and reasonable accuracy and it is the most validated turbulence model which gives excellent performance for many industrially relevant problems [Fluent (2006), p. 12-12; Versteeg and Malalasekera (2007), p. 80]. The time-averaged transport equation for the mean kinetic energy of turbulence, k, is given as follows [Fluent (2006), p. 12-13; Versteeg and Malalasekera (2007), p. 75]

$$\frac{\partial}{\partial t}(\rho k) + \frac{\partial}{\partial x_i}\left(\rho k \bar{u}_i\right) = \frac{\partial}{\partial x_j}\left[\left(\mu + \frac{\mu_t}{\sigma_k}\right)\frac{\partial k}{\partial x_j}\right] + G_k - \rho\varepsilon \tag{4.16}$$

where G_k is the generation of turbulent kinetic energy due to the mean velocity gradients and ε is the rate of dissipation of the mean turbulence kinetic energy. The transport equation for the rate of dissipation, ε, is given as [Fluent (2006), p. 12-13; Versteeg and Malalasekera (2007), p. 75]

$$\frac{\partial}{\partial t}(\rho\varepsilon) + \frac{\partial}{\partial x_i}\left(\rho\varepsilon \bar{u}_i\right) = \frac{\partial}{\partial x_j}\left[\left(\mu + \frac{\mu_t}{\sigma_k}\right)\frac{\partial \varepsilon}{\partial x_j}\right] + C_{1\varepsilon}\frac{\varepsilon}{k}G_k - C_{2\varepsilon}\rho\frac{\varepsilon^2}{k} \tag{4.17}$$

where $C_{1\varepsilon} = 1.44$, $C_{2\varepsilon} = 1.92$, $\sigma_k = 1.0$ and $\sigma_\varepsilon = 1.3$. The turbulent viscosity (eddy viscosity) given in Equation (4.16) and Equation (4.17) can based on dimensional analysis be calculated as [Fluent (2006), p. 12-13; Versteeg and Malalasekera (2007), p. 75]

$$\mu_t = \rho C_\mu \frac{k^2}{\varepsilon} \tag{4.18}$$

where C_μ = 0.09. The generation of turbulence kinetic energy due to the mean velocity gradients, G_k, is given as [Fluent (2006), p. 12-22; Versteeg and Malalasekera (2007), p. 75]

$$G_k = \mu_t \left(\frac{\partial \bar{u}_i}{\partial x_j} + \frac{\partial \bar{u}_j}{\partial x_i} \right) \frac{\partial \bar{u}_i}{\partial x_j} \tag{4.19}$$

In the turbulent cases using the Discrete Particle Model (DPM) the discrete stochastic Random Walk Model (RWM) (or "eddy lifetime") was used to simulate the dispersion of the particles. The discrete stochastic Random Walk Model (RWM) includes the effect of the instantaneous turbulent velocity fluctuations on the particle trajectories through the use of stochastic methods [Fluent (2006), p. 22-10].

4.4 Electrostatic Forces

Electrostatic forces (electrostatic dispersion) can take place because of the image force (polarization) between charged particles and a conductive wall (zero or constant potential), or because of electrostatic repulsion between particles charged with the same polarity (space-charge) or due to a total positive or negative average charge on a concentration of a cloud of charged aerosol particles. This space charge creates a migration of the charged particles to the boundaries of the system.

4.4.1 Eulerian-Eulerian Reference Frame

Using the Eulerian-Eulerian framework electrostatic dispersion due to electrostatic forces has been implemented through Equation (4.7) using a User Defined Scalar transport equation (Equation (4.5)) were the influence of gravity on the submicrometer particles has been neglected.

4.4.1.1 Migration Velocity

Pseudo steady-state motion (zero acceleration) of a single particle gives a balance on the particle between the external force field, $\vec{F}$, and the drag force, $\vec{F}_{drag}$, which can be stated as follows

$$\vec{F} = \vec{F}_{drag} \tag{4.20}$$

For small particles where the Stokes' law regime is valid the external force field can be stated as

$$\vec{F} = \vec{v}_m f \tag{4.21}$$

where $\vec{v}_m$ is the migration velocity and f is the Stokes' friction coefficient given in Equation (4.23). The migration velocity can then be expressed as

$$\vec{v}_m = \frac{\vec{F}}{f} \tag{4.22}$$

where the Stokes' friction coefficient is defined as

$$f = \frac{3\pi\mu D_p}{C_c} \tag{4.23}$$

4.4.1.2 Electrical Migration Velocity

When the external force field is an electric field e.g. due to space charging (induced by the charges particles because the particles are carrying i units of elementary charges, e) the electrostatic force, $\vec{F}_E$, on the particle is given by the electric field strength, $\vec{E}$, and the number, i, of elementary units of charges as follows

$$\vec{F}_E = ie\vec{E} \tag{4.24}$$

Substituting the electrical force given in Equation (4.24) into Equation (4.22) for the force balance with the Stokes' drag together with Equation (4.23) gives the electrical migration velocity, $\vec{v}_{el}$, as follows

$$\vec{v}_{el} = \frac{\vec{F}_E}{f} = \frac{ie\vec{E}C_c}{3\pi\mu D_p} = Z\vec{E} \tag{4.25}$$

The electrical mobility, Z, of the particle can be defined as

$$Z = \frac{ieC_c}{3\pi\mu D_p} \tag{4.26}$$

The general equation for conservation of the particle number concentration, n, in the presence of electrostatic forces can now be stated by substituting the electrical migration velocity, $\vec{v}_{el}$, given in Equation (4.25) into Equation (4.7) as follows

$$\frac{\partial n}{\partial t} + \vec{\nabla} \cdot \left(\vec{v} n + Z n \vec{E} \right) = D \vec{\nabla}^2 n \tag{4.27}$$

4.4.2 Eulerian-Lagrangian Reference Frame

The Discrete Phase Model (DPM) using a Lagrangian reference frame was also used to calculate the flow of the particulate phase of submicrometer and micrometer particles respectively including the effects of Brownian motion, electrostatic forces and shear-induced lift. Calculations of the volume fraction of the particulate based on the experimental measurements of the particle concentrations and size distributions in the gas-solid two-phase flow, has showed that it is very low and the effect of particle-particle interaction has therefore been neglected but a two-way coupling has been used because of the coupling between the particle distribution in the flow and the electrostatic potential. The electrostatic forces due to a electrostatic field neglecting the dielectrophoretic and the dipole-dipole force has been implemented based on Shah et al. (2007) as follows

$$\vec{F}_E = q\vec{E} - \frac{q^2}{16\pi\varepsilon_0 y^2}\vec{n}_p \tag{2.24}$$

where q is the particle charge, y the distance to the wall, $\vec{E}$ is the electric field strength and $\vec{n}_p$ the unit vector from the location of the particle to the point of the wall where the distance is smallest. The first term on the right-hand side is the Coulomb force due to an electric field and the second term on the right-hand side is the image force. Equation (2.24) has been implemented through the particle force balance given in Equation (4.8).

4.4.3 Space Charge

The space charge of aerosol particles each carrying a charge, q, creates a non-zero potential within the system, and if the particle number concentration, n, of the aerosol particles is large, its space charge forms a continuum where the electrostatic potential, Φ, is a smooth function given by Poisson's equation as follows

$$\vec{\nabla}^2 \Phi = -\frac{q\,n}{\varepsilon_0} = -\frac{ie\,n}{\varepsilon_0} \tag{2.30}$$

where $q=ie$ is the total average charge carried by a particle, ε_0 is the permittivity of air and n is the particle number concentration.

4.5 Particle-Wall Interaction

The main adhesive forces are the van der Waals force, the electrostatic force and forces arising from surface tension of adsorbed liquid films. These forces are influenced by the shape, surface roughness and size of the particle material and by the roughness of the surface material and by the duration of the collision and the particle initial contact velocity. The van der Waals forces are known to cause adhesion onto a wall or onto another particle and come from interaction between solid surfaces on the molecular level and become apparent when smooth surfaces are brought into contact.

4.5.1 Simple Model for Particle-Wall Adhesion

A simple quasi-stationary collision model based on the conservation of energy for whether a charged particle will adhere or not to the surface wall of e.g. a tube that has been grounded, is presented in the following section. When a charged particle approaches a pipe wall there will be two cases, where the one case is that the charged particle will adhere to the wall and the other is that it will bounce. A quasi-stationary model is of course a rough assumption to a real collision (or dynamic collision) which would be very complicated to model because it involves dynamic energy dissipation mechanisms including radiation of photons, surface acoustic waves, stress and flexural waves with associated viscoelastic and viscoplastic energy dissipation [Dahneke (1995)].

Conservation of energy for a quasi-stationary particle-wall collision based on the illustrated collision shown in Figure 4.1 can be stated as follows

$$\begin{gathered} Energy\ before\ collision = Energy\ after\ collision + Loss \\ \Downarrow \\ E_{kin,1} + W_{vdW,1} + E_{el,1} = E_{kin,2} + W_{vdW,2} + E_{el,2} + E_{deform} \\ \Updownarrow \\ E_{kin,1} + W_{vdW,1} + E_{el,1} = E_{elastic} + E_{deform} \end{gathered} \tag{4.28}$$

$$E_{elastic} = E_{kin,2} + W_{vdW,2} + E_{el,2}$$

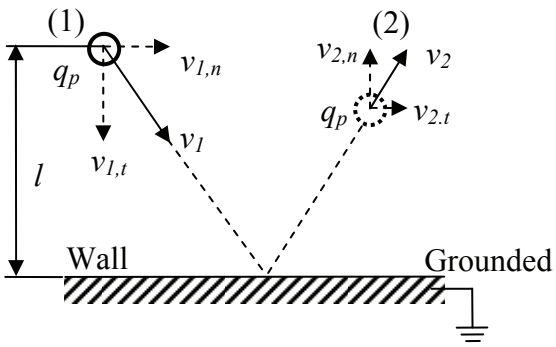

Figure 4.1: Schematic illustration of the particle wall collision

where $E_{kin,1}$ and $E_{kin,2}$ are the kinetic energies of the particle before and after the collision, $W_{vdW,1}$ and $W_{vdW,2}$ are the work done by the "attraction" (adhesion) due to the van der Waals forces before and after the collision, $E_{el,1}$ and $E_{el,2}$ are the electrostatic potential energies (work done by Coulombs force (mirror force) in moving a charged particle in an electrostatic potential) of the particle before and after the collision due to the particle charge, and E_{deform} is the energy loss of the particle due to the wall collision. It can be seen from Equation (4.28) that only a part of the kinetic energy, $E_{kin,1}$, before the collision and the work done by the attractive van der Waals forces, $W_{vdW,1}$, and the electrostatic potential energy, $E_{el,1}$, of the charged particle is transformed into elastic energy. A part of that energy is lost, E_{deform}, in overcoming the van der Waals adhesion forces and the attractive electrostatic force (mirror force). Rearranging Equation (4.28) gives

$$\begin{aligned} E_{kin,1} - E_{deform} &= W_{vdW,2} - W_{vdW,1} + E_{el,2} - E_{el,1} - E_{kin,2} \\ &\Updownarrow \\ E_{kin,1} - E_{deform} &= \Delta W_{vdW} + \Delta E_{el} - E_{kin,2} \end{aligned} \tag{4.29}$$

When adhesion of the particle occurs, $E_{kin,2} = 0$ and Equation (4.29) can be written as

$$\frac{E_{kin,1} - E_{deform}}{E_{kin,1}} E_{kin,1} = \Delta W_{vdW} + E_{el,2} - E_{el,1} \tag{4.30}$$

Introducing a coefficient of restitution, k, as follows

$$k^2 = \frac{E_{kin,1} - E_{deform}}{E_{kin,1}}; \qquad 0 \le k \le 1 \tag{4.31}$$

and substituting the coefficient of restitution, k, given in Equation (4.31) into Equation (4.30) gives a criterion for the maximum kinetic energy a particle can carry depending on the elasticity of the collision in order to adhere to the surface.

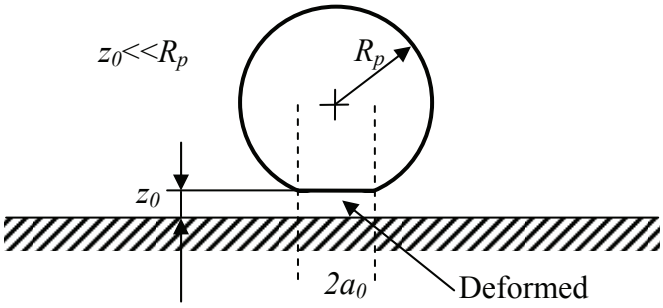

Figure 4.2: Schematic illustration of a deformed particle adhered to the wall.

$$k^2 E_{kin,1} \leq \Delta W_{vdW} + E_{el,2} - E_{el,1} \tag{4.32}$$

At the contact area the interaction forces increase the contact area until the attractive forces and the forces resisting further deformation at the interface (contact area) are in equilibrium [Krupp (1967)]. If it is assumed that the deformation of the particle at the contact point between the particle and the wall is very small compared with the particle radius, i.e. z_0<<R_p, then the attraction work done by the van der Walls forces from an initial position (1) before the collision with the wall (initial distance, z_∞) that is large compared to the separation distance, z_0, can be given by Krupp (1967) as follows

$$\Delta W_{vdW} = \int_{z_0}^{z_\infty} P_{vdW}^{-} A_{deform} dz \approx \int_{z_0}^{\infty} P_{vdW}^{-} A_{deform} dz \tag{4.33}$$

where z_0 is the separation distance due to the asperities between the particle and the wall and a_0 is the radius of the deformed area of the particle at the contact point as illustrated in Figure 4.2. In Equation (4.33), since $z_\infty >> z_0$ it is assumed that $z_\infty \to \infty$. The van der Waals pressure, P_{vdW}^{-}, is given by the macroscopic theory of Lifshitz [Lifshitz (1956)] as

$$P_{vdW}^{-} = \frac{h\varpi}{8\pi^2 z^3} \tag{4.34}$$

where $\hbar\varpi$ is Lifshitz/van der Waals energy. If it is assumed that the deformation of the particle at the contact point with the wall is done only by the van der Waals adhesion forces then the deformed area, A_{deform}, can be stated as

$$A_{deform} = \pi a_0^2 = \frac{K_{vdW}^{\circ}}{H} \tag{4.35}$$

where a_0 is the radius of the deformed area, H is a measure of the strength of the wall material and $K°_{vdW}$ is the van der Waals adhesion force between a sphere and a plane, given by Krupp (1967) as follows

$$K^{\circ}_{vdW} = \frac{h\varpi}{8\pi^2 z_0^2} R_p \tag{4.36}$$

Substituting Equation (4.36), Equation (4.35), Equation (4.34) and Equation (4.33) into Equation (4.32) for the maximum kinetic energy for adhesion of the particle to the wall gives the following expression

$$\begin{gathered} k^2 E_{kin,1} \le \int_{z_0}^{z_\infty} \frac{h\varpi}{8\pi^2 z^3} \frac{h\varpi R_p}{8\pi^2 z_0^2 H} dz + E_{el,2} - E_{el,1} \\ \Updownarrow \\ E_{kin,1} \le \frac{\left(h\varpi\right)^2 R_p}{k^2 8^2 \pi^4 z_0^2 H} \int_{z_0}^{z_\infty} \frac{dz}{z^3} + \frac{E_{el,2} - E_{el,1}}{k^2} \end{gathered} \tag{4.37}$$

Carrying out the integration in Equation (4.37) gives

$$\begin{gathered} E_{kin,1} \le \frac{\left(h\bar{\omega}\right)^2 R_p}{k^2 8^2 \pi^4 z_0^2 H} \left[-\frac{1}{2z^2} \right]_{z_0}^{\infty} + \frac{\Delta E_{el}}{k^2} \\ \Updownarrow \\ E_{kin,1} \le \frac{\left(h\bar{\omega}\right)^2 R_p}{k^2 8^2 \pi^4 z_0^2 H} \left[\lim_{z\to\infty} \left(-\frac{1}{2z^2} \right) - \left(-\frac{1}{2z_0^2} \right) \right] + \frac{\Delta E_{el}}{k^2} \end{gathered} \tag{4.38}$$

Taking the limit for $z\to\infty$ (since $z_\infty >> z_0$ it is assumed that $z_\infty \to \infty$) in Equation (4.38) and reducing the expression as follows

$$\begin{gathered} E_{kin,1} \le \frac{\left(h\bar{\omega}\right)^2 R_p}{k^2 8^2 \pi^4 z_0^2 H} \left[0 + \frac{1}{2z_0^2} \right] + \frac{\Delta E_{el}}{k^2} \\ \Updownarrow \\ E_{kin,1} \le \frac{\left(h\bar{\omega}\right)^2 R_p}{2k^2 8^2 \pi^4 z_0^4 H} + \frac{\Delta E_{el}}{k^2} \end{gathered} \tag{4.39}$$

The electrostatic potential energy is the work done by Coulombs force in moving a charged particle in an electrostatic potential to a given position, e.g. from position (1) before the collision with the wall and down to the wall. The electric field strength, $\vec{E}$, in a system comes from all other point charges in the system

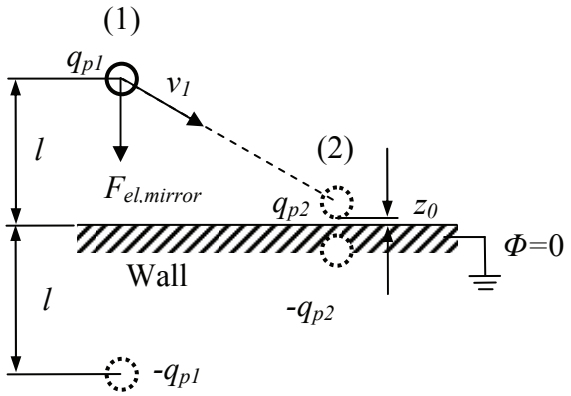

Figure 4.3: Schematic illustration of mirror force before and after the collision.

(e.g. the aerosol particle number concentration of charged particles in a pipe). The Coulomb force is stated as the force between two point charges, q and Q, at a distance, r, as [Griffiths (1999), p. 59]

$$\overrightarrow{F_q} = \frac{1}{4\pi\varepsilon_0}\frac{qQ}{r^2}\vec{n} \tag{4.40}$$

where $\vec{n}$ is a unit vector from q against Q and ε_0 is the permittivity of free space. For several point charges the Coulomb is given by the superposition principle [Griffiths (1999), p. 60] as follows

$$\overrightarrow{F_q} = \overrightarrow{F_{q_1}} + \overrightarrow{F_{q_2}} + \overrightarrow{F_{q_3}} + ... = \frac{1}{4\pi\varepsilon_0}\left(\frac{q_1 Q}{r_1^2}\overrightarrow{n_1} + \frac{q_2 Q}{r_2^2}\overrightarrow{n_2} + \frac{q_3 Q}{r_3^2}\overrightarrow{n_3} + ...\right) \tag{4.41}$$

The electric field strength, $\vec{E}$, is defined as the electric force, $\overrightarrow{F_q}$, per charge, Q, as follows [Griffiths (1999), p. 60]

$$\vec{E} = \frac{\overrightarrow{F_q}}{Q} = \frac{1}{4\pi\varepsilon_0}\frac{q}{r^2}\vec{n} \tag{4.42}$$

For several point charges the electric field strength, $\vec{E}$, is defined as [Griffiths (1999), p. 60]

$$\vec{E} = \frac{\overrightarrow{F_q}}{Q} = \frac{1}{4\pi\varepsilon_0}\sum_{i=1}^{n}\frac{q_i}{r^2}\vec{n}_i \tag{4.43}$$

The fundamental relationship between the electrostatic potential, Φ, and the irrotational electrostatic field, $\vec{E}$, can be stated as [Griffiths (1999), p. 78]

$$\vec{\nabla}\Phi = -\vec{E} \tag{4.44}$$

Only looking at a point charge and because the variation in the electrostatic potential, Φ, for a point charge is only in the radial direction (due to symmetry) it can be restated as follows

$$d\Phi = -\frac{1}{4\pi\varepsilon_0}\frac{q}{r^2}dr \tag{4.45}$$

The electrostatic potential, Φ, in an electrostatic field, $\vec{E}$, in the distance, r, from a point charge can now be determined as

$$\begin{gathered}\Phi = \int_0^{\phi} d\Phi = -\vec{E}\cdot d\vec{\breve{r}} = \int_{\infty}^{r} -\frac{1}{4\pi\varepsilon_0}\frac{q}{\breve{r}^2}d\breve{r} = \frac{1}{4\pi\varepsilon_0}\left[\frac{q}{\breve{r}}\right]_{\infty}^{r} \\ \Updownarrow \\ \Phi = \frac{1}{4\pi\varepsilon_0}\left[\frac{q}{r} - \lim_{r\to\infty}\left(\frac{q}{r}\right)\right] = \frac{1}{4\pi\varepsilon_0}\left[\frac{q}{r} - 0\right] \\ \Updownarrow \\ \Phi = \frac{1}{4\pi\varepsilon_0}\frac{q}{r}\end{gathered} \tag{4.46}$$

where $\breve{r}$ is an integration dummy. The electrostatic potential, Φ, infinitely away from the point charge q (r=∞) has been defined to zero, Φ=0. For a point charge, neglecting space charging, the electrostatic potential, Φ, due to the mirror force at the distance, r, from a grounded wall with zero potential (as shown in Figure 4.3) corresponds to the electrostatic potential, Φ, at the distance, 2r, from a point charge

$$\Phi = \frac{1}{4\pi\varepsilon_0}\frac{q}{2r} = \frac{1}{8\pi\varepsilon_0}\frac{q}{r} \tag{4.47}$$

The electrostatic potential energy, $E_{el,1}$, due to the mirror force, before the collision, can now be stated as the work done by Coulombs force (the mirror force) in moving a charged particle in an electrostatic potential infinitely far away from the point charge (where the potential is zero, which corresponds to the wall) to the given position (1) before the collision

$$E_{el,1} = -\int_{\infty}^{l}\vec{F}_{el,1}\cdot d\vec{r} = -\int_{\infty}^{l} q_1\vec{E}\cdot d\vec{r} = q_1\int_{\infty}^{l} d\Phi \tag{4.48}$$

Carrying out the integration in Equation (4.48) gives

$$E_{el,1} = q_1\left[\Phi\right]_{\infty}^{l} = \frac{q_1^2}{8\pi\varepsilon_0}\left[\frac{1}{l} - \lim_{r\to\infty}\left(-\frac{1}{r}\right)\right] = \frac{q_1^2}{8\pi\varepsilon_0}\left[\frac{1}{l} - 0\right] = \frac{q_1^2}{8\pi\varepsilon_0 l} \tag{4.49}$$

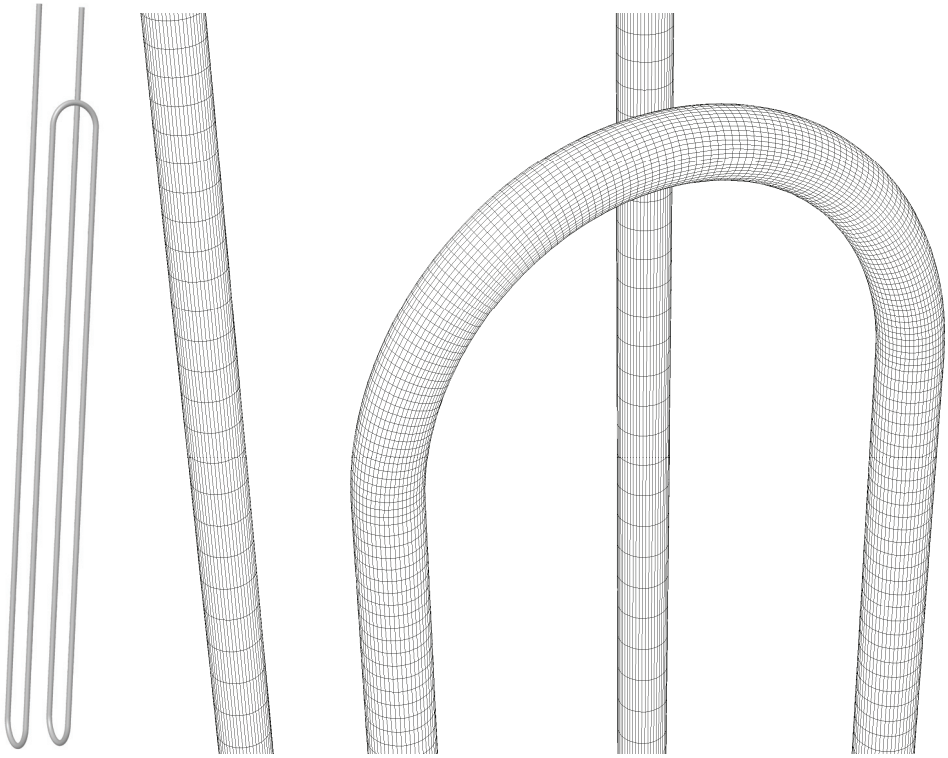

Figure 4.4: Numerical model of the three-meter long pipe bent in section of 75 cm. Pipe diameter 6 mm. The grid consists of 855540 hexahedral cells.

The electrostatic potential energy, $E_{el,2}$, after the collision can be determined in the same way as follows

$$\begin{aligned} E_{el,2} &= -\int_{\infty}^{z_0+R_p} \vec{F}_{el,2} \cdot d\vec{r} = -\int_{\infty}^{z_0+R_p} q_2 \vec{E} \cdot d\vec{r} = q_2 \int_{\infty}^{z_0+R_p} d\Phi \\ &\Updownarrow \\ E_{el,2} &= q_2 \left[\Phi\right]_{\infty}^{z_0+R_p} = \frac{q_2^2}{8\pi\varepsilon_0}\left[\frac{1}{z_0+R_p} - \lim_{r\to\infty}\left(-\frac{1}{r}\right)\right] \\ &\Updownarrow \\ E_{el,2} &= \frac{q_2^2}{8\pi\varepsilon_0}\left[\frac{1}{z_0+R_p} - 0\right] = \frac{q_2^2}{8\pi\varepsilon_0\left(z_0+R_p\right)} \end{aligned} \tag{4.50}$$

The change in electrostatic potential energy, ΔE_{el}, from position (1) before the collision to position (2) after collision is now

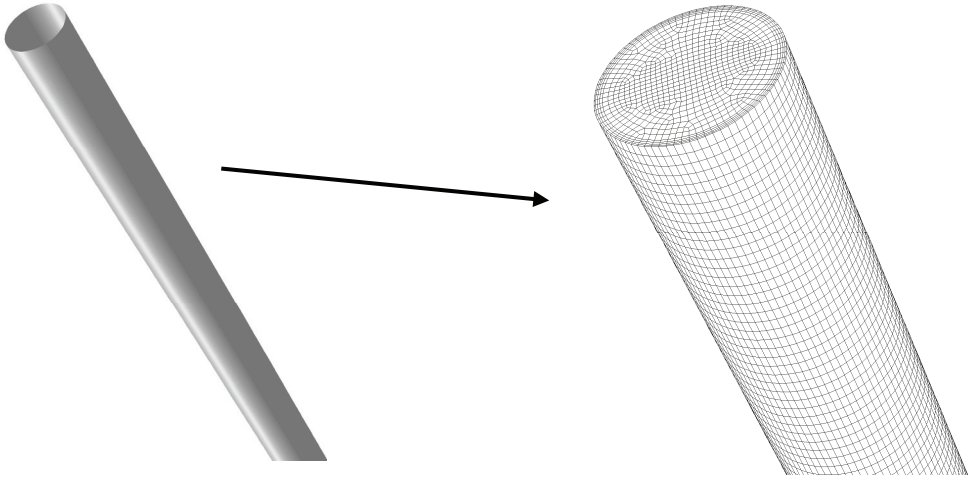

Figure 4.5: Numerical model of the one-meter long pipe. Pipe diameter 6 mm. The grid consists of 552900 hexahedral cells.

$$\Delta E_{el} = E_{el,2} - E_{el,1} = \frac{q_2^2}{8\pi\varepsilon_0\left(z_0 + R_p\right)} - \frac{q_1^2}{8\pi\varepsilon_0 l}$$
$$\Updownarrow \tag{4.51}$$
$$\Delta E_{el} = \frac{1}{8\pi\varepsilon_0}\left(\frac{q_2^2}{\left(z_0 + R_p\right)} - \frac{q_1^2}{l}\right)$$

The critical energy, $E_{kin,crit}$, for the particle exactly not to bounce can now be defined based on Equation (4.39) as

$$E_{kin,1} \le \frac{\left(h\overline{\omega}\right)^2 R_p}{2k^2 8^2 \pi^4 z_0^4 H} + \frac{\Delta E_{el}}{k^2}$$
$$\Downarrow \tag{4.52}$$
$$E_{kin,1} \le E_{kin,crit} = \frac{\left(h\overline{\omega}\right)^2 R_p}{2k^2 8^2 \pi^4 z_0^4 H} + \frac{\Delta E_{el}}{k^2}$$

The critical velocity for the particle, $w_{\mathrm{p,crit}}$, can therefore be determined by substituting the change in electrostatic potential energy, ΔE_{el}, given in Equation (4.51) in to Equation (4.52) as follows

$$\frac{1}{2} m_p w_{p,crit}^2 = \frac{\left(h\overline{\omega}\right)^2 R_p}{2k^2 8^2 \pi^4 z_0^4 H} + \frac{\frac{1}{8\pi\varepsilon_0}\left(\frac{q_2^2}{\left(z_0 + R_p\right)} - \frac{q_1^2}{l}\right)}{k^2} \tag{4.53}$$

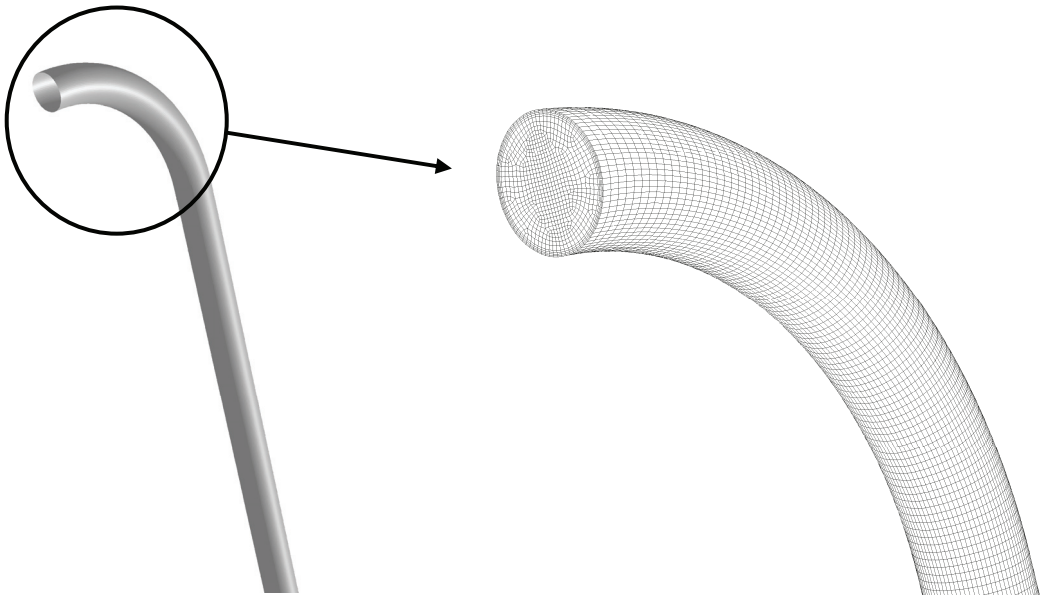

Figure 4.6: Numerical model of the one-meter long pipe including bend in the inlet. Pipe diameter 6 mm. The grid consists of 806760 hexahedral cells.

Reducing Equation (4.53) gives

$$w_{p,crit}^2 = \frac{3\left(h\overline{\omega}\right)^2 R_p}{4\pi R_p^3 \rho_p k^2 8^2 \pi^4 z_0^4 H} + \frac{2}{8\pi\varepsilon_0 k^2 \frac{4}{3}\pi R_p^3 \rho_p}\left(\frac{q_2^2}{\left(z_0 + R_p\right)} - \frac{q_1^2}{l}\right)$$

$$\Updownarrow \tag{4.54}$$

$$w_{p,crit} = \sqrt{\left(\frac{h\overline{\omega}}{kR_p 8\pi^2 z_0^2}\right)^2 \frac{3}{4H\rho_p} + \frac{3}{16\pi R_p^3 k^2}\frac{1}{\varepsilon_0 \rho_p}\left(\frac{q_2^2}{\left(z_0 + R_p\right)} - \frac{q_1^2}{l}\right)}$$

The critical velocity, $w_{p,crit}$, can also be written as a function of the particle diameter, D_p, as

$$w_{p,crit} = \sqrt{\left(\frac{h\overline{\omega}}{kD_p 4\pi^2 z_0^2}\right)^2 \frac{3}{4H\rho_p} + \frac{3}{2\pi^2 D_p^3 k^2}\frac{1}{\varepsilon_0 \rho_p}\left(\frac{2q_2^2}{2z_0 + D_p} - \frac{q_1^2}{l}\right)} \tag{4.55}$$

Equation (4.55) differs at the right hand side from Equation 17 in the paper from Heinl and Bohnet (2005) by a factor of two in the denominator in the second term under the square root. The reason for this is due to the fact that Heinl and Bohnet (2005) calculate the potential energy of the particle before and after the collision with the wall by assuming a point charge at the wall and then calculating the work

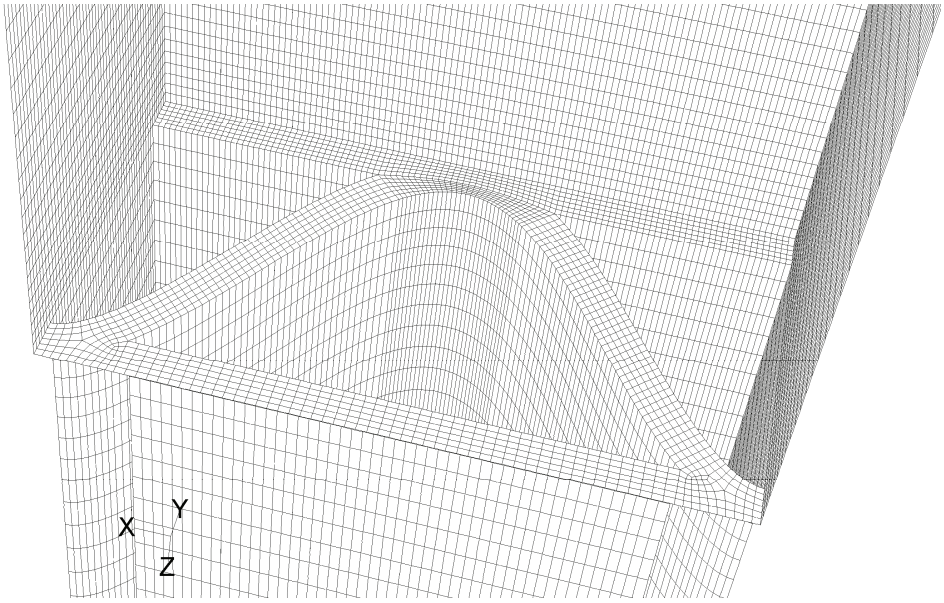

Figure 4.7: Numerical model of the Topsøe DNX x30 monolithic catalyst. The grid consists of 517400 hexahedral cells. Hydraulic diameter 3.4 mm. Dimensions: x-length = 8.2 mm, y-length=4.6 mm. Length of monolithic catalyst 50 cm.

due to Coulombs force between these to charges. This is only valid if the wall is not grounded. In Equation (4.55) the work is due to the mirror force and that corresponds to twice the distance to the wall, under the assumption that the wall has been grounded. Equation (4.55) can now give the condition for adhesion of the particle if the particle velocity is smaller than the critical particle velocity as follows

$$\left|\vec{w}_{p,1}\right| \leq w_{p,crit} \tag{4.56}$$

As it can be seen from Equation (4.56) adhesion is only dependent on the particle velocity not the particle concentration. Particles that reflect a wall as illustrated schematically in Figure 4.1 are given a new normal and tangential velocity based on a perfect reflection from the wall.

4.6 Numerical Models

The geometry, physical data and boundary conditions of the numerical models of the three-meter aerosol deposition pipe for submicrometer aerosol deposition, the 1 meter deposition pipe for micrometer particle deposition and the monolithic catalyst (Topsøe “sinus” geometry), respectively are described in the following.

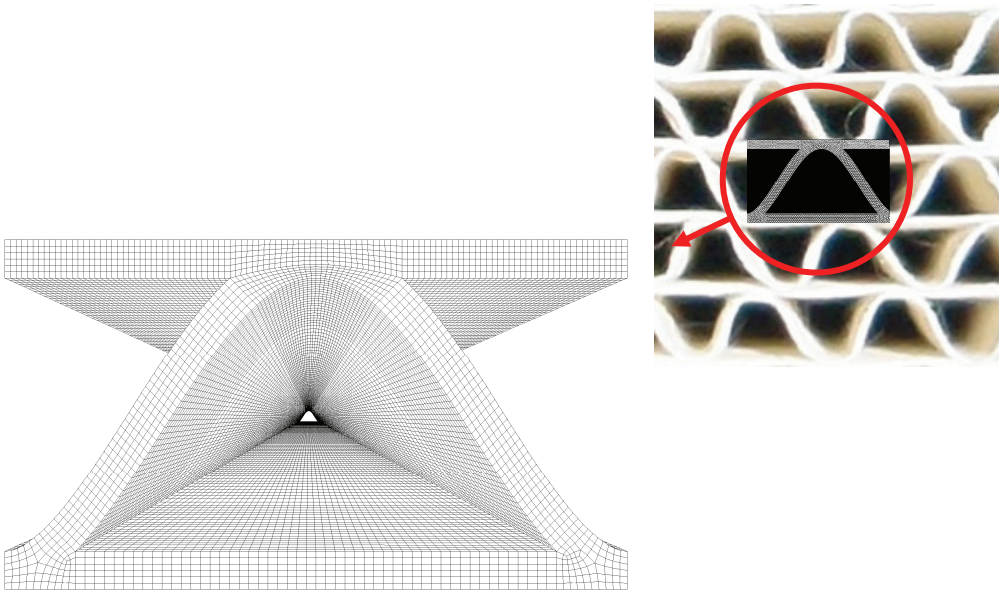

Figure 4.8: Illustration of the shape and grid of the Topsøe DNX x30 monolithic catalyst compared with a physical Topsøe DNX x30 monolithic catalyst geometry. The grid consists of 517400 hexahedral cells.

All simulations have been carried out using second order upwind discretization schemes. For the transient simulations first-order implicit time steps have been used. Grid independence investigations of the flow simulations have not been carried out, but the grid sizes have been selected in order to choose the best compromise between number of grid cells, computational time and numerical error.

4.6.1 Geometry

4.6.1.1 Submicron Aerosol Deposition Pipe

The physical geometry of the three-meter long aerosol deposition pipe can be seen in Figure 3.2 and the CFD model of the aerosol deposition pipe can be seen in Figure 4.4. The grid of the three-meter straight pipe has not been shown. The grid for the three-meter bend pipe consists of 855540 hexahedral cells. The grid for the three-meter straight pipe consists of 970000 hexahedral cells.

4.6.1.2 Micrometer Aerosol Deposition Pipe

The physical geometry of the one-meter aerosol deposition pipe can be seen in Figure 3.6 and the CFD model of the deposition pipe can be seen in Figure 4.5. The grid for the one-meter long pipe consists of 552900 hexahedral cells. The CFD model of the one-meter aerosol deposition pipe including the bend at the inlet can be seen in Figure 4.6. The grid consists of 806760 hexahedral cells.

4.6.1.3 Monolithic Catalysts

The CFD model of the Topsøe DNX x30 "sinus" monolithic catalyst can be seen in Figure 4.7 and in Figure 4.8. The grid consists of 517400 hexahedral cells. Only two channels of the monolithic catalyst have been modelled and symmetry has been assumed for the four sides of the inlet section. The dimension of the model is 8.2×4.6×600 mm.

4.6.2 Physical Data

4.6.2.1 Submicrometer Aerosol Deposition Pipe

Table 3 gives data used for the CFD simulations of the two different three-meter long aerosol deposition pipes.

Table 3: Data used for the CFD simulations of the two different three-meter long submicrometer aerosol deposition pipes.

Pipe length	3	[m]
Pipe diameter	$6 \cdot 10^{-3}$	[m]
Bend radius	$25 \cdot 10^{-3}$	[m]
Dynamic viscosity of air, μ	$1.85 \cdot 10^{-5}$	[kg/(m-s)]
Kinematic viscosity of air, v	$1.58 \cdot 10^{-5}$	[m^2/s]
Density of gas, ρ_f	1.17	[kg/m^3]
Pressure, p	101325	[Pa]
Temperature, T	300	[K]
Density of KCl particles, ρ_p	1950	[kg/m^3]
Average velocity in pipe	0.1651	[m/s]
Reynolds number in pipe	63	[-]
Dean number	22	[-]

Table 4: Data used for the CFD simulations of the two different one-meter micrometer deposition pipes.

Pipe length	1	[m]
Pipe diameter	$6 \cdot 10^{-3}$	[m]
Length of bend	0.11	[m]
Dynamic viscosity of air, μ	$1.85 \cdot 10^{-5}$	[kg/(m-s)]
Kinematic viscosity of air, v	$1.58 \cdot 10^{-5}$	[m^2/s]
Density of gas, ρ_f	1.17	[kg/m^3]
Pressure, p	101325	[Pa]
Temperature, T	300	[K]
Density of PMMA particles, ρ_p	1200	[kg/m^3]
Average velocity in pipe	2	[m/s]
Reynolds number in pipe	760	[-]

Table 5: Data used for the CFD simulations of the Topsøe "sinus" DNX x30 monolithic catalyst.

Catalyst length	0.5	[m]
Portion of the catalyst width, l_x	$8.2 \cdot 10^{-3}$	[m]
Portion of the catalyst height, l_y	$4.6 \cdot 10^{-3}$	[m]
Hydraulic diameter DNX x30	$3.4 \cdot 10^{-3}$	[m]
Dynamic viscosity of air, μ	$3.11 \cdot 10^{-5}$	[kg/(m-s)]
Kinematic viscosity of air, v	$5.51 \cdot 10^{-5}$	[m^2/s]
Density of gas, ρ_f	0.56	[kg/m^3]
Pressure, p	101325	[Pa]
Temperature, T	623.15	[K]
Density of KCl particles, ρ_p	1950	[kg/m^3]
Average velocity above channel	4.56	[m/s]
Average velocity in channel	6.5	[m/s]
Reynolds number of channel	400	[-]

4.6.2.2 Micrometer Deposition Pipe

Table 4 gives data used for the CFD simulations of the two different one-meter long deposition pipes.

Table 6: Boundary conditions used for the CFD simulations of the two different three-meter long aerosol deposition pipes

Inlet velocity	0.1651	[m/s]
Inlet flux of electrostatic potential	0	[V/m^2-s]
Inlet particle number concentration, n_0	$1.7 \cdot 10^{12}$	[#/m^3]
Gauge pressure outlet	0	[Pa]
Electrostatic potential at walls	0	[V]
Particle number concentration at walls	0	[#/m^3]

Table 7: Boundary conditions used for the CFD simulations of the two different one-meter long micrometer deposition pipes.

Inlet velocity	2	[m/s]
Gauge pressure outlet	0	[Pa]
Perfect adhering / reflecting walls (Eq. (4.55))	0	[-]

4.6.2.3 Monolithic Catalysts

Table 5 gives data used for the CFD simulations of the Topsøe "sinus" monolithic catalyst.

4.6.3 Boundary Conditions

4.6.3.1 Submicrometer Aerosol Deposition Pipe

The boundary conditions of the three-meter long bend and straight aerosol deposition pipes were given as uniform inlet velocity profile, uniform aerosol particle number concentration for the UDS transport equation transporting the particle number concentration and zero flux for the UDS transporting the electrostatic potential. Gauge pressure was set to zero at the outlet and the walls were given zero electrostatic potential to model a grounded wall and zero concentration in order to model perfect adhering walls. The boundary conditions can be seen in Table 6. In case of pure Brownian diffusion, the electrostatic potential was not simulated, and in the case of combined Brownian and electrostatic dispersion, the average charge on the particles was specified. In the polydisperse aerosol case, the particles were given a bipolar charge distribution

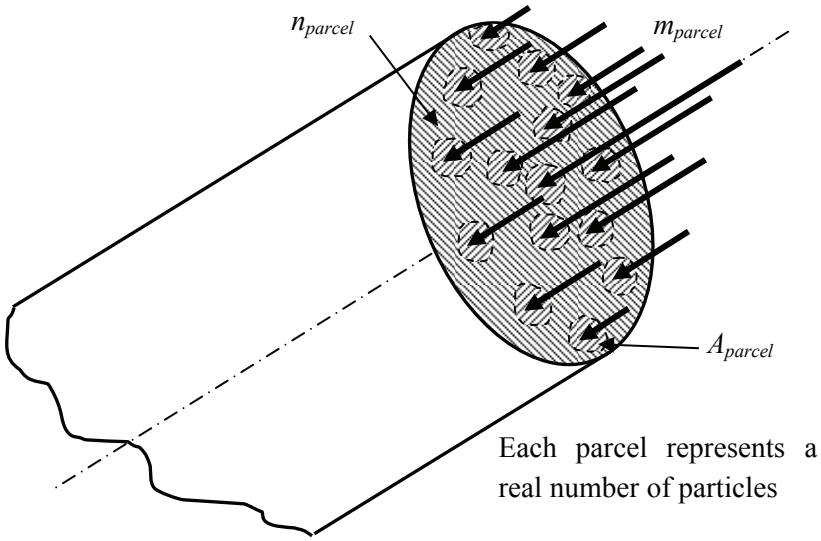

Figure 4.9: Schematic illustration of inlet conditions for particle mass flow in CFD using the Discrete Particle Model.

based on Equation (2.22). Particle diameters between 1 and 1000 nanometers were simulated.

4.6.3.2 Micrometer Aerosol Deposition Pipe

The boundary conditions of the two different one-meter deposition pipes were given as uniform inlet velocity profile and zero gauge pressure at the outlet. The boundary conditions can be seen in Table 7. For simulating the dispersed phase, using the Discrete Particle Model (DPM), the mass flow of the individual parcels, where each parcel represents a real number of particles, was given at the inlet as follows

$$\dot{m}_{parcel} = u_z A_{parcel} n \rho_p \frac{\pi}{6} D_p^3 \tag{4.57}$$

where u_z is the axial velocity of the fluid in the given position where the parcels of particles are released, n is the particle number concentration, ρ_p is the density of the particles and D_p is the particle diameter. The area surrounding the point at the inlet where the parcels of particles were released, is calculated as follows

Table 8: Boundary conditions for the injected particles used for the Discrete Particle Model in the CFD simulations of the two different one-meter long micrometer deposition pipes. Crossed-linked PMMA spherical particles were used.

Particle diameter [μm]	Fluid volume flow [m^3/s]	Particle number concentration [$\#/m^3$]	Particle mass concentration [kg/m^3]	Particle volume flow [m^3/s]	Particle mass flow [kg/s]
10	$5.65 \cdot 10^{-5}$	$9.22 \cdot 10^{10}$	0.06	$2.73 \cdot 10^{-9}$	$3.28 \cdot 10^{-6}$
20	$5.65 \cdot 10^{-5}$	$5.61 \cdot 10^{9}$	0.03	$1.33 \cdot 10^{-9}$	$1.59 \cdot 10^{-6}$
30	$5.65 \cdot 10^{-5}$	$6.43 \cdot 10^{9}$	0.11	$5.14 \cdot 10^{-9}$	$6.17 \cdot 10^{-6}$
40	$5.65 \cdot 10^{-5}$	$6.80 \cdot 10^{9}$	0.27	$1.29 \cdot 10^{-8}$	$1.55 \cdot 10^{-5}$

$$A_{parcel} = \frac{A_{inlet}}{n_{parcel}} \tag{4.58}$$

where A_{inlet} is the inlet area of the pipe and n_{parcel} is the number of parcels injected. The injected parcels of particles were stochastically distributed over the inlet surface using a random function as follows

$$\begin{aligned} x &= \sqrt{\psi} R_{pipe} \cos(\theta) \\ y &= \sqrt{\psi} R_{pipe} \sin(\theta) \end{aligned} \tag{4.59}$$

where ψ is a random number between 0 and 1, R_{pipe} is the radius of the pipe and x- and y-coordinates are located on the inlet surface. θ is the angle between the radius vector, $r(x,y)$ and the x-axis. Figure 4.9 shows a schematic illustration of the inlet conditions for the particle mass flow and Figure 4.10 shows the stochastic distribution of the parcels of particles at the inlet. Walls were treated either as perfect adhering walls or as reflecting walls based on the critical velocity given in Equation (4.55).

Table 8 gives the data used for the particulate phase in the Discrete Particle Model (DPM) in the CFD simulations of the two different one-meter long micrometer deposition pipes. 100000 parcels of particles were injected for each particle diameter. Particles diameters for 10, 20, 30 and 40 micrometer were simulated.

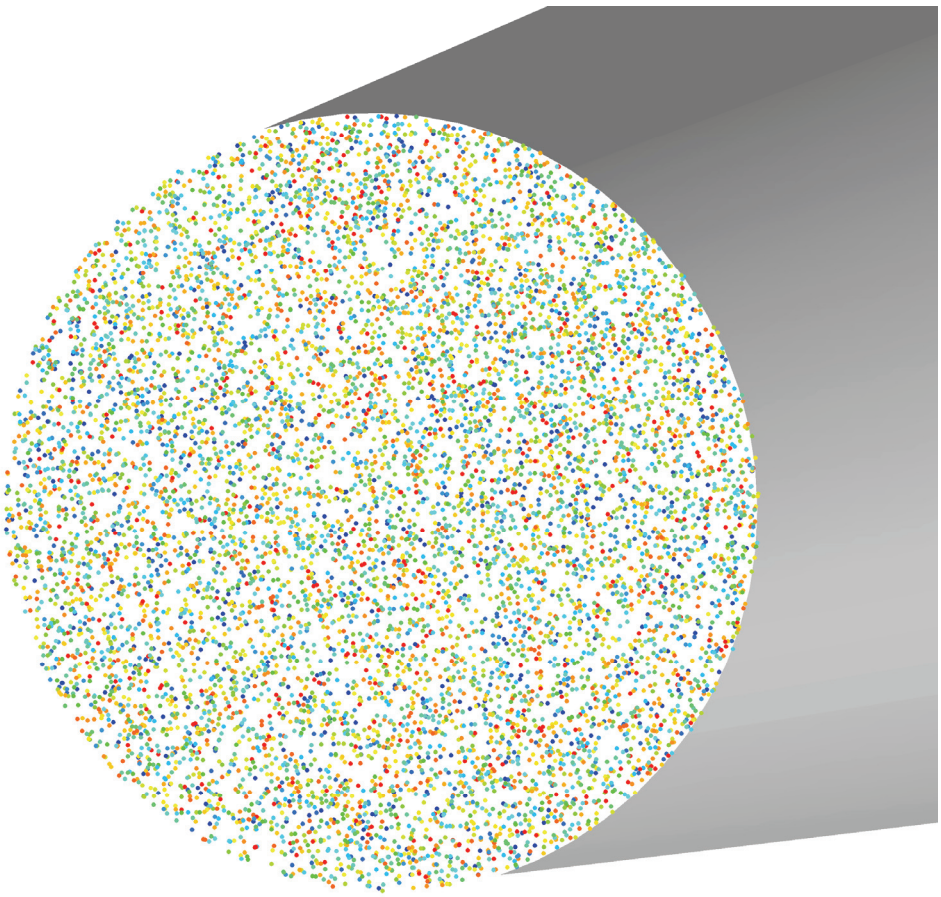

Figure 4.10: Stochastic distribution of particles (parcels) at the inlet of a pipe. 10000 parcels of particles are shown here.

4.6.3.3 Monolithic Catalysts

The boundary conditions of the monolithic catalyst (the Topsøe "sinus" geometry) were given as uniform inlet velocity profile and zero gage pressure at the outlet. The UDS transporting the electrostatic potential was given zero flux at the inlet and the walls were given zero electrostatic potential to model a grounded wall. The boundary conditions can be seen in Table 9.

The dispersed phase simulated using the Discrete Particle Model (DPM), were given the mass flow of the individual particle diameters which were measured in the pilot plant. The mass flow of the individual parcels of particles was given at the injection surface using Equation (4.57) and Equation (4.58).

Table 9: Boundary conditions used for the CFD simulations of the monolithic catalyst (the Topsøe "sinus" geometry).

Inlet velocity	4.56	[m/s]
Inlet temperature	623	[K]
Inlet flux of electrostatic potential	0	[V/m^2-s]
Inlet hydraulic diameter (only turbulent)	$5.89 \cdot 10^{-3}$	[m]
Inlet turbulence intensity (only turbulent)	10	[%]
Gage pressure outlet	0	[Pa]
Electrostatic potential at walls	0	[V]
Reflecting walls (Eq. (4.55))	-	[-]

The injected parcels of particles were stochastically distributed over the injection surface using a random function as follows

$$x = \sqrt{\psi} l_x$$
$$y = \sqrt{\psi} l_y \tag{4.60}$$

where ψ is a random number between 0 and 1 and l_x and l_y are the width and height of the injection surface. Walls were treated as perfect reflecting walls (which of course are a rough assumption) based on the critical velocity given in Equation (4.55). The separation distance due to the asperities between the particle and the wall, z_0, was set to a very low value of $4 \cdot 10^{-15}$ in order to suppress bouncing at the top of the catalyst. Bouncing was assumed negligible due to the relatively small particles present in the gas flow.

Enhanced wall treatment is used for near-wall modelling that combines a two-layer model with enhanced wall functions, where the two-layer model is used if the mesh is fine enough to resolve the laminar sublayer (typical $y^+ \approx 1$), otherwise standard wall functions are used [Fluent (2006), p. 12-68]. The particle size distribution was based on a linear scaling of the size distribution measured by Zheng et al. (2008) for a 0.5 M KCl solution in order to obtain the size distribution of the 0.1 M KCl solution used in the present work. The scaled size distribution for the 0.1 M KCl solution can be seen in Table 10.

Table 10: Boundary conditions for the injected particles used for the Discrete Particle Model in the CFD simulations of the pilot scale experiment. KCl particle concentration and mass flow based on a linear scaling of the size distribution measured by impactor measurements [Zheng et al. (2008)] from 0.5 M to 0.1 M KCl concentration.

Particle diameter [μm]	Fluid volume flow [m^3/s]	Particle number concentration [$\#/m^3$]	Particle mass concentration [kg/m^3]	Particle volume flow [m^3/s]	Particle mass flow [kg/s]
0.039	$1.72 \cdot 10^{-4}$	$2.09 \cdot 10^{12}$	$1.27 \cdot 10^{-7}$	$1.12 \cdot 10^{-14}$	$2.18 \cdot 10^{-11}$
0.070	$1.72 \cdot 10^{-4}$	$9.15 \cdot 10^{11}$	$3.14 \cdot 10^{-7}$	$2.77 \cdot 10^{-14}$	$5.40 \cdot 10^{-11}$
0.115	$1.72 \cdot 10^{-4}$	$9.72 \cdot 10^{11}$	$1.49 \cdot 10^{-6}$	$1.31 \cdot 10^{-13}$	$2.56 \cdot 10^{-10}$
0.195	$1.72 \cdot 10^{-4}$	$3.66 \cdot 10^{11}$	$2.77 \cdot 10^{-6}$	$2.45 \cdot 10^{-13}$	$4.77 \cdot 10^{-10}$
0.356	$1.72 \cdot 10^{-4}$	$3.94 \cdot 10^{10}$	$1.81 \cdot 10^{-6}$	$1.59 \cdot 10^{-13}$	$3.11 \cdot 10^{-10}$
0.697	$1.72 \cdot 10^{-4}$	$2.96 \cdot 10^{9}$	$1.02 \cdot 10^{-6}$	$9.02 \cdot 10^{-14}$	$1.76 \cdot 10^{-10}$
1.397	$1.72 \cdot 10^{-4}$	$7.91 \cdot 10^{7}$	$2.20 \cdot 10^{-7}$	$1.94 \cdot 10^{-14}$	$3.79 \cdot 10^{-11}$
2.775	$1.72 \cdot 10^{-4}$	$5.57 \cdot 10^{6}$	$1.21 \cdot 10^{-7}$	$1.07 \cdot 10^{-14}$	$2.09 \cdot 10^{-10}$
5.454	$1.72 \cdot 10^{-4}$	$5.81 \cdot 10^{5}$	$9.62 \cdot 10^{-8}$	$8.48 \cdot 10^{-15}$	$1.65 \cdot 10^{-11}$
10	$1.72 \cdot 10^{-4}$	$2.01 \cdot 10^{5}$	$2.05 \cdot 10^{-7}$	$1.81 \cdot 10^{-14}$	$3.53 \cdot 10^{-11}$

4.6.4 Numerical Simulations

4.6.4.1 Submicrometer Aerosol Deposition Pipe

The CFD simulations of the bend and the straight pipe were carried out as steady-state incompressible laminar flow. In the cases with only monodisperse Brownian diffusion the transport equation (UDS) for the particle number concentration was solved simultaneously with the Navier-Stokes equation for particle diameters between 1-1000 nm. In the cases with simultaneous monodisperse Brownian diffusion and electrostatic dispersion, the transport equation (UDS) for the particle number concentration and transport equation (UDS) for the electrostatic potential were solved simultaneously with the Navier-Stokes equation for particle diameters between 1-1000 nm. From the solution of the electrostatic potential, the electric field strength was obtained, based on the electrical migration velocity being calculated and added to the flux term of the convective velocity in the transport equation (UDS) for the particle number concentration. The space charge was given from the particle charge and particle concentration as a source term to the transport equation (UDS) for the electrostatic potential. In the polydisperse aerosol cases, the solution principle was the same but the number of transport

equation (UDS) for the particle number concentration corresponded to the number of particle diameters simulated for the polydisperse aerosol. Based on the concentration in and out of the pipe the deposition efficiency was calculated.

4.6.4.2 Micrometer Aerosol Deposition Pipe

Table 11: Model parameters for particle-wall interaction model.

Strenght of the wall material, H	$250 \cdot 10^{6}$	[MPa]
Liffschitz-van der Walls constant, $h\varpi$	$4 \cdot 10^{-19}$	[Nm]
Coefficient of restitution, k	1	[-]

The simulations of the bend and the straight pipe were carried out as steady-state incompressible laminar flow for four different particle diameters (10, 20, 30 and 40 micrometer). Navier-Stokes equations were simulated for the continuous phase and the DPM model was used for the dispersed phase. A one-way coupling was used and particles were tracked through the converged solution for the gas flow in order to obtain the mass flow of the particles penetrating the pipe and calculation of the deposition efficiency.

Table 12: The asperities, z_0, used in the particle-wall interaction model in order to obtain the deposition efficiency curves shown in Figure 5.21.

Particle diameter [μm]	Asperities, z_0 [m]
10	$2.300 \cdot 10^{-10}$
20	$2.620 \cdot 10^{-10}$
30	$1.276 \cdot 10^{-10}$
40	$8.165 \cdot 10^{-11}$

The parameter used in the particle-wall interaction model in Equation (4.55) is given in Table 11. The asperities used for the four different particle diameters are given in Table 12.

4.6.4.3 Monolithic Catalysts

The simulations of the monolithic catalysts were carried out both as transient incompressible laminar flow and transient incompressible turbulent flow. The Reynolds-averaged Navier-Stokes equations were solved simultaneously with the

transport equation (UDS) for the electrostatic potential for the continuous phases and the DPM model was used for the dispersed phase. In the turbulent flow cases the k-ε model was used to model the continuum phase turbulence, and the Random Walk Model was used to model the turbulent dispersion of the particles. The time steps were 3600 s (1 hour) in order to model the deposit build-up on the wall over time due to adhering particles. At the beginning of each time step, the grid and the solution were updated and 200 continuous phase iterations were carried out for each time step. After each 101 continuous phase iterations the particles were injected through the injection surface with the size distribution given from Table 10 and a stochastic distribution over the injection surface and tracked through the simulation domain. Based on the tracking of the particles through the domain the charge density was calculated, and the source term in the transport equation for the electrostatic potential was updated. Based on the interaction between the particles and walls, the grow-up velocity was calculated for a given porosity (in the present work a porosity of 0.4 was assumed) beside this the total accumulated mass and the deposition flux were also calculated. At the beginning of the next time step the solution was updated and the mesh movement was calculated due to the grow-up velocity. This is repeated for each time step until the convergence criteria for the solution has been obtained or the solution fails to continue because of negative volume due to errors in the grid update.

Table 13: Model parameters for particle-wall interaction model.

Separation distance, z_0	$4 \cdot 10^{-15}$	[m]
Strength of the wall material , H	$250 \cdot 10^{6}$	[MPa]
Liffschitz-van der Walls constant, $h\varpi$	$4 \cdot 10^{-19}$	[J]
Coefficient of restitution, k	1	[-]

The parameters used for the particle-wall interaction model in Equation (4.55) are given in Table 13.

4.7 Model Implementation in ANSYS-Fluent

The implementation through User Defined Functions (UDF) in the commercial Computational Fluid Dynamic (CFD) solver ANSYS-Fluent® version 6.23 and ANSYS-Fluent® version 12.0.1, respectively is described in the following paragraphs.

4.7.1 Euler-Euler Electrostatic Dispersion

The general equation for conservation of the particle number concentration, n, in the presence of electrostatic forces, given in Equation (4.27) in an Eulerian reference frame, can for incompressible steady-state flow be stated as follows using tensor notation

$$\frac{\partial}{\partial x_i}\left(\left(u_i n + ZnE_i\right) - D\frac{\partial n}{\partial x_i}\right) = 0 \tag{4.61}$$

The implementation in ANSYS-Fluent has been done through the User Defined Scalar (UDS) transport equation given in Equation (4.4) by setting the diffusion coefficient, $\Gamma_k = \rho D$ (the particle diffusion coefficient), the arbitrary scalar, ϕ, equal to the particle number concentration, n, the source term, $S_{\phi_k} = 0$ and adding the electrical migration velocity (electrical migration flux, ZnE_i) to the convective flux term as seen in Appendix J.1 and J.2 for respectively a monodisperse aerosol and a polydisperse aerosol.

The electrostatic potential due to space charge given in Equation (2.30) has been implemented through the User Defined Scalar (UDS) transport equation given in Equation (4.4) by setting the local acceleration term to zero, the convective term to zero ($u_i = 0$), the arbitrary scalar, ϕ, equal to the potential, Φ, the diffusion coefficient, $\Gamma_k = 1$ and the source term, $S_{\phi_k} = -ien/\varepsilon_0$ as follows

$$-\frac{\partial}{\partial x_i}\left(\frac{\partial \Phi}{\partial x_i}\right) = \frac{ie\,n}{\varepsilon_0} \tag{2.30}$$

In order to obtain the CFD solution of the electrostatic dispersion, Equation (4.61) and Equation (2.30) are solved simultaneously together with the Navier-Stokes equations for the fluid flow. The implementation using UDF is given in Appendix J.1 and J.2

4.7.2 Euler-Lagrange Electrostatic Dispersion

The electrostatic forces given in the Lagrangian reference frame in Equation (2.24) for the Coulomb force and the image force have been implemented directly into the DPM model in ANSYS-Fluent® version 6.23 and ANSYS-Fluent® version 12.0.1 using Equation (2.24) through the Used Defined Function (UDF) shown in Appendix J. The charge density in a computational cell is calculated based on the number of particles that are present simultaneously in the computational cell during the particle tracking (this is schematically illustrated in

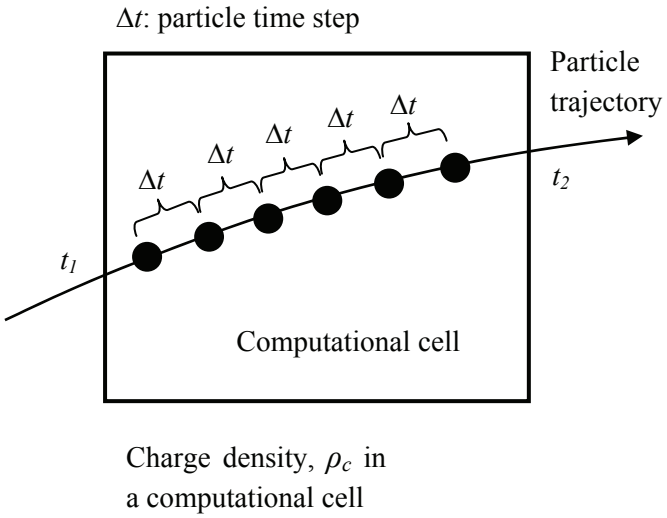

Figure 4.11: Schematic illustration of charge density in a computational cell. The integration time step, Δt, multiplied with the particle stream gives the number of particles in a computational cell in order to determine the charge density.

Figure 4.11). The calculation of the charge density is carried out by a summation of all charged particles in a computational cell as follows

$$\rho_c = \int_{t_1}^{t_2} \frac{q}{V_{cell}} \frac{\dot{m}_p}{m_p} dt = \int_{t_1}^{t_2} \frac{q}{V_{cell}} N dt \approx \sum_{\Delta t} \frac{ie}{V_{cell}} N \Delta t \left[\frac{C}{m^3} \right] \tag{4.62}$$

where q is the total charge on a particle, V_{cell} is the volume of a computational cell, $\dot{m}_p$ is the particle mass flow, m_p is the mass of a particle, i is the number of elementary charges on a particle, e is the elementary charge, N is the particle flow (number of particles per time) and dt is the particle time step during integration of the particle paths when tracking the particles through the computational domain.

4.7.3 Particle-Wall Interaction

A quasi-stationary collision model for particle-wall interaction has been implemented in ANSYS-Fluent® version 6.23 and ANSYS-Fluent® version 12.0.1 based on the critical velocity, $w_{p,crit}$, given in Equation (4.55) and the criteria for particle adhesion given in Equation (4.56). Particle reflection has been implemented based on a perfect reflection. In each particle tracking routine the absolute velocity for a particle hitting a boundary wall face is calculated and then checked with the criteria for the critical velocity for particle adhesion. If the

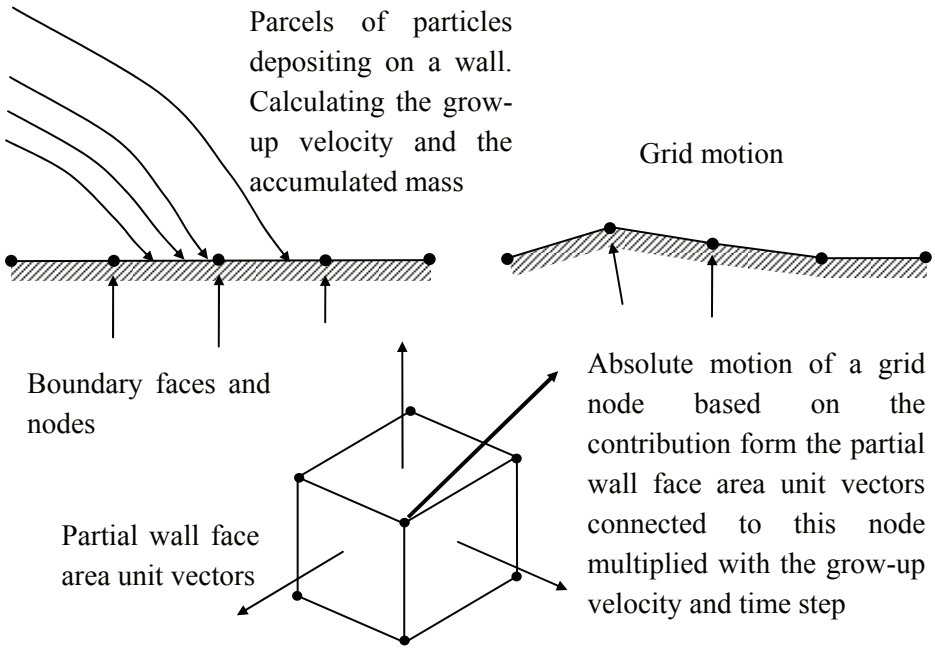

Figure 4.12: Schematic illustration of grid motion due to particle deposition.

absolute velocity of the particle is less than the critical velocity, the grow-up velocity for that boundary wall face will be calculated and a summation is carried out for all the particles hitting the wall face boundary in a given particle tracking The grow-up velocity is then calculated as

$$v_{grow-up} = \frac{\dot{m}_p}{\rho_p \left|\vec{A}_{wall}\right| \gamma} \tag{4.63}$$

where $\dot{m}_p$ is the particle mass flow, ρ_p is the particle density, $\left|\vec{A}_{wall}\right|$ is the magnitude of the face area vector and γ is the packing efficiency (one minus the porosity). The accumulated mass and the particle flux are also calculated. If the absolute velocity of the particle is larger than the critical velocity, the particle will bounce and the new normal and tangential velocity will be calculated. The implementation through the Used Defined Function (UDF) can be seen in Appendix K.

4.7.4 Particle Deposit Build-Up Model

A simplified model for the grow-up velocity and build-up of deposit has been implemented in ANSYS-Fluent® version 6.23 and ANSYS-Fluent® version 12.0.1

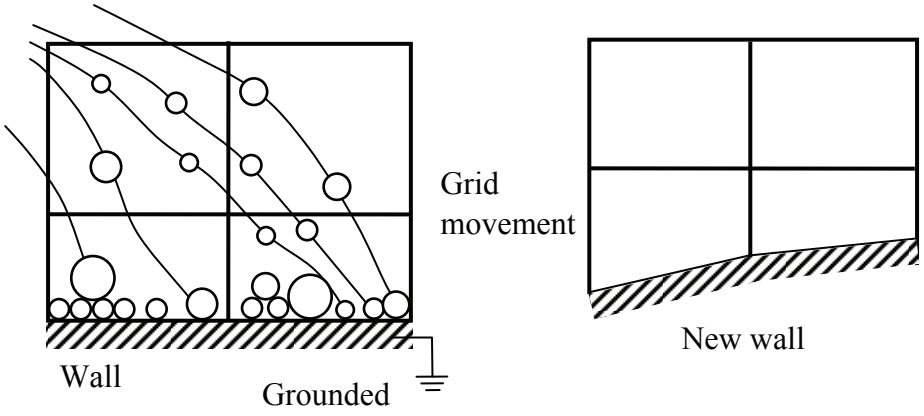

Figure 4.13: Schematic illustration of a growing layer of adhering particles and build-up of deposit.

based on the criteria for the critical particle velocity required just to adhere to the wall. The algorithm is as follows: For every mesh update there will be performed one loop over all wall faces. For every face of the wall the face area unit vector, divided by the number of nodes connected to that face, is computed. Then that vector is multiplied by the scalar product of grow-up velocity for that wall cell face and the current time step in order to get a partial node displacement (displacement due to grow-up on that particular wall cell face). For every wall cell face a loop over all connected nodes is performed, and every node will be displaced incrementally with the partial node displacement vector for that cell face. After the wall face loop is accomplished, the total node displacement vector for every node will be the sum over all partial node displacement vectors from all node adjacent faces of the wall. For each mesh update at each time step there is a cell and surface smoothing and re-meshing function connected internally in ANSYS-Fluent®. The algorithm for the mesh update is schematically illustrated in Figure 4.12, and the deposit build-up is illustrated in Figure 4.13. The implementation through the Used Defined Function (UDF) is given in Appendix K.

4.7.5 Drag Force

The drag force given in the Lagrangian reference frame in Equation (4.13) using the expression for the drag coefficient, C_D, (Equation (2.35)) for a spherical particle given by the correlation of Haider and Levenspiel (1989) has been implemented directly into the DPM model in ANSYS-Fluent® version 6.23 and ANSYS-Fluent® version 12.0.1 using Equation (2.24) through the Used Defined Function (UDF) shown in Appendix K.

4.8 Simple Empirical Deposition Model

A simple empirical deposition model based on turbulent diffusion in a tube has been implemented. The model uses the empirical models for deposition velocities given in section 2.4.9. The model is based on plug flow (assuming fully developed turbulent flow) and a uniform distribution of particles, n_0, at the inlet of the tube. A balance on the particle number concentration, n, over the section Δz shown in Figure 4.14 gives

$$\begin{gathered} IN - OUT + \cancel{PROD} = ACC \\ \Downarrow \\ v_{z,avg} A\left(n\big|_z - n\big|_{z+dz}\right) = J_w n \Delta z \pi d \\ \Updownarrow \\ Q\left(n\big|_z - n\big|_{z+dz}\right) = J_w n \Delta z \pi d \end{gathered} \tag{4.64}$$

where $v_{z,avg}$ is the average velocity of the flow, A is the cross-section area of the tube, Q is the volume flow through the pipe and $\pi d\Delta z$ is the wall area of the pipe where the particles are captured. Equation (4.64) can be reduced to the following

$$\begin{gathered} Q\left(n\big|_z - n\big|_{z+dz}\right) = J_w n \Delta z \pi d \\ \Updownarrow \\ \frac{n\big|_{z+dz} - n\big|_z}{\Delta z} = \frac{-J_w n \pi d}{Q} \end{gathered} \tag{4.65}$$

Taking the limit as $\Delta z \to 0$ gives the following first-order differential equation

$$\frac{1}{n}\frac{dn}{dz} = \frac{-J_w \pi d}{Q} \tag{4.66}$$

Substituting the particle flux, J_w, given in Equation (2.1) and integrating over the length of the channel, L, from the initial concentration n_0 at the inlet to the concentration, n_{out}, at the outlet

$$\begin{gathered} \int_{n=n_0}^{n=n_{out}} \frac{dn}{n} = \int_{z=0}^{z=L} \frac{-V_{dep}^{+} u^{*} n \pi d}{Q} dz \\ \Downarrow \\ \ln\left(n_{out}\right) - \ln\left(n_0\right) = \frac{-V_{dep}^{+} u^{*} \pi d L}{Q} \end{gathered} \tag{4.67}$$

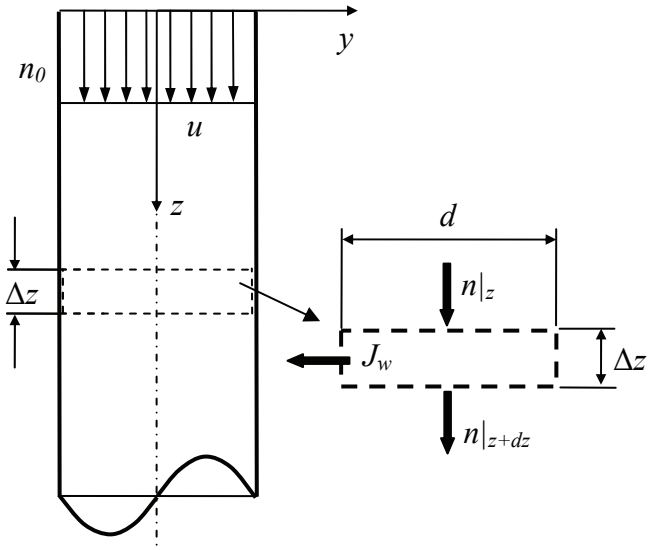

Figure 4.14: Schematic illustration of a fully developed turbulent flow (plug flow) in a pipe with uniform particle distribution at the inlet of the pipe.

Rearranging Equation (4.62) gives the following expression for the deposition

$$\frac{n_{out}}{n_0} = \exp\left(\frac{-V_{dep}^{+} u^{*} \pi dL}{Q}\right) \tag{4.68}$$

The deposition efficiency can be defined as follows

$$\eta = 1 - \frac{n_{out}}{n_0} \tag{4.69}$$

Substituting the expression for the deposition given in Equation (4.68) and the deposition velocity given in Equation (2.65) based on Wood (1981a) (valid for the turbulent eddy diffusion-impaction regime) for a straight tube into the expression for the deposition efficiency in Equation (4.69) gives

$$\eta = 1 - \frac{n_{out}}{n_0} = 1 - \exp\left(\frac{-\left(0.057 Sc^{-2/3} + 4.5 \cdot 10^{-4}\left(\tau_p^{+}\right)^2\right) u^{*} \pi dL}{Q}\right) \tag{4.70}$$

The friction velocity can be calculated for smooth pipes based on Blasius (1913)

$$u^{*} = \frac{0.2\, u_{avg}}{\mathrm{Re}^{1/8}} \tag{4.71}$$

Equation (4.70) can be used to calculate the turbulent deposition efficiency in a circular pipe for a fully developed turbulent flow (plug flow) with uniform particle distribution at the inlet.

Chapter 5

Results and Discussion

The following chapter describes the results of the experimental, analytical and numerical investigation of particle deposition due to the influence of Brownian diffusion, electrostatic forces, and Saffman lift force in laminar pipe flow and comparison with CFD. It also describes the results of pilot plant plugging experiments of SCR DNX monolithic catalysts and a comparison with a CFD model that takes deposit build-up into account.

5.1 Experimental Results of Submicron Particle Deposition

5.1.1 Polydisperse Aerosol

Measurements of submicrometer polydisperse particle deposition efficiency in respectively a three-meter straight aerosol deposition pipe and a three-meter aerosol deposition pipe, bent in sections of about 0.75 meter has been carried out. A schematic illustration of the setup is shown in Figure 3.1. The experimental setup consisted of a Scanning Mobility Particle Sizer^{TM} (SMPS^{TM}) Spectrometer Model 3936 *TSI Incorporated*, an Electrometer Model 3068B *TSI Incorporated*, a Six-Jet Atomizer Model 9306A *TSI Incorporated*, a Diffusion Dryer Model 3062 *TSI Incorporated*, an Aerosol Neutralizer Model 3054 *TSI Incorporated*, a three-meter long aerosol deposition pipe for measuring the deposition of aerosol particles and two sampling lines for Scanning Mobility Particle Sizer^{TM} (SMPS^{TM}) Spectrometer measurements and total average charge measurements using an Electrometer 3068B *TSI Incorporated*. The polydisperse aerosol particle size distribution and particle number concentration were measured at the top and bottom of the aerosol deposition pipe, respectively and the deposition efficiency

was determined by subtracting the polydisperse size distribution at the bottom from the size distribution at the top. Calculation of a polydisperse aerosol particle size distribution is shown in Appendix G. Aerosol particles were generated with a Six-Jet Atomizer Model 9306A *TSI Incorporated*, using a liquid solution consisting of potassium chloride, KCl. The atomizer in the experiments generated particles from liquid solutions between 0.0002-0.002 wt% KCl. The number of particles was controlled by the pressure in the atomizer. The particles were dried to solid particles through the diffusion dryer. The average velocity in the setup was 0.17 m/s, the residence time was 18 s and the Reynolds number was 63.

5.1.1.1 Bent Aerosol Deposition Pipe

In order to analyse the purity of the ultra pure water used for the KCl solutions the content of particles in the water was measured to ensure that impurities in the water would not interfere with the aerosol particles generated in the experiments. It was observed that the particle number concentration was very low with a maximum about 40 #/cm^3. The total particle number concentration calculated by integrating the size distribution measured using the LDMA at the top of the bent aerosol deposition pipe was 1129 #/cm^3. Based on these observations it was concluded that the impurities in the ultra pure water was very low and would not influence the aerosol particle size distributions generated by the atomizer and therefore the calculated deposition efficiency based on the measurements.

The effect of surface roughness on the particle deposition, measurements was initially investigated using an electro polished and a non-electro polished bent aerosol deposition pipe. It was observed that the deposition efficiency was not affected by the surface roughness, which was also expected due to laminar flow conditions. As seen from Equation (2.39) the deposition efficiency should only be affected by the diffusion coefficient, the length of the pipe and the volume flow through the pipe. Based on the comparison between an electro polished and a non-electro polished aerosol deposition pipe it was decided to use an electro polish aerosol deposition pipe in all experiments.

In order to analyze the effect of charged particles from the atomization process, measurements were carried out both with and without using an Aerosol Neutralizer in the setup as shown in Figure 3.1. Figure 5.1 shows the size distribution of charged and neutralized aerosol particles generated by a 0.002 wt% salt solution consisting of potassium chloride, KCl, measured at the top and bottom of the bent aerosol deposition pipe. Using the Aerosol Neutralizer

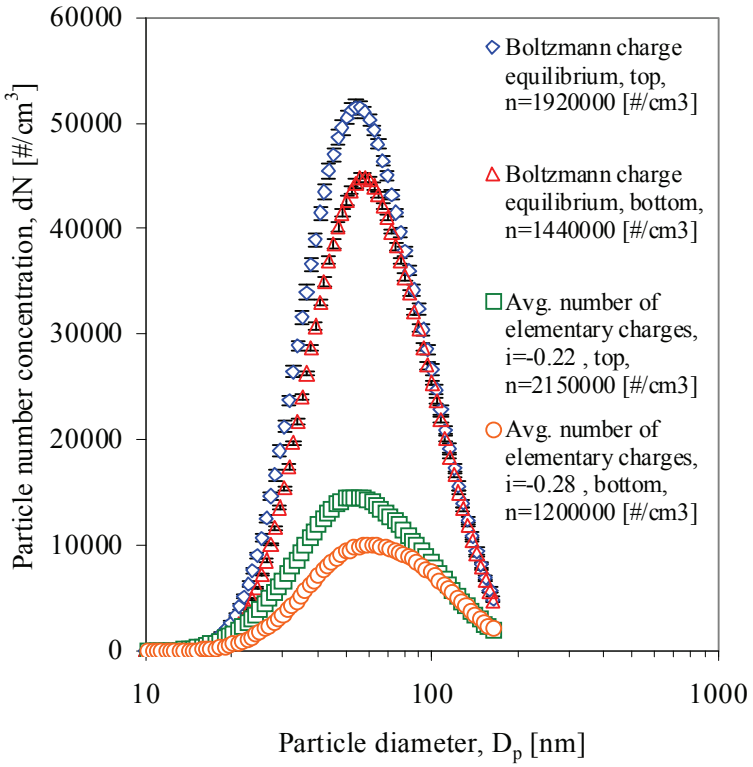

Figure 5.1: Size distribution of KCl particles both with and without using an Aerosol Neutralizer (AN) in an electro polished bent aerosol deposition pipe. Flow, Q = 300 ml/min. Temperature, T = 298K. KCl particles were generated from a 0.002 wt% KCl solution in the atomizer. Measured using the NDMA where n is the totale particle number concentration counted using the CPC. The atomizer was set to a pressure of 40 psi and 1 jet using the AN, and without the AN, the atomizer was set to a pressure of 20 psi and 2 jet.

neutralized the particles to a bipolar charge equilibrium (approximately Boltzmann charge equilibrium) before entering the aerosol deposition pipe.

As it can be seen from Figure 5.1 the particle number concentration, *dN,* measured at the top of the bent aerosol deposition pipe with the Aerosol Neutralizer had a maximum about 51500 #/cm^3 and at the bottom a maximum about 44800 #/cm^3. The total particle number concentration by integrating the size distribution measured using the NDMA at the top was around $1.68 \cdot 10^6$ #/cm^3 and at the bottom about $1.44 \cdot 10^6$ #/cm^3. The average number particle size was 56.1 nm and the average mass particle size was 101.7 nm at the top of the bent aerosol deposition pipe and at the bottom the average number particle size was 58.8 nm

and the average mass particle size was 103.2 nm. The total particle number concentration at the top counted using the CPC was about $1.92 \cdot 10^6$ #/cm^3. Here a shift in the size distribution towards larger mean values at the bottom of the deposition pipe can be observed due to the higher diffusivity of the smaller particles below about 80-90 nm as seen in Figure 5.3. The reason for the total particle number concentration counted using the CPC is higher than the total particle number concentration calculated by integrating the size distribution measured using the NDMA at the top of the aerosol deposition pipe is that the CPC counts particles above the limit of the NDMA which is 168 nm and up to about 1 micrometer. The average number of elementary charges calculated based on Wiedensohler (1988), Equation (2.22) for the neutralized aerosol particle size distribution using the Aerosol Neutralizer gives an average number of elementary charges i = -0.069 at the top of the bent aerosol deposition pipe and i = -0.071 at the bottom.

Without the Aerosol Neutralizer it can be observed from Figure 5.1 that the particle number concentration, *dN,* measured at the top of the aerosol deposition pipe had a maximum about 14600 #/cm^3 and at the bottom a maximum about 10100 #/cm^3. The total particle number concentration at the top was around $5.15 \cdot 10^5$ #/cm^3 and at the bottom about $3.62 \cdot 10^5$ #/cm^3 measured using the NDMA. The average number particle size was 56.1 nm and the average mass particle size was 105.7 nm at the top of the aerosol deposition pipe and at the bottom the average number particle size was 62.7 nm and the average mass particle size was 111.5 nm. The total particle number concentration at the top counted using the CPC was about $2.15 \cdot 10^6$ #/cm^3 and at the bottom about $1.2 \cdot 10^6$ #/cm^3. The difference in the total particle number concentration between the integrated value from the NDMA and the counted value using the CPC has not been explained. It does not sound reasonable that around $1.5 \cdot 10^6$ #/cm^3 should be outside the range of the NDMA, however the obtained deposition efficiency shown in Figure 5.3 seems reasonable indicating some relative error between the NDMA and the CPC. The shift in the size distribution towards larger mean values at the bottom of the deposition pipe can again be observed due to the higher diffusivity of the smaller particles below about 80-90 nm as seen in Figure 5.3. The average number of elementary charges measured using the electrometer was, i=-0.22 at the top of the bent aerosol deposition pipe and at the bottom the average number of elementary charges was, i=-0.28. It can be observed that the average number of elementary charges is higher measured at the bottom of the bent aerosol deposition pipe than at the top. The reason for this is probably because smaller particles in general carry less charges compared to larger particles and the smaller particles are more diffusive and get deposited through the pipe. The total particle number concentration of aerosol particles at the bottom will therefore

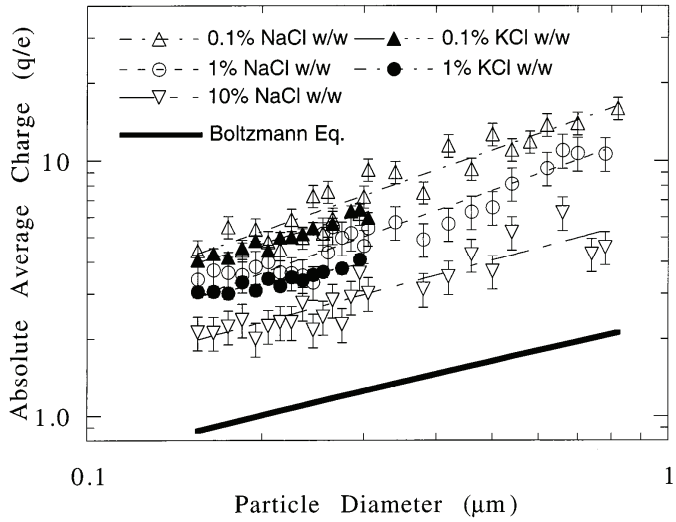

Figure 5.2: Charge level on potassium chloride (KCl) and sodium chloride (NaCl) particles after collision atomizer generation and Po-210 neutralization [Forsyth et al. (1998)].

only contain larger particles with higher charges which gives a higher average number of elementary charges than at the top.

Forsyth et al. (1998) investigated the particles charge distribution of e.g. KCl aerosol particles (0.1% w/w and 1% w/w) by measuring the charge distribution immediately after the generation using a collision atomizer and they also measured the charge distribution after neutralization. From their data shown in Figure 5.2 it can be observed that a decrease in concentration increases the absolute average number of elementary charges on the particles and also that the absolute average number of elementary charges for particles carrying Boltzmann charge equilibrium is less than the absolute average number of elementary charges on the particles generated from the collision atomizer. It can also be observed that the absolute number of elementary charges increases with increasing particle diameter. Forsyth et al. (1998) investigations therefore confirms that at the bottom of the aerosol deposition pipe the average number of elementary charges should be higher than at the top because the aerosol particles in average are larger at the bottom. It can also be observed that the average number of elementary charges is larger for aerosol particle size distributions that are not neutralized compared to aerosol particle size distributions that carry approximately Boltzmann charge equilibrium.

Figure 5.3 shows a comparison of the deposition efficiency in per cent of respectively charged KCl particles due to the atomization process and KCl

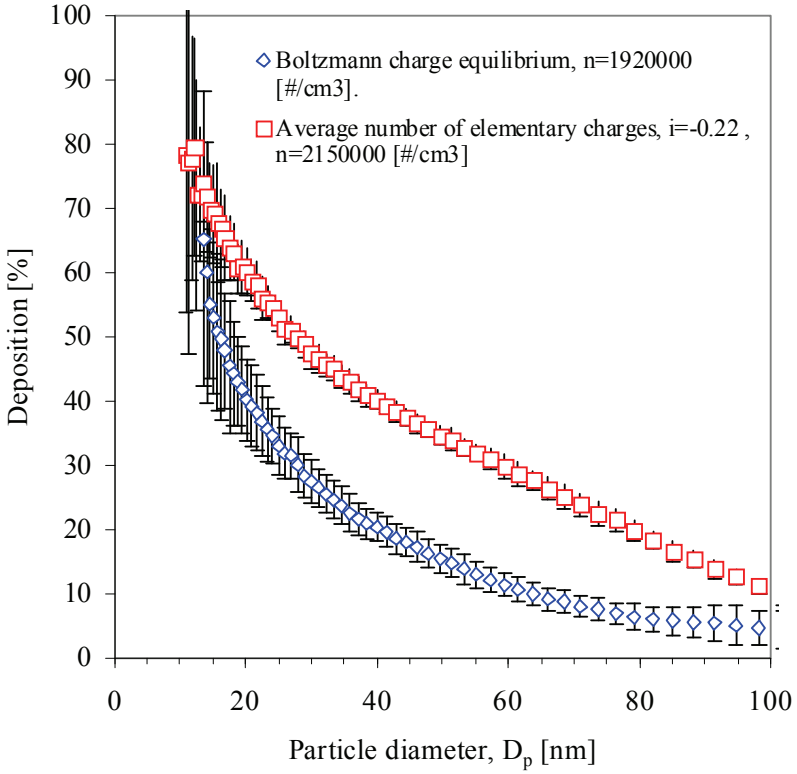

Figure 5.3: Comparison of deposition efficiency of respectively charged KCl particles from atomization process with an average number of elementary charges, i=-0.22 and KCl particles discharged to Boltzmann charge equilibrium in an electro polished bent aerosol deposition pipe. Flow, Q = 300 ml/min. Temperature, T = 298K. KCl particles were created from a 0.002 wt% KCl solution in the atomizer.

particles neutralized to nearly Boltzmann charge equilibrium versus particle size in the axial length of the aerosol deposition pipe. This comparison was based on the size distribution in Figure 5.1. The deposition efficiency was close to 70% for small particles in the neighbourhood of 10 nm and for particles around 100 nm and above 100 nm the deposition efficiency was below 10%. It can be observed that the particles discharged to approximately Boltzmann charge equilibrium in general shows a lower deposition rate in the range between about 20-80 nm than particles which have not been discharged and carry an average number of elementary charges, *i*=-0.22 at the top. The reason for this is due to their higher electrical mobility because the average number of elementary charges is larger and the space charge density for the high concentration is higher than for particles carrying approximately Boltzmann charge equilibrium.

This tendency has also been confirmed by Liu et al. (1985) whom investigated aerosol particle penetration through a conductive copper tubing with an internal diameter of 4.35 mm, a length of 3 meter and a flow rate of 1.0 l/min for singly charged aerosol particles, diffusion charged aerosol particles and aerosol particles with Boltzmann charge equilibrium as shown in Figure 2.19. The measurement of Liu et al. (1985) showed that the deposition efficiency for aerosol particles with Boltzmann charge equilibrium was lower than the deposition efficiency for singly charged aerosol particles and diffusion charged aerosol particles. This has also been confirmed by numerical solutions carried out by Li and Ahmadi (1993a); He and Ahmadi (1998) and He and Ahmadi (1999) where they showed that the deposition velocity was higher for particles carrying one elementary charge compared to particles carrying Boltzmann charge equilibrium which again was higher than for neutral particles (particles carrying zero charge). They also showed that the highest deposition velocities were for particles carrying saturation charge (particles carrying charge limit – see Figure 2.17). When calculating the difference in particle number concentration between the top and bottom of the aerosol deposition pipe as seen in Figure 5.3 the standard deviation on the individual particle sizes get dominating due to very small particle number concentrations generated below 20 nm. This is a general problem in all the experiments for the small particles.

In order to study the influence of particle number concentration for charged particles on the deposition due to electrostatic dispersion because of space charging, investigations were carried out for high and low concentrations of KCl aerosol particles. Figure 5.4 shows the size distributions of charged aerosol particles generated by a 0.002 wt% KCl solution. The size distributions were generated respectively with high and low total particles number concentration. The measurements were carried out both at the top and bottom of the bent aerosol deposition pipe. The size distribution generated with the high particle number concentration is plotted from Figure 5.1 together with the size distribution generated with low concentration. The low particle number concentration, *dN,* measured at the top of the aerosol deposition pipe had a maximum around 3200 #/cm^3 and at the bottom around 2200 #/cm^3. The integrated particle number concentration at the top was about $1.13 \cdot 10^5$ #/cm^3 measured using the NDMA and at the bottom around $77.9 \cdot 10^3$ #/cm^3. The average number particle size was 29 nm and the average mass particle size was 104.4 nm at the top of the aerosol deposition pipe and at the bottom the average number particle size was 34.2 nm and the average mass particle size was 106.4 nm. The total particle number concentration at the top counted using the CPC was about $1.93 \cdot 10^5$ #/cm^3 and at the bottom about $1.76 \cdot 10^5$ #/cm^3. The shift in the size distribution towards larger mean values at the bottom of the deposition pipe can also be observed for the

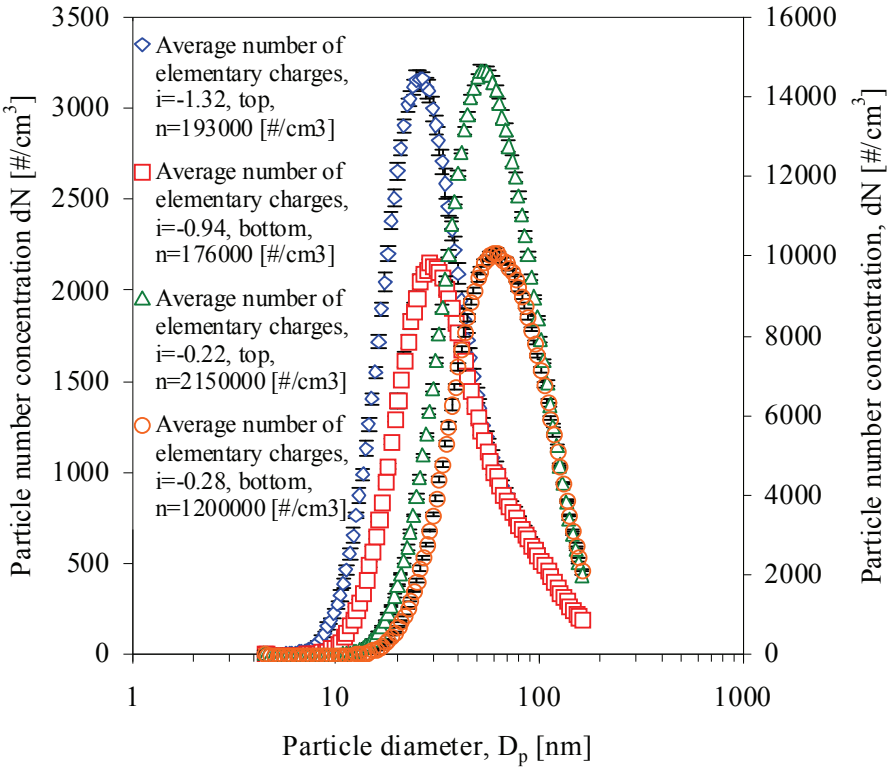

Figure 5.4: Size distribution of respectively high and low concentrations of KCl particles in an electro polished bent aerosol deposition pipe. Flow, Q = 300 ml/min. Temperature, T = 298K. KCl particles were generated from a 0.002 wt% KCl solution in the atomizer. Measured using the NDMA where n is the totale particle number concentration counted using the CPC. For high concentrations the atomizer was set to a pressure of 50 psi and 3 jets and for the low concentrations it was set to a pressure of 10 psi and 1 jet.

particle size distribution generated at low concentration due to the higher diffusivity of the smaller particles below about 40-50 nm as seen in Figure 5.5. The average number of elementary charges measured using the electrometer was, i=-1.32 at the top of the bent aerosol deposition pipe and at the bottom the average number of elementary charges was, i=-0.94.

For the low concentration of KCl it can be observed that the average number of elementary charges is lower at the bottom of the bent aerosol deposition pipe which is different from the high concentration of KCl. It can also be observed that the average number of elementary charges is higher for the low concentration of KCl aerosol particles. One explanation for this could be the natural discharge in the system due to random collisions between air ions present in the system and the

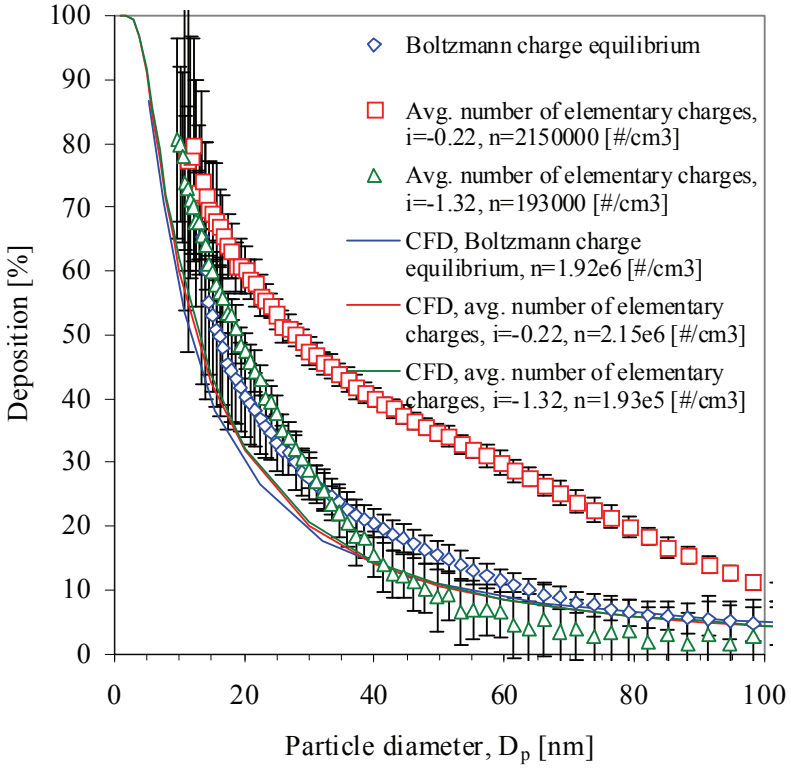

Figure 5.5: Comparison of deposition of respectively high and low concentrations of charged KCl particles and KCl particles neutralized to Boltzmann charge equilibrium in an electro polished bent aerosol deposition pipe. Flow, Q = 300 ml/min. Temperature, T = 298K. KCl particles were generated from a 0.002 wt% KCl solution in the atomizer.

KCl aerosol particles. These collisions are more likely to happen in the case of high KCl aerosol particle concentration than in the case of low concentration. As an example the concentration of ions in ambient air is about 10^3 cm^{-3}, with approximately equal numbers of positive and negative ions. These pairs of positive and negative ions are produced by collision of cosmic rays and energetic nuclear particles produced by radioactive decay with the gas molecules [Byron and Willeke (2005), p. 542].

Figure 5.5 shows a comparison of the deposition efficiency in per cent of respectively high and low concentrations of KCl particles in the axial length of the bent aerosol deposition pipe versus particle diameter and also a comparison with CFD simulation of charged and neutral KCl aerosol particles. The comparison is based on the size distribution given in Figure 5.4. In general, from Figure 5.5, it can be observed that high concentration of KCl particles carrying an average

number of elementary charges, i=-0.22 showed higher deposition rates (especially between particle diameters of 20-100 nm) than particles discharged to approximately Boltzmann charge equilibrium (average number of elementary charges, i=-0.07) and higher deposition rates than low concentration of KCl particles carrying an average number of elementary charges, i=-1.32. This was even though the average number of elementary charges was higher for the low concentration of KCl particles than for high concentrations of KCl particles and particles with a bipolar charges equilibrium. The reason is that the space charge density is higher in the case of high concentration of KCl aerosol particles than for the low concentration. The higher space charge density creates at higher electrostatic potential inside the pipe which again increases the electric field strength and thereby the electrostatic dispersion as seen from Equation (2.30) where the space charge density is the source term on the right hand-side of the Poisson equation and from Equation (2.26). It also has to be mentioned that real particles are not carrying an average number of elementary charges but are carrying integer number of elementary charges and a charged particle therefore have higher electrical mobility for a given number of elementary charges in a higher electric field strength. The lowest deposition rates were seen from the low concentration of KCl particles for particles larger than 30 nm. Below 30 nm the particles carrying Boltzmann charge equilibrium and particles generated with low concentration and low space charge showed more or less the same deposition rate. The reason for this is that the largest fraction of the particles below 30 nm will be neutral and it can be concluded that one can decrease (or totally suppress) the electrostatic dispersion of particles by decreasing the number concentration of aerosol particles because this will decrease the space charge density. Due to the small amount of particles generated for the size distribution with low particle number concentration the difference between top and bottom of the aerosol deposition pipe in particle number concentration gave a standard deviation that was much higher than the case of the KCl particles generated with high concentration.

From Figure 5.5 it can be observed that the both the CFD simulation of KCl particles carrying Boltzmann charge equilibrium, the CFD simulation with high concentrations of KCl particles carrying an average number of elementary charges, i=-0.22 and the CFD simulation with low concentrations of KCl particles carrying an average number of elementary charges, i=-1.32 all underestimate the experimental measured deposition efficiency of KCl aerosol particles. The reason for this probably is that the aerosol particles in the experiments do not carry an average number of elementary charges but only integer number of elementary charges. The average number of elementary charges in the CFD simulation will give the correct charge density and therefore the correct electrostatic potential and

electric field strength but underestimate the electrical mobility and therefore the electrical migration velocity of the charged particles. This has also been confirmed by Li and Ahmadi (1993a) who numerically studied deposition rates of charged aerosol particles in a vertical turbulent channel flow and concluded that using an average charge for simulating the effect of electrostatic forces leads to an underestimation of the deposition velocity, because the particles acquire integer number of charge. The reason for this is that assigning an average number of charge to all particles are not necessarily equivalent to the real case where a fraction of the particles are carrying one or more elementary charges and the rest of the particles are neutral. The aerosol particles carrying Boltzmann charge distribution has been simulated by discretizing the particle size distribution given in Figure 5.1 into ten classes by summation of the particle number concentration in each of the 101 measured classes between 4.4 nm and 163 nm and assigning them to ten average number particle sizes and then calculating the charge distribution on these classes based on Wiedensohler (1988). It can also be observed from Figure 5.5 that the CFD simulation with high concentrations of KCl particles carrying an average number of elementary charges are actually not predicting higher deposition efficiencies than for the low concentration KCl particles and the KCl particles carrying Boltzmann charge equilibrium. This again has to be due to the problem that the real charge distribution on the particles are not known and therefore can not be simulated. Overall it can be concluded that the general trend in the deposition efficiency is captured with the CFD simulations.

In the present work deposition has been determined based on the difference in particle number concentration at the top and bottom (where a decrease in particle number concentration at the bottom means deposition in the pipe) of the deposition pipe. This will only be valid if agglomeration can be neglected because the result of many collisions between particles will increase the particle size of the aerosol particles and decrease the particle number concentration. In the absence of any loss or removal mechanisms (deposition) there will be no change in mass concentration as a result of agglomeration [Byron and Willeke (2005)]. In order to investigate whether the reported deposition efficiency based on the difference in particle number concentration at the top and bottom of the bent aerosol particle deposition pipe was due to particle deposition or whether the change in particle number concentration in the outlet of the deposition pipe in reality was due to particle agglomeration the deposition efficiency based on particle number concentration and particle mass concentration was compared.

Figure 5.6 shows a comparison of the deposition efficiency versus particle diameter of aerosol particles generated by a 0.002 wt% KCl solution in an electro polished three-meter bent pipe based on the number concentration and mass

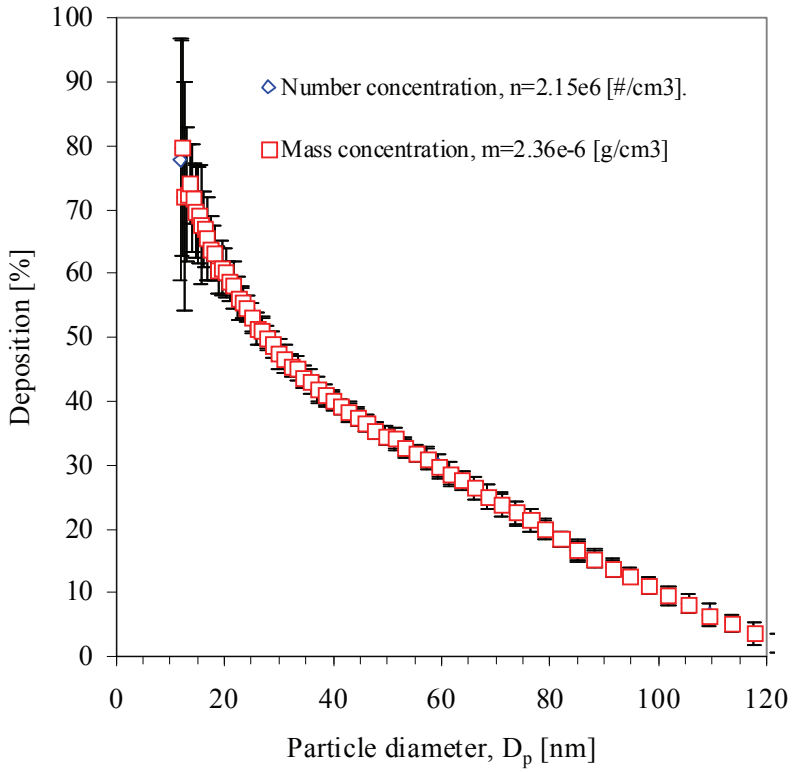

Figure 5.6: Comparison of deposition efficiency concentrations of charged (i=-0.22) KCl particles in a bent electro polished aerosol deposition pipe based on number concentration and mass concentration, respectively. Flow, Q = 300 ml/min. Temperature, T = 298K. KCl particles were generated from a 0.002 wt% KCl solution in the atomizer.

concentration, respectively. The total particle number concentration was $2.15 \cdot 10^6$ #/cm^3 and the initial particle mass concentration based on the size distribution was 236 μg/m^3. It can be observed from Figure 5.6 that the deposition efficiency based on respectively particle number concentration and particle mass concentration was identical and it can therefore be concluded that the change in particle number concentration from top to bottom of the aerosol deposition pipe was not due to agglomeration but only due to deposition. Calculation of the characteristic time for agglomeration given in Appendix H also confirms this.

5.1.1.2 Straight Aerosol Deposition Pipe

Figure 5.7 shows the size distribution of aerosol particles generated by a 0.002 wt% KCl solution. The size distribution was generated respectively with a high

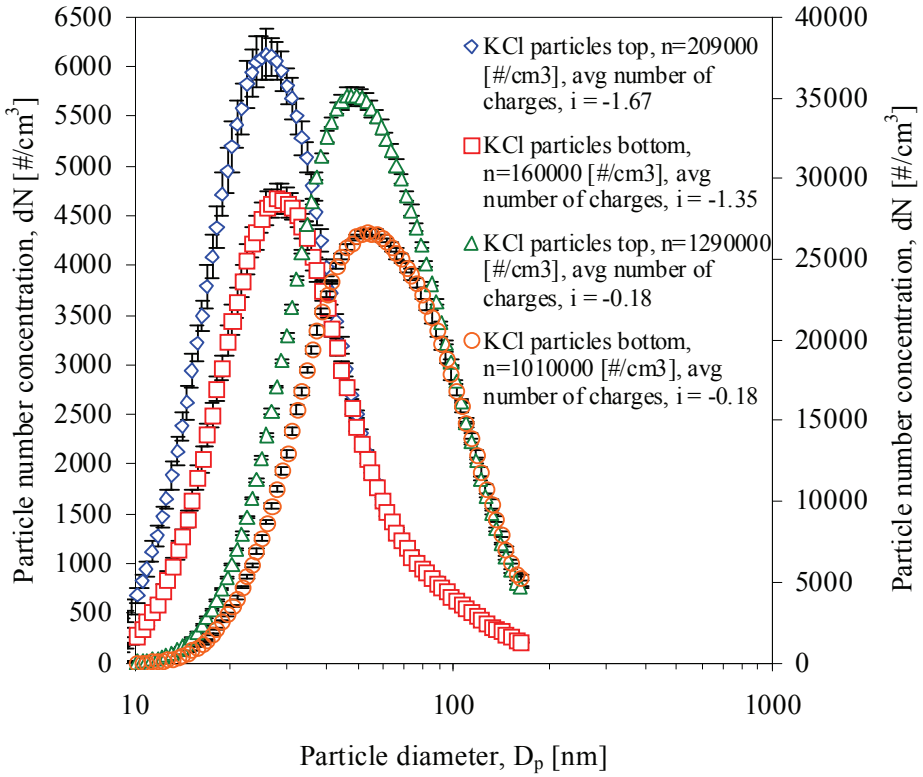

Figure 5.7: Size distribution of respectively high and low concentrations of KCl particles in an electro polished straight aerosol deposition pipe. Flow, Q = 300 ml/min. Temperature, T = 298K. KCl particles were generated from a 0.002 wt% KCl solution in the atomizer. Measured using the NDMA where n is the totale particle number concentration counted using the CPC. For high concentrations the atomizer was set to a pressure of 50 psi and 3 jets and for the low concentrations the atomizer was set to a pressure of 10 psi and 1 jet.

and low total particles number concentration. The measurements were carried out both at the top and bottom of the straight three-meter aerosol deposition pipe. As it can be seen from Figure 5.7 the high particle number concentration, *dN,* measured at the top of the aerosol deposition pipe had a maximum around 35100 #/cm^3 and at the bottom the maximum was about 27000 #/cm^3. The total particle number concentration at the top was around $1.3 \cdot 10^6$ #/cm^3 by integrating the size distribution measured using the NDMA and at the bottom around $1.0 \cdot 10^6$ #/cm^3. The average number particle size was 52.3 nm and the average mass particle size was 104.4 nm at the top of the aerosol deposition pipe and at the bottom the average number particle size was 57.3 nm and the average mass particle size was 109.4 nm.

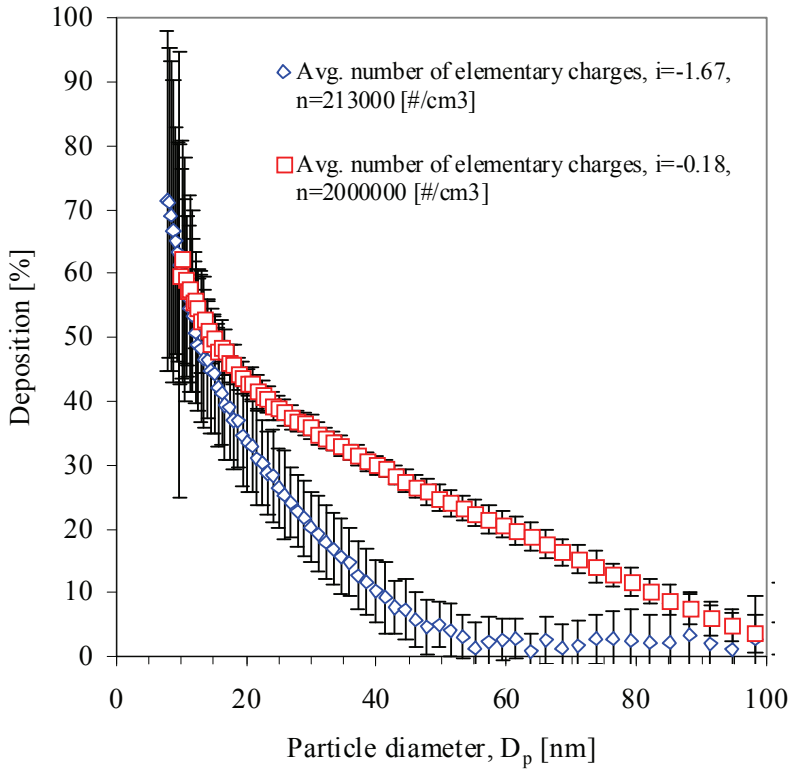

Figure 5.8: Comparison of deposition of respectively high and low concentrations of KCl particles in a straight electro polished aerosol deposition pipe. Flow, Q = 300 ml/min. Temperature, T = 298K. KCl particles were generated from a 0.002 wt% KCl solution in the atomizer.

The total particle number concentration at the top counted using the CPC was about $2.0 \cdot 10^6$ #/cm^3 and at the bottom about $1.4 \cdot 10^6$ #/cm^3. The average number of elementary charges measured using the electrometer was, i=-0.18 at the top of the straight aerosol deposition pipe and at the bottom the average number of elementary charges was, i=-0.18.

The low particle number concentration, *dN,* measured at the top of the deposition pipe had a maximum around 6100 #/cm^3 and at the bottom around 4700 #/cm^3. The total particle number concentration at the top was about $2.1 \cdot 10^5$ #/cm^3 measured using the NDMA and at the bottom around $1.6 \cdot 10^5$ #/cm^3. The average number particle size was 27.6 nm and the average mass particle size was 95.5 nm at the top of the aerosol deposition pipe and at the bottom the average number particle size was 30.5 nm and the average mass particle size was 97.2 nm. The total particle number concentration at the top counted using the CPC was about

$2.1 \cdot 10^5$ #/cm^3 and at the bottom about $1.9 \cdot 10^5$ #/cm^3. The average number of elementary charges measured using the electrometer was, i=-1.67 at the top of the straight aerosol deposition pipe and at the bottom the average number of elementary charges was, i=-1.35.

Figure 5.8 shows a comparison of the deposition efficiency in per cent of respectively high and low concentrations of KCl particles in the axial length of the aerosol deposition pipe versus particle size. The comparison is based on the size distribution in Figure 5.7. From Figure 5.8 it again can be observed that high concentrations of KCl particles in general showed higher deposition rates than low concentrations especially between 20-80 nm because of the high electrical mobility of the charged particles. Due to the small amount of particles generated for the size distribution with low particle number concentration the difference between top and bottom of the aerosol deposition pipe in particle number concentration gave a standard deviation that was much higher than the case of the KCl particles generated with high concentration. Again the shift in the size distribution towards larger mean values at the bottom of the deposition pipe can also be observed for both the particle size distributions.

5.1.1.3 Comparison Bent and Straight Pipe

Figure 5.9 shows a comparison of the deposition efficiency in per cent of high concentrations of KCl particles versus particle size in the axial length of respectively a three-meter bent pipe (bent in section of about 0.75 meter) and a three-meter straight pipe of the electro polished aerosol deposition pipe in Figure 3.1. Comparisons with CFD simulations for charged particles are also shown. As it can be observed the deposition efficiency was close to 80% for small particles in the neighbourhood of 10 nm for the bent pipe and the deposition efficiency was about 60-65% for particle sizes in the neighbourhood of 10 nm for the straight pipe. For particles around 100 nm and above 100 nm the deposition efficiency was below 10% for both the bent pipe and the straight pipe. In general it can also be observed that the deposition efficiency for the bent pipe was higher than for the straight pipe.

The deposition efficiency was about 15-20% point higher for the bent pipe than for the straight pipe for particles in the neighbourhood about 10 nm and about 5-10% point for particles in the neighbourhood of about 100 nm. When calculating the difference in particle number concentration between the top and bottom of the aerosol deposition pipe the standard deviation on the individual particle sizes get dominating due to very low particle number concentrations generated below 10-

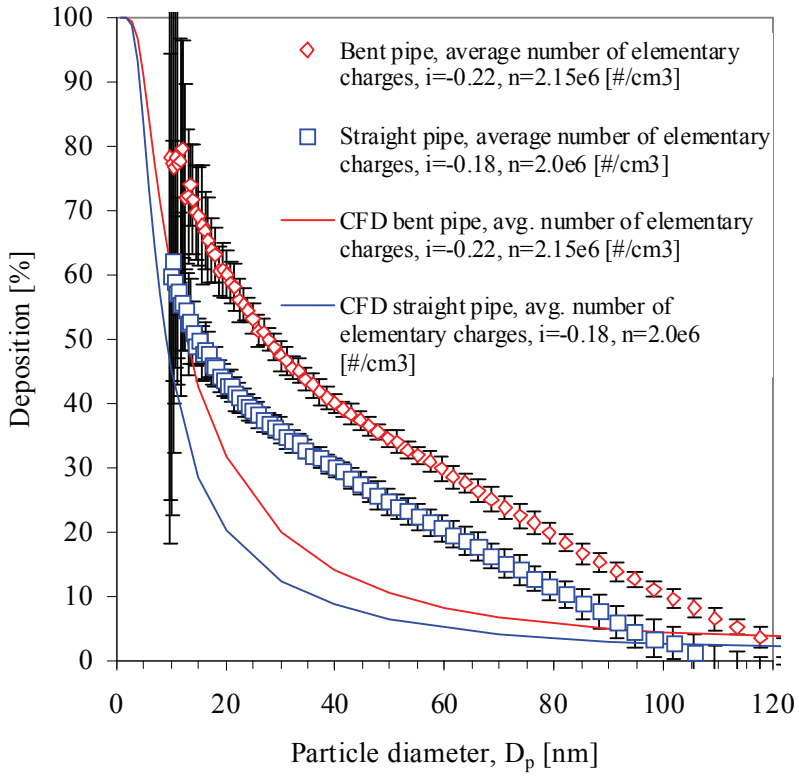

Figure 5.9: Comparison of deposition efficiency high concentrations of charged KCl particles in respectively a bent aerosol deposition pipe (bent in section of about 0.75 meter) and a straight aerosol deposition pipe. Flow, Q = 300 ml/min. Temperature, T = 298K. KCl particles were generated from a 0.002 wt% KCl solution in the atomizer.

15 nm. The difference in deposition efficiency between the charged aerosol particles in the bent pipe and the charged aerosol particles in the straight pipe is due to secondary flow in the bent pipe which also was confirmed by Liu et al. (1985) whom investigated deposition of charged particles through a varity of coiled tubes of length 3 m.

From Figure 5.9 it can be observed that both the CFD simulation with high concentrations of KCl particles in a bent pipe carrying an average number of elementary charges, i=-0.22 and the CFD simulation with high concentrations of KCl particles in a straight pipe carrying an average number of elementary charges, i=-0.18 underestimate the experimental measured deposition efficiency of KCl aerosol particles. The reason for this is again that the aerosol particles in the experiments do not carry an average number of elementary charges but only integer number of elementary charges. The average number of elementary charges

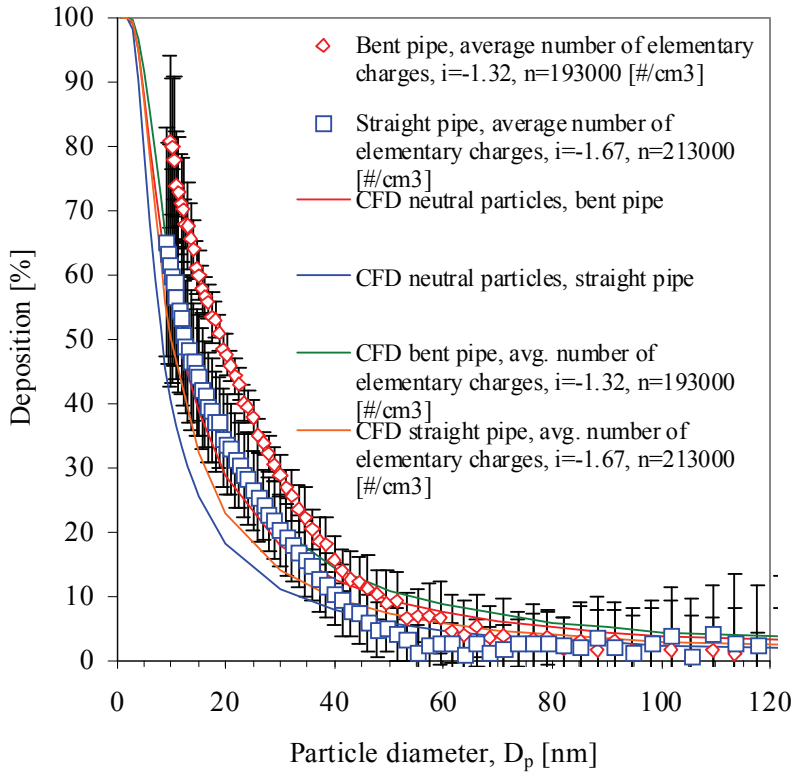

Figure 5.10: Comparison of deposition efficiency high concentrations of charged KCl particles in respectively a bent aerosol deposition pipe (bent in section of about 0.75 meter) and a straight aerosol deposition pipe. Flow, Q = 300 ml/min. Temperature, T = 298K. KCl particles were generated from a 0.002 wt% KCl solution in the atomizer.

in the CFD simulation will still give the correct charge density and therefore the correct electrostatic potential and electric field strength but underestimate the electrical mobility and therefore the electrical migration velocity of the charged particles. But the CFD simulations capture the relative difference in deposition efficiency between the bent pipe and the straight pipe due to secondary flow effects and the agreement in the relative difference is very well with the experimental results.

Figure 5.10 shows a comparison of the deposition efficiency in per cent of low concentrations of KCl particles versus particle size in the axial length of respectively a three-meter bent pipe (bent in section of about 0.75 meter) and a three-meter straight pipe of the electro polished aerosol deposition pipe in Figure 3.1. Comparisons with CFD simulations for charged and neutral particles are also shown. As it can be observed the deposition efficiency was close to 80% for small

particles in the neighbourhood of 10 nm for the bent pipe and the deposition efficiency was about 65% for particle sizes in the neighbourhood of 10 nm for the straight pipe. For particles around 60-70 nm the deposition efficiency was below 10% and close to zero for both the bent pipe and the straight pipe. In general, it again can also be observed that the deposition efficiency for the bent pipe was higher than for the straight pipe. The deposition efficiency was about 10-15% point higher for the bent pipe than for the straight pipe which again can be ascribed to the secondary flow in the bent pipe. What also can be observed when comparing the high and the low concentration of KCl aerosol particles is that the deposition efficiency is higher for the high concentration for both the bent and the straight pipe for particles above 20 nm due to higher space charge density which again creates a higher electrostatic potential inside the pipe and higher electrical migration velocity of the charged particles. Below 20 nm the deposition efficiency is more or less the same for high and low concentrations of KCl particles because only a small fraction of the particles will be charged. As seen from Figure 2.17 the maximum amount of charge a particle can carry e.g. for a 10 nm particle is 16 negative elementary charges and 365 positive elementary charges, but due to random collision with air ions the only a very small fraction will be charged. Aerosol particles that are initially charged will lose their charge slowly as charged particles attract oppositely charged ions.

From Figure 5.10 it can be observed that both the CFD simulation with low concentrations of KCl particles in a bent pipe carrying an average number of elementary charges, i=-1.32 and the CFD simulation with low concentrations of KCl particles in a straight pipe carrying an average number of elementary charges, i=-1.67 underestimate the experimental measured deposition efficiency of KCl aerosol particles. The reason for this is again that the aerosol particles in the experiments do not carry an average number of elementary charges but only integer number of elementary charges. It can also be observed that the CFD simulations of neutral particles are close to the CFD simulation with charged particles. This is due to the low space charge density because of the low aerosol particle number concentration by what means the electrostatic dispersion becomes negligible.

Based on the experimental investigation of polydisperse particle deposition it can be concluded that electrostatic dispersion is an important deposition mechanism for charged submicrometer particles and will influence the deposition in monolithic catalyst by the same order as Brownian diffusion.

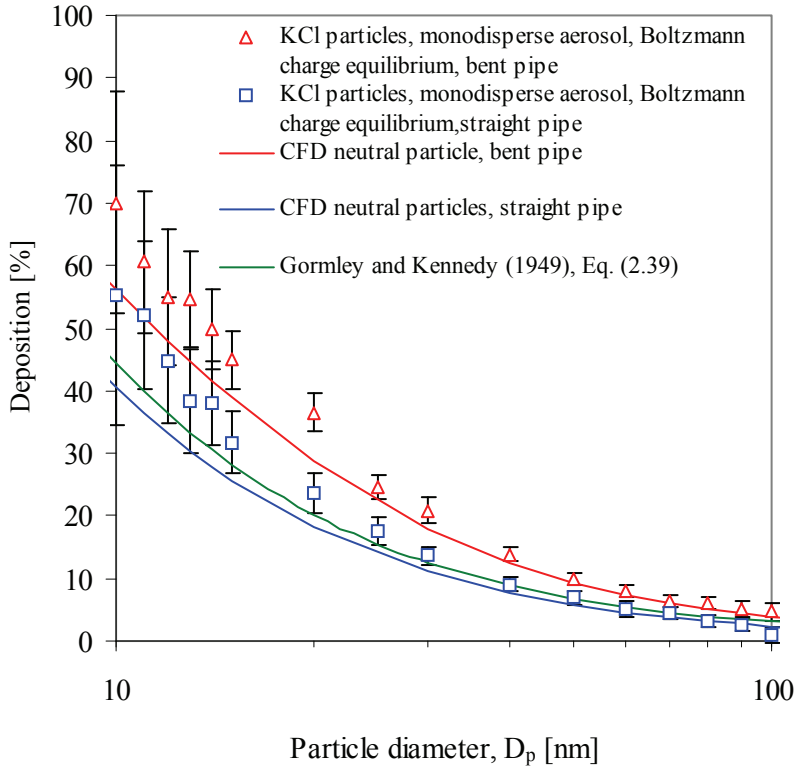

Figure 5.11: Deposition efficiency versus particle diameter for monodispersed KCl particles carrying a bipolar charge distribution (nearly a Boltzmann equilibrium charge distribution) and low initial particle number concentration, for respectively a straight three-meter long pipe and a three-meter long pipe bent in section of about 0.75 meter. Flow, Q = 300 ml/min. Temperature, T = 298K. KCl particles were generated from a 0.0002-0.002 wt% KCl solution in the atomizer.

5.1.2 Monodisperse Aerosol

In order to investigate the deposition efficiency of neutralized monodisperse submicrometer aerosol particles suppressing electrostatic effects, measurements of particle deposition efficiency in respectively a three-meter bent aerosol deposition pipe (bent in sections of about 0.75 meter) and a three-meter straight aerosol deposition pipe have been carried out. The observed effect of secondary flow on the deposition efficiency from the polydisperse aerosol measurements was also investigated. A schematic illustration of the setup is shown in Figure 3.4.

The experimental setup consisted of a Scanning Mobility Particle Sizer^{TM} (SMPS^{TM}) Spectrometer Model 3080 *TSI Incorporated*, a Six-Jet Atomizer Model 9306A *TSI Incorporated*, a Diffusion Dryer Model 3062 *TSI Incorporated*, a three-meter long aerosol deposition pipe for measuring the deposition of aerosol particles and two sampling lines for Scanning Mobility Particle Sizer^{TM} (SMPS^{TM}) Spectrometer measurements. The monodisperse aerosol particles were selected by the NDMA and the particle number concentration was counted respectively at top and bottom of the aerosol deposition pipe. The deposition efficiency was determined by subtracting the particle number concentration of the monodisperse aerosol particles at the bottom from the top. Aerosol particles were generated with a Six-Jet Atomizer Model 9306A *TSI Incorporated*, using a liquid solution consisting of potassium chloride, KCl. The atomizer in the experiments generated particles from liquid solutions between 0.0002-0.002 wt% KCl. The number of particles was controlled by the pressure in the atomizer. The particles were dried to solid particles through the diffusion dryer.

Figure 5.11 shows the deposition efficiency versus particle diameter for mono-disperse KCl particles carrying a bipolar charge distribution (approximately Boltzmann equilibrium charge distribution) and very low particle number concentration in the range from 14 to 15000 #/cm^3 for respectively a three-meter long pipe bent in 4 sections of about 0.75 meter and a straight three-meter long pipe. Figure 5.11 also shows the importance of secondary flow in a bent pipe compared to a straight pipe without secondary flow, where it can be observed that the particle deposition in the bent pipe is enhanced due to the secondary flow which is superimposed on the main flow. As it can be observed from Figure 5.11 the deposition is enhanced in the whole particle size range from 10 nanometer up to about 100 nanometer with a maximum in the deposition efficiency of about 15% point for the bent pipe compared to the straight pipe as seen from Figure 5.12. A comparison has also been carried out with CFD simulations of neutral (zero charge) particles with an initial particle number concentration, $n_0 = 2 \cdot 10^{12}$ #/m^3. As long as the secondary particle phase is diluted and agglomeration and electrostatic effects can be neglected the particle number concentration do not influence the deposition efficiency.

Figure 5.11 also shows a comparison between the experimental result, CFD and the empirical deposition model of Gormley and Kennedy (1949) (Equation (2.39)). As it can be observed from Figure 5.11 the agreement between the experimental data and the CFD simulations are very good and clearly shows an enhancement of the deposition efficiency in the bent pipe. This enhancement is shown in Figure 5.12. It can also be concluded that because the flow is laminar and the Reynolds number is very low also the entrance effects in the pipe can be

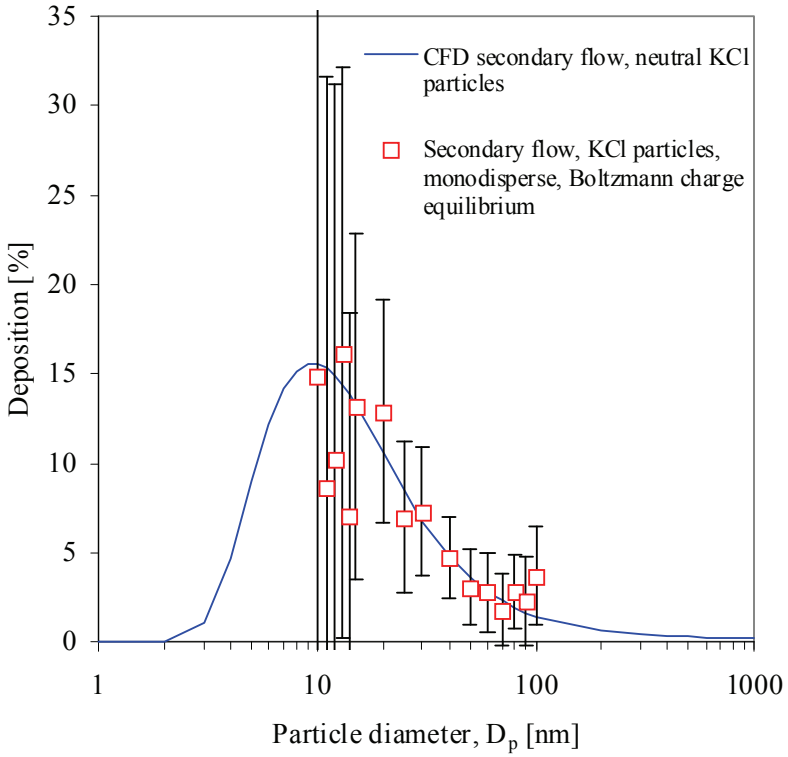

Figure 5.12: Deposition efficiency due to secondary flow versus particle diameter for monodispersed KCl particles carrying a bipolar charge distribution (nearly Boltzmann equilibrium charge distribution) and low initial particle number concentration in a 3 meter long pipe bent in sections of about 0.75 meter. Flow, Q = 300 ml/min. Temperature, T = 298K. KCl particles were generated from a 0.0002-0.002 wt% KCl solution in the atomizer.

neglected. With the same flow conditions in respectively the straight and the bent pipe the nanometer and submicrometer particles can be assumed only to be exposed to the same Brownian particle diffusion. It can also be assumed, because the Stokes' number, $Stk << 1$ (defined in Equation (2.12)), for the particle size range between 1-1000 nm, that the deposition in the bent pipe is not enhanced due to inertial impaction, as well as agglomeration and electrostatic dispersion can be neglected due to the very dilute secondary particle phase. The comparison with the empirical model of Gormley and Kennedy (1949) also shows very good agreement with the CFD simulation and the experimental result.

Figure 5.12 shows the comparison of the experimental result with the CFD simulation of secondary flow deposition efficiency versus particle diameter for

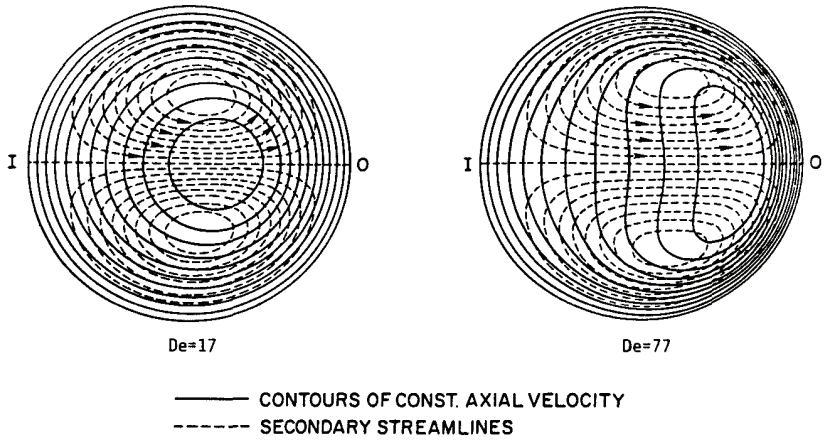

Figure 5.13: Secondary streamlines and axial velocity contours at low and intermediate Dean number [Pui et al. (1987)].

electrical neutral mono-disperse KCl particles in a three-meter long pipe bent in sections of about 0.75 meter. As it can be observed, the agreement is very good and the enhancement in deposition is believed only to be due to secondary flow. The reason for the very high standard deviation seen for particles below 20 nm is due to the very low particle number concentrations which were between 61 to 820 #/cm^3. In general it was very difficult to generate high particle number concentrations using the Six-Jet Atomizer for particles below 20 nm. The Dean number, *De*, (named after Dean (1927), who was the first to present a solution for flow in a curved tube with small curvature ratio) of the flow was 22 and is a single dimensionless quantity, which determines the flow field, and gives the relation between the flow Reynolds number and the square root of the curvature radius as follows

$$De = \frac{\mathrm{Re}}{\sqrt{R_b / R_{tube}}} \tag{5.1}$$

where Re is the Reynolds number, R_b is the bend radius and R_{tube} is the tube radius. The higher the value of the Reynolds number, Re, in the tube and the tighter the bend, the greater the value of the Dean number, *De,* and thereby the greater the degree to which the flow in the bend is pushed towards outside of the bend. The Dean number, *De*, represents the ratio of the square root of the product of centrifugal and inertial forces to the viscous forces and plays the role of the "Reynolds number" of the flow in curved pipes. Pui et al. (1987) stated that researchers have defined three different flow regimes for the flow around circular bends. For small Dean numbers ($De \leq 17$), due to the centrifugally induced pressure gradient that drives the slower moving fluid near the wall inward, while the faster moving fluid in the core is swept outward, a pair of counter rotating

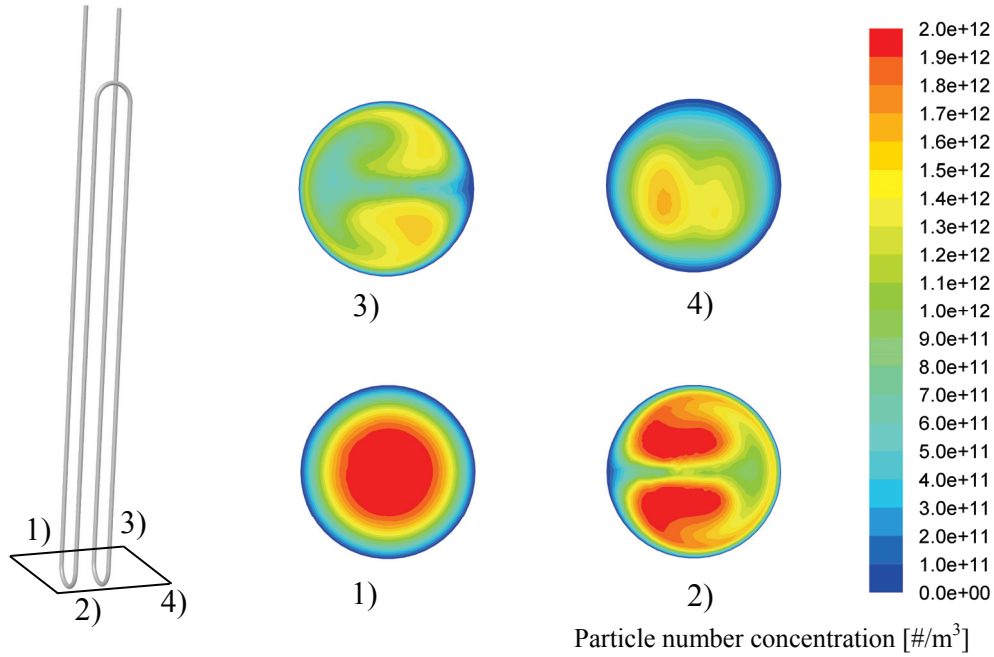

Figure 5.14: Contour plot of particle number concentration, $n = 2 \cdot 10^{12}$ [#/m^3], in a bent aerosol deposition pipe for a 10 nm KCl particle. Particle number concentration in the xy-plane in the bottom of the aerosol deposition pipe.

helical vortices placed symmetrically with respect to the plane of symmetry is formed, as seen on Figure 5.13. Due to this, the position of the maximum axial velocity is moved toward the outer bend and the flow is more stable than in straight tubes and e.g. the critical Reynolds number is around 5000 for a curvature ratio, R_0 = 31.9 ($R_0 = R_b/R_{tube}$), because of the stabilizing effect produced by the curvature.

For intermediate Dean numbers ($De \leq 370$), the flow pattern is the same as before as seen on Figure 5.13, but with a distortion of the secondary streamlines due to a secondary boundary layer that is developed on the wall and with the peak velocity closer to the outer bend. In the intermediate regime, the flow structure is characterized by an inviscid rotational core surrounded by a thin boundary layer. This is especially the case when the Dean number gets larger. For small and intermediate Dean number ($De \leq 370$) the flow is considered laminar. For large Dean Number ($De > 370$) more fluid is drawn into the boundary layer near the outer bend because the centrifugal force leads to an increase in axial velocity and the secondary boundary layer then adjust by thinning near the outer bend and thickening near the inner bend. With the De = 22, which is in the intermediate flow regime secondary flow is present in the bent pipe and will therefore enhance

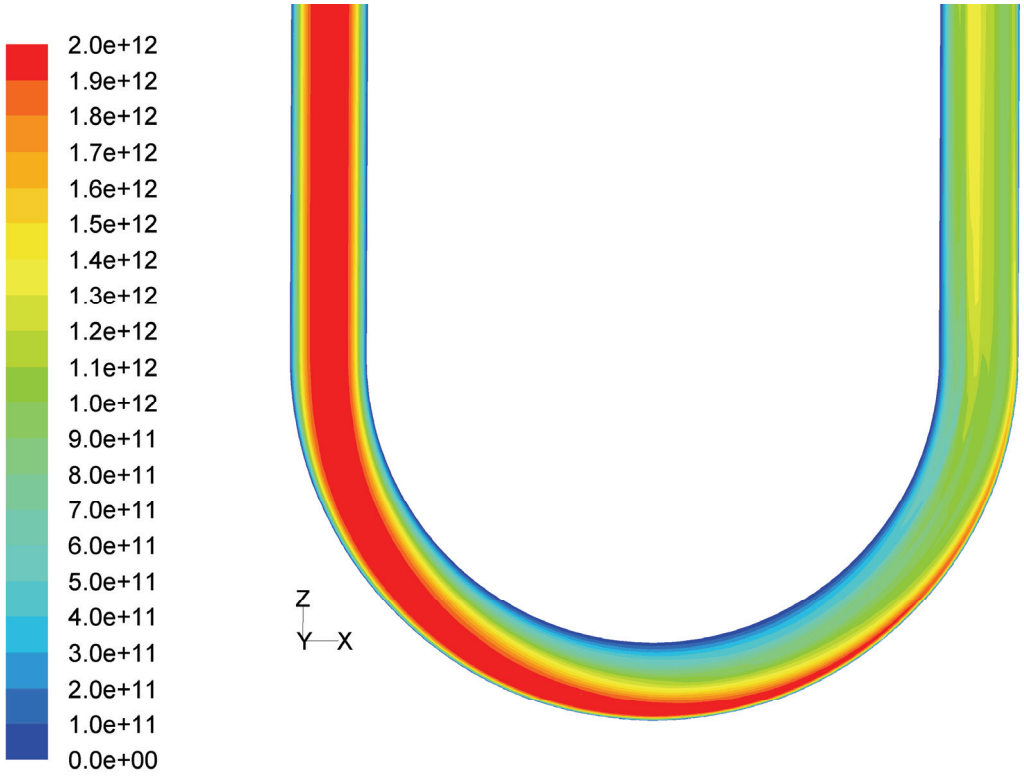

Figure 5.15: Contour plot of particle number concentration, $n = 2 \cdot 10^{12}$ #/m^3, in a bent aerosol deposition pipe for a 10 nm KCl particle. Particle number concentration in the xz-symmetry plane of the aerosol deposition pipe.

deposition. The observation in Figure 5.11, that for particles below about 40 nanometer, the experimental results start to deviate from the numerical results and show slightly higher deposition efficiency is believed to be due to additional contribution from uncharged particle being carried out through the sampling slit in the NDMA (which consist of an Aerosol Neutralizer and an Electrostatic Classifier) together with the desired positive charged particles.

In general the NDMA classifies the size of the particles due to their electrical mobility and because particles are being exposed to bipolar ions in the Aerosol Neutralizer in order to maximize the number of particles carrying single charge before entering the Electrostatic Classifier, particles with a very narrow range of electric mobility can be carried out through the sampling slit in the bottom of the Electrostatic Classifier and carried out with the sampling flow to the CPC, which then count the monodisperse aerosol from the sampling slit. The sampling flow from the Electrostatic Classifier then consists of singly charged particles of the desired particle size as well as double, triply and so on charged particles of

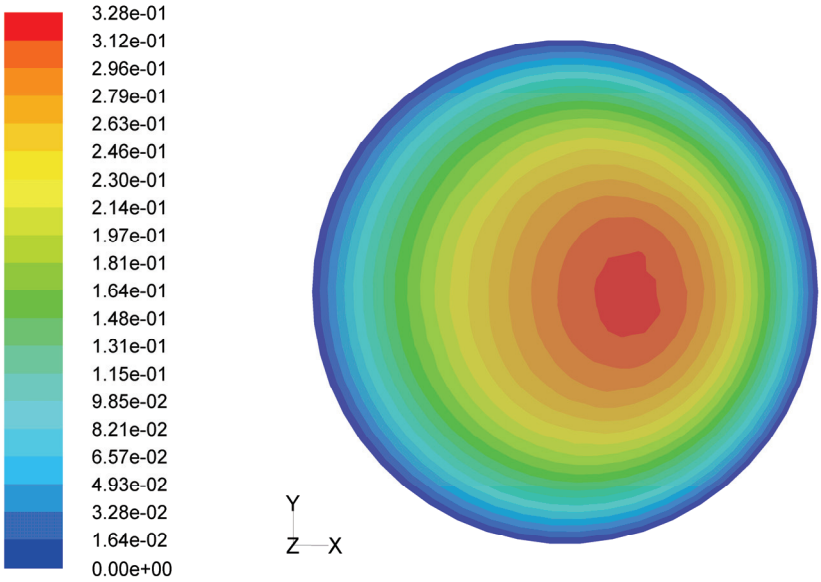

Figure 5.16: Contour plot of velocity magnitude in the plane perpendicular to the pipe axis at the outlet of the first bend (after the inlet).

correspondingly larger particle size [Knutson and Whitby (1975)]. Because the bipolar charge distribution on the particles is known the size distribution and number concentration can be determined. The problem is that when the particles become very small (e.g. below 40 nanometer) the fraction of particles that are uncharged is very high (see Table 1 or Table E.1) and at the same time these particles are also very diffusive. Therefore especially uncharged particles of sizes below the desired size classified by the NDMA will diffuse through the sampling slit and the monodisperse aerosol will then contain both the charged particles of the desired size and a fraction of uncharged particles especially of sizes below the desired size. When using the NDMA for selecting monodisperse aerosol particles and counting them at the top and bottom of the three-meter long aerosol deposition pipe the total particle number concentration counted by the CPC at the top contains charged particles at the desired size and a fraction of uncharged, smaller size and more diffusive particles. Because these particles are more diffusive than the desired size they will diffuse faster to the pipe wall and thereby increase the deposition efficiency. This is especially a problem when selecting particles of small particle diameter because the fraction of uncharged neutral particles are very high compared to the charged fraction of particles and therefore the deviation from the numerical results increases as the particle size become smaller.

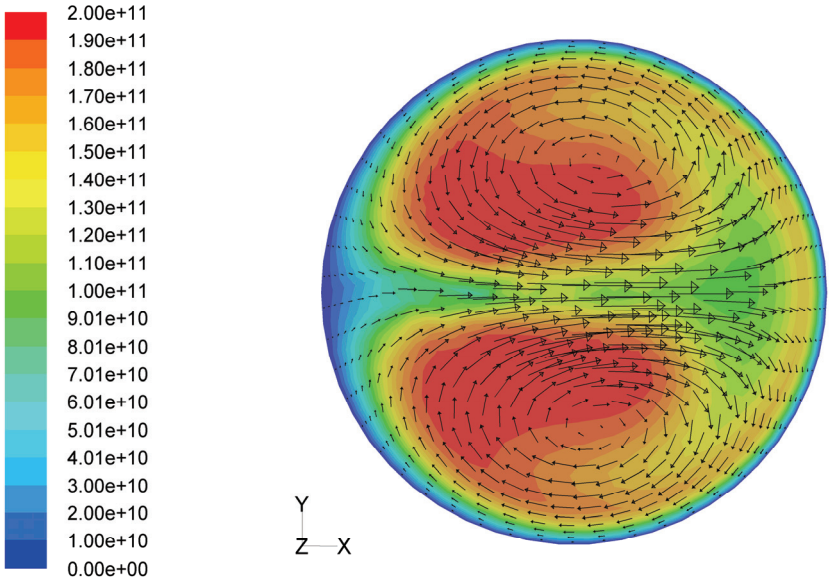

Figure 5.17: Contour plot of particle number concentration, $n = 2 \cdot 10^{12}$ #/m^3, in a bent aerosol deposition pipe for a 10 nm KCl particle. Particle number concentration in the plane perpendicular to the pipe axis at the outlet of the first bend (after the inlet).

In general Figure 5.11 and Figure 5.12 shows the importance of secondary flow in a bent pipe compared to a straight pipe without secondary flow, because the particle deposition is enhanced due to secondary flow which is superimposed on the main flow. The reason for this enhancement is that the secondary flow transports particles from the core of the pipe to the near-wall region where the particles are deposited due to Brownian diffusion. This importance is clearly seen from Figure 5.14 and Figure 5.15, where the particle number concentration for 10 nm particles in the first bend after the inlet is shown. The development of the particle diffusion boundary layer upstream of the bend and the thinning near the outer bend and the thickening near the inner bend due to the development of the secondary flow is clearly observed and the particle number concentration is therefore much lesser at the outlet of the first bent than the case would have been if only diffusion were taking place. Figure 5.14 also shows the development in the particle diffusion boundary layer through the other bends at the bottom of the aerosol deposition pipe and shows the importance of secondary flow.

The distortion of the magnitude of the velocity and the movement of the position of the maximum axial velocity toward the outer bend is clearly seen in Figure 5.16. The reason for this is the centrifugally induced pressure gradient that drives the slower moving fluid near the wall inward, while the faster moving fluid in the

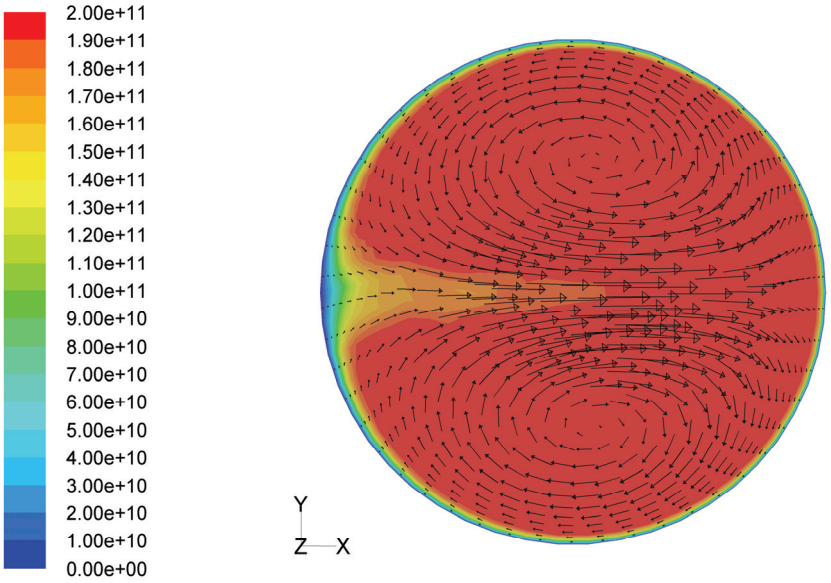

Figure 5.18: Contour plot of particle number concentration, n = 2·10^{12} [#/m^3], in a bent aerosol deposition pipe for a 100 nm KCl particle. Particle number concentration in the plane perpendicular to the pipe axis at the outlet of the first bend (after the inlet).

core is swept outward, i.e. slower-moving fluid particles have to move along paths whose radii of curvature are smaller than those of faster-moving, because the momentum balance between the centrifugal force and the pressure gradient has to be maintained. This lead to the onset of secondary flow whereby fluid near the wall moves toward the inner wall along upper and lower halves of the torus wall while fluid far from it flows to the outer wall and a pair of counter rotating helical vortices placed symmetrically with respect to the plane of symmetry is formed, as shown in Figure 5.17. Due to this, the position of the maximum axial velocity is moved toward the outer bend. The convective transport of more concentrated aerosol particles from the centre of the pipe, due to the secondary flow, to the vicinity of the pipe wall and thereby increasing the rate of diffusive deposition is clearly observed in Figure 5.17.

It can therefore be concluded that secondary flow is a very important mechanism in depositing small particles. This importance can be quantified by comparing the contour plots of the concentration field for the particle number concentration for 10 nm and 100 nm particles for the same secondary flow in the same cross section. It can be observed that the two counter rotating helical vortices placed symmetrically with respect to the plane of symmetry in both cases transport the particles to the near wall vicinity, but due to the fact that the effect of Brownian

diffusion on a 100 nm particle is much lesser than on a 10 nm particle the 100 nm particles will not have residence time enough to diffuse to the wall and will just be transported around in the secondary plane by convection due to the secondary flow. This effect for the 100 nm particle is clearly seen in Figure 5.18 because of the thin particle diffusion boundary layer and uniform particle number concentration field in the core of the pipe. In general the maximum enhancement of the deposition efficiency is about 15% point for a particle size about 10 nanometer and the relative effect of deposition due to secondary flow for the given pipe configuration is about 1/3 of the Brownian diffusivity.

5.1.3 Brownian Diffusion and Electrostatic Dispersion

Brownian diffusion and electrostatic dispersion has been modelled in CFD using both an Eulerian-Eulerian reference frame and an Eulerian-Lagrangian reference frame. In the Eulerian-Lagrangian reference frame 10.000 parcels of particles were tracked for each particle diameter. Two numerical test cases have therefore been carried out on the three-meter straight aerosol deposition pipe in order to validate the two different CFD models against each other. Figure 5.19 show a comparison between an Euler-Euler and an Euler-Lagrange simulation of the deposition efficiency due to pure electrostatic dispersion in a three-meter straight vertical pipe with a diameter of 6 mm. The average velocity in the pipe was 0.17 m/s and the particles were carrying one elementary charge. The Reynolds number, Re, based on the pipe diameter was 63 and the dynamic viscosity, μ, was $1.85 \cdot 10^{-5}$ Pa·s. The two simulations were compared with the empirical model from Alonso and Alguacil (2007), given in Equation (2.51) using the same data as for the CFD simulations where the penetration due to Brownian diffusion was set to one in order to have pure electrostatic dispersion. As it can be seen from Figure 5.19 the agreement between the Euler-Euler simulation and the Euler-Lagrange simulation is very good, whereas the empirical model from Alonso and Alguacil (2007) underpredicts the deposition efficiency a bit in the whole particle size range from 1 to 1000 nm. The reason for this can be due to the fact that the empirical model from Alonso and Alguacil (2007) is based on fully developed flow whereas the CFD simulations were done for developing flow and developing particle diffusion boundary layer. In general the deposition efficiency for developing flow is higher than for fully developed flow due to the entrance effects. This has been confirmed by Lin and Tsai (2003) who carried out numerical investigations of the entrance effect on the deposition efficiency of particles in laminar tube flow due to thermophoresis. They observed higher deposition efficiency from developing flow than from fully developed flow and concluded that both temperature and flow field should be developing in order for higher deposition efficiency to take place.

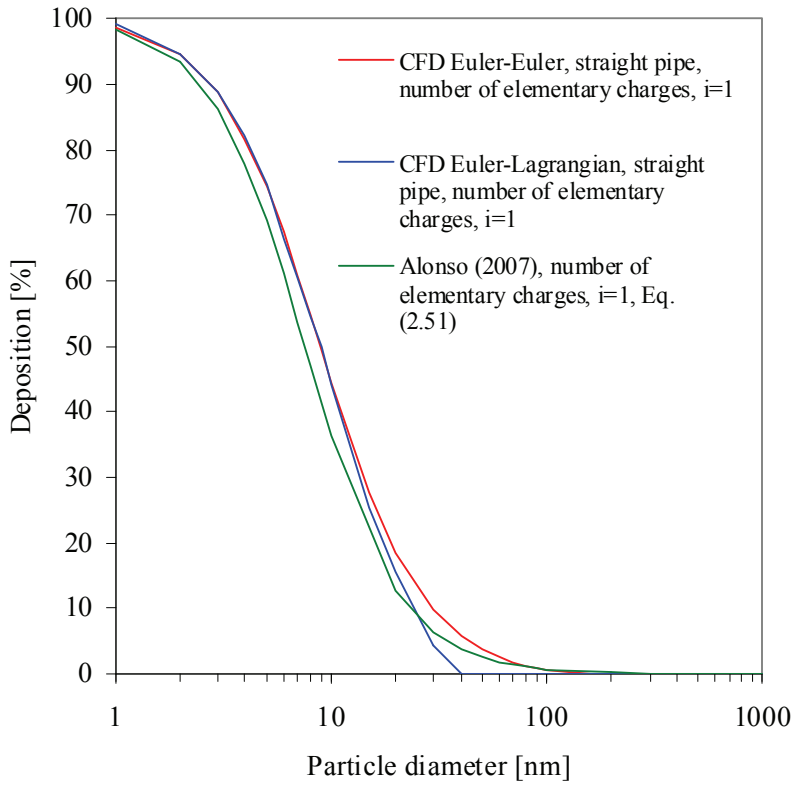

Figure 5.19: Deposition efficiency versus particle diameter for monodispersed KCl particles carrying one elementary charge, i=1, in a straight three-meter long aerosol deposition pipe. d_{pipe} = 6 mm. Flow Q = 300 ml/min, average velocity, u_{avg} = 0.17 m/s. Comparison between Euler-Euler and Euler-Lagrange simulation of pure electrostatic dispersion (no diffusion).Comparison with the empirical model Eq. (2.51) [Alonso and Alguacil (2007)]. Tracking 10.000 parcels of particles (for each particle diameter) stochastic distributed at the inlet of the deposition pipe as shown in Figure 4.10.

The reason for the higher deposition is the larger gradients due to the entrance effects in both the flow field and particle diffusion boundary layer. For low deposition efficiencies (below about 20%) some deviation between the Euler-Euler and the Euler-Lagrange simulation of the deposition efficiency can be observed. The reason for this is probably due to pure statistical representation of the number of particles hitting the wall in the Euler-Lagrange simulation, where only 10.000 parcels of particles were tracked.

Figure 5.20 show a comparison between an Euler-Euler and an Euler-Lagrange simulation of the deposition efficiency due to pure Brownian diffusion in a 3 meter straight vertical pipe. In the Eulerian-Lagrange simulation 10.000 parcels of

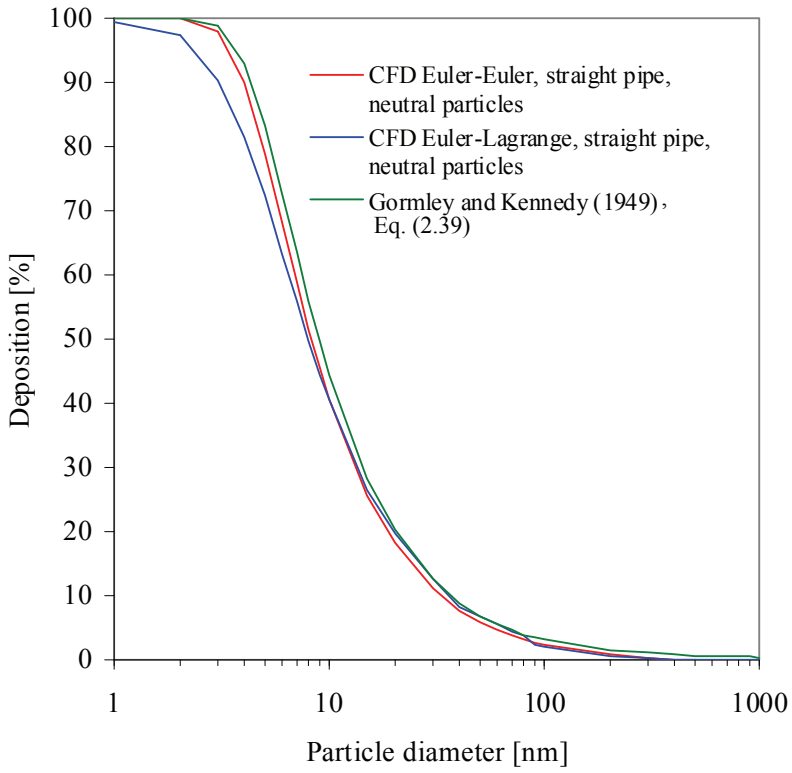

Figure 5.20: Deposition efficiency versus particle diameter for monodispersed neutral KCl particles, in a straight three-meter long aerosol deposition pipe. Pipe diameter, d_{pipe} = 6 mm. Flow, Q = 300 ml/min, average velocity, u_{avg} = 0.17 m/s. Comparison between Euler-Euler and Euler-Lagrange simulation of pure Brownian diffusion. Tracking 10.000 parcels of particles (for each particle diameter) stochastic distributed at the inlet of the deposition pipe as shown in Figure 4.10.

particles were tracked for each particle diameter. The physical data were the same as in the case with simulation of pure electrostatic dispersion shown in Figure 5.19.

The two simulations were compared with the analytic solution based on Gormley and Kennedy (1949), Equation (2.39) using the same data as for the CFD simulations. It can again be observed that the agreement between the Euler-Euler simulation and the Euler-Lagrange simulation is very good, whereas the analytic solution based on Gormley and Kennedy (1949) overpredict the deposition efficieny a little bit. But overall the agreement between CFD simulations and the analytic solution is very good. Based on the test cases it can be concluded that models using an Eulerian-Eulerian or an Eulerian-Lagrangian reference frame,

respectively predicts the same deposition efficiency and agree well with empirical and analytical models from the literature.

5.2 Experimental Results of Micrometer Particle Deposition

Measurements of monodisperse micrometer particle (10, 20, 30 and 40 μm, respectively) deposition efficiency due to shear-induced lift (Saffman lift) and inertial impaction in a bend and a vertical straight pipe with a length of 1.0 m and a diameter of 6 mm has been carried out. Figure 3.5 shows a schematic illustration of the experimental setup. The experimental setup consisted of a particle filter, a flow regulator, a Palas RBG-2000 Powder Disperser, a 0.10 meter bend, a one-meter deposition pipe, a container, a high efficiency filter, a valve and a flow meter. The Powder Disperser contained monodisperse cross-linked PMMA particles (respectively 10, 20, 30 and 40 μm) as compacted powder in a cylindrical container. The flow rate was set to 3.4 l/min corresponding to a Reynolds number of about 760 and an average velocity of 2 m/s.

Figure 5.21 shows the experimental results of particle deposition due to inertial impaction and shear-induced lift for 10, 20, 30 and 40 μm cross-linked PMMA particles, respectively versus particle diameter in a vertical straight one-meter long deposition pipe with a diameter of 6 mm and with gravity in the direction of the flow. Shear-induced lift is a mechanism that in shear flow migrate a particle in the normal direction compared to the flow direction. If the flow direction is in the same direction as gravity and the density of the particle is greater than the fluid the particle velocity will be faster than the fluid velocity and the particle will migrate towards the wall. If the flow direction is opposite of gravity and the density of the particle is greater than the fluid the particle velocity will be slower than the fluid velocity and the particle will migrate towards the centre of the pipe. From Figure 5.21 it can be observed that the combined deposition efficiency of the bend and pipe due to inertial impaction and shear-induced lift is an increasing function of particle diameter up to 30 μm where it has a maximum. For 40 μm particles the deposition efficiency is decreasing. The reason for this is the particle inertia which is becoming important and particles impinging the wall in the bend will bounce and be re-suspended in the flow. Another reason for this is also that the particles are becoming so big that the gravity and fluid dynamic forces on the particles impinging the wall in the vertical pipe are so large that they overcome the adhesive van der Waals forces. Particles will therefore slide down the wall or be detached and re-suspended. It can also be observed from Figure 5.21 that the deposition efficiency due to shear-induced lift is increasing with particle diameter

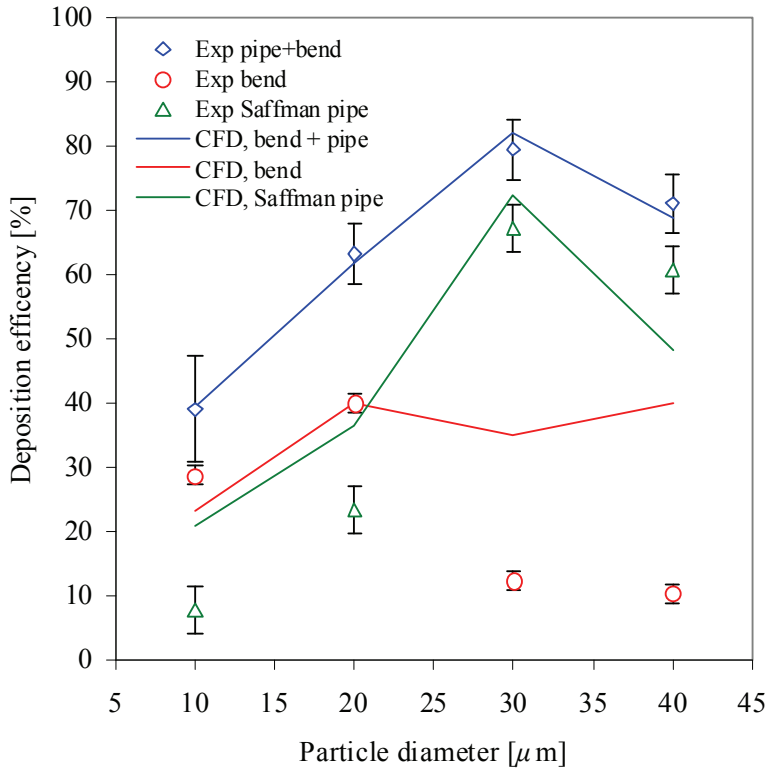

Figure 5.21: Experimental result of particle deposition efficiency for 10, 20, 30 and 40 μm, respectively in a one-meter vertical straight pipe due to inertial impact and shear-induced lift versus particle diameter. CFD results of developing flow in a one-meter vertical straight pipe. Tracking 100.000 parcels of particles (for each particle diameter) stochastic distributed at the inlet of the deposition pipe as shown in Figure 4.10.

up to 30 μm where there is a maximum because gravity and fluid dynamic forces on the particles impinging the wall in the vertical pipe are so large that they overcome the adhesive van der Waals forces and particles will therefore either slide down the wall or be detached and re-suspended.

From Figure 5.21 it is further observed that the deposition efficiency in the bend alone due to inertial impaction is an increasing function of particle diameter with a maximum at 20 μm where particle inertia starts becoming important. The reason for this is that particle inertia is becoming important and particles impinging the wall of the bend will bounce and be re-suspended in the flow. The Stokes numbers, *Stk*, for the bend is shown in Table 14, calculated based on Equation (2.12).

Table 14: Stokes number for 10, 20, 30 and 40 micrometer cross-linked PMMA particles in bend. Average velocity in bend, U_{avg} = 2, density of particle, ρ_p = 1200 kg/m^3, radius of pipe, R_{pipe} = 3 mm and dynamic viscosity, $\mu = 1.85 \cdot 10^{-5}$ Pa·s.

Particle diameter [μm]	Stokes number *Stk*
10	0.24
20	0.96
30	2.16
40	3.84

As it can be seen from Table 14, *Stk* = 0.24 for a 10 μm particle which means that not all the particles will follow the streamlines perfectly but continue in straight lines when these are curved and therefore impact and adhere to the wall of the bend. For 20 μm particles the *Stk* = 0.96, for 30 μm particles *Stk* = 2.16 and for 40 μm particles *Stk* = 3.84 and inertial impaction becomes more dominating for increasing particle diameter. From Figure 5.21 it can be observed that the total deposition efficiency for the bend and pipe is about 40% for 10 micrometer particles and most of the deposition is due to inertial impaction which contributes with about 29% of the mass. For the about 70% of the 10 micrometer particles penetrating the bend only about 8% of these are deposited due to Saffman lift. For 20 μm particles the total deposition efficiency is about 64% and inertial impact is responsible for about 40% of the deposition whereas Saffman lift is responsible for about 23%. For 30 μm particles the overall deposition efficiency is about 80% and it can be observed that inertial impaction only is responsible for about 12% due to increased bouncing. Saffman lift is responsible for about 67% and it can be observed that this is the maximum measured value of the deposition efficiency due to Saffman lift. For larger particles e.g. 40 micrometer the deposition efficiency due to Saffman lift is about 61%. The overall deposition efficiency is about 71% and the deposition efficiency due to inertial impaction is only about 10%.

The particle-wall interaction model implemented in CFD and described in section 4.5 was validated against the experimental data in Figure 5.21 by fitting the asperities, z_0, for the four different particle diameters in order to obtain the overall deposition efficiency. The particles in the simulations were assumed to be neutral, because the real charge distribution was not known and the contribution from electrostatic forces when calculating the critical particle velocity for adhesion was neglected. 100.000 parcels of particles were tracked for each particle diameter.

Table 15: The asperities, z_0 used in the particle-wall interaction model in order to obtain the deposition efficiency curves shown in Figure 5.21.

Particle diameter [μm]	Asperities, z_0 [m]
10	$2.300 \cdot 10^{-10}$
20	$2.620 \cdot 10^{-10}$
30	$1.276 \cdot 10^{-10}$
40	$8.165 \cdot 10^{-11}$

The average velocity in the pipe was 2 m/s and the dynamic viscosity of the fluid was $1.85 \cdot 10^{-5}$ Pa·s. As it can be observed from Figure 5.21 agreement with the overall efficiency is very well as well as the deposition efficiency for 10 and 20 micrometer particles due to inertial impaction. For 10 and 20 μm particles the deposition efficiency due to Saffman lift is overpredicted but for 30 and 40 μm particles the deposition efficiency due to Saffman lift agrees very well with the experimental results. For 30 and 40 μm particles the model underpredicted the deposition efficiency due to inertial impaction. The differences between the experimental results and the CFD model is believe to be due to differences between the CFD model of the bend (which was modelled as a perfect 90-degree bend with a radius of 2.4 mm and a straight piece in order to have a total length of 0.1 m) and the bend in the experiments which consisted of a 0.1 m silicone pipe connecting the horizontal outlet from the powder disperser with the vertical deposition pipe. The different asperities used in the model are given in Table 15. In general it can be concluded that the particle-wall interaction model predicts the trends in the experimental results for both the overall deposition efficiency as well as the deposition efficiency due to inertial impaction and Saffman lift force.

Figure 5.22 shows a comparison between experimental results and CFD simulations of developing flow in a vertical one-meter long deposition pipe with a diameter of 6 mm. Calculation of the same situation based on the analytical expression for deposition due to Saffman lift based on Lipatov et al. (1989) given in Equation (2.50) and the deposition efficiency given in Equation (2.49) has also been compared. Particles were stochastic distributed at the inlet and the inlet velocity was assumed uniform in order for the flow to develop and the wall was treated as a perfect adhering wall. This is a rough assumption, because in real the flow would also be rotating because of the bend upstream of the inlet to the pipe and the particles will develop a concentration profile through the bend and not be completely uniform distributed as well as the pipe wall is not perfect adhering. But in the experimental setup the rotation of the flow and the bouncing from the

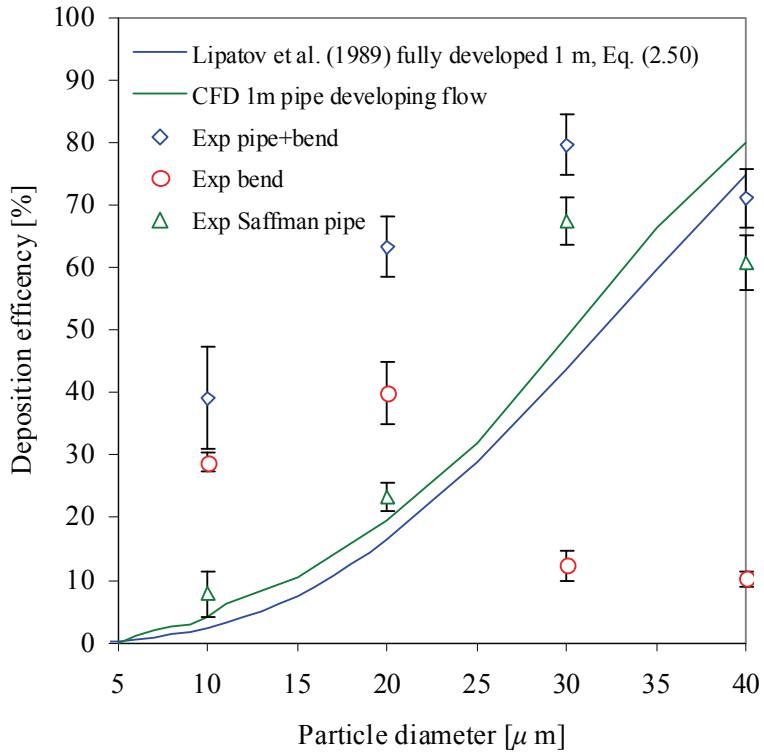

Figure 5.22: Experimental result of particle deposition efficiency for 10, 20, 30 and 40 μm, respectively in a one-meter vertical straight pipe due to inertial impact and shear-induced lift versus particle diameter. CFD results of developing flow in a one-meter vertical straight pipe tracking 100.000 particles and calculation of the Saffman deposition efficiency, Eq. (2.50) based on Lipatov et al. (1989) for developing flow in a vertical straight pipe.

wall in the bend will help in redistributing the particles in the inlet of the pipe to become more uniform distributed. It can therefore be observed from Figure 5.22 that the agreement between the experimental result of deposition due to Saffman lift and the simulation of developing flow and particle concentration profile is very well.

The comparison with the simple pseudo steady-state model based on Lipatov et al. (1989) gives also very good agreement. It can also be observed that due to the assumption of perfect adhering walls the CFD simulations and the simple model does not capture the maximum in deposition efficiency for 30 μm particles. It can also be observed that for larger particles above 30 μm that the deviation between the CFD simulation and the pseudo steady-state model gets larger because

acceleration of the particles becomes important. Therefore for larger particles the pseudo steady-state assumption is a crude assumption. Based on the experimental investigations it can be concluded that Saffman lift force is an important mechanism for deposition of micrometer particles. It is a mechanism that will be important in deposition and plugging of the channels in monolithic catalysts, especially downstream in the channels after the flow have gone into transition from turbulent to laminar flow where Saffman, for uncharged particles, is the only mechanism responsible for deposition.

5.3 Pilot Scale Experimental Results

Pilot scale potassium chloride (KCl) aerosol particle plugging experiments using commercial corrugated-type SCR monolithic catalysts obtained from Haldor Topsøe A/S have been carried out. The monolithic catalysts used in the tests were DNX x30 and DNX x80, respectively and were dummies in the sense that they consisted only of a corrugated, fibre-reinforced titanium dioxide (TiO_2) carrier and were not impregnated by divanadium pentaoxide (V_2O_5) and wolfram (tungsten) trioxide (WO_3). The sizes of the monolithic catalysts were 7.5×7.5×50 cm and the weight of the DNX x30 was about 528 g and the weight of the DNX x80 was about 595 g. Figure 3.7 shows a schematic illustration of the SCR pilot plant used for the plugging test of the monolithic catalysts and Figure 3.8 shows the DNX x30 and DNX x80 monolithic catalyst, respectively. The pilot plant consisted of a 50 kW natural gas burner, a water cooled lance for injecting liquid solutions for generating aerosol particles, a square duct (SCR reactor) hosting a full length commercial monolith, a soot blowing system, two different heat exchangers and two 100 litre containers for the liquid 0.1 M KCl solution.

Zheng et al. (2008) carried out impactor measurements of KCl aerosol particle mass size distribution in the pilot plant above the monolithic catalyst where the aerosol particles were generated based on a 0.5 M KCl liquid solution. These measurements showed that the KCl particle mass size distribution mainly consisted of particles between 0.1 to 1 μm. The pilot scale experiments therefore mainly consisted of particle sizes of the same order as corresponding to what is expected in low-dust applications. In the case of low-dust applications (after the electrostatic precipitator) the flue gas mainly contains particles between about 0.1 to 1 μm due to the low particle removal efficiency of the electrostatic precipitator in the diffusion impaction regime between 0.1 to 1 μm [Flagan and Seinfeld (1988), p. 425]. The KCl aerosol particles used for plugging the monolithic catalysts in the present experiments were generated by injecting a 0.1 M KCl solution in the flue gas. In order to use a realistic mass size distribution of KCl

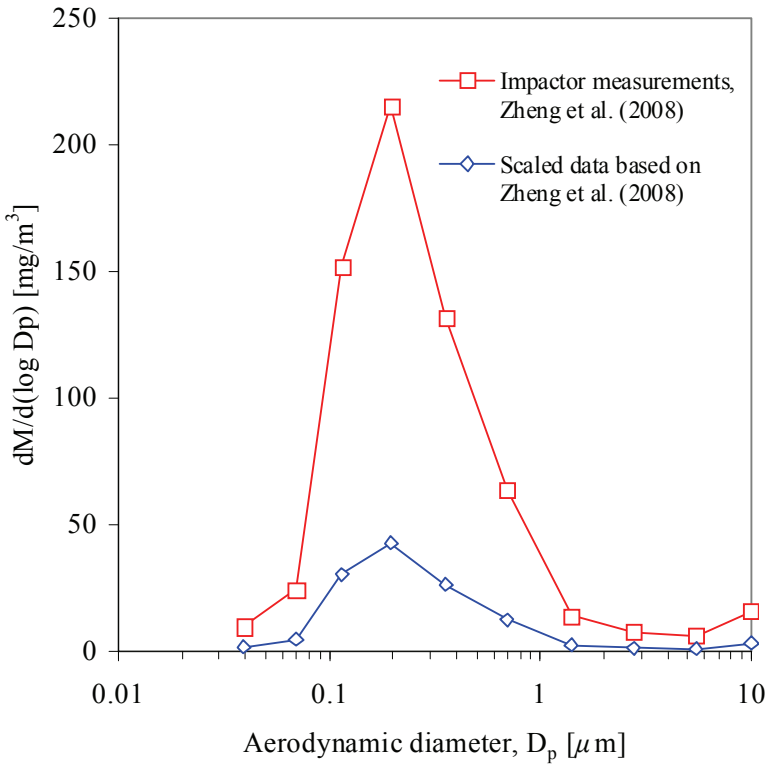

Figure 5.23: KCl aerosol particle mass size distribution in the Pilot plant. The KCl aerosol particles were generated by injecting 0.1 M KCl solution in the flue gas. The particle size distribution was based on a linear scaling (from 0.5 M KCl to 0.1 M KCl) of the impactor measurements carried out by Zheng et al. (2008) for a 0.5 M KCl solution.

aerosol particles in the CFD simulations the KCl aerosol particle mass size distribution measured by Zheng et al. (2008) was linear scaled by a factor of 5 from a 0.5 M KCl solution to a 0.1 M KCl solution in order to obtain an approximation of the mass size distribution in the pilot scale experiments.

The mass size distribution measured by Zheng et al. (2008) above the monolithic catalyst in the pilot plant and the linearly scaled mass size distribution based on a 0.1 M KCl solution is shown in Figure 5.23. It can be argued that generating the aerosol particles based on a 0.1 M KCl solution would shift the size distribution to the left in Figure 5.23 giving aerosol particles with a smaller particle diameter because the mass of KCl in the droplets generated are 5 times smaller than the mass in the droplets generated based on a 0.5 M KCl solution. This would then create primary particles with a diameter, which is about 1.7 ($D_{p,0.1M\ KCL} \approx D_{p,0.5M\ KCL} / \sqrt[3]{5} = D_{p,0.1M\ KCL} / 1.7$) times smaller than the primary particles generated in the experiments of Zheng et al. (2008). However, the size

distribution above the monolithic catalyst consisted of agglomerates of primary particles and how this size distribution would change due to the diameter change in the primary particles has been neglected in the CFD simulations.

5.3.1 Catalyst with 3 mm Hydraulic Diameter

DNX x30 SCR monolithic catalysts (dummies) with a hydraulic diameter of 3.4 mm were exposed to KCl particles over time for 0-24, 0-48, 0-78, 0-120 and 0-158 hours. For each of the experiments with different exposure time a new catalyst was used. The KCl aerosol particles in the pilot plant were generated using a 0.1 M KCl liquid solution. The deposited mass of KCl aerosol particles in the monolithic catalysts was determined by washing the monoliths after each experiment in ultra pure water. In order to determine the axial deposition profile the monoliths were also cuts in 6 pieces (0-1 cm, 1-10 cm, 10-20 cm, 20-30 cm, 30-40 cm and 40-50 cm). Each piece was washed in 4 or 5 l of ultra pure water and 50 ml samples were taken and sent to analysis for detecting the weight per cent of potassium, K, in the samples. The total amount of KCl aerosol particles deposited in the monolithic catalysts was then estimated based on the equimolar ratio of K and Cl in the KCl molecule. The injected mass flow of KCl into the pilot plant was about $8.22 \cdot 10^{-7}$ kg/s. The mass flow of KCl particles in the flue gas flow above the monolithic catalyst was about $2.1 \cdot 10^{-7}$ kg/s. This mass flow was calculated assuming a linear relation between the mass flow injected into the setup and that above the monolithic catalyst using the linear scaled particle size distribution measured by Zheng et al. (2008) for a 0.5 M KCl solution. The calculated particle size distribution is shown in Figure 5.23. The overall loss of KCl aerosol particles from the point of injecting the KCl solution into the pilot plant and up to the SCR reactor hosting the monolithic catalyst was about 26%.

The influence of electrostatic forces in the pilot plant was investigated by measuring the average number of elementary charges, i, measured on the KCl aerosol particles in the pilot plant using an Electrometer. The average number of elementary charges, i, was, $i = 0.001$ and the KCl aerosol particles were thus carrying a positive average charge.

The experiments with exposure to KCl particles over time for 0-24, 0-48, 0-120 and 0-158 hours were carried out using an old heat exchanger in the pilot plant. The experiment with 0-78 hours of exposure to KCl particles was the last experiment carried out in the present Ph.D. study and just before this experiment the pilot plant was totally cleaned and a new heat exchanger was installed due to corrosion of the old one. The new heat exchanger gave less pressure loss due to

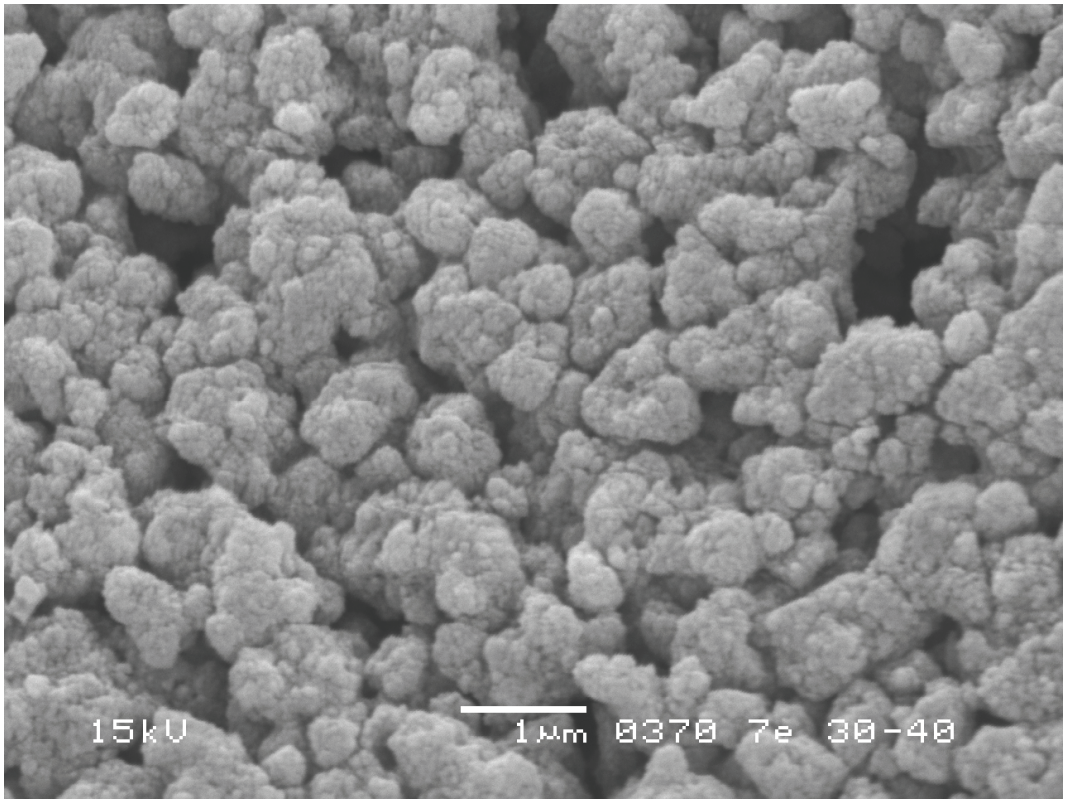

Figure 5.24: SEM image of KCl after 120 hours of exposure. Position 30-40 cm downstream in the axial length of the DNX x30 monolithic catalyst.

less plugging compared to the old one and therefore fewer KCl particles were deposited in the new heat exchanger reducing the particle loss upstream the monolithic catalyst. This probably created a higher particle load upstream the monolith (less loss through the channels of the pilot plant downstream the injection point of the KCl solution) during the 78 hours experiment compared to the earlier experiments.

5.3.1.1 Qualitative Discussion of Experimental Results

Based on the KCl aerosol particle mass size distribution measured by Zheng et al. (2008) it was shown that the particle mass size distribution in the pilot plant mainly consisted of particles between 0.1 to 1 μm. It is therefore believed that the particle mass size distribution and the plugging pattern obtained in the pilot scale experiments correspond to what is expected in low-dust applications. Figure 5.24 and Figure 5.25 shows SEM pictures of the KCl aerosol particle deposition on the outer surface of the monolithic catalyst after 120 hours of exposure to KCl

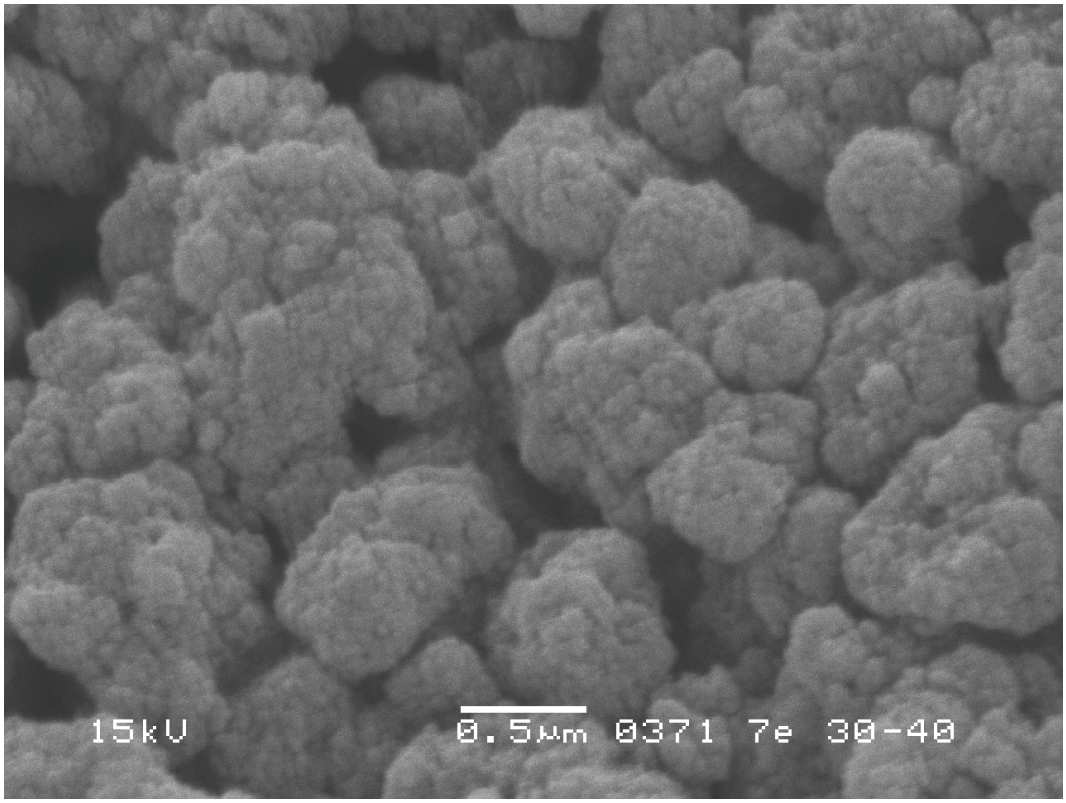

Figure 5.25: SEM image of KCl after 120 hours of exposure. Position 30-40 cm downstream in the axial length of the DNX x30 monolithic catalyst.

particles. The position of the SEM pictures is 30-40 cm downstream in the axial length of the DNX x30 monolith catalyst. Figure 5.24 shows particle sizes which are in the order of 1 μm and consist of agglomerates of primary particles. Figure 5.25 is a close-up of the particles in Figure 5.24 and shows particles of the order of 0.5 μm which again consist of agglomerates of primary particles. The SEM pictures therefore confirm that the pilot scale experiments mainly consisted of particles between 0.1 to 1 μm and the deposition pattern observed in the pilot scale experiments correspond to low-dust applications. It is therefore also believed that the deposition mechanisms explaining these deposition patterns in the pilot scale experiments also explain the deposition patterns observed in full-scale low-dust applications.

Figure 5.26 shows the experimental obtained plugging due to KCl particles after 24, 48, 78, 120 and 158 hours of exposure, respectively. The increased mass deposition is clearly seen from the pictures for increased exposure time to KCl particles. The observed deposition pattern is a ”volcano type” of deposition which is characteristic for low-dust applications.

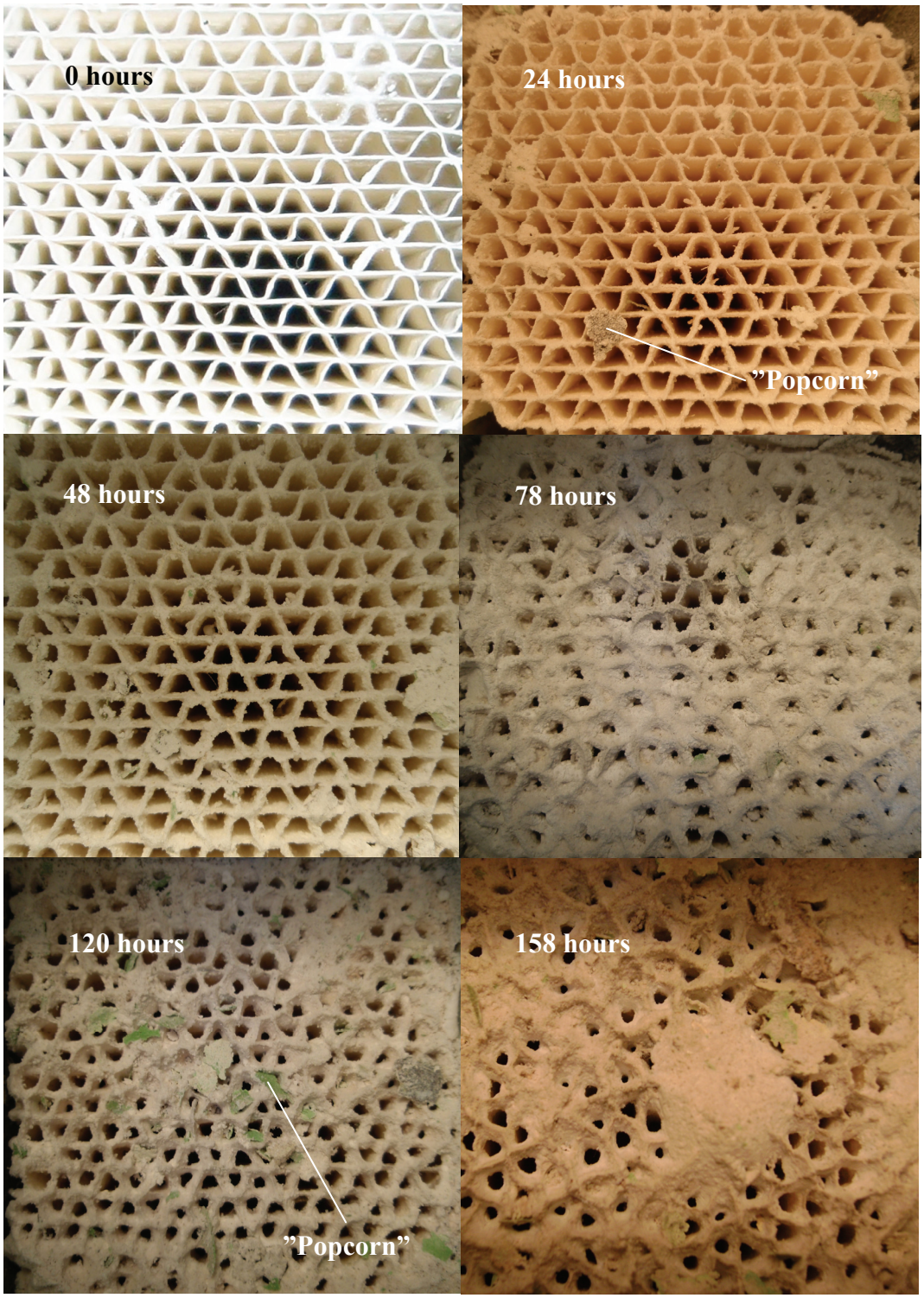

Figure 5.26: Plugging of SCR DNX x30 monolithic catalysts due to KCl particles after 24, 48, 120, and 158 hours of exposure.

For the first 24 and 48 hours of exposure to KCl particles the deposit does not really change the geometry of the monolith very much and there is no influence from the depositon on the flow field which is constant (steady-state) in average over time. At longer exposure time the inlet becomes more streamlined and the flow stagnation area on top of the monolithic catalyst decreases as well as the sharp corners in the channels due to deposition of KCl particles. From Figure 5.26 it can also be observed that that there are areas where the channels in the monolithic catalyst are totally plugged due to deposition of small fragments of agglomerates ("popcorn") on top of the catalyst during the experiments. This was perhaps the most important problem during the experiments where these fragments were formed when deposit onto the walls broke off upstream of the catalyst. These fragments then initiate channel plugging and accelerated deposition on top of the catalyst. "Popcorn" particles can be observed on Figure 5.26 e.g. after 24 hours and 48 hours of exposure time and the results of total channel plugging due to these "popcorn" can be identified after e.g. 78, 120 and 158 hours of exposure. It can also be observed from Figure 5.26 for example after 120 hours of exposure that some of the "popcorns" are green. These "popcorns" are agglomerates of old deposit from earlier experiments carried out in the pilot plant during a previous Ph.D. study with the purpose of investigating deactivation of SCR catalysts by additives [Castellino (2008)]. These agglomerates consisted of polyphosphoric acid and even though the pilot plant was cleaned several times and every time before start up of a new plugging experiment these agglomerates of polyphosphoric acid were very difficult to avoid.

Figure 5.27 shows the deposition pattern from a full-scale low-dust application from a waste incineration plant in Brussels where the same type of "volcano" deposition pattern as obtained in the pilot scale experiments (Figure 5.26) is clearly observed. This "volcano type" of deposition is very different from the deposition pattern obtained in high-dust applications as seen from Figure 1.5 which shows plugging of channels in a monolithic catalyst, DNX 664 (hydraulic diameter is 6.4 mm) from Nordjyllandsværket. The reason for the very different deposition pattern observed between high-dust and low-dust applications is due to different size distributions of the fly ash particles. High-dust applications usually contains larger micrometer size particles (fly ash particles larger than 20 μm) with high inertia which also have a positive influence on the deposition because they can have a cleaning effect on the monolithic catalysts by detachment and re-suspension of already deposited particles [Thorhauge (2004)]. The reason for this is that the impact of particles with high level of kinetic energy can/may overcome the attractive forces of already deposited particles. Therefore, this "volcano type" of deposition on top of the monolithic catalysts will not be seen, because it will be eroded (removed by larger particles). Figure 5.28 schematically illustrates the

Figure 5.27: Low dust application. Example of "volcano type" of deposition in a waste incineration plant from Brussels after 15,000 to 20,000 hours of operation. Hydraulic diameter about 3.4 mm. Courtesy Topsøe.

"volcano type" deposition pattern observed in the experimental measurements and observed in full-scale low-dust applications as shown in Figure 5.26 and Figure 5.27.

Figure 5.28 illustrates the turbulent flow upstream the monolithic catalyst and turbulent eddies which are convected into the monolithic channels. Turbulent diffusion is therefore expected to be the dominating deposition mechanism in the top part of the monolithic channels and the influence of the Reynolds number is also expected to be important on the deposition mass flow. CFD simulations and calculations with a simple empirical and analytical deposition model also confirm that turbulent flow and turbulent particle diffusion are responsible for most of the plugging measured in the pilot scale experiments.

A qualitative description of the obtained "volcano type" of deposition pattern is given as follows: initially (clean catalyst) the particle deposition in the flow stagnation area (zero velocity aera) on the top of the monolithic catalyst is

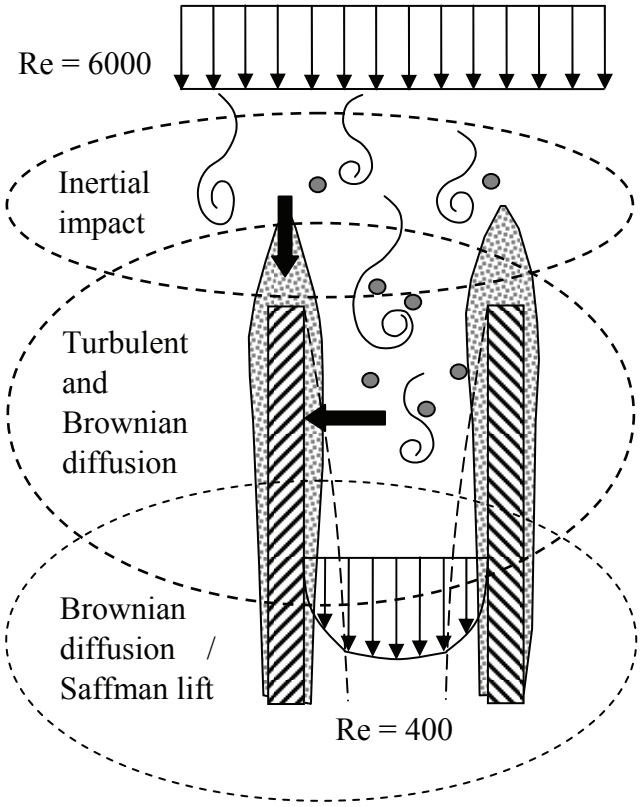

Figure 5.28: Schematic illustration of "volcano type" of deposition with possible deposition mechanisms based on the pilot scale experiments. Ellipsis with the red dashed line indicates the most important deposition mechanisms. Blue dashed line indicates viscous boundary layer.

expected to be due to Brownian and turbulent diffusion, inertial impaction, gravitation settling, and electrostatic forces and these mechanisms are constant over time in average as long as the flow pattern is unchanged. In the channels of the monolith deposition are due to Brownian and turbulent diffusion, Saffman lift and electrostatic forces which also in average are constant over time in steady-state flow. For the first 24 and 48 hours of exposure to KCl particles the deposit does not really change the geometry of the monolith very much and there is no influence from the depositon on the flow field which therefore is constant. This can be observed from Figure 5.26.

At longer exposure time the inlet becomes more streamlined and the flow stagnation area on top of the monolithic catalyst decreases as well as the sharp corners in the channels due to deposition of KCl particles. Therefore, the hydraulic diameter measured at the inlet of the channels in the monolithic

catalysts becomes smaller due to deposition and the deposit now begins to influence the flow field over time which again increases the inlet velocity. This deposit based streamlining of the inlet and reduction of the sharp corners in the channels creates more circular inlet channels in the monolithic catalysts with higher inlet velocity which again increases the Reynolds number in the top part of the monolith (inlet section of channels) more than further downstream in the axial length of the monolithic channels where less particles have deposited and the influence on the flow field is less. The deposition efficiency due to turbulent diffusion in the entrance length is therefore expected to increase due to the increased inlet velocity. The deposition efficiency due to inertial impaction and gravitational settling in the flow stagnation area on the top of the monolith is expected to decrease because of the streamlining and deposition of KCl particles on the top of the catalyst, after long exposure time, is then expected to be more controlled by Brownian and turbulent diffusion. Brownian and turbulent diffusion is therefore expected to increase because of the increased surface area on top of the monolith due to the streamlining. The increased deposition on top of the catalyst and in the entrance length also increases the surface roughness in this area which then again is expected to increase the deposition efficiency. After long exposure times (158 hours or longer) an increase in particle detachment and re-entrainment at the inlet might be expected due to increased surface shear stresses from the increased inlet velocity. The increased inlet velocity then might be expected to overcome the attractive forces of already deposited particles by increasing the shear and lift forces on the deposited particles and therefore prevent further increase in deposition mass flow due to decreased hydraulic diameter at the entrance length. Equilibrium between particle deposition and particle detachment and re-entrainment might therefore be expected at very long exposure times.

The increased deposition due to increased surface roughness has been confirmed e.g. by Li and Ahmadi (1993b) who made computer simulation of deposition of particles in a turbulent channel flow with rough walls. They explained how the increase of wall roughness increased the number of deposited particles due to increased turbulent intensity with increased roughness. They explained that the increase of roughness increased the particle capture distance from the wall and that the turbulent fluctuations remained finite at the tip of the roughness (for a smooth wall they would be zero at the wall) thereby causing the turbulent dispersion to be more efficient. They stated that as the roughness increased the turbulent eddy impaction process became the dominating mechanism for deposition even for relatively small particles and as a result the deposition velocity remained constant at high roughness for particles less than 2 μm.

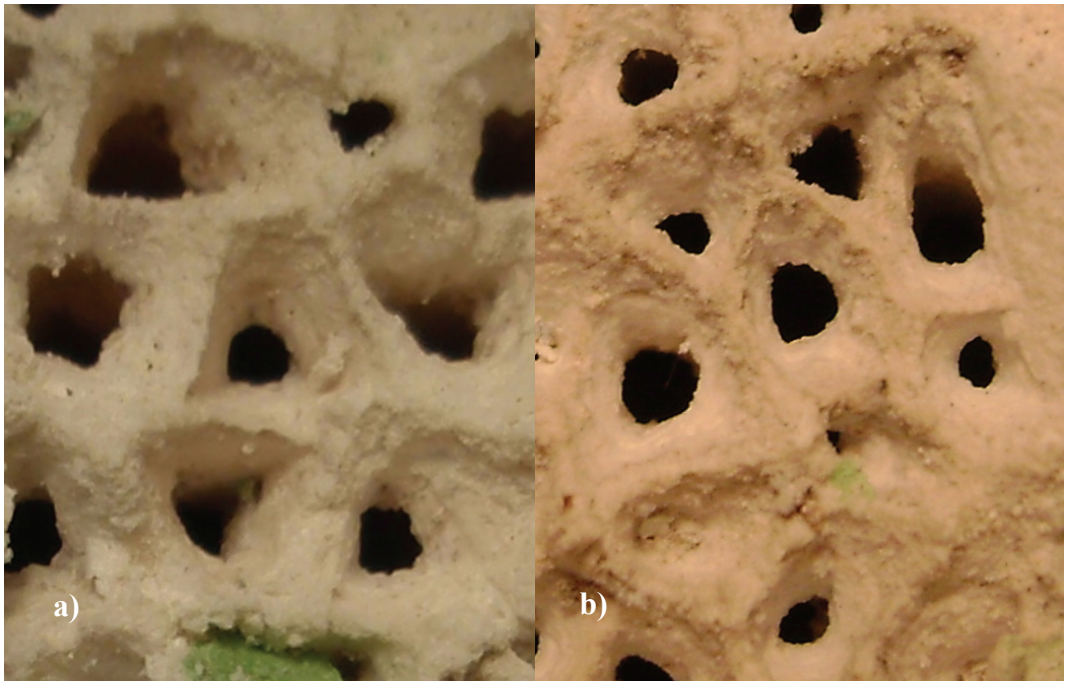

Figure 5.29: Close-up of of the deposit on the top of the Topsøe DNX x30 monolithic catalyst ("sinus" shape) after a) 120 hours and b) 158 hours of exposure to KCl particles, respectively.

The influence of increased Reynolds number on the number of deposited particles has been confirmed by Abuzeid et al. (1991) who numerically studied dispersion of small particles suspended in a turbulent channel flow and the effect of the Reynolds number on the wall deposition.

Abuzeid et al. (1991) found that an increasing Reynolds number increased the deposition rate and they explained this to be caused by an increasing fluctuating turbulence kinetic energy in the flow. The Reynolds number based on the hydraulic diameter in the DNX x30 monolithic catalysts in the pilot scale experiments was about 400 and the flow in the pilot plant channel upstream the catalyst was about 6000 and was therefore fully turbulent. Calculations based on Langhaar (1942) showed that the transition length from turbulent to laminar flow in the channels of the monolithic catalyst is about half the channel length (≈ 25 cm). Turbulent eddies up to the size of the diameter of the monolithic channels would therefore be convected into the channels and dominate deposition in the entrance length (about half of the axial length) of the monolith. In the entrance length of the channels turbulent eddies would be expected to penetrate into the viscous boundary layer and increase mass deposition as illustrated in Figure 5.28.

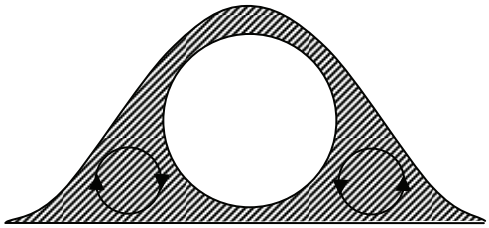

Figure 5.30: Schematic illustration of deposition in a Topsøe monolithic catalyst ("sinus" shape) and flow optimization against a cylindrical channel.

Figure 5.29 shows a close-up of the deposit on the top of the Topsøe DNX x30 monolithic catalyst ("sinus" shape) after a) 120 hours and b) 158 hours of exposure to KCl particles, respectively. It can be observed from these pictures how the flow and KCl particle deposition in the monolithic catalyst "tries to optimize" the flow geometry to obtain more cylindrical channels. This can also be observed from Figure 5.26 where it is clearly seen, from the flow field, that it tries to optimize the shape of the monolithic catalyst by reducing the pressure loss (wall shear stress) through the monolithic channels by filling op the corners with deposit in order to obtain more cylindrical channels through the monolith. Figure 5.30 shows a schematic illustration of the deposition in a Topsøe monolithic catalyst ("sinus" shape) and flow optimization against a cylindrical channel. The reason for the cylindrical channel shape is that it has a minimum surface area with respect to the volume when compared to other types of channel geometries with the same cross-sectional area and thereby a minimum friction compared to the same volume flow.

Figure 5.31 shows a schematic illustration of the three-dimensional development of the velocity profile and boundary layer in a monolith channel. Figure 5.32 shows a two-dimensional schematic illustration of the three-dimensional boundary layer illustrated in Figure 5.31. Figure 5.31 and Figure 5.32 can be used to give a qualitative description of the mechanism which is believed to be responsible for the deposit build-up in the corners of the monolith. The mechanism is the following: when the flow due to entrance effects develops from the inlet region down through the channels, as schematically illustrated in Figure 5.31, and a boundary layer therefore builds up there will be a transport of fluid (mass flow) into the boundary layer, because the boundary layer grow in thickness in the axial direction of the monolith until it is fully developed (this is illustrated schematically for a two-dimensional boundary layer in Figure 5.32). Because the boundary layer is growing in the entrance length of the monolith the flow is not

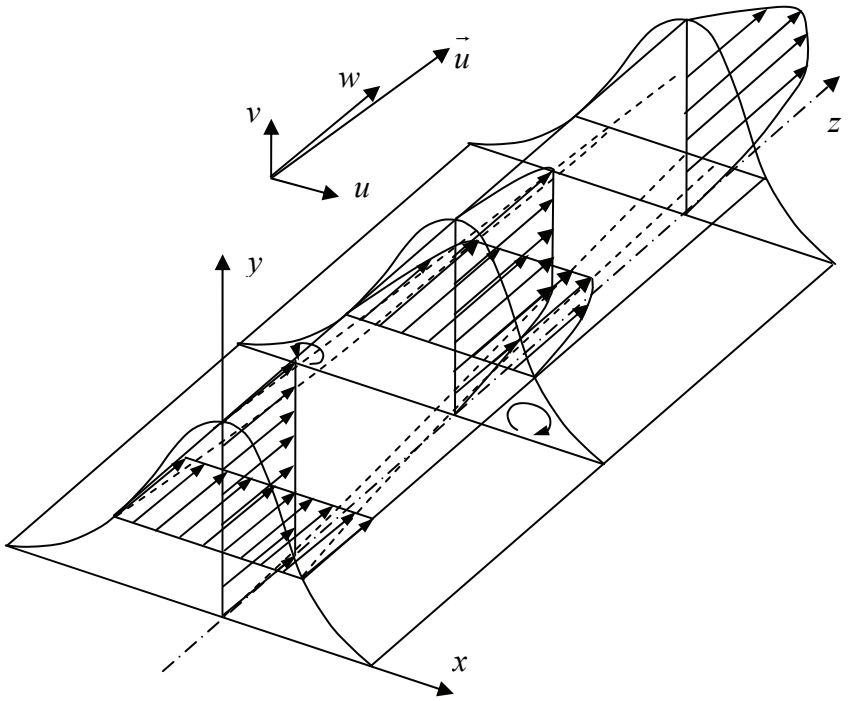

Figure 5.31: Schematic illustration of three-dimensional development of velocity profile and boundary layer in a monolith channel.

parallel to the wall and due to continuity the flow in the "inviscid" uniform core is accelerated whereas it is deaccelerated in the boundary layer due to viscous forces as schematically illustrated both in Figure 5.31 and Figure 5.32. The derivative $\partial w/\partial z$ of the velocity, w, in the axial direction of the monolith (z-direction) is therefore non-zero. Looking at the continuity equation stated here for a Cartesian coordinate system for an incompressible steady-state flow as follows

$$\frac{\partial u}{\partial x}+\frac{\partial v}{\partial y}+\frac{\partial w}{\partial z}=0 \tag{5.2}$$

the continuity equation shows that when $\partial w/\partial z \neq 0$ then $\partial u/\partial x + \partial v/\partial y \neq 0$ which requires that one or both of the velocities u, $v \neq 0$ in the xy-plane perpendicular to the axial flow direction (the z-direction) of the monolith. This confirms that the flow is not parallel to the walls in the entrance length. The flow in the entrance length will therefore be three-dimensional and there will be velocities (secondary flow) in the xy-plane perpendicular to the axial flow direction of the monolith as illustrated on Figure 5.31. Due to the asymmetry of the monolith geometry (the monolith is only symmetrical around the yz-plane as illustrated on Figure 5.31), especially in the corners, it is unlikely that the derivatives, $\partial u/\partial x$, $\partial v/\partial y$ of the

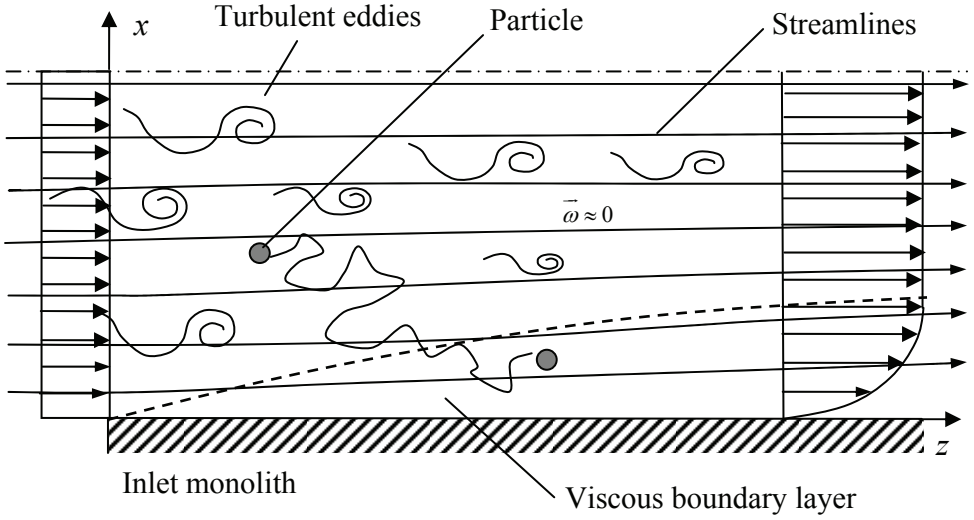

Figure 5.32: Schematic illustration of a two-dimensional boundary layer.

velocities, u, v, in the xy-plane perpendicual to the axial flow direction will be equal ($\partial u/\partial x = \partial v/\partial y$) and therefore there will be rotation, ω_z, of the secondary flow in this plane in the entrance length given as

$$\omega_z = \frac{1}{2}\left(\frac{\partial u}{\partial x} - \frac{\partial v}{\partial y}\right) \tag{5.3}$$

The rotation (vorticity) is discussed in detail in Section 5.3.1.3. For fully developed laminar flow in non-circular straight channels there will be no secondary flow and it will only be present as long as the flow is developing in the entrance length of the channel. When the flow is fully developed the flow will be parallel to the wall and the u, v, velocities will be zero. Muralidhar and Biswas (1996) have stated on page 74 that flow in tubes having sharp corners depending on the inlet conditions and tube geometry at Reynolds numbers in the range of 500-1000 undergo transition to a three-dimensional laminar state with re-circulating pools of secondary flow near the sharp corners. For fully developed turbulent flow, opposit to fully developed laminar flow, there will be a turbulent-driven secondary flow superimposed upon the main flow due to the turbulent stresses created by the turbulent fluctuation [Gessner and Jones (1965]. Because of the sharp corners (initially non-circular channels) in the Topsøe DNX x30 monolithic catalyst ("sinus" shape) the viscous boundary layer will be much thicker in the corner regions than on the smooth surfaces of the channels in the monolith. The transport of fluid to the boundary layer is therefore larger in the corner regions than on the smooth surfaces and more fluid especially with

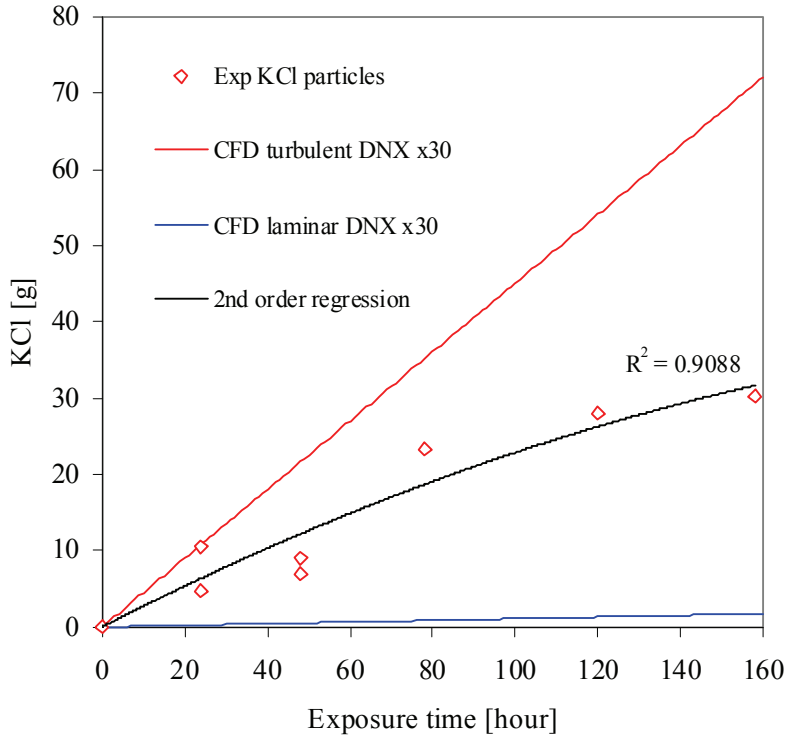

Figure 5.33: Experimental measurements of the total deposition of KCl particles (accumulated mass) in a DNX x30 monolithic catalyst versus exposure time. Volume flow, V = 40 Nm^3/h and temperature, T=623 K. Comparison with CFD simulations of DNX x30 monolith catalyst. Average velocity above catalyst, v_{avg} = 4.56 m/s, temperature, T = 623 K and dynamic viscosity, $\mu = 3.11 \cdot 10^{-5}$ kg/m-s. Particles modelled using DPM tracking 1.000.000 particles representing the real particle size distribution obtained from Figure 5.23.

submicrometer particles with low inertia will be transported to the boundary layer of the sharp corner regions. Due to the sharp corners and the thick viscous boundary layer in these regions, re-circulating pools of fluid will be created and submicrometer particles with low inertia will be captured in the sharp corner regions where they deposit due to Brownian and turbulent diffusion, respectively.

The turbulent eddies convected into the monolithic channels as schematically illustrated in Figure 5.32 from the turbulent flow upstream the monolithic catalyst probably further increases the deposition in the sharp corner regions by a turbulence-driven secondary flow which increases the mass transport of especially submicrometer particles to the corner regions. The turbulence-driven secondary

flow from the turbulence convected into the top part of the channels is therefore expected to enhance the deposition in the corners of the channels together with the secondary flow due to entrance effects (developing flow). The Saffman lift force will also transport larger particles to the boundary layer where they are captured. Due to these different transport mechanisms the flow stagnation areas (sharp corners) in the boundary layer in the channels will gradually be minimized due to the deposit and the channel geometry becomes more and more circular which for longer exposure time decreases the secondary flow and the effect on deposition of submicrometer particles.

5.3.1.2 Quantitative Discussion of Experimental Results

Figure 5.33 shows the total accumulated mass of KCl particles versus exposure time up to 158 hours. The deposited mass of KCl particles was about 30.3 g after 158 hours of exposure time. It can be observed that the data points show some scattering for the repeated experiments for 24 and 48 hours, respectively. This is due to the fact that it is difficult to re-create exactly the same conditions in each new experiment due to e.g. small differences in flame temperature, gas flow, particle concentration, etc. From Figure 5.33 the initial deposition rate of KCl particles on a fresh catalyst is about 0.2 g/h. At exposure times above 48-78 hours the data indicate a decreasing deposition rate. Overall the data seem to fit to a second order polynomial. Initially the deposition mass flow is controlled by inertial impaction and gravitational settling in the flow stagnation areas on the top of the monolithic catalyst and Brownian and turbulent diffusion in the channels. Due to the streamlining over time where the deposition in general becomes dominated by Brownian and turbulent diffusion especially in the entrance length with increasing Reynolds number one may have expected the deposition rate to increase with the total accumulated mass of KCl particles over time showing a concave curvature. This is not observed from the experimental data in Figure 5.33 where the total accumulated mass shows a convex curvature.

Figure 5.34 shows the accumulated mass of KCl particles on the top of the catalyst (first 0-1 cm) versus exposure time up to 120 hours and the relative deposition on the top of the catalyst with respect to the total accumulated mass in the catalyst. In general the data showed an increasing trend in the mass deposited while the fraction deposited on the top is rather constant at 6-7 %. The data point at 78 hours is an exception and the reason is not clear. It is possible that relatively more “popcorn” have fallen on the top of the monolith leading to accelerated deposition. But this is actually not observed from Figure 5.26 after 78 hours of exposure. Another and probably the most likely reason could be due to a higher

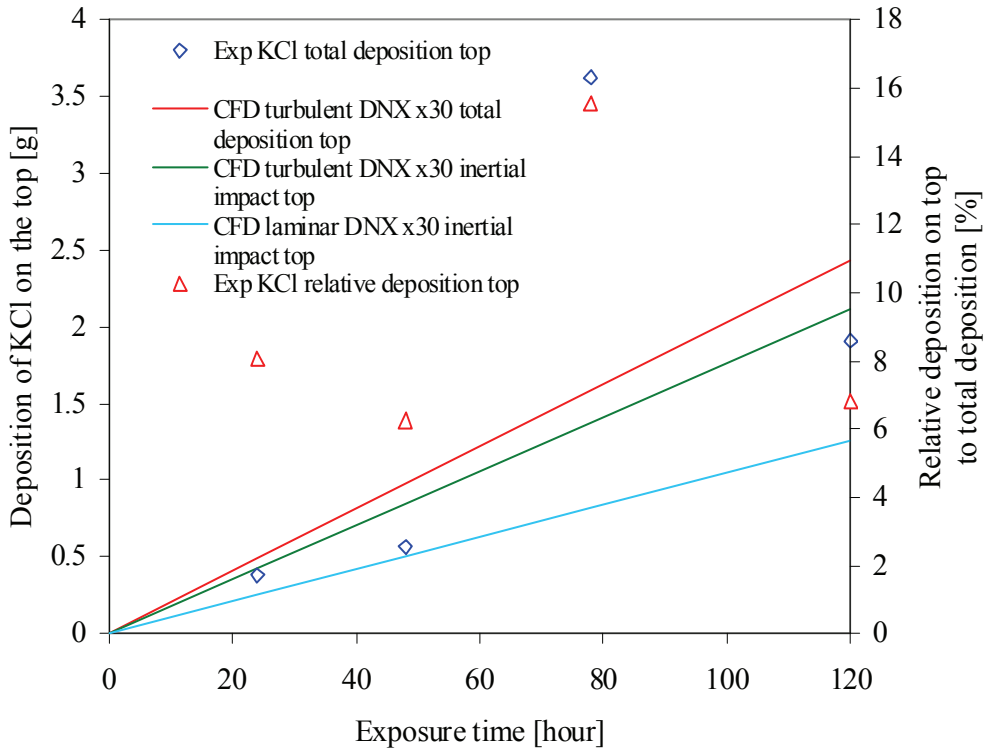

Figure 5.34: Experimental measurements of deposition of KCl particles (accumulated mass) on the top of a DNX x30 monolithic catalyst versus exposure time. Volume flow, V = 40 Nm^3/h and temperature, T=623 K. Comparison with CFD simulations of DNX x30 monolith catalyst. Primary y-axis (left) shows the total deposition on top of the catalyst. Secondary y-axis (right) shows the relative deposition on top of the catalyst in relation to the total deposition. Average velocity above catalyst, v_{avg} = 4.56 m/s, temperature, T = 623 K and dynamic viscosity, $\mu = 3.11 \cdot 10^{-5}$ kg/m-s. Particles modelled using DPM tracking 1.000.000 particles representing the real particle size distribution obtained from Figure 5.23.

particle load upstream the monolith because of the new heat exchanger used in the 78 hours experiment.

Figure 5.35 shows the total accumulated mass of KCl particles in the channels of the monolithic catalyst (1-50 cm) versus exposure time up to 120 hours. It can be observed that the accumulated mass deposition in the channels probably shows a linear build-up over time, i.e. that the deposition rate is constant. This is also supported by a linear regression, but because the deposition in the channels of the monolith was not investigated after 158 hours of exposure time the trend in the deposition rate in the channels are different from the trend in the overall deposition rate of the entire monolith. If the data point for 158 hours was not

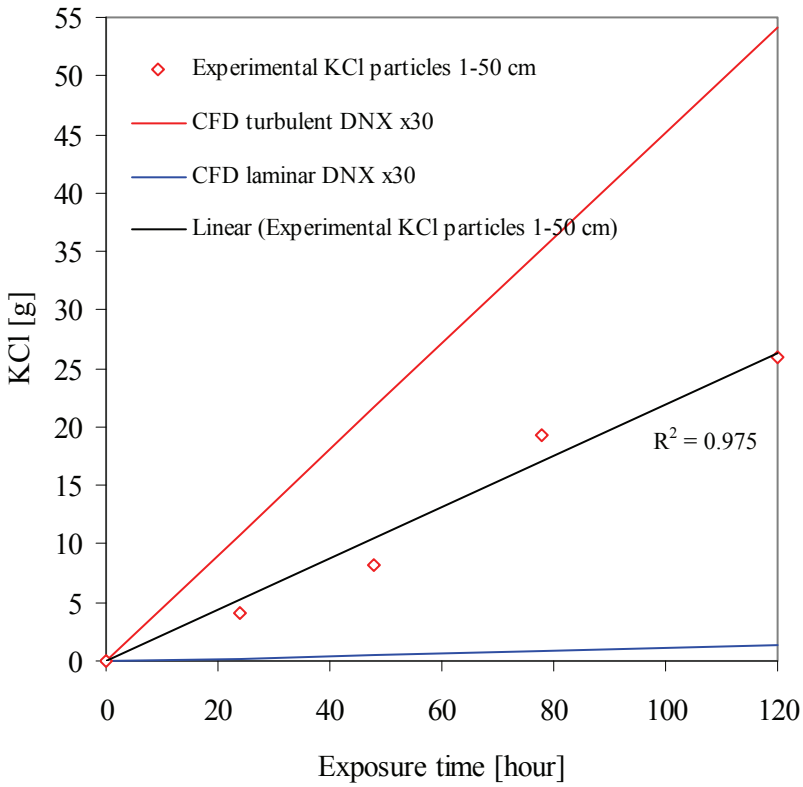

Figure 5.35: Experimental measurements of deposition of KCl particles (accumulated mass) on the channels of a DNX x30 monolithic catalyst versus exposure time. Volume flow, V = 40 Nm^3/h and temperature, T=623 K. Comparison with CFD simulations of DNX x30 monolith catalyst. Average velocity above catalyst, v_{avg} = 4.56 m/s, temperature, T = 623 K and dynamic viscosity, $\mu = 3.11 \cdot 10^{-5}$ kg/m-s. Particles modelled using DPM tracking 1.000.000 particles representing the real particle size distribution obtained from Figure 5.23.

taken into account in Figure 5.33 a linear regression would probably be a better representation of the total accumulated mass of KCl particles in the monolith over time.

Figure 5.36 shows the total deposition mass flow of KCl particles in the DNX x30 monolithic catalysts versus exposure time. It can be observed that the particle deposition mass flow is constant or perhaps a slightly decreasing function of time. From Figure 5.36 the average rate of particle deposition in the DNX x30 catalysts based on the experiments was $6.3 \cdot 10^{-8}$ kg/s which gave an overall mass based deposition efficiency of about 30%.

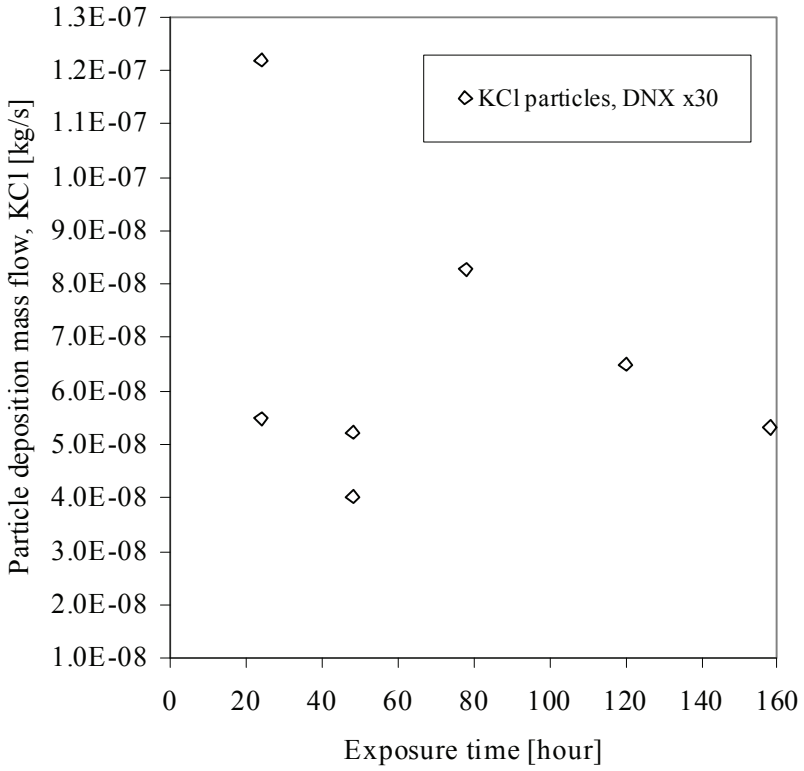

Figure 5.36: Particle deposition mass flow of KCl particles to the DNX x30 monolithic catalyst walls versus exposure time based on experimenta data. Average deposition rate $6.3 \cdot 10^{-8}$ *kg/s.*

Figure 5.37 shows the accumulated mass deposition of KCl particles in the axial length of the monolithic catalyst channels, where the accumulated mass has been determined in the channels of the monolith in the intervals from 1-10 cm, 10-20 cm, 20-30 cm, 30-40 cm and 40-50 cm, respectively. From Figure 5.37 a general increase in the accumulated mass in the channels for increasing exposure time to KCl particles can be observed.

Figure 5.38 shows the corresponding average deposition rate of KCl particles in the axial length of the monolithic catalyst channels, where the average deposition also has been determined in the channels of the monolith in the intervals from 1-10 cm, 10-20 cm, 20-30 cm, 30-40 cm and 40-50 cm, respectively. From Figure 5.38 the increase in deposition rate due to especially turbulent diffusion in the top part (about half of the channel length) of the channels due to the entrance length with developing flow in transition from turbulent to laminar flow and higher Reynolds number in that part of the channel compared to further downstream are clearly observed. It can also be observed that for the first 24 and 48 hours of

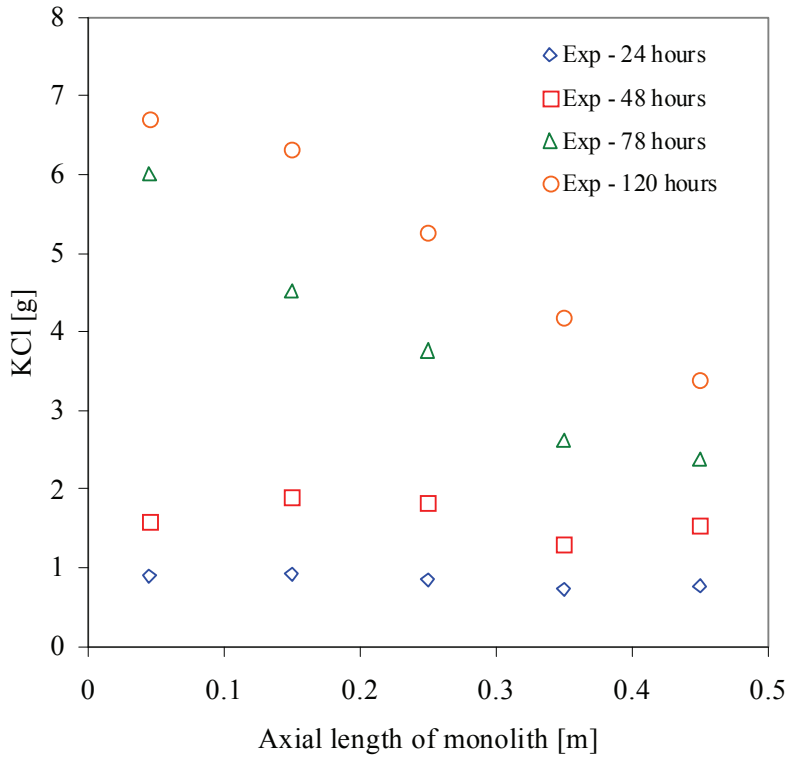

Figure 5.37: Deposition of accumulated mass of KCl particles in the axial length of a DNX x30 monolithic catalyst channels for 24, 48, 78 and 120 hours of exposure time, respectively. The accumulated mass has been determined in the channels of the monolith in the intervals 1-10 cm, 10-20 cm, 20-30 cm, 30-40 cm and 40-50 cm, respectively.

exposure of KCl particles the average deposition rate is more or less constant, maybe with a tendency of a maximum after 15-25 cm due to the entrance length which also can be observed form turbulent CFD simulations.

For longer exposure time after 78 and 120 hours there is a clear tendency for the average deposition rate to increase in the first part of the monolith and to decrease in the bottom part in the axial length of the monolith. This supports the hypothesis that the increased average deposition rate is due to the increased Reynolds number at the inlet section, because of the reduced hydraulic diameter from the streamlining of the top part of the channels and the acceleration of the flow in the entrance length. Due to the deposited KCl particles the higher Reynolds number increases the turbulent diffusion in the entrance length and this again may increase the entrance length with transition from turbulent to laminar flow before the flow becomes fully developed laminar, which again increases the deposition rate in the top part of the monolith. Further downstream after the entrance length the

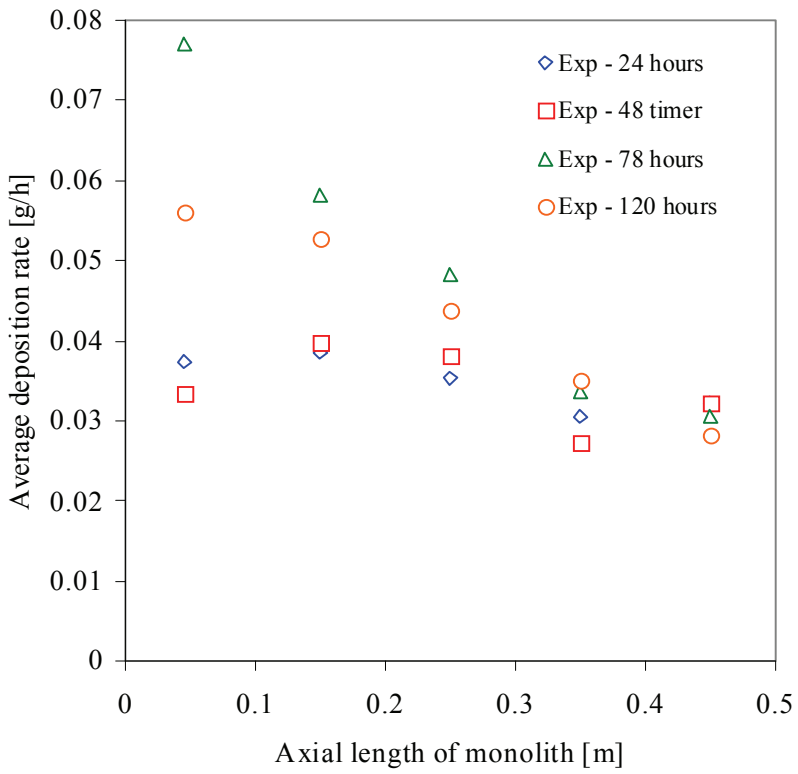

Figure 5.38: Average deposition rate of KCl particles in the axial length of a DNX x30 monolithic catalyst channels for 24, 48, 78 and 120 hours of exposure time, respectively. The average deposition rate has been determined in the channels of the monolith in the intervals 1-10 cm, 10-20 cm, 20-30 cm, 30-40 cm and 40-50 cm, respectively.

decrease in average deposition rate in the channels in the axial length of the monolith is due to the decreased Reynolds number in the bottom part of the monolithic catalyst which decreases the deposition rate in this area. Another reason for the decrease in average deposition rate in the channels in the axial length of the monolith could probably be because of a lower particle concentration in the bulk flow in the bottom part of the monolith due to the increased deposition rate in the top part. For the last 15 cm of the monolithic catalysts, as seen from Figure 5.38, the average deposition rate is more or less constant for all exposure times indicating that the flow has become fully developed laminar and Brownian diffusion, Saftman lift force and electrostatic forces are the only forces responsible for deposition in the bottom part of the monolith. The data for the average deposition rate shown in Figure 5.38 support the hypothesis that turbulent particle diffusion is the dominating mechanism for particle deposition in the top part of the monolithic catalysts.

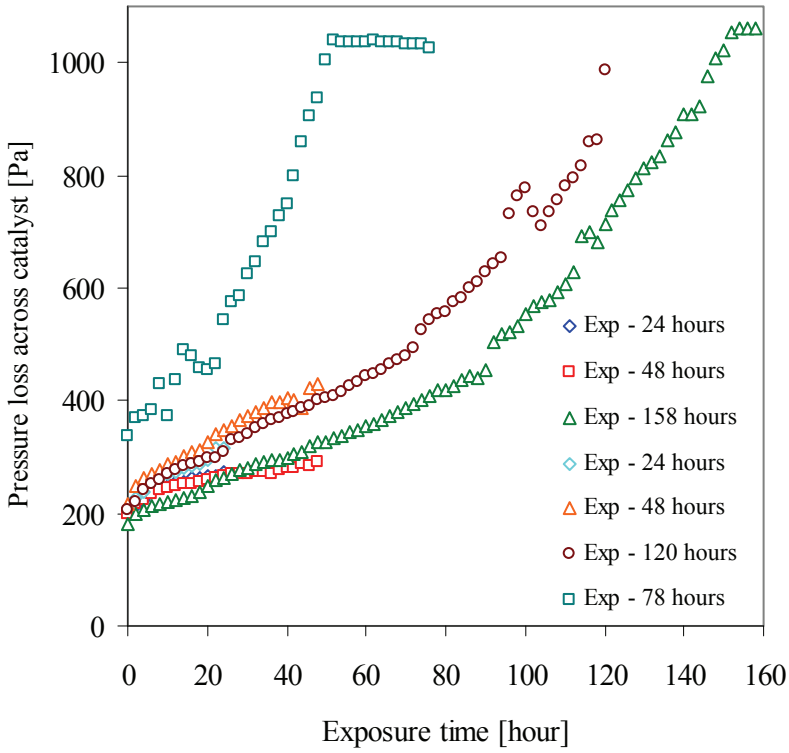

Figure 5.39: Pressure loss across DNX x30 monolithic catalyst versus exposure time.

Figure 5.39 shows the pressure loss across the DNX x30 monolithic catalyst versus exposure time in the pilot scale experiments. It can be observed that the reproducibility in the development of the pressure loss across the DNX x30 monolithic catalyst versus exposure time is reasonable except for the 78 hours experiment where the heat exchanger was renewed. For the 78 hours experiment the excepted higher particle concentration above the monolith catalyst due to the new heat exchanger created a much steeper increase in pressure loss across the catalyst over time which plugged the monolith faster than obtained in the other experiments.

It can also be observed from the 78 hours and 158 hours of exposure to KCl particles that a maximum in the pressure loss is reached at about 1050 Pa. The reason for the maximum in pressure loss was probably because at this point it was difficult to keep the volume flow up at 40 Nm^3/h due to the plugging in the catalyst and further plugging then resulted in a decrease in the volume flow and temperature instead of increased pressure loss. This was due to the way the pilot plant was constructed.

Table 16: CFD simulation of the deposition efficiency in a DNX x30 monolithic catalyst for laminar and turbulent flow and the different particle diameters used in the CFD simulation.

		DNX x30 Laminar flow		DNX x30 Turbulent flow	
Particle diameter [μm]	Particle mass flow in [kg/s]	Particle mass flow out [kg/s]	Deposition efficiency [%]	Particle mass flow out [kg/s]	Deposition efficiency [%]
0.039	$2.18 \cdot 10^{-11}$	$2.13 \cdot 10^{-11}$	2.5	$6.34 \cdot 10^{-12}$	70.92
0.070	$5.40 \cdot 10^{-11}$	$5.37 \cdot 10^{-11}$	0.6	$1.99 \cdot 10^{-11}$	63.07
0.115	$2.56 \cdot 10^{-10}$	$2.55 \cdot 10^{-10}$	0.4	$1.02 \cdot 10^{-10}$	60.02
0.195	$4.77 \cdot 10^{-10}$	$4.75 \cdot 10^{-10}$	0.5	$1.98 \cdot 10^{-10}$	58.51
0.356	$3.11 \cdot 10^{-10}$	$3.10 \cdot 10^{-10}$	0.5	$1.29 \cdot 10^{-10}$	58.50
0.697	$1.76 \cdot 10^{-10}$	$1.75 \cdot 10^{-10}$	0.4	$8.66 \cdot 10^{-11}$	54.22
1.397	$3.79 \cdot 10^{-11}$	$3.77 \cdot 10^{-11}$	0.6	$1.79 \cdot 10^{-11}$	52.67
2.775	$2.09 \cdot 10^{-11}$	$2.03 \cdot 10^{-11}$	3.0	$7.07 \cdot 10^{-12}$	66.18
5.454	$1.65 \cdot 10^{-11}$	$1.37 \cdot 10^{-11}$	17.1	$2.86 \cdot 10^{-12}$	82.65
10	$3.53 \cdot 10^{-11}$	$2.57 \cdot 10^{-11}$	27.1	$6.99 \cdot 10^{-13}$	98.02
Total	$1.41 \cdot 10^{-9}$	$1.39 \cdot 10^{-9}$	≈1.3	$5.65 \cdot 10^{-10}$	≈59.8

5.3.1.3 Comparison with CFD Simulations

CFD simulations with a general CFD model for prediction of particle deposition and deposit build-up in SCR $DeNO_x$ monolithic catalysts have been carried out for both laminar and turbulent flow fields through the monoliths in order to investigate the influence of the assumption of the flow type on deposition due to flow effects. This was done because the transition from turbulent to laminar flow through the monolithic catalyst not was possible to model due to computational time and memory limitations.

Table 16 shows the deposition efficiency for laminar and turbulent flow in a DNX x30 monolithic catalyst calculated based on the CFD simulations. As is can be observed from Table 16 the total deposition efficiency for the DNX x30 monolithic catalyst calculated based on the CFD simulations in laminar flow is about 1.3% and for the turbulent flow simulation it is about 59.8%. For comparison the physical experiment had a deposition efficiency about 30%.

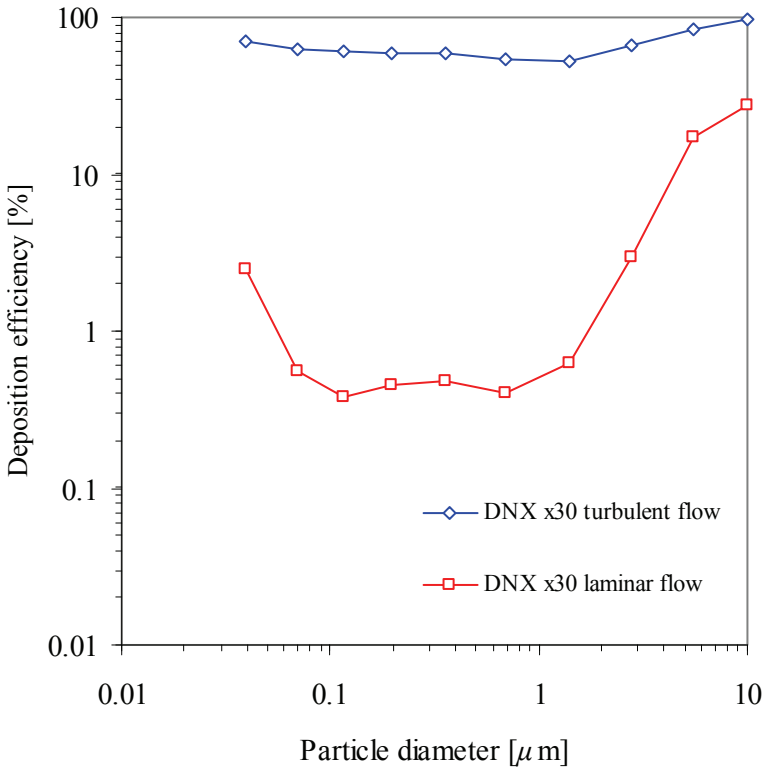

Figure 5.40: Deposition efficiency for laminar and turbulent flow field above and through the DNX x30 monolithic catalyst. Average velocity above catalyst, v_{avg} = 4.56 m/s, temperature, T = 623 K and dynamic viscosity, $\mu = 3.11 \cdot 10^{-5}$ kg/m-s. Particles modelled in CFD using DPM tracking 100.000 particles representing the real particle size distribution obtained from Figure 5.23

For the laminar flow case the CFD model underpredicted the total deposition efficiency with a factor of about 23 and for the turbulent flow case the overall deposition efficiency was overpredicted by a factor of about 2 which confirms the hypothesis that the deposition is dominated by turbulent spreading of the particles.

Figure 5.40 shows the deposition efficiency calculated from the CFD simulation based on the particle size distribution measured in the pilot scale experiments (given in Table 16). For the CFD simulation of laminar flow the minimum in deposition efficiency for particles between about 0.1 and 1 μm can be identified due to the negligible influence of Brownian motion, electrostatic forces (because of low average charge), Saffman lift and inertial impaction in that region. The influence of Saffman lift and inertial impaction can also be identified for larger particles above about 5 μm where an increase in the deposition efficiency is observed.

Table 17: CFD simulation of the deposition efficiency in a DNX x30 monolithic catalyst for laminar and turbulent flow.

DNX x30 monolith	Laminar flow Deposition efficiency [%]	Turbulent flow Deposition efficiency [%]
Top: Inertial impact	1.32	2.27
Top: Inertial impact and Brownian diffusion	1.33	-
Top: Inertial impact and turbulent diffusion	-	2.71
Top: Inertial impact, turbulent diffusion, Saffman lift and electrostatic forces	1.33	2.71
Channel: Inertial impact, turbulent diffusion, Saffman lift and electrostatic forces	0.01	55.8
Top and Channel: Inertial impact, turbulent diffusion, Saffman lift and electrostatic forces	1.33	59.8

The deposition efficiency due to Saffman lift in laminar flow in the monolith for a given particle size can be compared with the Saffman deposition efficiency for pipe flow given in Figure 5.21 and Figure 5.22 which show a deposition efficiency of the same order magnitude. For the turbulent cases great impact of turbulent diffusion on particles below 1 μm can be identified compared to laminar flow. The impact on larger particles above 1 μm due to increased inertial impaction because of increased mixing of the particles can also be identified from Figure 5.40. The small increase in deposition efficiency observed for the laminar CFD simulation between 0.1 and 1 μm is probably due to numerical uncertainties.

Figure 5.33 shows a comparison of the experimental results with CFD simulations of the accumulated mass of KCl particles in a DNX x30 monolithic catalyst. The

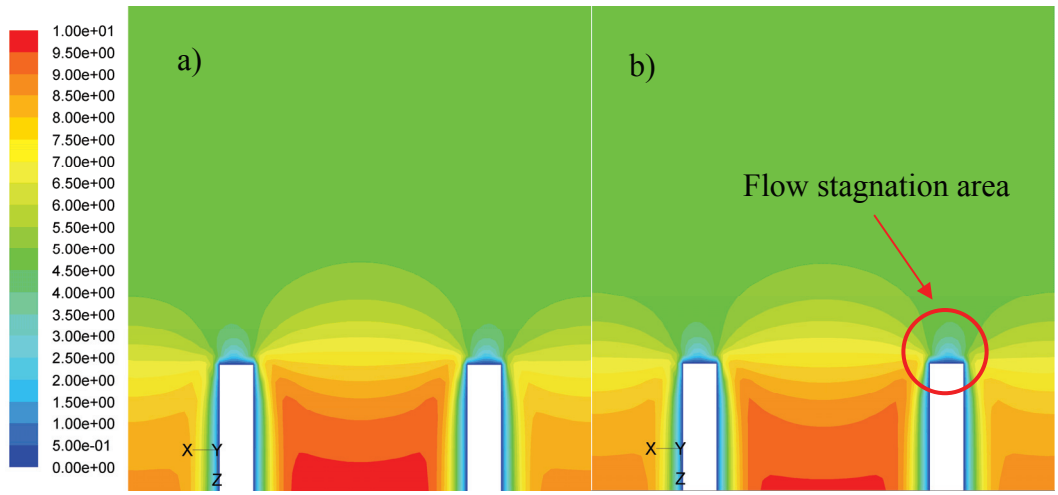

Figure 5.41: Comparison of velocity magnitude in the xz-plane through the monolith. a) assuming laminar flow, b) assuming turbulent flow..

accumulated mass of KCl particles in the CFD simulations is based on a linear extrapolation of the mass deposited during one time step (one hour).

From Figure 5.33 it can be observed that the CFD simulations assuming laminar flow above the catalyst and in the channels in general underpredict the development of the accumulated mass greatly with a factor of about 17 (total accumulated mass after 158 hours of exposure was about 1.7 g). The reason for this is that the mechanism responsible for most of the particle deposition on the top of the catalyst in laminar flow is inertial impaction and gravitational settling in the flow stagnation area (zero velocity) in front of the top of the monolithic catalyst as seen from Table 17.

The flow stagnation area on the top of the catalyst can be identified on Figure 5.41. Inertial impaction on the top of the monolithic catalyst is responsible for about 99% of the total deposition in the monolith in laminar flow and corresponds to a deposition efficiency of about 1.32%. The reason for this is that Brownian diffusion and electrostatic forces in laminar flow will only spread the KCl aerosol particles slightly and due to the lack of turbulent spreading of the particles, deposition is considerable less in laminar flow than in turbulent flow. In the channels Brownian diffusion together with Saffman lift force and electrostatic forces will be the only mechanisms responsible for the transport of particles to the surface in laminar flow. Saffman lift force has no impact on submicrometer

particles and the electrostatic forces are weak because the average number of elementary charges only was about 0.001. Brownian particle diffusion is also first important for particles less than 0.1 μm and as seen from Figure 5.23 the majority of the particles in the pilot plant are between 0.1 and 1 μm where the deposition efficiency is low which can be observed from Table 16 and Figure 5.40. As it also can be seen from Table 16 and Figure 5.40 inertial impaction and Saffman lift is only important for particles larger than 5 μm where increased deposition efficiency is observed. The total deposition efficiency in laminar flow for a DNX x30 monolithic catalyst calculated based on the CFD simulations was only about 1.33% (of which about 1.32% point is on the top of the monolith and about 0.01% point is in the channels of the monolith) as seen from Table 17.

From Figure 5.33 it can also be observed that the CFD simulations assuming turbulent flow above the catalyst and in the channels predict the development over time in the accumulated mass better compared to the experimental results, even though the CFD simulation overpredicts the results with a factor of about 2.4 (total accumulated mass after 158 hours of exposure based on the turbulent CFD simulation was about 71 g compared to 30.3 g experimentally). The reason for the overprediction is probably due to the fact that the CFD simulations for turbulent flow assumes turbulent flow through the whole monolith whereas the flow field in the physical experiments are in transition from turbulent to laminar flow and the transition length is of the order of half the channel length. The last half of the monolith channels will then be dominated by laminar flow without turbulent diffusion.

As seen from Figure 5.34 the deposition on the top of the monolith is predicted within the experimental uncertainty assuming laminar and turbulent flow. From Figure 5.35 it can be observed that the total accumulated mass measured in the monolith cannot be only due to Brownian particle diffusion, inertial impaction, electrostatic forces and Saffman lift. Because the deposition in the channel is so underpredicted in laminar flow simulations compared to turbulent flow simulations it has to be due to contribution from turbulent diffusion in the entrance length of the channel. It can also be observed from Figure 5.34 that the suppression of bouncing on top of the catalyst which was done in the CFD model by lowering the asperities, z_0, in the particle-wall interaction model indicates that bouncing from the top of the catalyst was negligible in the experiments. The mass deposited on the top of the channel in the flow stagnation area upstream of the monolithic catalyst due to inertial impaction and gravitational settling is only about 2.27% in turbulent flow and is about the double compared to laminar flow (without turbulent diffusion). The reason for this is due to small differences between the laminar and turbulent flow simulations in the flow distribution

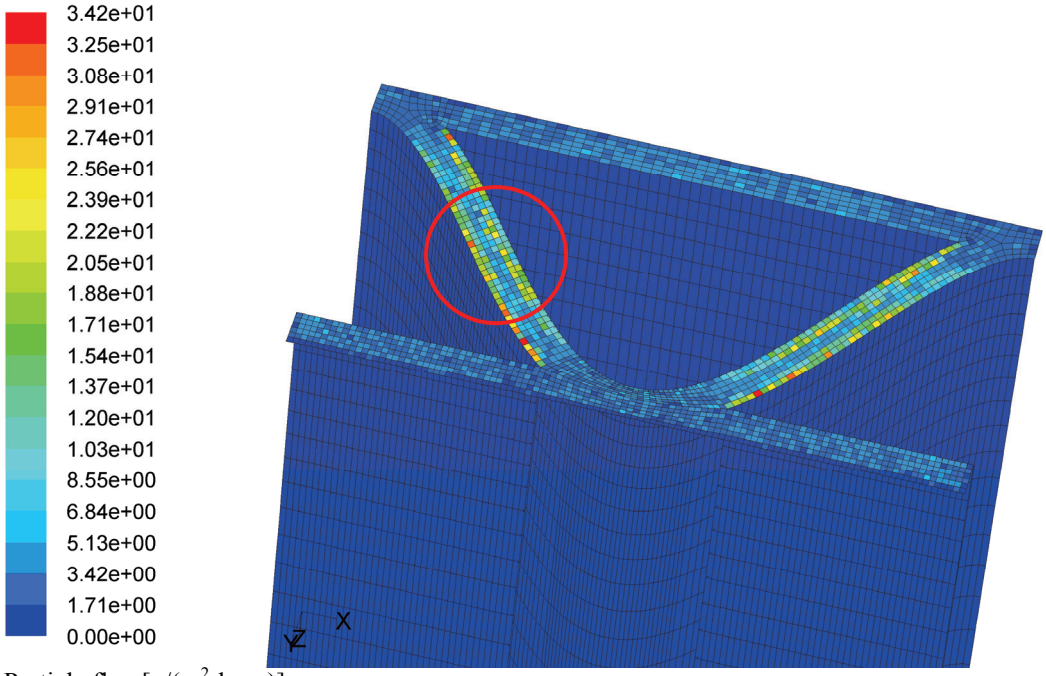

Figure 5.42: CFD simulation of particle deposition flux in a DNX x30 monolith catalyst after initially one time step (one hour) of exposure of KCl particles in laminar flow. Average velocity above catalyst, v_{avg} = 4.56 m/s, temperature, T = 623 K and dynamic viscosity, $\mu = 3.11 \cdot 10^{-5}$ kg/m-s. Particles modelled using DPM tracking 1.000.000 particles representing the real particle size distribution obtained from Figure 5.23.

upstream the monolithic catalyst and therefore small differences in the flow stagnation area on top of the catalyst as seen from Figure 5.41. It can also be observed from Table 17 that turbulent diffusion increases the deposition efficiency for the top to about 2.7% which is an increase in the deposition efficiency for the top with about 19% due to turbulent diffusion.

Figure 5.42 shows a contour plot of the KCl particle deposition flux after one time step (one hour) assuming laminar flow above the catalyst and in the channels of a DNX x30 monolithic by tracking 1.000.000 particles representing the real particle size distribution obtained from Figure 5.23. A variation in the particle flux of the deposit of KCl particles on the top of catalyst channels can be identified. As it can be observed the particle deposition flux is larger at the top of the channels which are in the middel of the flow in the model (as illustrated with the red circle). These surfaces are hit by particles from the flow on both sides above the channels, whereas surfaces on the top of the catalyst channel that are located next to a

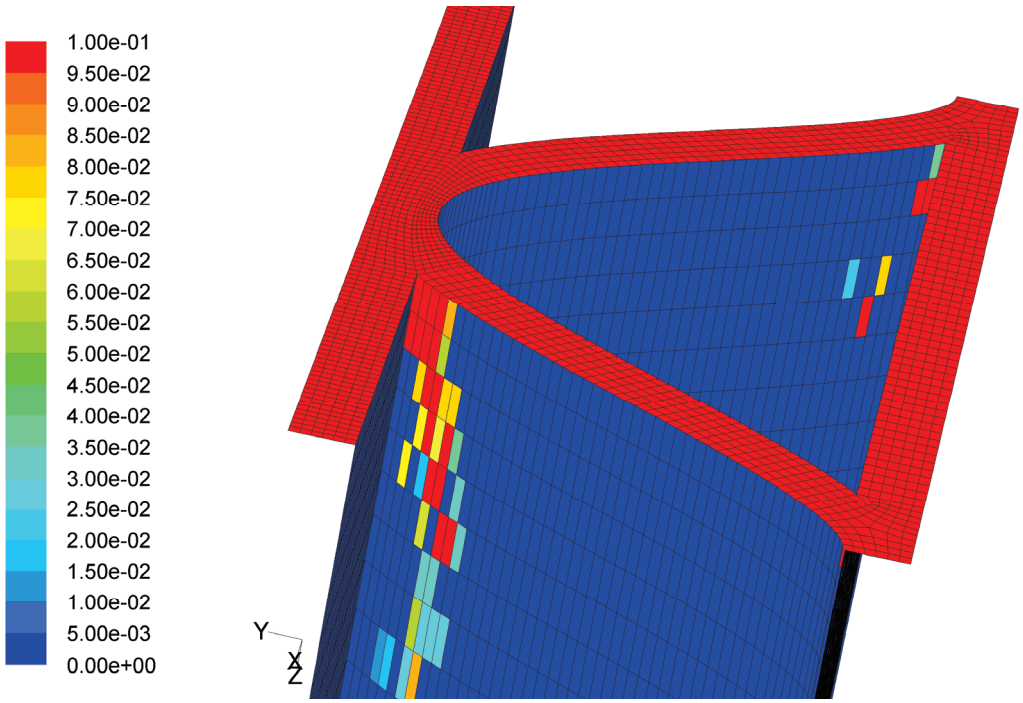

Figure 5.43: Close-up of particle deposition at the inlet of a DNX x30 monolithic catalyst after initially one time step (one hour) of exposure of KCl particles in laminar flow. Red colour scale shows particle deposition flux larger than or equal to 0.1 g/(m^2-hour). The particle flux is given in gram per square meter per hour.

symmetry boundary only are hit by particles from the flow from one side above the channel. This is a drawback of the model because only one channel and two half channels due to computational memory and time limitations were modelled.

Figure 5.43 shows a close-up of the particle deposition flux in the corners of the monolith close to the inlet after one time step (one hour) of exposure to KCl particles in laminar flow where the deposition in the corners due to Brownian diffusion and secondary flow in the *xy*-plane normal to the main axial flow, because of the developing flow at the entrance length of the channel, can be identified.

Figure 5.44 shows the particle deposition flux of KCl particles assuming turbulent flow above the catalyst and in the channels of a DNX x30 monolithic after one time step (one hour). The difference in particle deposition flux of KCl particles on the top of catalyst channels and also higher deposition flux compared to the laminar case can be identified.

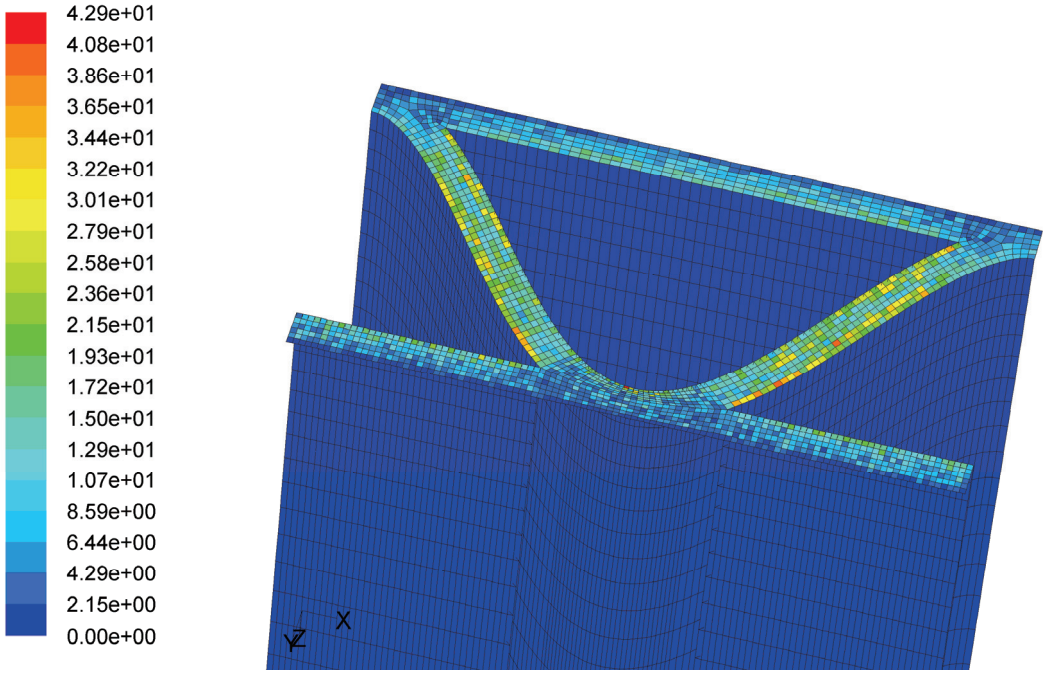

Figure 5.44: CFD simulation of particle deposition flux in a DNX x30 monolith with turbulent flow. Average velocity above catalyst, v_{avg} = 4.56 m/s, temperature, T = 623 K and dynamic viscosity, $\mu = 3.11 \cdot 10^{-5}$ kg/m-s. Particles modelled using DPM tracking 1.000.000 particles representing the real particle size distribution obtained from Figure 5.23.

Figure 5.45 shows a close-up of the particle deposition flux of KCl particles in the corners of the monolith at the inlet after one time step (one hour) of exposure to KCl particles in turbulent flow. Here more deposition in the corners are observed for turbulent flow compared to laminar flow because of the increased mass flow of particles to the re-circulation zones in the sharp corners due to the turbulent diffusion (turbulent transport of particles).

Figure 5.46 shows a comparison of the particle deposition flux in laminar and turbulent flow, respectively and as it can be observed the particle deposition flux are significantly larger in the monolith channels in turbulent flow compared to laminar flow, due to the turbulent diffusion in the channels. It can also be observed for the turbulent case that the particle deposition flux is very low for the first one to two centimetres of the channel. This is explained below from Figure 5.47.

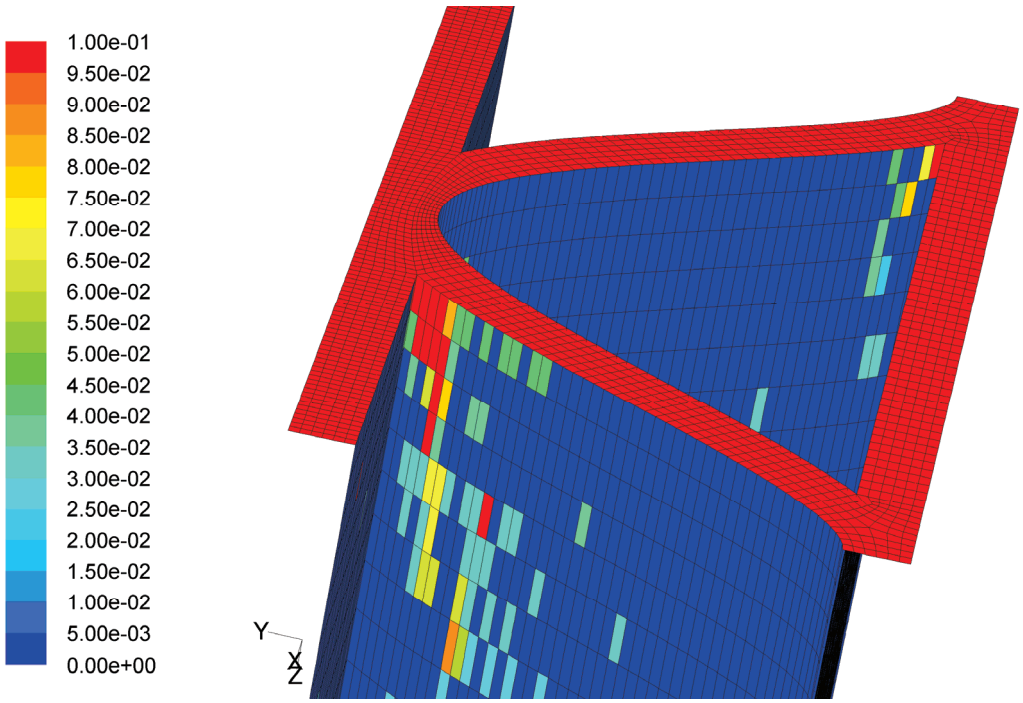

Figure 5.45: Close-up of particle deposition flux at the inlet of a DNX x30 monolithic catalyst after initially one time step (one hour) of exposure of KCl particles in turbulent flow. Red colour scale shows particle deposition flux larger than or equal to 0.1 g/(m^2-hour). The particle flux is given in gram per square meter per hour.

Figure 5.47 shows the development in the concentration boundary layer in the axial length of the monolith channel after 0.1, 1, 5, 10, 15, 20, 30 and 50 mm. Due to the deposition of particles on the top of the monolith the particle concentration in the vicinity of the walls just at the inlet is very low as seen from Figure 5.47. At the same time the viscous velocity boundary layer and the particle concentration boundary layer starts to develop. But because the viscous velocity boundary layer is thicker than the particle concentration boundary layer due to large Schmidt numbers and the capture of particles at the top of the monolith the particle concentration will be very low at the beginning in the viscous velocity boundary layer. At the same time the bulk flow is accelerated in the entrance and due to the time it takes for the particles to be transported from the bulk flow into the viscous velocity boundary layer (mainly due to turbulent diffusion) the particles at the same time will be convected one to two centimetres in the axial length of the monolith channel. Therefore, as seen from Figure 5.46 the particle flux has a much higher value in the downstream direction after a couple of centimeters.

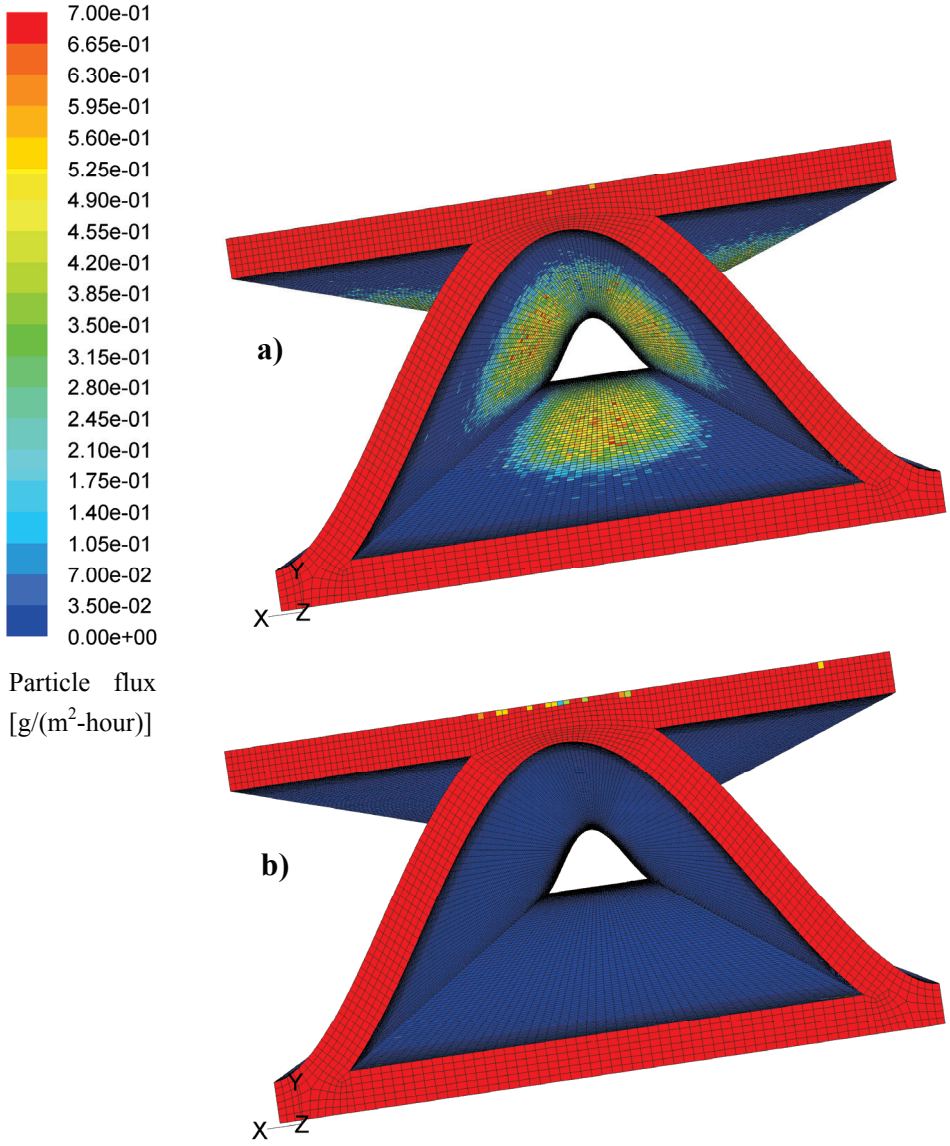

Figure 5.46: Contour plot of particle deposition flux in a DNX x30 monolithic catalyst after initially one time step (one hour) of exposure of KCl particles in a) turbulent flow and b) laminar flow, respectively.

The increase in the particle concentration just outside the particle concentration boundary layer but still inside the viscous velocity boundary layer can be observed from Figure 5.47 after a couple of centimeters.

Figure 5.48 shows a contour plot of the axial velocity in turbulent flow in three *xy*-planes in the entrance length after 2, 10 and 20 mm, respectively. The *u*-, *v*-

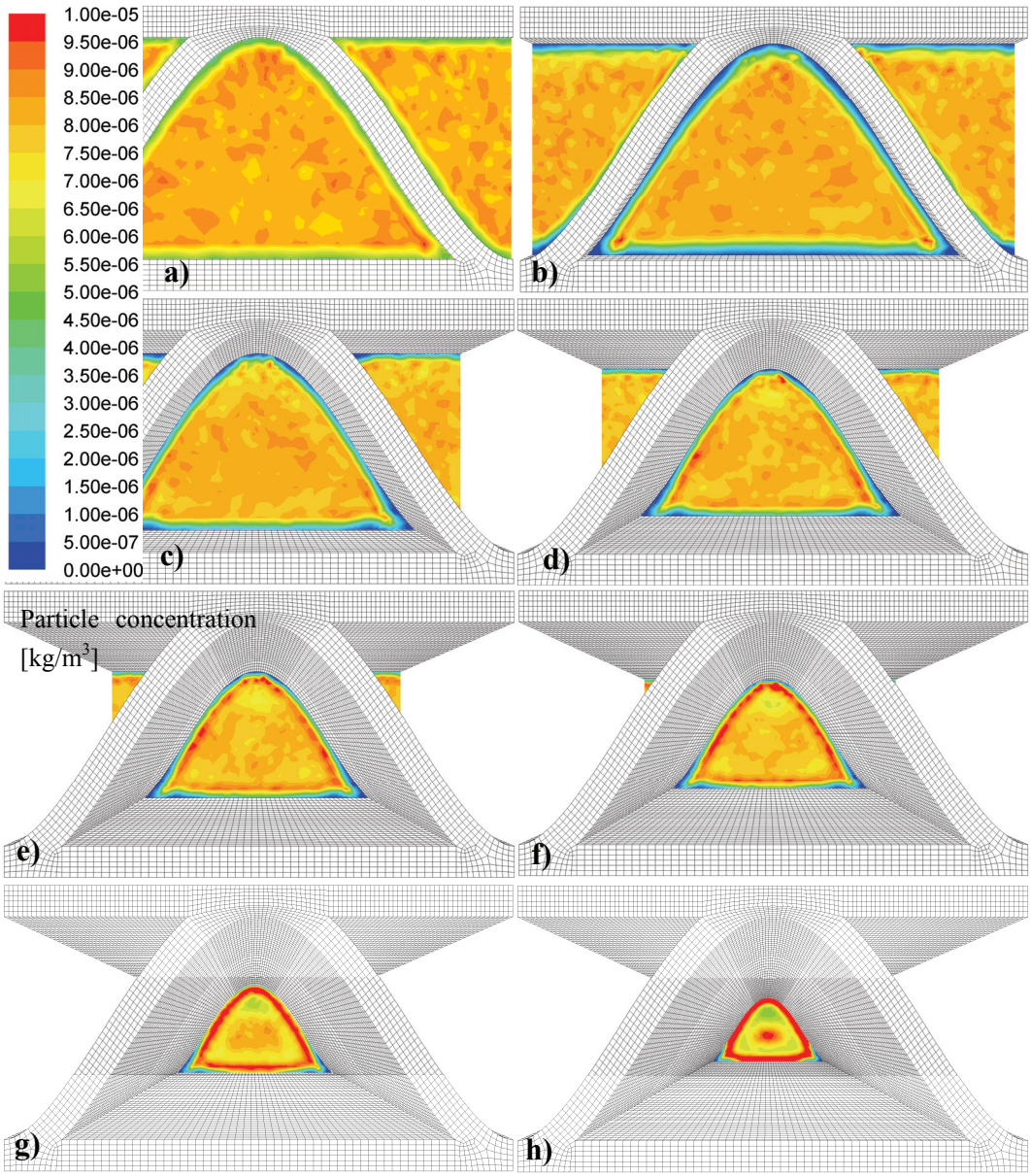

Figure 5.47: Particle concentration boundary layer in xy-planes in the axial length of the DNX x30 monolithic catalys. a) After 0.1 mm b) After 1 mm. c) After 5 mm. d) After 10 mm. e) After 15 mm. f) After 20 mm. g) After 30 mm. h) After 50 mm.

velocities in the *xy*-planes have been shown on the same plots but with scaled velocity vectors.

The development in the viscous velocity boundary layer (decreased velocity) is clearly identified as well as the acceleration of the "inviscid" core. Re-circulation

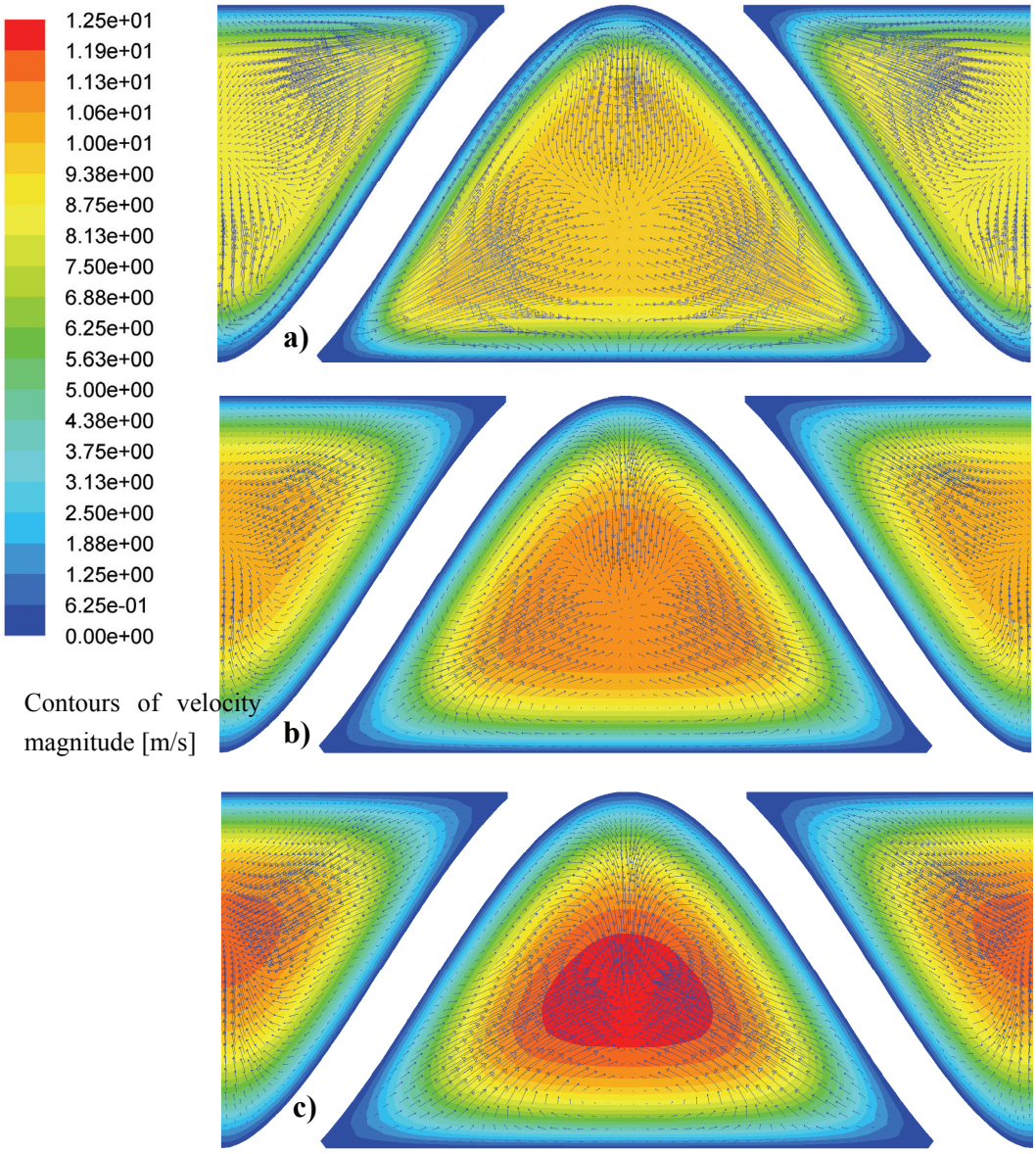

Figure 5.48: CFD simulation with contour plot of axial velocity and scalede vectors of the secondary flow in turbulent flow. Illustrate the development of the viscous boundary layer. a) Axial velocity and secondary flow after 2 mm. b) Axial velocity and secondary flow after 10 mm. c) Axial velocity and secondary flow after 20 mm.

pools are observed in the sharp corners. But in order to really capture these effects the grid should have been more resolved in the sharp corners.

The *z*-vorticity which is twice the rotation given in Equation (5.3) can be observed in Figure 5.49 and the decrease in the vorticity in the axial length as the flow

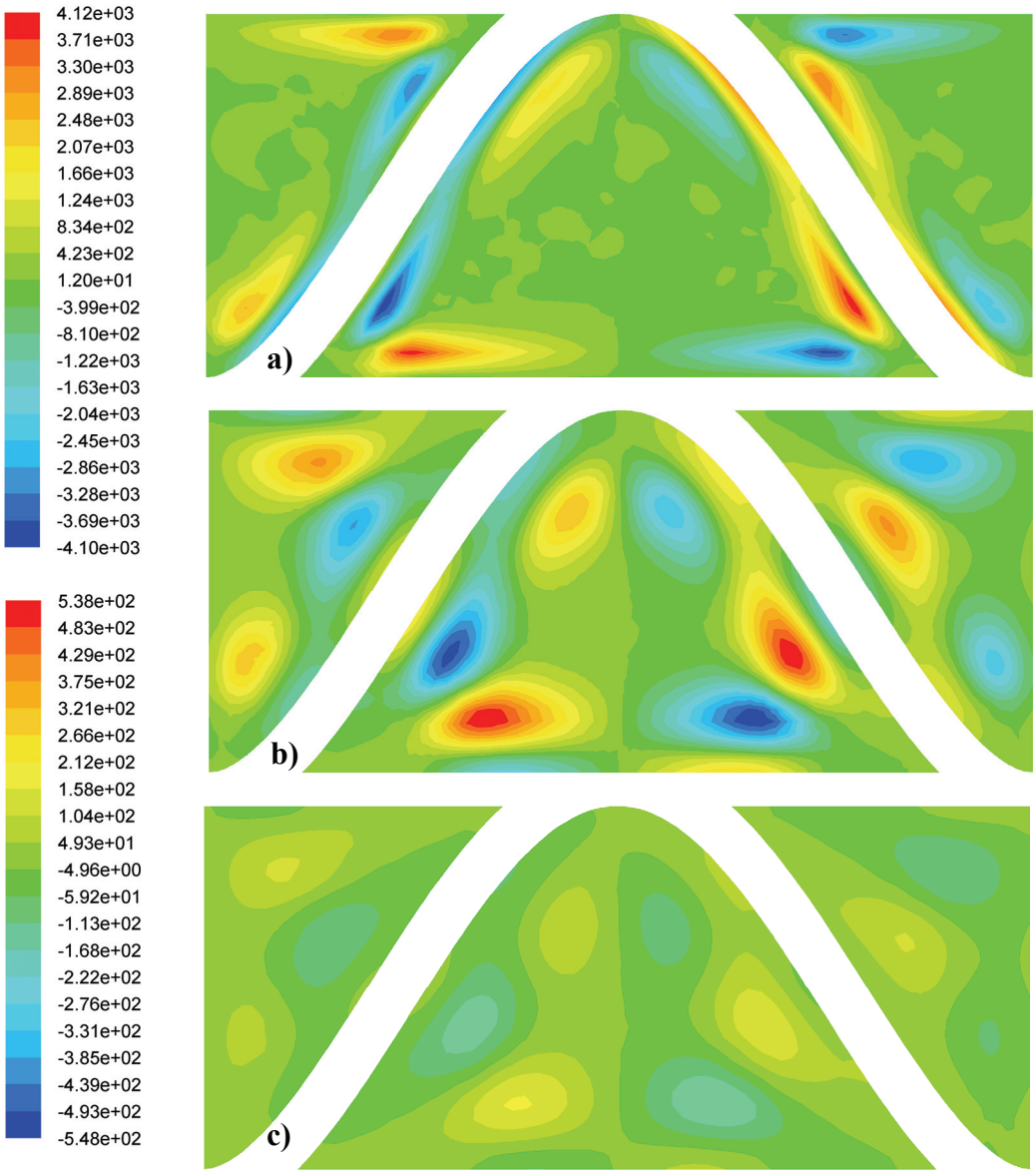

Figure 5.49: CFD simulation with contour plot of z-vorticity in turbulent flow. a) z-vorcity after 2 mm (upper colourbar). b) z-vorticity after 10 mm (lower colourbar). c) z-vorticity after 20 mm (lower colourbar).

develops can be identified. Due to the direction of the rotation the *z*-vorticity will either be positive (into the page) or negative (out of the page). This secondary flow pattern in the entrance length is expected to cause the deposition of submicrometer particles in the sharp corners and gradually change the geometry to become circular as observed from the experiment shown in Figure 5.26.

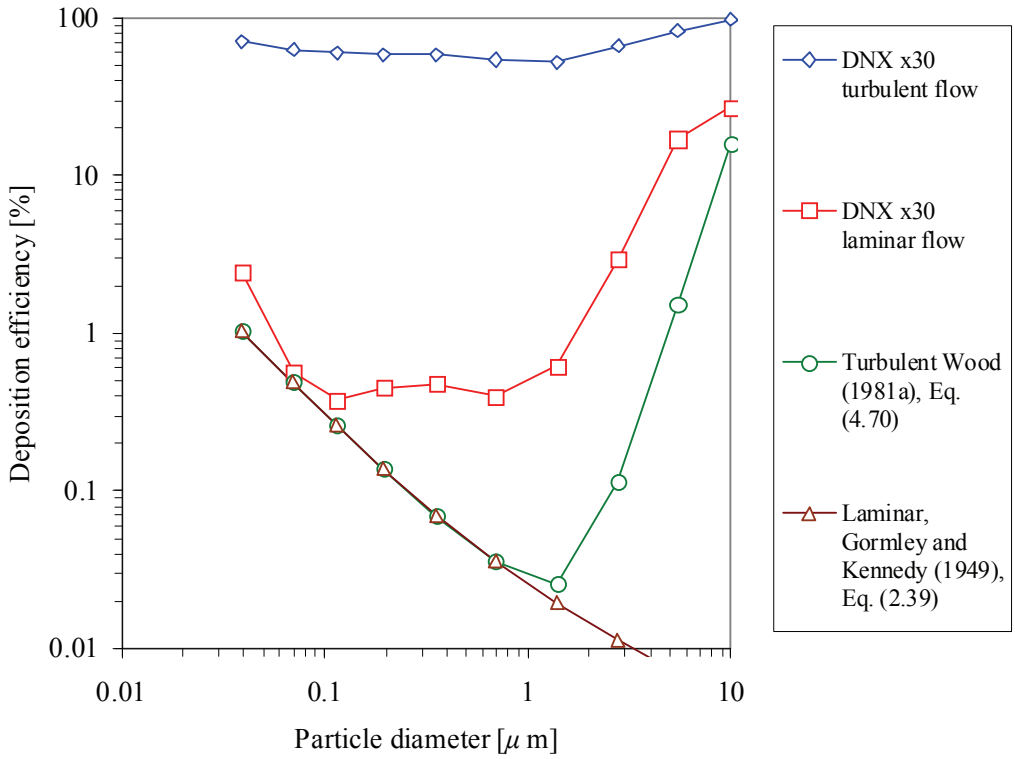

Figure 5.50: Deposition efficiency for laminar and turbulent flow field above and through the DNX x30 monolithic catalyst. Comparison with an empirical model, Eq.(4.69) for turbulent flow based on the deposition velocity given by Wood (1981a) and an analytic model for Brownian deposition in laminar flow, Eq.(2.39) [Gormley and Kennedy (1949)] for deposition in a 50 cm long pipe with a diameter of 3.4 mm. Average velocity above catalyst, v_{avg} = 4.56 m/s, temperature, T = 623 K and dynamic viscosity, $\mu = 3.11 \cdot 10^{-5}$ kg/m-s. Particles modelled in CFD using DPM tracking 100.000 particles representing the real particle size distribution obtained from Figure 5.23.

Figure 5.50 shows the deposition efficiency calculated from the CFD simulations based on the particle size distribution measured in the pilot scale experiments (given in Table 16).

These results have been compared with a simple empirical model for turbulent tube flow, Equation (4.69) using the deposition velocity from Wood (1981a) and a simple analytic model for laminar tube flow given by Gormley and Kennedy (1949), Equation (2.39) for deposition in a 50 cm long pipe with a diameter of 3.4 mm which is equal to the hydraulic diameter of the monolithic channels. For the CFD simulations of laminar flow the minimum in deposition efficiency for particles between about 0.1 and 1 μm can be identified due to the negligible

influence of Brownian motion, electrostatic force (because of low average charge), Saffman lift and inertial impaction in that region. The influence of Saffman lift and inertial impaction can also be identified for larger particles above about 5 μm where an increase in the deposition efficiency is observed. For the turbulent case great impact of turbulent diffusion on particles below 1 μm can be identified compared to laminar flow. The impact on larger particles above 1 μm due to increased inertial impact because of increased mixing of the particles can also be identified from Figure 5.50. For the simple analytical deposition model given by Gormley and Kennedy (1949) in Equation (2.39) for laminar tube flow the same decrease in deposition efficiency can be observed for increasing particle diameter. But because Brownian diffusion is the only deposition mechanism in the model there is no minimum in the deposition efficiency and it goes practically to zero for particle sizes above a couple of micrometers. It can also be observed that the simple analytical laminar deposition model underestimate the deposition compared to the CFD simulations. The reason for this is that it is valid only for fully developed laminar flow and does not take entrance effects into account and the inertial deposition on the top of the monolithic catalyst. The simple empirical deposition model, Equation (4.69) for turbulent tube flow is able to model the minimum in deposition efficiency for particles between about 0.1 and 1 μm and capture the increase in deposition efficiency for an increasing particle diameter above 1 μm due to increasing turbulent diffusion. It can also be observed that it underestimates the deposition considerably compared to CFD modelling of turbulent deposition, because the model is used in the laminar flow regime (Reynolds number about 400) were it is not valid. Another drawback of the simple empirical deposition model, Equation (4.69) for turbulent tube flow is that it does not take the entrance effect due to the turbulence in front of the catalyst, and the transition from turbulent to laminar flow through half of the channel, into account. With a velocity of 4.56 m/s and a void fraction of 0.66 the velocity in the channels is about 6.9 m/s which gives a Reynolds number in the tube of about 400, i.e. the flow is laminar and the turbulent diffusion is negligible once the flow is developed.

Figure 5.51 shows a comparison between the experimental data, the simple empirical model for particle deposition, Equation (4.69) in turbulent tube flow based on Wood (1981a) and the analytical solution for particle deposition in laminar tube flow given by Gormley and Kennedy (1949) (Equation (2.39)). The data shown are deposition in the channels from 1 cm to 50 cm (the monolith minus the first 1 cm) in the axial length of the monolith whereby the deposition due to inertial impaction on the top has been removed. It can be observed from Figure 5.51 that the simple empirical model for turbulent deposition underestimate the deposition significantly because the physical flow is developing

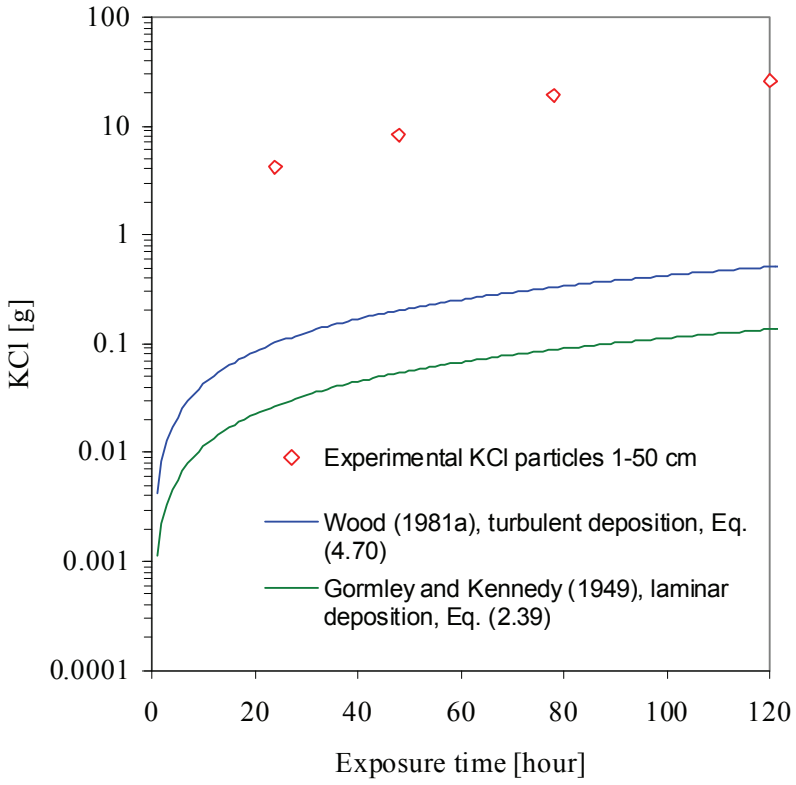

Figure 5.51: Experimental measurements of deposition of KCl particles (accumulated mass) in a DNX x30 monolithic catalyst versus exposure time. The experimental data is without inertial impact (the first 1 cm of the catalyst). Volume flow, V = 40 Nm^3/h and temperature, T=623 K. Comparison with a simple empirical model for turbulent flow Equation (4.69) and a simple analytic model for laminar flow, Equation (2.39) given by Gormley and Kennedy (1949) for deposition in a 40 cm long pipe with a diameter of 3.4 mm. Average velocity, v_{avg} = 4.56 m/s, temperature, T = 623 K and dynamic viscosity, $\mu = 3.11 \cdot 10^{-5}$ kg/m-s.

through the monolithic channels and the presence of turbulence in about half the length of the monolithic channels. The model, Equation (4.69) is only valid for fully developed turbulent flow but used for a Reynolds number only about 400 which corresponds to laminar flow. It can also be observed that the deposition model for laminar tube flow, Equation (2.39) given by Gormley and Kennedy (1949) underestimate the deposition even more.

Figure 5.52 shows a comparison of the experimental results for the average deposition rate of KCl particles in the axial length of the monolithic catalyst channels with CFD simulations of the average deposition rate of KCl particles for

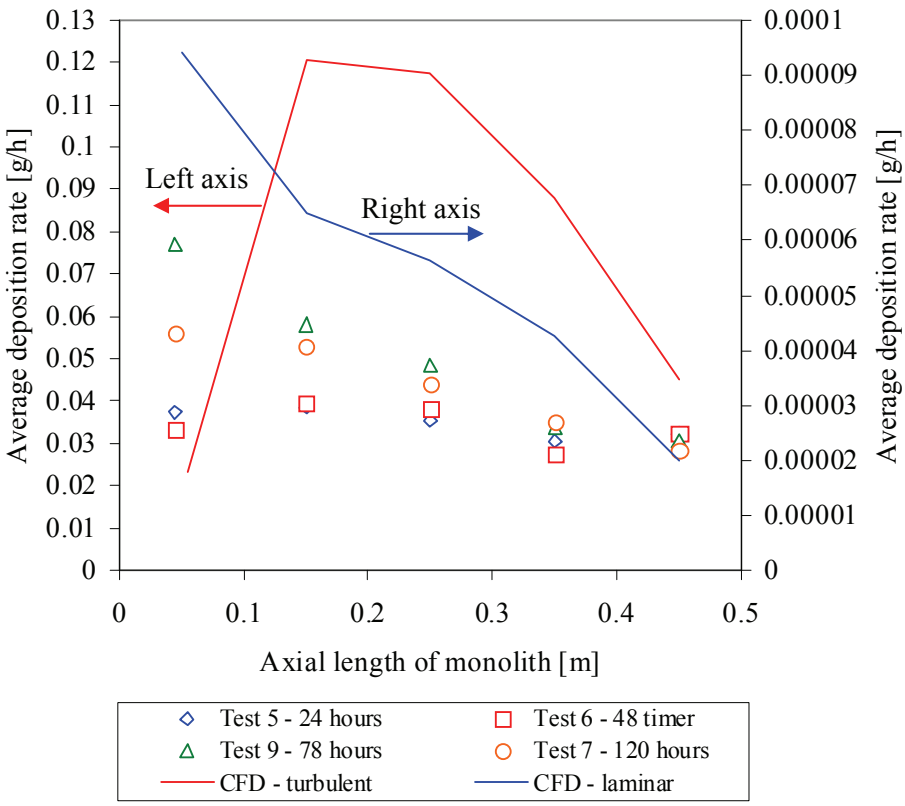

Figure 5.52: Average deposition rate of KCl particles in the axial length of a DNX x30 monolithic catalyst channels for 24, 48, 78 and 120 hours of exposure time, respectively. The average deposition rate has been determined in the channels of the monolith in the intervals 1-10 cm, 10-20 cm, 20-30 cm, 30-40 cm and 40-50 cm, respectively. Comparison with turbulent CFD simulations of DNX x30 monolith catalyst. Left y-axis is for the experiemtal results and the turbulent CFD case. Right y-axis is for the laminar CFD case. Average velocity above catalyst, v_{avg} = 4.56 m/s, temperature, T = 623 K and dynamic viscosity, $\mu = 3.11 \cdot 10^{-5}$ kg/m-s. Particles modelled using DPM tracking 1.000.000 particles representing the real particle size distribution obtained from Figure 5.23.

laminar and turbulent flow through the catalyst, respectively. The average deposition has been determined in the channel of the monolith in the corresponding intervals from 1-10 cm, 10-20 cm, 20-30 cm, 30-40 cm and 40-50 cm, respectively. It can be observed that the qualitative agreement between the average deposition rate for the turbulent CFD simulation and the experimental results are reasonable but the CFD simulation overpredicts the average deposition flux in the channels by a factor of about 2.

The laminar CFD simulation underpredicts the average deposition flux in the channels by several orders of magnitude. The reason for this is that in laminar flow about 99% of the total particle deposition is on the top of the monolithic catalyst.

The maximum in the average deposition flux for the turbulent case from 15 to 25 cm in the axial length of the monolith is due to entrance effects while the decrease in average deposition flux in the last half of the monolith is because the flow is now being fully developed. An increase in the average deposition flux in the first part of the monolith is also observed as seen in the deposition flux from Figure 5.46.

The average deposition flux observed from the turbulent CFD simulations compared to the laminar CFD simulations support the hypothesis that turbulence is the dominating deposition mechanism in the channels of the monolithic catalyst.

5.3.2 CFD model for deposit build-up

A general dynamic CFD model for prediction of particle deposition and deposit build-up in SCR DeNO$_x$ monoliths has been implemented. The model is based on a particle-wall interaction model in the Euler-Lagrangian frame of reference where the grow-up velocity of the deposit has been calculated based on the accumulated mass from the particles adhering to the walls. Based on the grow-up velocity the deposit has been modelled with a moving mesh. The implemented CFD model for deposit build-up has shown to have some drawbacks because of the way the grow-up velocitites was implemented. The grow-up velocity was calculated by looping over all wall faces and for every face of the wall the face area unit vector was computed by dividing with the number of nodes connected to a given face. This vector was then multiplied by the scalar product of the grow-up velocity for this wall cell face and the current time step in order to get a partial node displacement (displacement due to grow-up on this particular wall cell face). For every wall cell face a loop over all connected nodes is performed, and every node will be displaced incrementally with the partial node displacement vector for this cell face. After the wall face loop is accomplished, the total node displacement vector for every node will be the sum over all partial node displacement vectors from all node adjacent faces of the wall

This only works well if the number of particles hitting and becoming attached to a wall is very high in order to get a very uniform distribution of particles on the wall

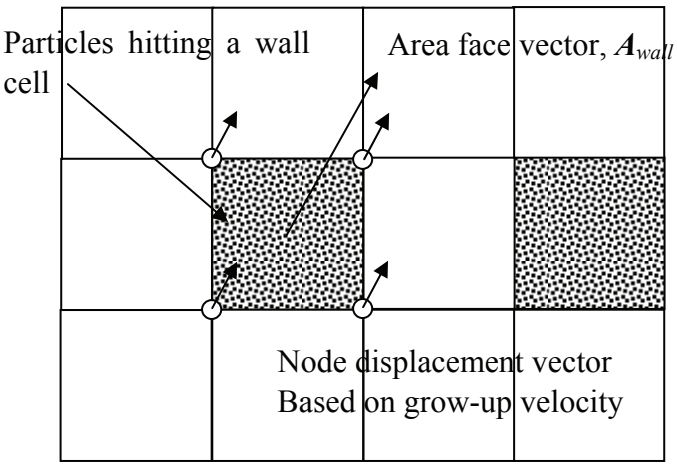

Figure 5.53: Schematic illustration of "chess board" effect for a wall surface hex mesh.

cell faces and thereby a statistically safe number for the particles hitting and attaching to a given wall cell face. This is especially a problem on the top of the monolithic catalyst because the deposition efficiency is very low and only about 2% in the CFD calulations. This means that when tracking "only" 1.000.000 parcels of particles representing the real mass flow of particles only about 20.000 parcels of particles hit the top surface. With only about 1750 wall cell faces in the mesh on the top surface of the monolith this gives an average of about 11 particles per wall cell face, which gives a very poor statistically representation of the particle deposition. The very poor statistically particle representation therefore gives a kind of "chessboard" effect as schematically illustrated in Figure 5.53. This can be seen from e.g. Figure 5.54 showing the number of hits for both a laminar and turbulent flow simulation, where the maximum number of hits per cell is 162 hits. This is a very low number of hits and as also can be seen from Figure 5.54, which gives this kind of "chessboard" effect with a very uneven distribution of the particle mass flow in each cell. For a hex mesh the number of nodes connected to a given surface is four and therefore the grow-up velocity in each node is one-fourth of the total grow-up velocity for that given surface. The node displacement is therefore underestimated with one-fourth if the particle distribution on the surfaces that have been hit has a "chessboard" distribution.

From Figure 5.54 it can be observed that the distribution is non-uniform because the number of parcels representing the real number of particle is to low in order to have a representative statistic of the particles especially hitting the top surface of

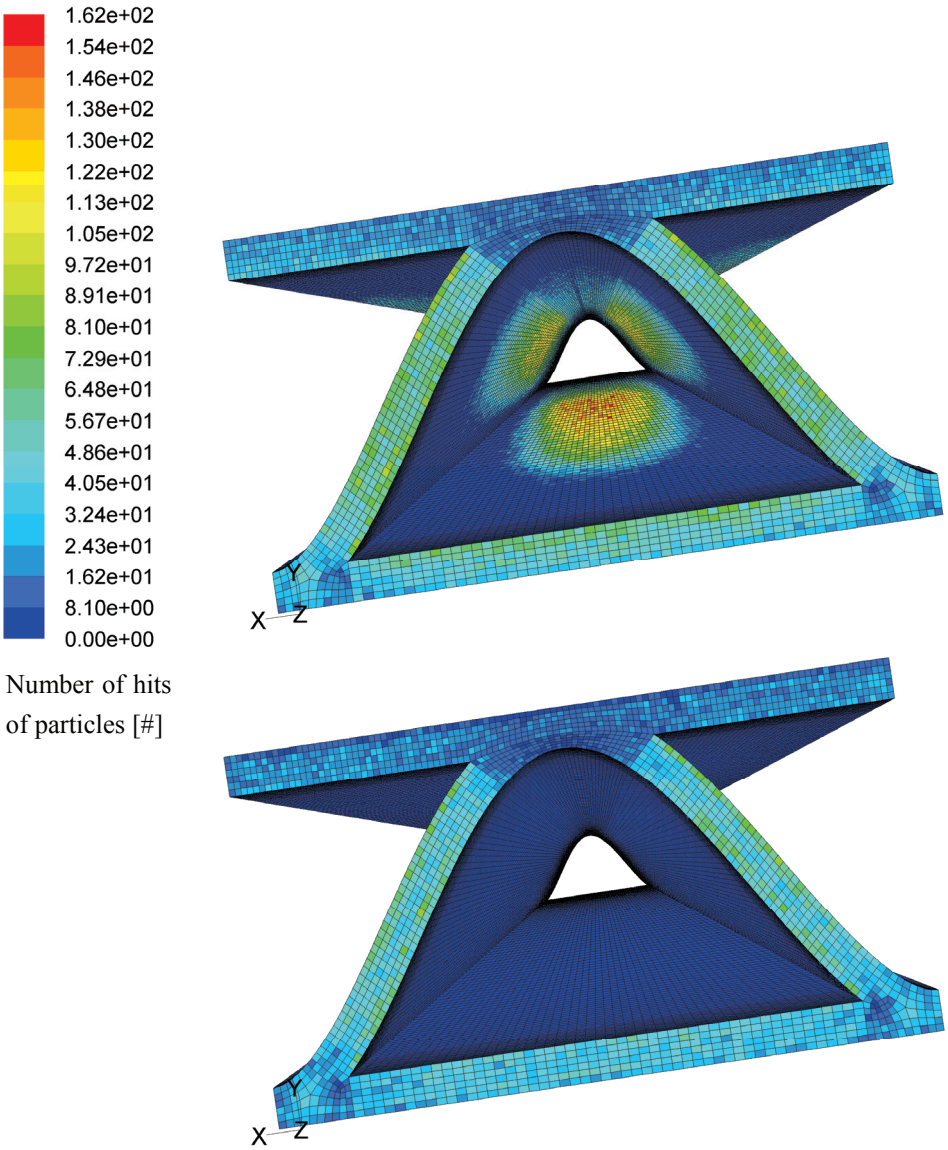

Figure 5.54: Contour plot of number of hits of particles in a DNX x30 monolithic catalyst after initially one time step (one hour) of exposure of KCl particles in turbulent flow and laminar flow, respectively.

the monolithic catalyst and the inlet section. The grid movement due to deposition of KCl particles over time is therefore underestimated in worst case up to a factor of four. The general CFD model for prediction of particle deposition and deposit build-up in SCR DeNO$_x$ monoliths can still be used to detect critical areas of deposit grow-up even though is underestimates the real geometric changes due to particle deposition.

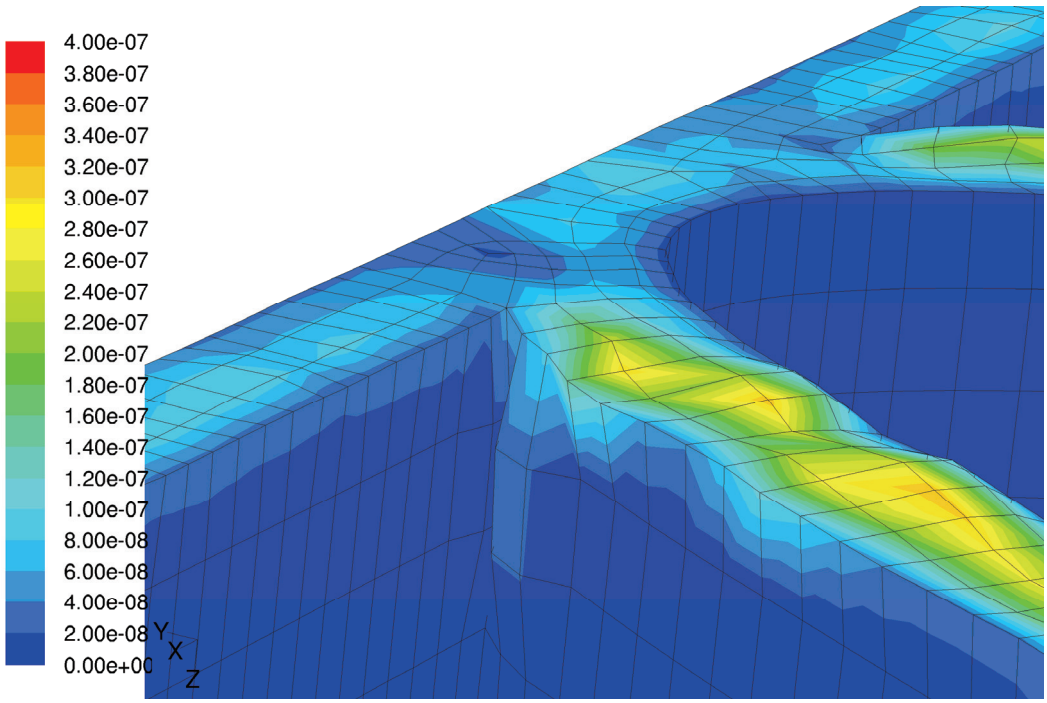

Figure 5.55: Close-up of grow-up velocity in the corner at the inlet of a DNX x30 monolithic catalyst after 372 hours of exposure to KCl particles in turbulent flow. Average velocity above catalyst, v_{avg} = 4.56 m/s, temperature, T = 623 K and dynamic viscosity, $\mu = 3.11 \cdot 10^{-5}$ kg/m-s. Particles modelled using DPM tracking 100.000 particles representing the real particle size distribution obtained from Figure 5.23.

Figure 5.55 shows the grow-up velocity after 372 hours of exposure to KCl particles for a turbulent flow simulation and deposition on the top and in the sharp corners are clearly identified.

5.3.3 Catalyst with 8 mm Hydraulic Diameter

Experimental investigations were also carried out on a SCR DNX x80 monolithic catalyst (dummy) with a hydraulic diameter of 8 mm which was exposed to potassium chloride, KCl, particles over 10 days.

Figure 5.56 illustrates the plugging after 10 days and a severe deposition can be identified. It can be observed that the same “volcano type” of deposition and streamlining is found on top of the monolith as also observed on full-scale low-dust applications – see Figure 5.27.

Figure 5.56: Plugging of SCR DNX x80 monolithic catalyst due to KCl particles after 10 days of exposure.

It can again also be observed that deposition is "optimizing" the flow geometry of the channels in order to obtain circular channels. Unfortunately the catalyst in the experiment was eroded during the exposure time as seen on Figure 5.56 and it was therefore not possible to detect the accumulated mass in the catalyst. But deposition due to inertial impaction on the top of the catalyst is clearly identified and also enhanced deposition due to entrance effect and turbulent diffusion is clearly seen in the top part of the catalyst.

5.4 Concluding Remarks

5.4.1 Experimental Results of Submicrometer Particle Deposition

Polydisperse and monodisperse KCl aerosol particle deposition measurements of submicrometer particles in a three-meter straight and bent pipe have been carried out. The experimental results showed that electrostatic forces, because of space charging due to charged particles, was an important deposition mechanism in laminar pipe flow having the same order of magnitude as deposition due to Brownian diffusion. Measurements of the total average charge on high and low aerosol particle number concentrations showed that the particles were carrying negative average charges. It was also shown that particles neutralized to approximately a Boltzmann charge equilibrium compared to particles with the same initial particle number concentration carrying an average charge due to the process of generation had lower deposition efficiency. The experimental measurements showed that the space charging more or less could be suppressed by lowering the particle number concentration. Secondary flow was shown to have an impact on the deposition efficiency for particles below 100 nm in a bent pipe for the given flow configuration.

The experimental measurements were compared with CFD simulations and in general the agreement between simulations and experiments were very good. It was observed that CFD simulations with particles carrying an average charge underestimated the deposition efficiency compared to the experimental results. The reason for this was that real particles are not carrying an average number of elementary charges but are carrying an integer number of elementary charges and therefore have higher electrical mobility than if they were carrying an average number of elementary charge less than one.

For the monodisperse particles it was shown that the electrostatic effects could be suppressed due to very low particle concentrations by selecting the particles with the NDMA. Very good agreement was observed when comparing with CFD simulations. For particles below about 40 nanometers, it was observed that the experimental results started to deviate from the numerical results and show slightly higher deposition efficiency and this was believed to be due to additional contribution from uncharged particles being carried out through the sampling slit in the NDMA together with the desired positive charged particles.

5.4.2 Experimental Results of Micrometer Particle Deposition

Particle deposition measurements in a bend in connection with a straight vertical pipe were carried out using monodisperse micrometer cross-linked PMMA particles with diameters of 10, 20, 30 and 40 μm, respectively. The particle-wall interaction model implemented in CFD was validated against the experimental results and good agreement was found when fitting the asperities, z_0, for the individual particle diameters against the total deposition efficiency. The experiments also showed that the deposition efficiency for the bend due to inertial impact and the deposition efficiency for the straight pipe due to Saffman lift force showed some differences between the experimental results and the CFD results. This was believed to be due to differences between the CFD model of the bend (which was modelled as a perfect 90-degree bend and a straight piece) and the bend in the experiments. The experimental investigations showed a maximum for the total deposition efficiency of about 80% (Saffman and inertial impact) and about 70% for the Saffman lift force for 30 μm particles. The deposition efficiency due to inertial impact in the bend showed a maximum of about 40% for 20 μm particles because particle inertia started to become important and the particles began to bounce and be re-suspended. In general, it was concluded based on comparison between the experimental results and CFD simulations that the particle-wall interaction model predicted the trends in the experimental results for both the overall deposition efficiency as well as the deposition efficiency due to inertial impact and Saffman lift force.

Comparison between the experimental results for deposition efficiency due to Saffman lift in a vertical deposition pipe, CFD simulations and a pseudo steady-state model has also been carried out. The CFD simulations were based on developing flow in the same vertical deposition pipe and the pseudo steady-state model was based on an analytical expression for Saffman lift. The agreement between the experimental result of deposition due to Saffman lift and the simulation of developing flow and particle concentration profile was good and comparison with the analytical expression for deposition due to Saffman lift also gave good agreement. It was also observed that due to the assumption of perfect adhering walls the CFD simulations and the simple model does not capture the experimental observed maximum in deposition efficiency for 30 μm particles. It was also observed that for particles above 30 μm the deviation between the CFD simulation and the analytical expression becomes larger because acceleration of the particles becomes important. Therefore, for larger particles the pseudo steady-state assumption is a crude assumption.

5.4.3 Pilot Scale Experimental Results

Pilot scale KCl aerosol particle plugging experiments using commercial corrugated-type SCR monolithic catalysts obtained from Haldor Topsøe A/S have been carried out. DNX x30 SCR monolithic catalysts (dummies) with a hydraulic diameter of 3.4 mm were exposed to potassium chloride, KCl, particles over time for 24, 48, 78, 120 and 158 hours. The deposited mass of KCl aerosol particles in the monolithic catalysts was determined by washing the monoliths after each experiment.

It was observed that the data points showed some scattering for the repeated experiments for 24 and 48 hours, respectively due to the fact that it was extremely difficult to re-create exactly the same conditions in each new experiment. Another problem was deposition of small fragments ("popcorn"), which broke of the walls upstream the catalyst, on top of the catalyst during the experiments and initiated channel plugging and accelerated deposition on top of the catalyst due to inertial impact. Nevertheless, the experiments provided interesting results of particle deposition under low-dust conditions. The experiments showed a total deposition efficiency in the monolithic catalyst of about 30% and a "volcano type" of deposition pattern was observed which has also been seen in full-scale low-dust applications. Impactor measurements data from a previous study showed that the particle size distribution consisted of particles between 0.04 and 10 μm. This is corresponding to what is found in full-scale low-dust application. Measurement of the average number of elementary charges on the aerosol particles showed that the average number of elementary charges was about 0.001 and that the particles were positively charged. Comparison with CFD simulations assuming laminar and turbulent flow in the monolith, respectively have confirmed that turbulent diffusion in the top part of the monolith channels and inertial impact and gravitational settling in the flow stagnation area on the top of the monolith are the domination mechanisms for plugging of the catalyst.

A general dynamic CFD model for prediction of particle deposition and deposit build-up in SCR DeNO$_x$ monoliths has been implemented. The model is based on a particle-wall interaction model in the Euler-Lagrangian frame of reference where the grow-up velocity of the deposit has been calculated based on the accumulated mass from the particles adhering to the walls. Based on the grow-up velocity the deposit has been modelled with a moving mesh. The model has shown to have some drawbacks because of the way the grow-up velocitites was implemented which underestimates the grid movement due to deposition of particles. The particle-wall interaction model was used to estimate accumulated mass of KCl particles over time. For laminar flow the CFD model underpredicted

the accumulated mass compared to the experimental results with a factor of about 17 and for turbulent flow the CFD model overpredicted the experimental result with a factor of about 2.4. A comparison with the deposition profile in the axial length for turbulent flow show reasonable agreement with the experimental results and confirmed that inertial impact and gravitational settling together with turbulent diffusion in the flow stagnation area on top of the monolith and turbulent diffusion and entrance effects in the channels were the dominating mechanisms for deposition. The comparison between experiments and CFD simulation also support the hypothesis that turbulent diffusion because of turbulent flow above the catalyst and turbulence convected in to the monolith in the entrance length (because of transition from turbulent to laminar flow through the monolithic channels) must be responsible for most of the deposition observed in full-scale applications. In general, it was concluded that in order to reduce plugging of the catalyst corner effects in the monolith should be reduced and the surface area on the top of the monolith should be reduced.

Experimental investigation were also carried out on a SCR DNX x80 monolithic catalyst (dummy) with a hydraulic diameter of 8 mm, which were exposed to potassium chloride, KCl, particles over 10 days and severe deposition was identified. The same “volcano type” of deposition and streamlining was identified on the top of the monolith. The same kind of “optimization” of the inlet of the monolith in order to obtain cylindrical channels was observed as was seen from the experiments with DNX x30 SCR monolithic catalysts. Unfortunately the SCR DNX x80 monolithic catalyst in the experiment was eroded during the exposure time and it was therefore not possible to detect the accumulated mass in the catalyst. But deposition due to inertial impact on the top of the catalyst was clearly identified as well as enhanced deposition due to entrance effect and turbulent diffusion in the top part of the catalyst.

Chapter 6

Summary, Conclusions and Suggestions for Further Work

The objective of this work is to contribute to an increased knowledge about particle dispersion and deposition mechanisms in pipe flow and plugging of SCR $DeNO_x$ monolithic catalysts. A comprehensive literature study on particle dispersion and deposition mechanisms was carried out and experimental investigations of submicrometer and micrometer particle deposition in laminar pipe flow were carried out. Furthermore pilot scale KCl aerosol particle plugging experiments using commercial corrugated-type SCR monolithic catalysts obtained from Haldor Topsøe A/S were carried out. The results are summarized below and suggestions to further work are given.

6.1 Submicrometer Aerosol Particle Deposition

6.1.1 Summary and Conclusions

An experimental setup has been designed and built with the purpose of investigating polydisperse and monodisperse submicrometer aerosol particle deposition in laminar flow. The experimental setup used a Six-Jet Atomizer for generating aerosol particles based on a salt solution (KCl) in the atomizer. The deposition of aerosol particles were measured using a Scanning Mobility Particle Sizer (SMPS) Spectrometer in order to determine the size distribution and number concentration at the inlet and outlet of a three-meter straight and bent aerosol deposition tube and the average number of elementary charges was measured using and Electrometer.

The experimental results for KCl aerosol particle deposition showed that electrostatic forces, because of space charging due to charged particles, were an important deposition mechanism in laminar flow and it was found that it had the same order of magnitude as deposition due to Brownian motion. Measurements of the total average charge on the aerosol particles for high and low aerosol particle number concentrations showed that the particles were carrying negative average charges. It was also shown that particles which were neutralized to approximately Boltzmann charge equilibrium had a lower deposition efficiency compared to particles with the same initial particle number concentration carrying an average charge due to the process of generation. The measurements also showed that the space charging more or less could be suppressed by lowering the particle number concentration an order of magnitude, e.g. from $2 \cdot 10^6$ to $2 \cdot 10^5$ #/cm^3. Secondary flow was shown to have an impact on the deposition efficiency for particles below 100 nm in a bent pipe and enhanced the deposition efficiency about 15% point for KCl aerosol particles in the experimental setup.

In general, good agreement was found between the experimental results and CFD simulations. However, CFD simulations with particles carrying an average charge underestimated the deposition efficiency up to 20 to 30 per cent point compared to the experimental results because real particles are not carrying an average number of elementary charges but integer number of elementary charges. The particles therefore have higher electrical mobility than if they were carrying an average number of elementary charges less than one. For the monodispersed particles it was shown that the electrostatic effects could be suppressed due to very low particle concentrations by selecting the particles with the NDMA. When comparing with CFD simulations very good agreement was observed. For particles below about 40 nanometers, it was observed that the experimental results started to deviate from the numerical results and show slightly higher deposition efficiency. This is believed to be due to additional contribution from uncharged particles being carried out through the sampling slit in the NDMA together with the desired positive charged particles.

6.1.2 Suggestions for Further Work

The experimental work presented in this thesis for submicrometer particles has shown that electrostatic forces are a very important dispersion and deposition mechanisms. The work also showed that in order to simulate the electrostatic dispersion with CFD the charge distribution on the aerosol particles has to be known because simulations only using the average charge on the particles underestimated the electrostatic dispersion. Measurements of the charge

distribution on the aerosol particles should therefore be further investigated in detail and implemented in the CFD models.

6.2 Micrometer Particle Deposition

6.2.1 Summary and Conclusions

An experimental setup has been built for measuring deposition of micrometer particles in a 1.0 meter straight pipe using monodisperse micrometer cross-linked PMMA particles with diameters of 10, 20, 30 and 40 μm, respectively. The particle-wall model implemented in CFD was validated against the experimental results and good agreement was found when fitting the asperities, z_0, for the individual particle diameters against the total deposition efficiency. However, the CFD simulations of the deposition efficiency in the bend due to inertial impact and the deposition efficiency for the straight pipe due to Saffman lift force showed some deviation from the experimental results. This was believed to be due to differences between the CFD model of the bend and the bend in the experiments. The experimental investigations showed a maximum for the total deposition efficiency of about 80% (Saffman and inertial impact) and about 70% for the Saffman lift force for 30 μm particles. The deposition efficiency due to inertial impact in the bend showed a maximum of about 40% for 20 μm particles because particle inertia started to become important and the particles began to bounce and be re-suspended. In general, it was concluded that the particle-wall interaction model predicted the trends in the experimental results for both the overall deposition efficiency as well as the deposition efficiency due to inertial impact and Saffman lift force.

CFD simulations of the deposition efficiency due to Saffman lift force in a developing flow in a vertical deposition pipe with a perfectly adhering wall were compared with the deposition efficiency based on a pseudo steady-state analytical model and very good agreement was found. Comparison was also carried out with the experimental data for the deposition efficiency due to Saffman lift force and the agreement was very good. However, due to the assumption of perfect adhering walls the CFD simulations and the simple model did not capture the maximum in deposition efficiency for 30 μm particles as observed from the experimental data. It was also observed that for particles above 30 μm that the deviation between the CFD simulation and the analytical expression based on a pseudo steady-state model becomes larger because acceleration of the particles becomes important.

Therefore, for larger particles the pseudo steady-state assumption is a crude assumption.

6.2.2 Suggestions for Further Work

The experimental work presented in this thesis for micrometer particles have shown the importance of the Saffman lift force on the deposition efficiency. But more experimental work should be carried out with different particle sizes and particle densities. Detailed experiments of the influence of the direction of gravity, fluid velocity, etc. should be carried out. The influence of electrostatic forces has been neglected in the present work on micrometer particle deposition but should be investigated in detail because it could influence the deposition efficiency.

6.3 Pilot Scale Plugging Experiments

6.3.1 Summary and Conclusions

A major issue using SCR $DeNO_x$ for both high dust and low-dust applications of a coal fired power stations is the risk of deposition and plugging of the monolithic catalysts during operation due to fly ash particles in the flue gas. Besides fly ash particles, plugging can also be due to deposition of ammonium sulphates on the catalyst which would also cause deactivation. Plugging of the monolith will make the pressure loss across the monolith increase which is another undesired effect. Sometimes it is observed that the fly ash found in the plugged channels has been hardened, and often a crust of hardened fly ash is found especially at the top and bottom of the plugged channels.

In order to investigate plugging in SCR $DeNO_x$ monolithic catalysts pilot scale KCl aerosol particle plugging experiments using commercial corrugated-type SCR monolithic catalysts obtained from Haldor Topsøe A/S have been carried out. The monolithic catalysts used in the tests were respectively DNX x30 and DNX x80, and the monoliths were dummies in the sense that they consisted only of a corrugated, fibre-reinforced titanium dioxide (TiO_2) carrier and were not impregnated by divanadium pentaoxide (V_2O_5) and tungsten trioxide (WO_3). DNX x30 SCR monolithic catalysts (dummies) with a hydraulic diameter of 3.4 mm were exposed to potassium chloride, KCl, particles over time for 24, 48, 78, 120 and 158 hours. The deposited mass of KCl aerosol particles in the monolithic catalysts was determined by washing the monoliths after each experiment.

The total deposition efficiency of the DNX x30 SCR monolithic catalysts in the pilot scale experiments was about 30%. The deposition pattern observed was a "volcano type" of deposition pattern which was also seen in full-scale low-dust applications. Impactor measurements data from a previous study showed that the particle size distribution consisted of particles between 0.04 and 10 μm corresponding to what is found in full-scale low-dust applications. The average number of elementary charges was also measurement on the KCl aerosol particles in the pilot scale experiments and showed that the particles were positively charged and carried 0.001 numbers of elementary charges.

A general CFD model for prediction of particle deposition and deposit build-up in SCR $DeNO_x$ monoliths has been implemented. CFD simulations assuming laminar and turbulent flow through the monolith, to test the assumption of the type of flow, has shown that turbulent diffusion and turbulent flow is the dominating mechanism for particle deposition and plugging of the catalyst. It was observed that for laminar flow the CFD model underpredicted the accumulated mass compared to the experimental results with a factor of about 17 and for turbulent flow the CFD model overpredicted the experimental results with a factor of about 2.4. It was also confirmed that inertial impact and gravitational settling on top of the monolith and turbulent diffusion and entrance effects were the dominating mechanisms for deposition. This was based on a comparison with the average deposition flux in the axial length for laminar and turbulent flow, where turbulent flow showed good agreement with the experimental results. The hypothesis that turbulent flow above the catalyst and the flow pattern arising from the developing flow from turbulent to laminar flow through the monolithic channels must be responsible for most of the deposition observed in full-scale applications was also supported by comparison between experiments and CFD simulations. In general, it was concluded that in order to reduce the plugging of the catalyst corner effects in the monolith should be reduced and the surface area on the top of the monolith should be reduced.

Experimental investigations were also carried out on a SCR DNX x80 monolithic catalyst (dummy) with a hydraulic diameter of 8 mm which were exposed to potassium chloride, KCl, particles over 10 days and severe deposition was identified. Deposition due to inertial impact on the top of the catalyst was clearly identified and also enhanced deposition due to entrance effect and turbulent diffusion was clearly identified in the top part of the catalyst. The same "volcano type" of deposition and streamlining was identified on the top of the monolith and also the same kind of "optimization" of the inlet of the monolith in order to obtain cylindrical channels was observed as was seen from the experiments with DNX x30 SCR monolithic catalysts.

6.3.2 Suggestions for Further Work

The experimental work presented in this thesis has shown that it is difficult to obtain repeatable results from pilot scale experiments. One of the problems was to re-create exactly the same conditions in each new experiment due to e.g. small differences in flame temperature, gas flow, particle concentration, etc. Another problem was also small fragments of agglomerates ("popcorn") which broke of the walls upstream of the catalyst and was deposit on top of the catalyst during the experiments and initiate channel plugging and accelerated deposition on top of the catalyst due to inertial impact. This could e.g. be avoided by adding a cyclone upstream the monolithic catalyst in order to remove the fragments. In order to obtain better average values for the accumulated mass of KCl particles in the monolithic catalyst more samples should be obtained for a given exposure time. Measurements should be carried out where the flue gas volume flow would be varied and the aerosol concentration in the flue gas should also be varied in order to investigate the influence on plugging.

CFD modelling of deposition build-up is an extremely difficult task due to the complexity of the particle-wall interaction and due to the flow in the experiments being in transition from turbulent to laminar flow through the monolith. Large Eddy Simulations (LES) should therefore be carried out in order to simulate the flow transition through the monolith. Due to the fact that detailed experimental information regarding bouncing from the surface of the catalyst material does not exist the particles were assumed not to bounce in the CFD simulations. Therefore, detailed measurements of bouncing from the catalyst surface in order to model bouncing correct in the CFD model should be carried out. Studies of re-entrainment from the catalyst should also be carried out and studies with larger micrometer-sized particles corresponding to high-dust applications should also be carried out.

References

Abuzeid, S., Busnaina, A.A. and Ahmadi, G. (1991). Wall Deposition of Aerosol Particles in a Turbulent Channel Flow. Journal of Aerosol Science, 22(1) pp. 43-62.

Ahmadi, G. and Guo, S. (2007). Bumpy Particle Adhesion and Removal in Turbulent Flows including Electrostatic and Capillary Forces. *The Journal of Adhesion*, **83**, pp. 289-311.

Albrecht, F. (1931). Theoretische Untersuchungen über die Ablagerung von Staub aus strömender Luft und ihre Anwendung auf die Theorie der Staubfilter. *Physikalische Zeitschrift,* **32**(1), pp. 48-56.

Alonso, M and Alguacil, F.J. (2007). Penetration of Aerosol Undergoing combined Electrostatic Dispersion and Diffusion in a Cylindrical Tube. *Aerosol Science*, **38**, pp. 481-493.

Bartholomew, C. (2007). Catalyst Deactivation and Regeneration. *ChemInForm*, **38**(38), pp. 255-322.

Beeckman, J.W. and Hegedus, L.L. (1991). Design of Monolith Catalysts for Power Plant NO_x Emission Control. *Industrial & Engineering Chemistry Research*, **30**, pp. 969-978.

Benson, S.A., Laumb, J.D., Crocker, C.R. and Pavlish, J.H. (2005). SCR Catalyst Performance in Flue Gases Derived from Subbituminous and Lignite Coals. *Fuel Processing Technology*, **86**, pp. 577-613.

Bird, R.B., Stewart, W.E. and Lightfoot, E.N. (2002). *Transport Phenomena* (2nd ed.). John Wiley & Sons, Inc., New York.

Blasius, H. (1913). Das Aehnlichkeitsgesetz bei Reibungsvorgaengen in Fluessigkeiten. pp. 1-42.

Bosch, H. and Janssen, F. (1988). Catalytic Reduction of Nitrogen Oxides – A Review on the Fundamentals and Technology. *Catalysis Today*, **2**, pp. 369-532.

Bowling, R.A. (1985). An Analysis of Particle Adhesion on Semiconductor Surfaces. *J. Electrochem. Soc.: Solid-state science and Technology*. **132**(9), pp. 2208-2214.

Byron P.A. and Willeke, K. (2005). *Aerosol Measurement. Principles, Techniques and Applications* (2nd Edition). John Wiley & Sons, Inc., Hoboken, New Jersey.

Castellino, F. (2008). *Deactivation of SCR Catalysts by Additives*. Department of Chemical and Biochemical Engineering, Technical University of Denmark, Ph.D. Thesis.

Chen, D.-R. and Pui, D.Y.H. (1995). Numerical and Experimental Studies of Particle Deposition in a Tube with a Conical Contraction – Laminar Flow Regime. *Journal of Aerosol Science*, **26**(4), pp. 563-574.

Chen, F. and Lai, A.C.K. (2004). An Eulerian Model for Particle Deposition under Electrostatic and Turbulent Conditions. Journal of Aerosol Science, **35**, pp. 47-62.

Chen, Y.K. and Yu, C.P. (1993). Particle Deposition from Duct Flow by Combined Mechanisms. *Aerosol Science and technology*, **19**, pp. 389-395.

Cherkaduvasala, V., Murphy, D.W. and Ban, H. (2007). Aerodynamic Characteristics of Popcorn Ash Particles. *Particulate Science and Technology*, **25**, pp. 275-287.

Cherukat, P. and McLaughlin, J.B. (1994). The Inertial Lift on a Rigid Sphere in a Linear Shear Field near a Flat Wall. *Journal of Fluid Mechanics*, **263**, pp. 1-18.

Cleaver, J.W. and Yates, B. (1975). A Sub Layer Model for the Deposition of Particles from a Turbulent Flow. *Chemical Engineering Science*, **30**, pp. 983-992.

Corn, M. (1966). In: *Aerosol Science*, by Davis, C.N. Academic Press, London, pp. 359-392.

Couch, G. (2006). Ash Management in Coal-Fired Power Plants. CCC/118, London, UK, IEA Clean Coal Centre.

Dahneke, B. (1995). Particle Bounce or Capture – Search for an Adequate Theory: I. Conservation-of-Energy Model for a Simple Collision Process. *Aerosol Science and Technology,* **23**, pp. 25-39.

Davies, C.N. (1966a). Deposition of Aerosols from Turbulent Flow through Pipes. *Proceedings of the Royal Society of London series A-Mathematical and Physical Sciences*, **289**(1417), pp. 235-246.

Davies, C.N. (1966b). Brownian Deposition of Aerosol Particles from Turbulent Flow through Pipes. *Proceedings of the Royal Society of London series A-Mathematical and Physical Sciences*, **290**(1423), pp. 557-562.

Davies, C.N. (1966c). *Aerosol Science*. Academic Press, London.

Davies, C.N. (1973). Diffusion and Sedimentation of Aerosol Particles From Poiseuille Flow in Pipes. *Aerosol Science*, **4**, pp. 117-128.

Dean, W.R. (1927). Note on the Motion of Fluid in a Curved Pipe. *Philosophical Magazine and Journal of Science*. **4**(20), pp. 208-223.

Delmas, R., Serça, D. & Jambert, C. (1997). Global Inventory of NO_x Sources. *Nutrient Cycling in Agroecosystems*, **48**, pp. 51-60.

Ebert, F. (1992). Interaction Between the Motion of Particles and Their Turbulent Carrier Fluid Flow. *Particle & Particle Systems Characterization*, **9**(2), pp. 116-124.

Einstein, A. (1905). Motion of Suspended Particles in Stationary Liquids Required from the Molecular Kinetic Theory of Heat. *Annalen der Physik*, **17**, pp. 549-560.

Energi E2. *Amagerværket* (in Danish). Brochure.

Evans, A.G., Gulden, M.E. and Rosenblatt, M. (1978). Impact Damage in Brittle Materials in the Elastic-Plastic Response Regime. *Proceedings of the Royal Society of London. Series A, Mathematical and Physical Sciences*, **361**(1706), pp. 343-365.

Fan, F.G. and Ahmadi, G (1993). A Sublayer Model for Turbulent Deposition of Particles in Vertical Ducts with Smooth and Rough Surfaces. *Journal of Aerosol Science*, **24**(1), pp. 45-64.

Fan, F.G. and Ahmadi, G. (2000). Wall Deposition of Small Ellipsoids from Turbulent Air Flows – A Brownian Dynamics Simulation. *Journal of Aerosol Science*, **31**(10), pp. 1205-1229.

Flagan R.C (1979). Submicron Particles from Coal Combustion. *Symposium (International) on Combustion, [Proceedings]*, **17**, pp. 97-104.

Flagan, R.C. and Friedlander, S.K. (1978). Particle Formation in Pulverized Coal Combustion – A Review. *Recent Developments on Aerosol Science*. [Symp. Aerosol Sci. Technol.], pp. 25-59.

Flagan, R.C. and Seinfeld, J.H. (1988). *Fundamentals of Air Pollution Engineering*. Prentice-Hall, Inc. New Jersey.

Fluent 6.3 User's Guide (2006). Fluent.Inc.

Forsyth, B., Liu, B.Y.H. and Romay, F.J. (1998). Particle Charge Distribution Measurement for Commonly Generated Laboratory Aerosols. *Aerosol Science and Technology*, **28**, pp. 489-501.

Forzatti, P. (2001). Present Status and Perspectives in De-NO_x SCR Catalysis. *Applied Catalysis A:* General 222, pp. 221-236.

Forzatti, P. and Lietti, L. (1996). Recent Advances in De-NO_xing Catalysis for Stationary Applications. *Heterogeneous Chemistry Reviews*, **3**, pp. 33-51.

Forzatti, P. and Lietti, L. (1999). Catalyst Deactivation. *Catalysis Today*, **52**, pp. 165-181.

Frandsen, F. and Østberg M. (1995). *Forbrænding og røggasrensning* (in Danish). Department of Chemical Engineering, Technical University of Denmark, Lyngby.

Frey, M. (2001). *Product Recovery from Spray Dryers*. Department of Chemical Engineering, Technical University of Denmark, Ph.D. Thesis.

Friedlander, S.K. (2000). *Smoke, Dust, and Haze. Fundamentals of Aerosol Dynamics* (2nd ed.). Oxford University Press, New York.

Friedlander, S.K. and Johnstone, H.F. (1957). Deposition of Suspended Particles from Turbulent Gas Streams. *Industrial & Engineering Chemistry*, **49**(7), pp. 1151-1156.

Fuchs, N.A. (1963). On the Stationary Charge Distribution on Aerosol Particles in a Bipolar Ionic Atmosphere. *Geophys. Pure Appl.*, **56**, pp. 185-193.

Gessner, F.B. and Jones, J.B. (1965). On Some Aspects of Fully-developed Turbulent Flow in Rectangular Channels. *Journal of Fluid Mechanics*, **23**(4), pp. 689-713.

Glarborg, P., Jensen, A.D. and Johnsson, J.E. (2003). Fuel Nitrogen Conversion in Solid Fuel Fired Systems. *Progress in Energy and Combustion Science*, **29**, pp. 89-113.

Goodwin, J.E., Sage, W. and Tilly, G.P. (1969). Study of Erosion by Solid Particles. *Proc. Instn. Mech. Engrs*. **184**(15) Pt. 1, pp. 279-289.

Gormley, P.G. and Kennedy, M. (1949). Diffusion from a Stream Flowing through a Cylindrical Tube. Proceedings of the Royal Irish Academy, Vol. 52, Sect. A., pp. 163-169.

Griffiths, D.J. (1999). *Introduction to Electrodynamics*, 3rd edition. Prentice Hall, New Jersey.

Guha, A. (1997). A Unified Eulerian Theory of Turbulent Deposition to Smooth and Rough Surfaces. *Journal of Aerosol Science*, **28**(8), pp. 1517-1537.

Guha, A. (2008a). Transport and Deposition of Particles in Turbulent and Laminar Flow. *Annual Review of Fluid Mechanics*, **40**, pp. 311-341.

Guha, A. (2008b). A Generalized Mass Transfer Law Unifying Various Particle Transport Mechanisms in Diulute Dispersion. *Heat Mass Transfer*. 44(**11**), pp. 1289.

Gunn, R. (1956). The Ratio of the Positive and Negative Light Ion Conductivities within a Neutral Aerosol Space. *Journal of Colloid Science*, **11**, pp. 691-696.

Gutfinger, C., Pnueli, D., Moldavsky, L. and Fichman, M. (2003). Particle Motion in Simple Shear Flow with Gravity. *Aerosol Science and Technology*, Vol. 37, pp. 841-845.

Haider, A. and Levenspiel, O. (1989). Drag Coefficient and Terminal Velocity of Spherical and Nonspherical Particles. *Powder Technology*, **58**, pp. 63-70.

He, C. and Ahmadi, G. (1998). Charged Particle Deposition in a Short Vertical Duct. *Proceedings of FEDSM'98*, 1998 ASME/FED Third International Symposium on Numerical Methods for Multiphase Flows, June 21-26, 1998, Washington, D.C., USA.

He, C. and Ahmadi, G. (1999). Particle Deposition in a Nearly Developed Turbulent Duct Flow with Electrophoresis. *Journal of Aerosol Science*, **30**(6), pp. 739-758.

Heinl, E. and Bohnet, M. (2005). Calculation of Particle-Wall Adhesion in Horizontal Gas-Solid Flow using CFD. *Powder Technology*, **159**, pp. 95-104.

Hilgraf, P. and Cohrs, H. (1992). The Practicability of the YPG Erosion Tester for the Determination of Erosion in Pneumatic Conveying Systems. *Powder Handling & Processing*, **4**(2), pp. 189-197.

Hinds, W.C. (1999). *Aerosol Technology. Properties, Behavior, and Measurement of Airborne Particles* (2nd ed.). John Wiley & Sons, Inc., New York.

Hughes, W.F. and Brighton, J.A. (1999). *Fluid Dynamics*, third edition. Schaums Outline Series, McGraw-Hill, New York.

Ingham, D.B. (1975). Diffusion of Aerosol from a Stream Flowing through a Cylindrical Tube. *Aerosol Science*, **6**, pp. 125-132.

Ingham, D.B. (1983). Diffusion from a Viscous Stream Flowing through a Rectangular Channel. *Journal of Aerosol Science*, **14**(6), pp. 741-745.

Ingham, D.B. (1984). Diffusion of Aerosols from a Stream Flowing through a Short Cylindrical Pipe. *Journal of Aerosol Science*, **15**(5), pp. 637-641.

Jensen, A.D. (1996). *Nitrogen Chemistry in Fluidized Bed Combustion of Coal*. Department of Chemical Engineering, Technical University of Denmark, Ph.D. Thesis.

Jensen, J.R. (2002). *Prediction of Fly Ash Propensities*. Internal Haldor Topsøe A/S report, 35019 JMJ/JMJ, 12/8.

Jensen, J.R. (2004). *DeNO$_x$ Deactivation Model and Experience*. Internal Haldor Topsøe A/S report, 39313 JMJ/JMJ, 26/3.

Jørgensen, S.L. (2001). *Undersøgelse af monolitter fra Nordjyllandsværket*. (In Danish) Internal Haldor Topsøe A/S report, 39313 CRH/SLJ/br, 26/11.

Kane, R.S. (1986). Comparison of two Models for Aerosol Deposition and Plugging of Pipes. *Atmospheric Environment*, **20**(1), pp. 147-149.

Kasper, G. (1981). Electrostatic Dispersion of Homopolar Charged Aerosols. *Journal of Colloid and Interface Science*, **81**(1), pp. 32-40.

Kotwal, R. and Tabakoff, W. (1981). A New Approach for Erosion Prediction Due To Fly Ash. *Journal of Engineering Power*, **103**, pp. 265-270.

Krupp, H. (1967). Particle Adhesion Theory and Experiment. *Advan. Colloid Interface Science*, **1**, pp. 111-239.

Langhaar, H.L. (1942). Steady Flow in the Transition Length of a Straight Tube. *Journal of Applied Mechanics*, **9**, pp. A55-A58.

Li, A. and Ahmadi, G. (1992). Dispersion and Deposition of Spherical Particles from a Point Source in a Turbulent Channel Flow. *Aerosol Science and Technology*, **16**, pp. 209-226.

Li, A. and Ahmadi, G. (1993a). Aerosol Particle Deposition with Electrostatic Attraction in a Turbulent Channel Flow. *Journal of Colloid and Interface Science*, **158**, pp. 476-482.

Li, A. and Ahmadi, G. (1993b). Computer Simulation of Deposition of Aerosols in a Turbulent Channel Flow with Rough Walls. *Aerosol Science and Technology*, **18**, pp. 11-24.

Li, A. and Ahmadi, G. (1993c). Deposition of Aerosol on Surfaces in a Turbulent Channel Flow. *International Journal of Engineering Science*, **31**(3), pp. 435-451.

Lifshitz, E.M. (1956). The Theory of Molecular Attractive Forces between Solids. *Soviet Physics*, **2**(1), pp. 73-83.

Lin, J.-S. and Tsai, C.-J. (2003). Thermophoretic Deposition Efficiency in a Cylindrical Tube Taking into account Developing Flow at the Entrance Region. *Aerosol Science*, **34**, pp. 569-583.

Lipatov, G.N., Grinshpun, S.A. and Semenyuk, T.I. (1989). Properties of Crosswise Migration of Particles in Ducts and Inner Aerosol Deposition. *Jounal of Aerosol Science*, **20**(8), pp. 935-938.

Lipatov, G.N., Semenyuk, T.I. and Grinshpun, S.A. (1990). Aerosol Migration in Laminar and Transition Flows. *Journal of Aerosol Science*, **21**(1), pp. S93-S96.

Liu, B.Y.H., Pui, D.Y.H, Rubow, K.L. and Szymanski, W.W. (1985). Electrostatic Effects in Aerosol Sampling and Filtration. *Annals of Occupational Hygiene*, **29**(2), pp. 251-269.

Löffler, F. and Muhr, W. (1972). Die Abschdung von Feststoffteilchen und Tropfen an Kreiszylindern infolge von Trägheitskräften. *Chemie-Ing.-Techn*. **44**(8), pp. 510-514.

Masuda, H., Higashitani, K. and Yoshida, H. (2006). *Powder Technology Handbook* (3rd edition). Taylor & Francis Group, New York.

Matsuyama, T. and Yamamoto, H. (1995). Electrification of Single Polymer Particles by Successive Impacts with Metal Targets. *IEEE Transactions on Industry Applications*, **31**(6), pp. 1441-1445.

Mayya, Y.S. and Sapra, B.K. (2002). Image Forces on a Collection of Charged Particles near Conducting Surfaces. *Journal of Aerosol Science*, **33**, pp. 817-828.

McLaughlin, J.B. (1989). Aerosol Particle Deposition in Numerically Simulated Channel Flow. *Phys. Fluids A*, **1**(7), pp. 1211-1224.

McLaughlin, J.B. (1991). Inertial Migration of a Small Sphere in Linear Shear Flows. *Journal of Fluid Mechanics*. **224**, pp. 261-274.

McLaughlin, J.B. (1993). The Lift on a Small Sphere in Wall-Bounded Linear Shear Flows. *Journal of Fluid Mechanics*. **246**, pp. 249-265.

Muralidhar, K. and Biswas, G. (1996). *Advanced Engineering Fluid Mechanics. Narosa Publishing House*, London.

Novick, V.J. (1994). Plugging Passages with Particles: Refining the Morewitz Criteria. *Aerosol Science and Technology*, **21**, pp. 219-222.

Papavergos, P.G. and Hedley, A.B. (1984). Particle Deposition Behaviour from Turbulent Flows. *Chemical Engineering Research and Design*, **62**(5), pp. 275-295.

Pui, D.Y.H, Romay-Novas, F. and Liu, B.Y.H. (1987). Experimental Study of particle Deposition in Bends of Circular Cross Section. *Aerosol Science and Technology*, **7**, pp. 301-315.

Raask, E. (1985). *Mineral Impurities in Coal Combustion: Behavior, Problems and Remedial Measures*. Taylor & Francis, U.K.

Ranade, M.B. (1987). Adhesion and Removal of Fine Particles on Surfaces. *Aerosol Science and Technology*, **7**, pp. 161-176.

Reeks, M. W. (1983). The Transport of Discrete Particles in Inhomogeneous Turbulence. *Journal of Aerosol Science*, **14**(6), pp. 729-739

Rubinow, S.I. and Keller, J.B. (1961): The Transverse Force on a Spinning Sphere Moving in a Viscous Fluid. *Journal of Fluid Mechanics*, **11**(3), pp. 447-459.

Saffman, P.G. (1965). The Lift on a Small Sphere in a Slow Shear Flow. *Journal of Fluid Mechanics*, **22**(2), pp. 385-400.

Saffman, P.G. (1968). Corrigendum to "The lift on a Small Sphere in a Slow Shear Flow". *Journal of Fluid Mechanics*, **31**, page 624.

Schlichting, H. and Gersten, K. (2000). *Boundary Layer Theory*. Springer-Verlag, Berlin Heidelberg.

Seinfeld, J.H. and Pandis, S.N. (2006). *Atmospheric Chemistry and Physics. From Air Pollution to Climate Change* (2nd ed.). John Wiley & Sons, New Jersey.

Shah, U., Zhang, C., Zhu, J., Wang, F. and Martinuzzi, R. (2007). Validation of a Numerical Model for the Simulation of an Electrostatic Powder Coating Process. *International Journal of Multiphase Flow*, **33**, pp. 557-573.

Shirolkar, J.S., Coimbra, C.F.M. and Queiroz McQuay, M. (1996). Fundamental Aspects of Modeling Turbulent Particle Dispersion in Dilute Flows. *Prog. Energy Combustion Sci.*, **22**, pp. 363-399.

Soltani, M. and Ahmadi, G. (1995). Direct Numerical Simulation of Particle Entrainment in Turbulent Channel Flow. *Phys. Fluids*, **7**(3), pp. 647-657.

Soltani, M. and Ahmadi, G. (1998). On Particle Adhesion and Removal Mechanisms in Turbulent Flows. *Journal of Adhesion Science*, **8**(7), pp. 763-785.

Soud, H.N. and Fukasawa, K. (1996). *Developments in NO_x Abatement and Control*. IEACR/89 IEA Coal Research, London, UK.

Singer, J.G. (1991). *Combustion Fossil Power. A Reference Book on Fuel Burning and Steam Generation* (4th ed.). Combustion Engineering, Inc. Windsor.

Slabiak, T. (2005). *DeNO_x med SCR* (in Danish). Internal Haldor Topsøe A/S report, 2005.

Sloss, L.L. (1991). *NOx Emissions from Coal Combustion*. IEACR/36 IEA Coal Research, London, UK.

Soltani, M., Ahmadi, G. Ounis, H. and McLaughlin, J.B. (1998). Direct Simulation of Charged Particle Deposition in a Turbulent Flow. *International Journal of Multiphase Flow*, **24**(1), pp. 77-92.

Soltani, M. and Ahmadi, G. (1999). Charged Particle Trajectory Statistics and Deposition in a Turbulent Channel Flow. *Aerosol Science and Technology*, **31**, pp. 170-186.

Spitznagel, G.W., Hüttenhofer, K. and Beer, J.K. (1994). NO_x Abatement by Selective Catalytic Reduction. *ACS Symposium Series* (1994), 552 (Environmental Catalysis), pp. 172-89.

Tabor, D. (1977). Surface Forces and Surface Interactions. *Journal of Colloid and Interface Science*, **58**(1), pp. 2-13.

Talbot, L. (1981). Thermophoresis – A review. *Rarefied Gas Dynamics*, Part 1, Fisher, S. (Ed.), **74**, pp. 467-488.

Thorhauge, M. (2004). *DNX – Fly Ash Deposition and Removal*. Internal Haldor Topsøe A/S report, 35019 MAT/MAT, 16/1.

Tian, L. and Ahmadi, G. (2007). Particle Deposition in Turbulent Duct Flows-Comparisons of Different Model Predictions. *Journal of Aerosol Science*, **38**, pp. 377-397.

Tsai, C-J., Lin, J-S., Deshpande, C.G. and Liu, L-C. (2005). Electrostatic Charge Measurement and Charge Neutralization of Fine Aerosol Particles during the Generation Process. *Particle & Particle Systems Characterization*. **22**, pp. 293-298.

TSI Incorporated (2003a). *Model 9360A Six-Jet Atomizer*. Atomizer Instruction manual (part number 1930099).

TSI Incorporated (2003b). *Model 3062 Diffusion Dryer*. Instruction manual (part number 1933062).

TSI Incorporated (2003c). *Models 3054/3054A Aerosol Neuralizers*. Instruction manual (part number 1933054).

TSI Incorporated (2005a). *Model 3775 Condensation Particle Counter*. Operation and Service Manual (part number 1980527).

TSI Incorporated (2005b). *Model 3936 Scanning Mobility Particle Sizer™ (SMPS) Spectrometer*. Instruction manual (part number 1933796).

TSI Incorporated (2006). *Model 3068B Electrometer*. User's manual (part number 1930077).

Uhlenbeck, E. G. and Ornstein, S. L. (1930). On the Theory of the Brownian Motion. *Physical Review*, **36**, pp. 823-841.

Vauge, C. (2002). On the Concept of "Image-Force". *Aerosol Science*, **33**, pp. 829-832.

Vaughan, E.U. (1978). Simple Model for Plugging of Ducts by Aerosol Deposits. *ANS Trans*. **28**, pp. 507-508.

Versteeg, H.K. and Malalasekera, W. (2007). *An Introduction to Computational Fluid Dynamics. The Finite Volume Methods*. Second edition. Prentice Hall. Harlow, England.

Welty, J.A., Wicks, C.E., Wilson, R. E. and Rorrer, G. (2001). *Fundamentals of Momentum, Heat and Mass Transfer 4th edition*. John Wiley & Sons, Inc. New York.

Wiedensohler, A. (1988). An Approximation of the Bipolar Charge Distribution for Particles in the Submicron Size Range. *Journal of Aerosol Science*, **19**(3), pp. 387-389.

Wood, N.B. (1981a). The Mass Transfer of Particles and Acid Vapour to Cooled Surfaces. *Journal of the Institute of Energy*, **76**, pp 76-93.

Wood, N.B. (1981b). A Simple Method for the Calculation of Turbulent Deposition to Smooth and Rough Surfaces. *Journal of Aerosol Science*, **12**(3), pp. 275-290.

Wu, Z. (2002). *NO_x Control for Pulverised Coal Fired Power Stations*. CCC/69, London, UK, IEA Clean Coal Centre.

Wu, Z. (2005). *Fundamentals of Pulverised Coal Combustion*. CCC/95, London, UK, IEA Clean Coal Centre.

Young, J. and Leeming, A. (1997). A Theory of Particle Deposition in Turbulent Pipe Flow. *Journal of Fluid Mechanics,* **340**, pp. 129-159.

Yu, C.P. (1977). Precipitation of Unipolarly Charged Particles in Cylindrical and Spherical Vessels. Journal of Aerosol Science, **8**, pp. 237-241

Yu, C.P. and Chandra, K. (1978). Deposition of Charged Particles from Laminar Flows in Rectangular and Cylindrical Channels by Image Force. *Journal of Aerosol Science*, **9**, pp. 175-180.

Zhang, H. and Ahmadi G. (2000a). Aerosol Particle Transport and Deposition in Vertical and Horizontal Turbulent Duct Flows. *Journal of Fluid Mechanics*, **406**, pp. 55-80.

Zhang, H. and Ahmadi, G. (2000b). Aerosol Particle Removal and Re-Entrainment in Turbulent Channel Flows – A Direct Numerical Simulation Approach. *Journal of Adhesion*, **74**, pp. 441-493.

Zhang, X., Wang, L. and Zhu, K. (2005). A Simple Criterion for Particle-Wall Adhesion in a Wire-Plate Electrostatic Precipitator. *Aerosol Science*, **36**, pp. 411-417.

Zheng, Y., Jensen, A.D. and Johnsson, J.E. (2005). Deactivation of V_2O_5-WO_3-TiO_2 SCR Catalyst at a Biomass-Fired combined Heat and Power Plant. *Applied Catalysis B*: Environmental **60**, pp. 253-264.

Zheng, Y., Jensen, A.D., Johnsson, J.E. and Thøgersen, J.R. (2008). Deactivation of V_2O_5-WO_3-TiO_2 SCR Catalyst at a Biomass-Fired combined Plants: Elucidation of Mechanisms by Lab- and Pilot-Scale Eexperiments. *Applied Catalysis B*: Environmental, **83**, pp. 186-194.

Živcová, Z., Gregorová, E. and Pabst, W. (2007). Porous Alumina Ceramics Produced with Lycopodium Spores as Pore-Forming Agents. *Journal of Material Science*, **42**, pp. 8760-8764.

References

Appendix A

Six-Jet Atomizer

The Six-Jet Atomizer model 9306A *TSI Incorporated*, consist of a built-in pressure regulator and pressure gauge including a self-contained dilution system and one to six particle-generating atomizer jets. The six atomizer jets give a broad range of control over both particle number concentration and over total particle output. Figure A.1 shows an illustration of the Six-Jet Atomizer.

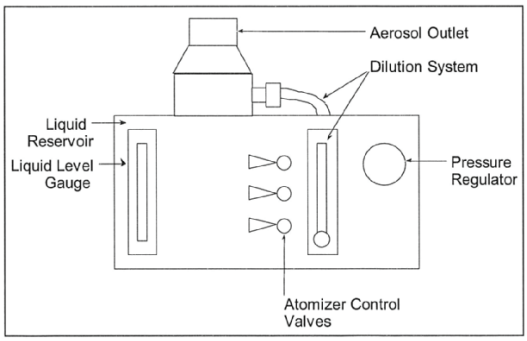

Figure A.1: Illustration of Model 9306A Six-Jet Atomizer [TSI Incorporated (2003a)].

The atomizer can generate particles from almost any liquid and it can also produce solid particles from solutions or from suspensions of for example particles from uniform polystyrene latex (PSL) spheres [TSI Incorporated (2003b)].

The pressure regulator on the atomizer controls the input pressure and is displayed on the gauge. The relation between input pressure and aerosol output can be seen in Figure A.3.

Six-Jet Atomizer

The atomizer consists of six jets and Figure A.2 shows an illustration of one of the jets. The operating principle is that pressurized air is converted to high velocity through a 0.015 inch-diameter nozzle. The pressure drop from the acceleration of the velocity draws liquid up through a narrow tube and the high velocity jet breaks it up into droplets. The larger droplets will be separated from the atomized liquid by the spherical impactor due to inertial impact and the smaller droplets will form an aerosol that exits through the outlet of the atomizer. The aerosol dilution system can be used to vary the output concentration and help to dry the solid particles generated from the atomizer.

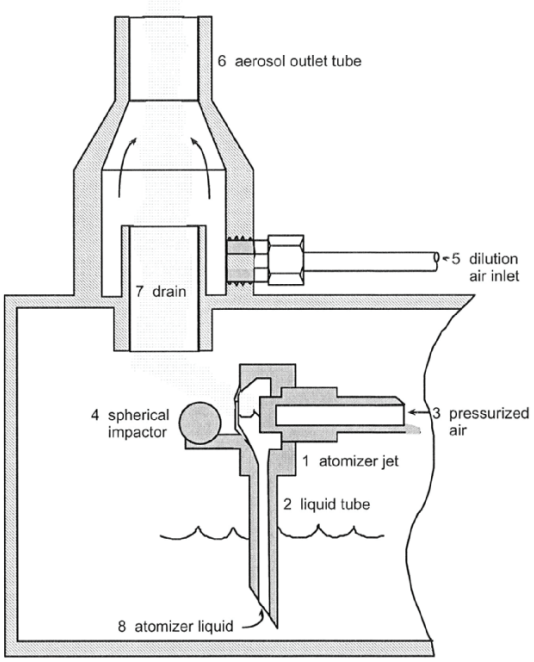

Figure A.2: Schematic illustration of the atomizer showing the atomizer jet (1), the liquid tube (2), the pressurized air inlet (3), the spherical impactor (4), the dilution air inlet (5), the aerosol outlet tube (6), the internal drain (7) and the atomizer liquid (8)[TSI Incorporated (2003a)].

Typical flow rates at several input pressures for a single atomizer jet at atmospheric pressure can be seen in Table A.1. The total aerosol flow rate is directly proportional to the number of jets used and if the atomizer is used to seed a flow under pressure, the aerosol output will naturally differ from the value given in Table A.1. In the experimental setup described in section 3.1 the atomizer is used at atmospheric pressure.

Figure A.3 shows the relationship between aerosol particle output and input pressure and the total number of aerosol particle output depends on the input

pressure and the number of jets operated. For a fixed input pressure the particle output is directly proportional to the number of jets used in the atomizer.

Table A.1: Aerosol flow rate per jet [TSI Incorporated (2003a)].

Input pressure		Aerosol output
psi	kPa	L/min
5	34.5	2.4
10	68.9	3.7
15	103	4.7
20	138	5.7
25	172	6.6
35	241	8.3
45	310	10.2
55	379	12

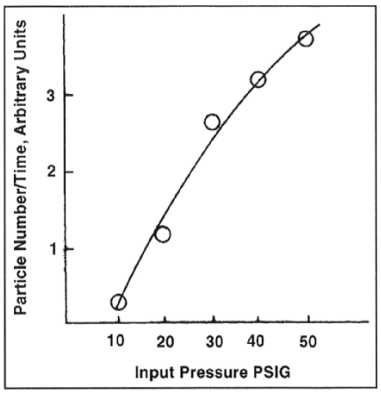

Figure A.3: Relationship between numbers of atomizer particles generated and input pressure [TSI Incorporated (2003a)].

Appendix B

Scanning Mobility Particle Sizer™ (SMPS™) Spectrometer

The Scanning Mobility Particle Sizer™ (SMPS™) spectrometer model 3936 *TSI Incorporated*, consist of an Electrostatic Classifier model 3080 *TSI Incorporated* used with either a Long Differential Mobility Analyser (LDMA) model 3081 *TSI Incorporated* or a Nano Differential Mobility Analyser (NDMA) model 3085 *TSI Incorporated* and a Condensation Particle Counter (CPC) model 3775 *TSI Incorporated*.

Figure B.1: SMPS spectrometer with a model 3085 NDMA and a model 3025A CPC [TSI Incorporated (2005b)].

Figure B.1 shows the SMPS system with a model 3085 NDMA and a model 3025A CPC. The SMPS can measure the size distribution of polydisperse aerosols in the particle size range between 2.5-1000 nm depending on the setting of the system. The particles are classified by size by the use of a Differential Mobility Analyser (DMA) using an electrical mobility detection technique where particles

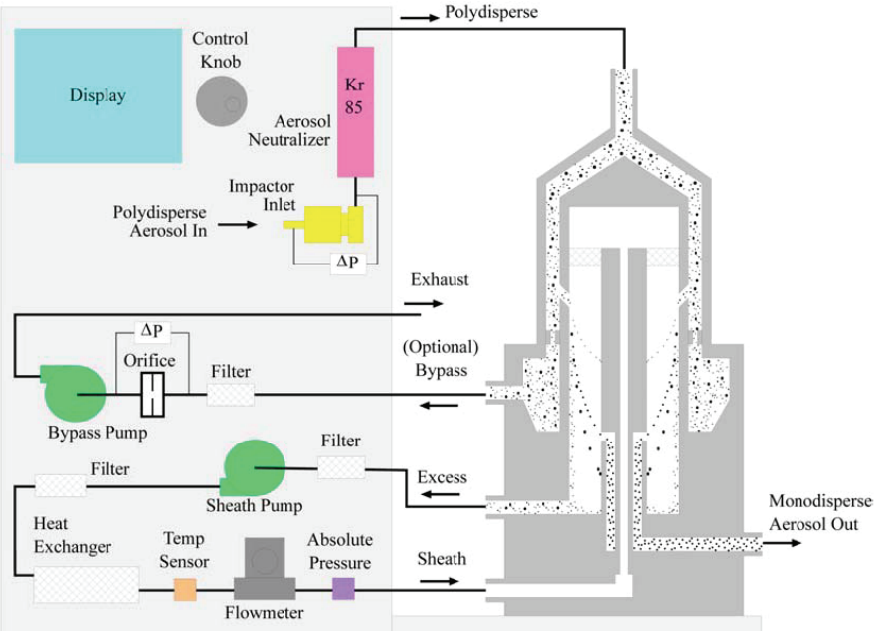

Figure B.2: Schematic illustration for the Electrostatic Classifier with NDMA [TSI Incorporated (2005b)].

are charged to a known charge distribution. The particles are then classified according to their ability to traverse an electrical field. The concentrations are measured using a Condensation Particle Counter.

B.1 Electrostatic Classifier

The general principle of the Electrostatic Classifier is to extract a known size fraction of submicron particles from an incoming polydisperse aerosol. Figure B.2 and Figure B.3 show a schematic illustration of the electrostatic classifier. In the Electrostatic Classifier aerosols enters a Kr-85 bipolar charger (or Aerosol Neutralizer – the Aerosol Neutralizer is described in Appendix E) which exposes the aerosol particles to high concentrations of bipolar ions. Due to the random thermal motion of ions the particles and ions will undergo frequent collisions. The charged aerosol particles then enter from the neutralizer into the main section of the Differential Mobility Analyser which consists of two concentric metal cylinders. The polydisperse aerosol and sheath air is introduced at the top of the classifier and flows down the annual space between the two concentric cylinders. The sheath air and the aerosol flow are both laminar and do not mix so that the aerosol flow will surround the inner core of sheath air. Because the inner cylinder (collector rod) is maintained at a controlled negative voltage while the outer

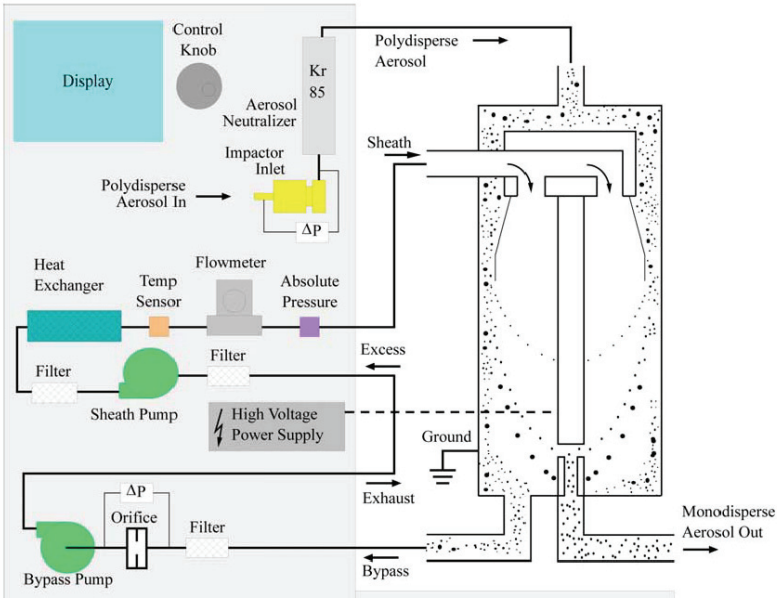

Figure B.3: Schematic illustration for the Electrostatic Classifier with LDMA [TSI Incorporated (2005b)].

cylinder is electrically grounded an electric field is created between the two cylinders whereby the positively charged aerosol particles are attracted through the sheath air to the negative charged collector rod. The particles are precipitated along the length of the collector rod and the location depends on the particle electrical mobility, the classifier flow rate and the classifier geometry. The aerosol particles with a high electrical mobility (small particles) are precipitated along the upper portion of the rod and aerosol particles with a low electrical mobility (large particles) are collected on the lower portion of the rod. The only particles that exit with the monodisperse air through a small slit at the bottom of the collector rod are particles within a narrow range of electrical mobility and are thereafter transferred to a particle sensor to determine the particle concentration. The remaining particles are removed from the classifier via the excess air flow.

B.2 Condensation Particle Counter

The Model 3775 Condensation Particle Counter (CPC) is illustrated in Figure B.4. It operates by continuously drawing an aerosol sample through a heated saturator where butanol is vaporized and diffuses into the aerosol sample stream. The aerosol sample and butanol vapour then passes through a cooled condenser where the butanol becomes supersaturated. Particles in the aerosol sample stream then acts as condensation nuclei for the supersaturated butanol and the particles then

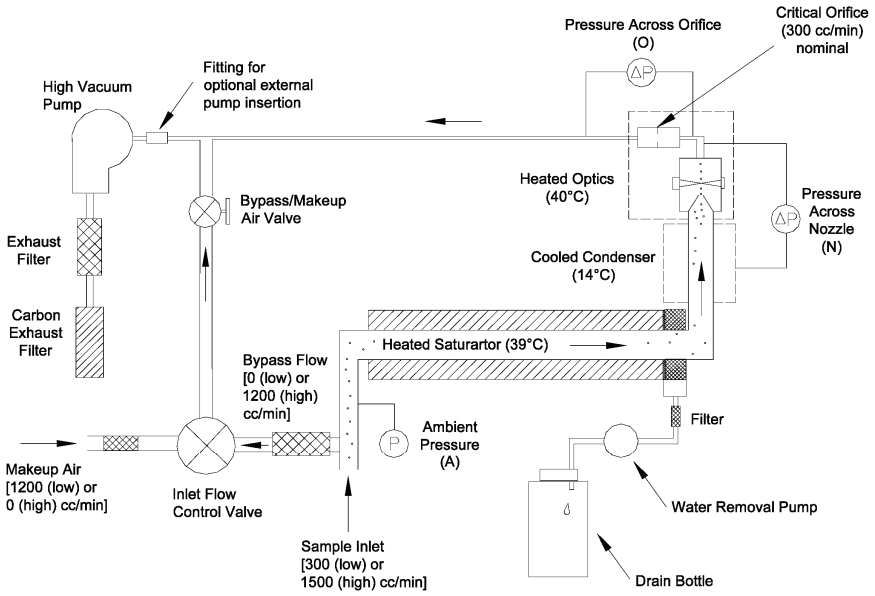

Figure B.4: Schematic illustration of Model 3775 Condensation Particle Counter [TSI Incorporated (2005b)].

quickly grows into larger droplets during condensation. The enlarged droplets then pass through an optical detector where they are counted easily.

Internal the CPC a vacuum pump is responsible for drawing the aerosol sample and the flow can be configured for either 1.5 l/min high flow mode operation to improve response time and minimize particle transport loss, or a 0.3 l/min low-flow mode operation, used as part of an SMPS system. In the high-flow mode 1.2 l/min of the inlet flow to the CPC is diverted as a bypass flow and in the low-flow mode 1.2 of clean air enters as makeup air through the back panel of the CPC. In both cases 0.3 l/min of aerosol flow passes through the sensor assembly which consists of the saturator, condenser, and optics [TSI Incorporated (2005a)].

Appendix C

Electrometer

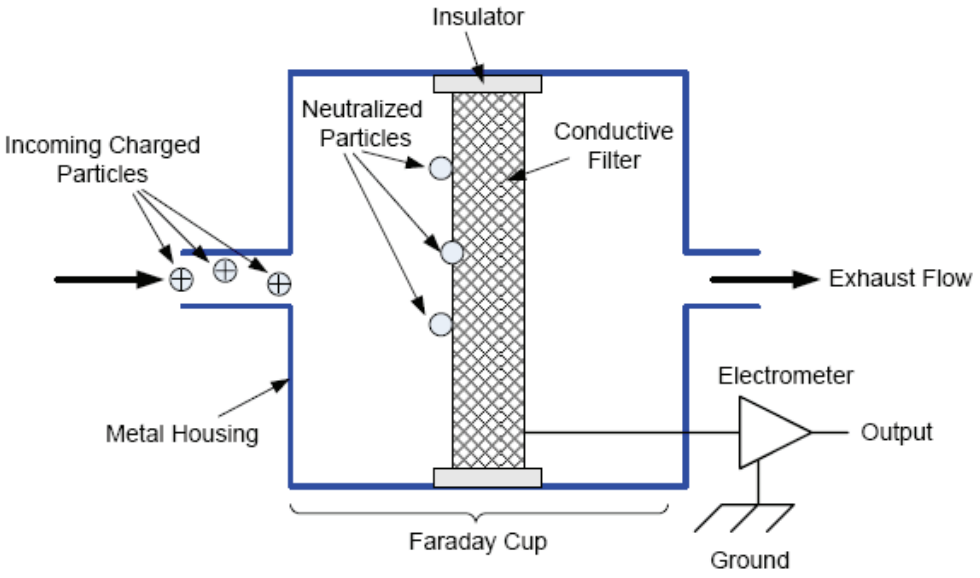

Figure C.1: Schematic illustration of the principle of the electrometer [TSI Incorporated (2006)].

The aerosol Electrometer model 3068B *TSI Incorporated*, consists of a Faraday cup and an electrometer as illustrated schematically in Figure C.1. The Faraday cup collect aerosol particles in the sample flow in a high efficiency conductive filter housed in a metal enclosure, where the metal shields the electrometer input from stray electric fields. The high efficiency conductive filter is connected to the ground through an electrometer sensor and isolated from the metal housing. Positively charged aerosol particles collected on the filter will be neutralized by

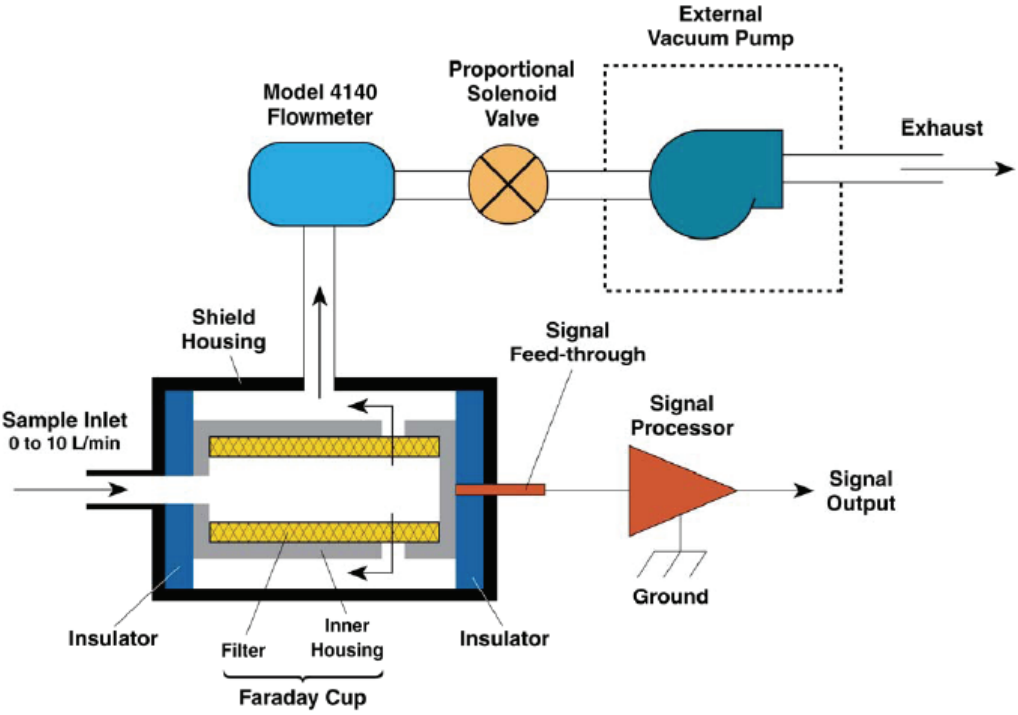

Figure C.2: Schematic illustration of the aerosol Electrometer [TSI Incorporated (2006)].

electrons moving from the ground to the filter and negatively charged aerosol particles collected on the filter will be neutralized by electrons that move from the filter to the ground. This current of electrons is measured by the electrometer current sensor and the current is proportional to the charge collection rate on the filter. The particle number concentration can therefore be calculated from this current if the number of charges on each particle and the aerosol flow rate are known. If the particle number concentration and the flow are known then the average number of elementary charges per particle, i, can be determined as follows

$$i = \frac{I}{NeQ} \tag{C.1}$$

where I (A) is the current measured by the Electrometer, N (particles/cm^3) is the aerosol concentration, e is the elementary unit charge (e = 1.6·10^{-19} C) and Q (cm^3/s) is the volume flow of the sample flow. The operation principle of the electrometer is shown schematically in Figure C.2.

Appendix D

Diffusion Dryer

D.1 Principle of the Diffusion Dryer

When generating aerosols from solid solute in the atomizer it is necessary to dry the particles because they are still wet when coming out of the atomizer. The particles can therefore be passed through a diffusion dryer as shown in Figure D.1. The diffusion dryer consists of two concentric cylindrical pipes where the aerosol stream passes through an inner tube made of a wire screen. The area between the inner and outer cylindrical pipes is filled with silica gel and the water vapour diffuses into the silica gel through the wire screen. Particle losses are minimized because the aerosol particles do not come into contact with the silica gel.

Silica gel is an amorphous form of silicon dioxide, which is synthetically produced in the form of hard irregular granules or hard irregular beads. A micro porous structure of interlocking cavities gives a very high surface area (800 square meters per gram). It is this structure that makes silica gel a high capacity desiccant. Water molecules adhere to the gels surface because it exhibits a lower vapour pressure than the surrounding air. When pressure equilibrium is reached, no more adsorption occurs. The beauty of silica gel is the physical adsorption of water vapour into its internal pores. There is no chemical reaction, no by-products or side effects. Even when saturated with water vapour, silica gel still has the appearance of a dry product and its shape unchanged. The silica gel is easily regenerated in an oven at 120°C. The silica gel used in the model 3062 diffusion dryer [TSI Incorporated (2003b)] contains indicator crystals that are blue when dry and become pink when wet and the blue colour returns when baked in a pan in an oven.

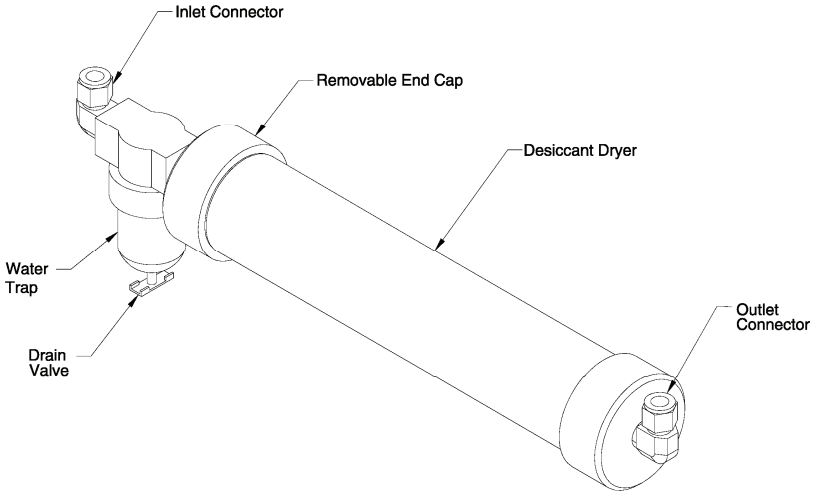

Figure D.1: Model 3062 diffusion dryer [TSI Incorporated (2003b)].

D.2 Droplet Evaporation through a Diffusion Dryer

The evaporation process through a diffusion dryer of a water droplet consisting of an e.g. two per cent KCl solution is a case of simultaneous heat and mass transfer. Due to the small temperature differences the mass transfer will be low. The physical transport process is as follows: water vapour diffuses from the surface of the water droplet through the surrounding air and against the porous wall inside the diffusion dryer and thereafter into the Silica gel. The diffusion of water vapour from the surface of the liquid water droplet is controlled by the water vapour pressure at the liquid interface, and simultaneously latent heat will be absorbed from the surroundings at the liquid interface when vapour is created. This tends to cool the surface, (lowering the surface temperature of the droplet) lowering the vapour pressure and reducing the evaporation rate. Figure D.2 shows a schematic illustration of the diffusion dryer.

The evaporation of a water droplet can be modelled by a film model of mass transfer. This model is based on the idea that the flow is split in two distinct regions where one is a very thin film region of thickness, δ, where the flow is laminar, and the other region is the main fluid stream. Figure D.3 shows the film model of a liquid surface along which a gas flows. Near the surface there is a slowly moving film through which A diffuses. The model will also hold for a stagnant fluid without any flow. The film model is bounded by the surfaces $x=x_1$ and $x=x_2$. In the model it is assumed that there is a sharp transition from a

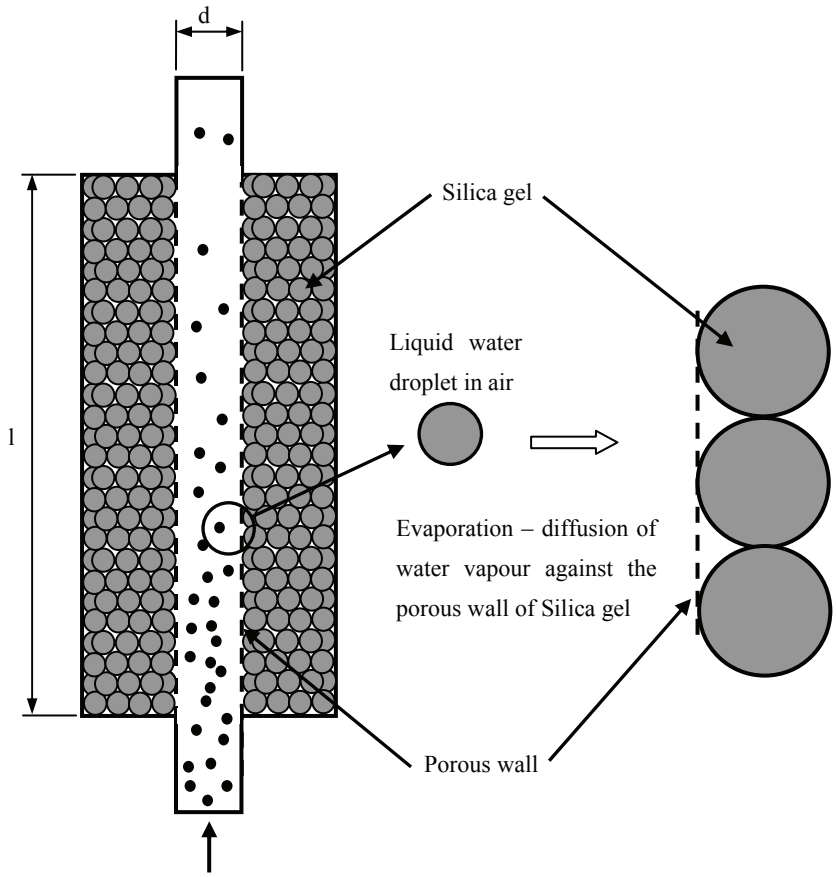

Figure D.2: Schematic illustration of a diffusion dryer. The water vapour diffuses into the Silica gel because the vapour pressure is lower than the vapour pressure of the surrounding air.

stagnant film to a well-mixed fluid, in which the concentration gradients are negligible.

D.3 Mass Transfer from a Liquid Droplet

Because the water droplets are very small (between 4 and 800 nm) it is assumed that they follow the air flow through the diffusion dryer so there is no relative velocity between water droplets and air, and the case can be interpreted as water droplets in stagnant air. This means that there will only be transport of water vapour from the liquid interface due to diffusion and there will be no transport due to convection. The process can then be modelled as diffusion in stagnant air.

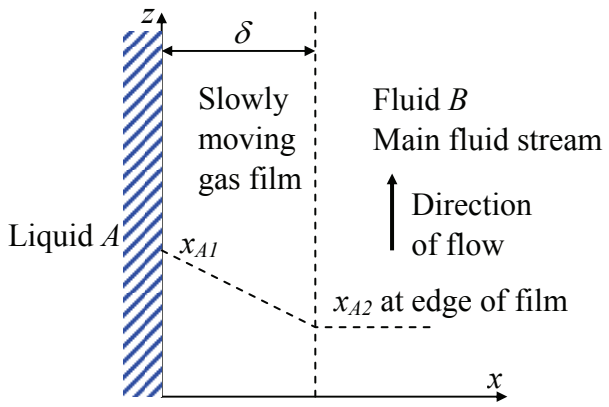

Figure D.3: Film model of mass transfer where component A is diffusing from the interface surface into the gas stream through a hypothetical stagnant gas film.

Based on Figure D.4 a mass balance for the diffusion of vapour from a water droplet into the air can then be written by using the film model on the phase interface between the droplet and the surrounding air. It is here assumed that the film thickness, δ, is very small compared to the radius, R, of the droplet (that is $\delta << R$) and that there is no internal circulation in the droplet and only transport in the radial direction. A mass balance (in terms of molar flow) on the differential element shown in Figure D.4 can be stated as follows

$$\begin{gathered} IN - OUT + \cancel{PROD} = \cancel{ACC} \\ \Downarrow \\ N_{Ar|r} 4\pi r^2 - N_{Ar|r+\Delta r} 4\pi r^2 \Big|_{r+\Delta r} = 0 \end{gathered} \tag{D.1}$$

It is in this case assumed that the condition at the gas-liquid interface is quasi-steady state. This means that the evaporation rate from the liquid droplet is so slow that the gas phase concentration of A (vapour) corresponds to equilibrium at the liquid interface. Also there is no production in the system because the mass balance is in the gas film. Rearranging Equation (D.1) and taking the limit for $\Delta r \to 0$ gives a second-order differential equation for the mass balance, in terms of molar flow

$$\begin{gathered} \frac{r^2 N_{Ar|r+\Delta r} - r^2 N_{Ar|r}}{\Delta r} = 0; \qquad \Delta r \to 0 \Rightarrow \\ \\ \frac{d}{dr}\left(r^2 N_{Ar}\right) = 0 \end{gathered} \tag{D.2}$$

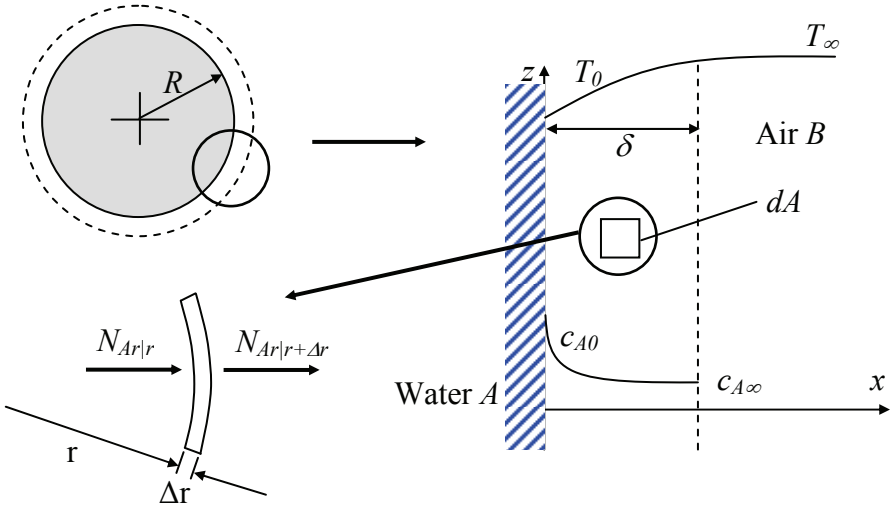

Figure D.4: Schematic illustration of film model of mass diffusion of vapour from a water droplet into stagnant air.

The combined molar flux vector, $\boldsymbol{N}_A$, which is the number of moles of A that go through a unit area (being fixed in space) in unit time can be stated as follows for the radial-direction

$$N_{Ar} = -cD_{AB}\frac{\partial x_A}{\partial r} + x_A\left(\underline{N_{Ar} + N_{Br}}\right) \approx -cD_{AB}\frac{dx_A}{dr} \tag{D.3}$$

where c is the total molar concentration, D_{AB} is the mass diffusivity and x_A the mole fraction. The convective terms in Equation (D.3) shown with the dashed-underlined term, are neglected because A moves predominantly by diffusion in the radial direction, and there is almost no convective transport. The solubility of B (air) in water is negligible. Substituting the molar flux from Equation (D.3) into Equation (D.2) for the mass balance (in terms of molar fluxes) gives a second-order differential equation for the mole fraction of A, x_A(r)

$$\begin{gathered}\frac{d}{dr}\left(-r^2 cD_{AB}\frac{dx_A}{dr}\right) = 0 \\ \Updownarrow \\ cD_{AB}\frac{d}{dr}\left(r^2\frac{dx_A}{dr}\right) = 0\end{gathered} \tag{D.4}$$

$$r > R$$

It has been assumed in Equation (D.4) that the mass diffusivity D_{AB} is constant. For an ideal gas mixture the equation of state is $p=cRT$ and, therefore, at constant temperature and pressure, c must be constant. For gases D_{AB} is very nearly independent of composition. Equation (D.4) can then be integrated twice, giving the mole fraction

$$\begin{gathered} cD_{AB}\frac{d}{dr}\left(-r^2\frac{dx_A}{dr}\right)=0 \\ \Downarrow \\ \int d\left(-r^2\frac{dx_A}{dr}\right)=C_1 \\ \Downarrow \\ -r^2\frac{dx_A}{dr}=C_1 \\ \Downarrow \\ \int dx_A=-C_1\int\frac{1}{r^2}dr+C_2 \\ \Downarrow \\ x_A=\frac{C_1}{r}+C2 \end{gathered} \tag{D.5}$$

The boundary conditions for Equation (D.5) can be stated as follows

$$\begin{gathered} at\ r=R\ \rightarrow\ x_A=x_{AR} \\ at\ x=\infty\ \rightarrow\ x_A=0 \\ r>R \end{gathered} \tag{D.6}$$

The first boundary condition derives from the fact that at the gas liquid interface, the mole fraction of A is expressed as the mole fraction of x_{AR}. This is taken to be the gas phase concentration of A corresponding to equilibrium with the liquid at the interface. This means that x_{AR} is the vapour pressure of A divided by the total pressure $p_{A,vap}/p_{tot}$ under the assumption that A and B forms an ideal gas mixture and the solubility of air B in water A is negligible. The second boundary condition assumes that all water vapour has been absorbed by the silica gel so there is no water vapour outside the film boundary. Substituting the boundary conditions from Equation (D.6) into Equation (D.5) gives the values of the integration constants, as shown in Equation (D.7)

$$0 = \frac{C_1}{\infty} + C_2$$
$$\Downarrow$$
$$0 = 0 + C_2 \Leftrightarrow C_2 = 0 \tag{D.7}$$

$$x_{AR} = \frac{C_1}{R} \Leftrightarrow C_1 = Rx_{AR}$$

The equation for the mole fraction of A as a function of r can now be stated as follows

$$x_A = \frac{Rx_{AR}}{r} \ , \ r > R \tag{D.8}$$

The local mass flux at the gas-liquid interface at $r=R$ can now be found by differentiating Equation (D.8) with respect to the variable r and substituting it into Equation (D.3) setting r equal to the radius R of the water droplet

$$N_{Ar|r=R} = -cD_{AB}\frac{dx_A}{dr}\Big|_{r=R} = -cD_{AB}\frac{d}{dr}\left(\frac{Rx_{AR}}{r}\right)\Big|_{r=R}$$

$$N_{Ar|r=R} = -cD_{AB}\left(-\frac{Rx_{AR}}{r^2}\right)\Big|_{r=R} \tag{D.9}$$

$$N_{Ar|r=R} = cD_{AB}\frac{Rx_{AR}}{R^2} = cD_{AB}\frac{x_{AR}}{R}$$

The molar flow across the gas-liquid interface at $r=R$ can now be found by integration across the interface

$$W_{AR} = \int_0^{2\pi}\int_0^{\pi} N_{Ar|r=R}R\sin\varphi d\varphi R d\theta = \int_0^{2\pi}\int_0^{\pi} cD_{AB}x_{AR}R\sin\varphi d\varphi d\theta \tag{D.10}$$

$$W_{AR} = 4\pi RcD_{AB}x_{AR} = 2\pi DcD_{AB}x_{AR}$$

Based on the assumption of quasi-steady state, equilibrium is assumed at the interface and ideal gas behaviour in the film layer and the mole fraction, x_{AR}, can then be estimated as

$$x_{AR} = \frac{p_{A,vap}}{p_{tot}} \tag{D.11}$$

Substituting Equation (D.11) into Equation (D.10) gives

$$W_{AR} = 4\pi RcD_{AB}x_{AR} = \frac{2\pi DcD_{AB}p_{A,vap}}{p_{tot}} \tag{D.12}$$

Based on the molar flow across the gas liquid interface a mass balance for the change in mass of the liquid water droplet can now be stated as

$$-\frac{d}{dt}\left(\frac{m_{H_2O,liq}}{M_{H_2O}}\right) = W_{AR} = \frac{2\pi DcD_{AB}p_{A,vap}}{p_{tot}}$$

$$\frac{d}{dt}\left(\frac{V\rho_{H_2O,liq}}{M_{H_2O}}\right) = \frac{d}{dt}\left(\frac{\frac{\pi}{6}D^3\rho_{H_2O,liq}}{M_{H_2O}}\right) = \frac{-2\pi DcD_{AB}p_{A,vap}}{p_{tot}}$$

$$\frac{\pi}{6}\left(\frac{\rho_{H_2O,liq}}{M_{H_2O}}\right)\frac{d}{dt}\left(D^3\right) = \frac{-2\pi DcD_{AB}p_{A,vap}}{p_{tot}} \tag{D.13}$$

$$\frac{\pi}{6}\left(\frac{\rho_{H_2O,liq}}{M_{H_2O}}\right)3D^2\frac{dD}{dt} = \frac{-2\pi DcD_{AB}p_{A,vap}}{p_{tot}}$$

$$\frac{dD}{dt} = \frac{-4cD_{AB}M_{H_2O}p_{A,vap}}{D\rho_{H_2O,liq}p_{tot}}$$

where a positive molar flow W_{AR} equals a decrease in mass of the water droplet. In order to be able to estimate the water vapour pressure $p_{A,vap}$ of pure A at the surface temperature, T_0, at the gas-liquid interface (r=R), an energy balance across the interface has to be stated. An energy balance (in terms of molar energy flux) on the differential element shown in Figure D.5 can be stated as follows

$$\begin{gathered} IN - OUT + \cancel{PROD} = \cancel{ACC} \\ \Downarrow \\ e_{Ar|r}4\pi r^2 - e_{Ar|r+\Delta r}\,4\pi r^2\Big|_{r+\Delta r} = 0 \end{gathered} \tag{D.14}$$

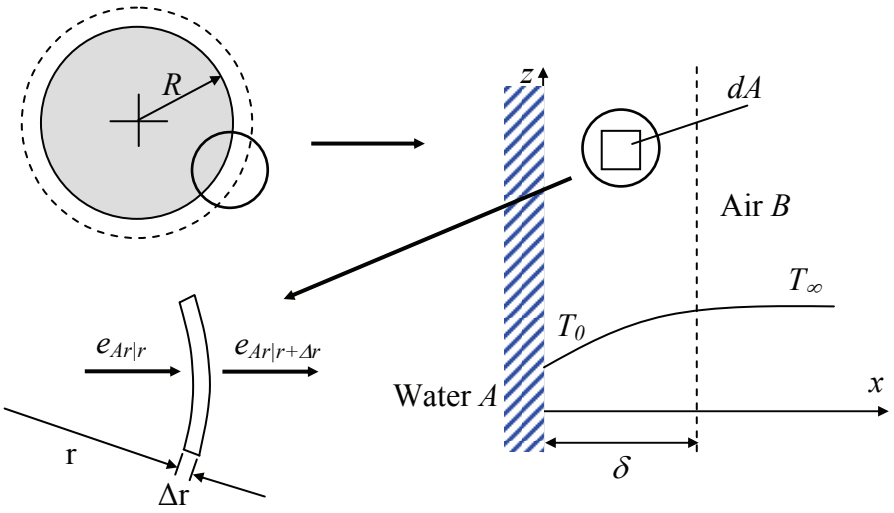

Figure D.5: Schematic illustration of film model of energy transport from a water droplet into stagnant air.

Again it is assumed that the condition at the gas-liquid interface is quasi-steady state. Also there is no production in the system because the energy balance is in the gas film. Rearranging Equation (D.14) and taking the limit for $\Delta r \to 0$ gives a second-order differential equation for the energy balance (conservation of energy)

$$\frac{r^2 e_{r|r+\Delta r} - r^2 e_{r|r}}{\Delta r} = 0$$

$$\Delta r \to 0 \qquad \text{(D.15)}$$

$$\Downarrow$$

$$\frac{\partial}{\partial r}\left(r^2 e_r\right) = 0$$

The combined molar energy flux vector, $\boldsymbol{e}_A$, which is the energy of A through a unit area (being fixed in space) in unit time, can be stated as follows for the radial-direction [Bird et al. (2002)]

$$\vec{e} = -k\vec{\nabla}T + \left(\vec{N}_A \overline{H}_A + \vec{N}_B \overline{H}_B\right)$$

$$\text{(D.16)}$$

$$e_r = -k\frac{dT}{dr} + \left(N_{Ar} \overline{H}_A + N_{Br} \overline{H}_B\right)$$

Equation (D.16) describes the combined energy flux vector and shows it as a scalar equation in the radial direction. The first tem describe the heat transport by conduction (diffusion of energy) and the second term describes heat transport by each of the diffusing species. $\overline{H}_A$ and $\overline{H}_B$ is the partial molar enthalpy of the species *A* and *B*. Because the solubility of *B* (air) in water is negligible there will only be energy transport due to conduction and energy transport due to the mass diffusion of vapour *A* and the term $N_{Br}H_B$ can therefore be neglected. Substituting Equation (D.16) into Equation (D.15) gives a second-order differential for the temperature, *T(r)*

$$\frac{d}{dr}\left(r^2 e_r\right) = 0$$

$$\Downarrow$$

$$\frac{d}{dr}\left(r^2\left(-k\frac{dT}{dr} + \left(N_{Ar}\overline{H}_A + N_{Br}\overline{H}_A\right)\right)\right) = 0 \qquad \text{(D.17)}$$

$$r > R$$

Integrating Equation (D.17) gives a function for the temperature variation.

$$\frac{d}{dr}\left(r^2\left(-k\frac{dT}{dr} + N_{Ar}\overline{H}_A\right)\right) = 0$$

$$\Downarrow$$

$$\int d\left(r^2\left(-k\frac{dT}{dr} + N_{Ar}\overline{H}_A\right)\right) = \int 0\, dr$$

$$\Downarrow \qquad \text{(D.18)}$$

$$r^2\left(-k\frac{dT}{dr} + N_{Ar}\overline{H}_A\right) = C_1$$

$$\Downarrow$$

$$-k\frac{dT}{dr} + N_{Ar}\overline{H}_A = \frac{C_1}{r^2}$$

Substituting the combined molar flux, $\boldsymbol{N}_{Ar}$, from Equation (D.3) and the equation for the mole fraction of *A* from Equation (D.8) into Equation (D.18) and integrating gives

$$-k\frac{dT}{dr}-cD_{AB}\frac{d}{dr}\left(\frac{Rx_{AR}}{r}\right)\overline{H}_A=\frac{C_1}{r^2}$$

$$\Downarrow$$

$$k\frac{dT}{dr}=cD_{AB}\frac{Rx_{AR}}{r^2}\overline{H}_A-\frac{C_1}{r^2}=\left(cD_{AB}Rx_{AR}\overline{H}_A-C_1\right)\frac{1}{r^2}$$

$$k\int dT=\left(cD_{AB}Rx_{AR}\overline{H}_A-C_1\right)\int\frac{dr}{r^2}+C_2 \tag{D.19}$$

$$\Downarrow$$

$$kT=-\left(cD_{AB}Rx_{AR}\overline{H}_A-C_1\right)\frac{1}{r}+C_2$$

$$\Downarrow$$

$$kT=\left(C_1-cD_{AB}Rx_{AR}\overline{H}_A\right)\frac{1}{r}+C_2$$

It has been assumed that the conductivity, k, the mass diffusivity D_{AB}, the total concentration of the film mixture, c, and the partial molar enthalpy, $\overline{H}_A$, is constant through out the film layer and determined by the average film temperature, T_f, defined in Equation (D.35). The boundary conditions for Equation (D.19) are the following

$$\begin{aligned} &at\ r=R\ \rightarrow\ T=T_0\\ &at\ x=\infty\ \rightarrow\ T=T_\infty \end{aligned} \tag{D.20}$$

The first boundary condition derives from the fact that, at the gas liquid interface, the temperature of A is expressed as the surface temperature of the liquid water droplet. The second boundary condition assumes that outside the film layer the temperature is equal to the bulk flow temperature. Substituting the boundary conditions from Equation (D.20) into Equation (D.19) gives

$$kT_\infty=\left(C_1-cD_{AB}Rx_{AR}\overline{H}_A\right)\frac{1}{\infty}+C_2$$

$$\Downarrow$$

$$kT_\infty=0+C_2\Leftrightarrow C_2=kT_\infty \tag{D.21}$$

$$kT_0=\left(C_1-cD_{AB}Rx_{AR}\overline{H}_A\right)\frac{1}{R}+kT_\infty$$

Solving Equation (D.21) for the values of the integration constants as follows

$$C_1 = Rk\left(T_0 - T_\infty\right) + cD_{AB}Rx_{AR}\overline{H}_A \tag{D.22}$$

The equation for the temperature distribution in the film layer can now be stated as follows

$$\begin{gathered} kT = \left(Rk\left(T_0 - T_\infty\right) + cD_{AB}Rx_{AR}\overline{H}_A - cD_{AB}Rx_{AR}\overline{H}_A\right)\frac{1}{r} + kT_\infty \\ \Downarrow \\ T = \left(T_0 - T_\infty\right)\frac{R}{r} + T_\infty \end{gathered} \tag{D.23}$$

The local energy flux at the gas-liquid interface at $r=R$ can now be found by differentiating Equation (D.23) with respect to the variable, r, and substituting it into Equation (D.16) for the combined energy flux and setting the radial distance equal to the radius, R, of the water droplet

$$\begin{gathered} e_r\big|_{r=R} = -k\left.\frac{dT}{dr}\right|_{r=R} + N_{Ar}\overline{H}_A\big|_{r=R} \\ \Downarrow \\ e_r\big|_{r=R} - N_{Ar}\overline{H}_A\big|_{r=R} = -k\left.\frac{d}{dr}\left(\left(T_0 - T_\infty\right)\frac{R}{r} + T_\infty\right)\right|_{r=R} \\ \Downarrow \\ e_r\big|_{r=R} - N_{Ar}\overline{H}_A\big|_{r=R} = k\left(T_0 - T_\infty\right)\left.\frac{R}{r^2}\right|_{r=R} \\ \Downarrow \\ e_0 - N_{AR}\overline{H}_A = k\left(T_0 - T_\infty\right)\frac{1}{R} \end{gathered} \tag{D.24}$$

Substituting the local mass flux at the gas-liquid interface at $r=R$ from Equation (D.9) gives the expression for the local surface temperature, T_0, at the water droplet during evaporation

$$\begin{gathered} -cD_{AB}\frac{x_{AR}}{R}\Delta\tilde{H}_{vap} = k\left(T_0 - T_\infty\right)\frac{1}{R} \\ \Downarrow \\ T_0 = T_\infty - \frac{cD_{AB}x_{AR}\Delta\tilde{H}_{vap}}{k} \end{gathered} \tag{D.25}$$

where the total energy flux, e_0, minus the enthalpy flux through the gas-liquid interface can be assumed equal to the enthalpy of vaporisation. Substituting the expression for the mole fraction given in Equation (D.11) gives the expression for the local surface temperature, T_0, at the water droplet during evaporation based on the vapour pressure at the water droplet surface

$$T_0 = T_\infty - \frac{cD_{AB}\dfrac{p_{A,vap}}{p_{tot}}\Delta\tilde{H}_A}{k} \quad \Downarrow \quad T_0 = T_\infty - \frac{\Delta\tilde{H}_{vap}cD_{AB}}{k}\frac{p_{A,vap}}{p_{tot}} \tag{D.26}$$

The surface temperature, T_0, at the gas-liquid interface could also be determined directly from the combined molar energy flux vector, $\boldsymbol{e}_A$, in Equation (D.16). Expressing the energy flux vector directly at the gas liquid interface at the surface of the water liquid droplet (r=R) gives

$$e_0 - \left(N_{A0}\overline{H}_{A0} + N_{B0}\overline{H}_{B0}\right) = -k\left.\frac{dT}{dr}\right|_{r=R} \tag{D.27}$$

The local fluxes for mass and energy for a differential area dA normal to the radial direction at the gas-liquid interface can be stated as follows:

$$\frac{dW_{A0}}{dA} = N_{A0} \quad ; \quad \frac{dE_0}{dA} = e_0 \tag{D.28}$$

Substituting Equation (D.28) into Equation (D.27) and integrating gives

$$\int_{Area}\frac{dE_0}{dA}dA - \int_{Area}\left(\frac{dW_{A0}}{dA}\bar{H}_{A0} + \frac{dW_{B0}}{dA}\bar{H}_{A0}\right)dA = -\int_{Area}k\left.\frac{dT}{dr}\right|_{r=R}dA \tag{D.29}$$

$$E_0 - \left(W_{A0}\overline{H}_{A0} + W_{B0}\overline{H}_{B0}\right) = h_{loc}A\Delta T$$

where W_{A0} is the number of moles of species, A, per unit time going through the gas-liquid interface and E_0 is the total amount of energy going through the interface. Because the solubility of B (air) in liquid water, A, is negligible W_{B0} can be assumed negligible, reducing Equation (D.29) to

$$E_0 - W_{A0}\overline{H}_{A0} = h_{loc}A\Delta T \tag{D.30}$$

It has been recognised that species A is the only species going through the gas liquid interface – as liquid on the one side and vapour on the other side and therefore W_{A0} must be equal on both sides. The total energy, E_0, minus the enthalpy transport, $W_{A0}H_{A0}$, going through the gas liquid interface can be assumed equal to the enthalpy of vaporisation times the molar flow, $\Delta H_{vap}W_{A0}$. Substituting the surface area for the water liquid droplet and expressing the heat transfer coefficient as a mean value for the droplet surface and the temperature difference ΔT as the temperature outside the film layer minus the temperature at the water droplet surface, (T_∞ -T_0), gives the following expression

$$E_0 - W_{A0}\overline{H}_{A0} = \Delta\tilde{H}_{vap}W_{A0} = h_m\pi D^2\Delta T \qquad \text{(D.31)}$$

$$\Delta\tilde{H}_{vap}W_{A0} = h_m\pi D^2\left(T_\infty - T_0\right)$$

By substituting Equation (D.12) into Equation (D.31) it is now possible to estimate the surface temperature of the water droplet during evaporation.

$$T_0 = T_\infty - \frac{\Delta\tilde{H}_{vap}W_{A0}}{h_m\pi D^2} \qquad \text{(D.32)}$$

$$\Downarrow$$

$$T_0 = T_\infty - \frac{\Delta\tilde{H}_{vap}2cD_{AB}}{h_m D}\frac{p_{A,vap}}{p_{tot}}$$

Equation (D.32) expresses the simultaneous heat and mass transfer for evaporation of the droplet. In order to determine the vapour pressure, $p_{A,vap,}$ at the water droplet surface the surface temperature must be known. Therefore Equation (D.32) must be solved by iteration. The mean heat transfer coefficient, h_m, in Equation (D.32) can be determined from the Nusselts number as follows

$$Nu_m = \frac{h_m D}{k} \Leftrightarrow h_m = \frac{Nu_m k}{D}$$

$$Nu_m = 2 + 0.60\,\mathrm{Re}^{1/2}\,\mathrm{Pr}^{1/3} \qquad \text{(D.33)}$$

$$\mathrm{Re} \to 0 \Rightarrow Nu_m \to 2$$

$$h_m = \frac{2k}{D}$$

Equation (D.33) can now be substituted into Equation (D.32) explicitly expressing the surface temperature of the water droplet as a function of the temperature outside the film layer, enthalpy of vaporisation, ΔH_{vap}, the total concentration c of the mixture, the binary diffusivity, D_{AB}, the thermal conductivity, k, the vapour pressure, $p_{A,vap,}$ and the total pressure, p_{tot}, of the mixture

$$T_0 = T_\infty - \frac{\Delta\tilde{H}_{vap} 2cD_{AB}}{\frac{2k}{D}D} \frac{p_{A,vap}}{p_{tot}}$$
$$\Downarrow$$
$$T_0 = T_\infty - \frac{\Delta\tilde{H}_{vap} cD_{AB}}{k} \frac{p_{A,vap}}{p_{tot}} \tag{D.34}$$

$$c = \frac{p_{tot}}{RT}$$
$$\Downarrow$$
$$T_0 = T_\infty - \frac{\Delta\tilde{H}_{vap} D_{AB}}{k} \frac{p_{A,vap}}{RT_f}$$

Comparing Equation (D.34) with Equation (D.26) it can be concluded that they are identical. The film conditions needed for estimating the physical properties in Equation (D.34) can be obtained as follows:

$$T_f = T_\infty - T_0 \tag{D.35}$$

The diffusivity, D_{AB}, can be estimated as follows for water vapour in air [Welty et al. (2001)]

$$D_{AB}P = 0.260\left[\frac{cm^2 atm}{s}\right]$$
$$P = 1\,atm$$
$$\Downarrow \tag{D.36}$$
$$D_{AB} = 0.260\left[\frac{cm^2}{s}\right] = 0.260\cdot 10^{-4}\left[\frac{m^2}{s}\right]$$

The physical conditions used for calculating the surface temperature of the water droplet during vaporization and the time for vaporization can be seen in Table D.1

Table D.1: Physical conditions for the water droplet.

Initial diameter of water droplet, D_1	800	nm
Final diameter of water droplet, D_0	0	nm
Temperature of gas flow, T_∞	293	K
Temperature of film, T_f	285	K
Temperature at surface, T_0	277	K
Density of water, $\rho_{H2O,liq}$	999.8	kg/m^3
Density of air mixture, ρ	1.247	kg/m^3
Vapour pressure, $p_{A,vap}$	813	Pa
Total pressure, p_{tot}	101325	Pa
Enthalpy of vaporisation, ΔH_{vap}	2492.1	kJ/kg
Heat conductivity, k = 0.0261	0.0245	W/m-K
Universal gas constant, R	8314	J/kmol-K
Molecular weight of air, M_{H20}	18	kg/kmol

The surface temperature can be found by iteratively solving Equation (D.34)

$$T_0 = T_\infty - \frac{\Delta\tilde{H}_{vap} D_{AB}}{k} \frac{p_{A,vap}}{RT_f}$$

$$\Downarrow$$

$$T_0 = 293 - \frac{2492100 \cdot 0.260 \cdot 10^{-4}}{0.0245} \frac{813 \cdot 18}{8.314 \cdot 285} \tag{D.37}$$

$$T_0 \approx 293 - 16 = 277\left[K\right]$$

which corresponds to the wet bulb temperature for a totally dry air at 293 K. After determining the surface temperature the time for evaporation of the water droplet can be determined by integrating Equation (D.13) as follows

$$\int_{D_1}^{D_0} DdD = -\int_0^t \frac{4cD_{AB}M_{H_2O}p_{A,vap}}{\rho_{H_2O,liq}p_{tot}} d\tau = \frac{-4cD_{AB}M_{H_2O}p_{A,vap}}{\rho_{H_2O,liq}p_{tot}} \int_0^t d\tau$$

(D.38)

$$\frac{D^2}{2}\bigg|_{D_1}^{D_0} = \frac{-4cD_{AB}M_{H_2O}p_{A,vap}}{\rho_{H_2O,liq}p_{tot}} \tau \bigg|_0^t$$

Substituting the integration boundaries into Equation (D.38) gives the evaporation time of the water droplet

$$t = -\frac{\left(D_0^2 - D_1^2\right)\rho_{H_2O,liq}\, p_{tot}}{8cD_{AB}M_{H_2O}p_{A,vap}} \quad ; \quad c = \frac{p_{tot}}{RT_f}$$

$$\Downarrow$$

$$t = \frac{\left(D_1^2 - D_0^2\right)\rho_{H_2O,liq}\, RT_f}{8D_{AB}M_{H_2O}p_{A,vap}} \tag{D.39}$$

$$t = \frac{\left(800\cdot 10^{-9} - 0^2\right)^2 1000\cdot 8314\cdot 285}{8\cdot 0.260\cdot 10^{-4}\cdot 18\cdot 813} \approx 5\cdot 10^{-4}\left[s\right]$$

The residence time for the particles through the diffusion dryer with a volume flow, Q = 300 ml/min can be found as follows

$$v = \frac{Q}{A} = \frac{4Q}{\pi d^2} = \frac{l}{\tau}$$

$$\Downarrow$$

$$\tau = \frac{l\pi d^2}{4Q} \tag{D.40}$$

$$\Downarrow$$

$$\tau = \frac{0.5\pi 0.01^2}{4\cdot 5\cdot 10^{-6}} \approx 7.9\left[s\right]$$

In a worst case scenario the evaporation from the water droplets in the diffusion dryer is controlled only by heat and mass diffusion without convection. The evaporation time of the droplets is still much smaller than the residence time in the diffusion dryer. A diffusion dryer model 3062 from *TSI* can dry particles with a flow up to 4 l/min.

Appendix E

Aerosol Neutralizer

In order to neutralize electrostatic charges on aerosol particles an aerosol neutralizer can be used.

Figure E.1: TSI model 3054/3054A Aerosol Neutralizer [TSI Incorporated (2003c)].

Figure E.1 shows a picture of a TSI, Aerosol Neutralizer Model 3054A from *TSI Incorporated*. The Neutralizer contains 20 millicuries of Krypton-85 and is able to neutralize a flow up to 300 l/min. The half-life of the Krypton-85 source is 10 years. The Aerosol Neutralizer produces both positive and negative air ions that are attracted to oppositely charged particles and by means of diffusion charging the aerosol particles are neutralized.

Table E.1: Calculated bipolar charge equilibrium distribution based on information from Wiedensohler (1988).

	Percent of particle carrying N_p elementary charge units												
D_p(µm)	N_p=-6	-5	-4	-3	-2	-1	0	+1	+2	+3	+4	+5	+6
0.01						5.14	90.75	4.11					
0.02					0.02	10.96	80.57	8.64	0.01				
0.04					0.54	19.50	64.79	14.86	0.31				
0.06				0.02	1.92	24.32	54.13	18.51	1.09	0.01			
0.08				0.11	3.73	26.81	46.75	20.46	2.10	0.05			
0.10				0.37	5.63	27.31	42.28	20.91	3.30	0.17			
0.20		0.05	0.53	3.40	12.38	25.49	29.66	19.51	7.26	1.53	0.18	0.01	
0.40	0.27	1.14	3.60	8.54	15.24	20.46	20.65	15.66	8.93	3.83	1.24	0.03	0.05
0.60	1.21	3.00	6.19	10.53	14.82	17.25	16.60	13.20	8.69	4.73	2.13	0.79	0.24
0.80	2.42	4.64	7.71	11.12	13.90	15.06	14.15	11.53	8.15	4.99	2.65	1.22	0.49
1.00	3.56	5.84	8.53	11.13	12.96	13.45	12.46	10.30	7.59	5.00	2.93	1.54	0.92

Given sufficient residence time in the Aerosol Neutrilizer, the aerosol particles can be reduced to a charge equilibrium as shown in Table E.1. The equilibrium charge distribution in Table E.1 is slightly different from the Boltzmann equilibrium charge distribution, because it is not a perfectly symmetrical distribution around the zero charge, but a little skewed distribution toward a higher negative number of elementary charges than positive charges. The reason for this is that the electrical mobility of negative air ions is a little higher than for positive air ions.

Appendix F

Powder Disperser

The Palas RBG-2000 powder disperser is used for continuous feeding of particles in the particle size range below 100 μm. It transfers dry, non-cohesive powder and dust particles into an airborne state.

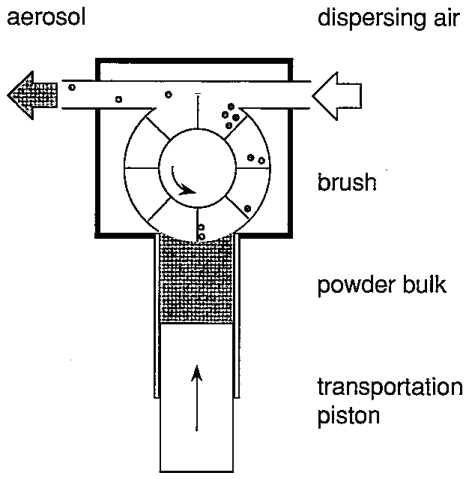

Figure F.1: Schematic illustration of the operating principle of the RBG-2000 [Frey (2001)].

Figure F.1 illustrates the operation principle of the powder disperser. It consist of a stainless steel block (the dispersion head) in which a pivoted cylindrical brush is positioned. The cylindrical powder reservoir is located below the cylindrical brush and is filled with the bulk material to be dispersed. The transportation piston pushes the compacted powder at a given speed out of the reservoir and onto the rotating brush. Powder loosened by the brush is transported into the upper part of

the dispersion head and blown away by a high velocity air stream of compressed air through the dust-exit-nozzle. The high air velocity is important because the dispersion of small particles requires high energies. The flow rate of the compressed air can be adjusted by means of a flow meter. During continuous operation, a constant speed drive moves the piston forward at the present speed.

The powder disperser is suitable for flow rates of 0.5 to 7 m^3/h with dry oil-free compressed air and depending on the piston diameter and speed of the powder flow rates of 20 g/h to 400 g/h can be achieved with powders compacted to a density of 1 g/cm^3.

Appendix G

Aerosol Particle Size Distribution Function

For high concentrations of aerosol particles the diameters of these particles can span over several orders of magnitude from a few nanometres up to several micrometers. To be able to appreciate this wide range of diameters it is necessary to consider the number and mass of both the very small particles and the very large particles. The problem here is that the mass of e.g. a 10 μm particle compared to a 10 nm particle is one billon times heavier and the aerosol size distribution has to be able to show this.

The number size distribution function $n(D_p)$ with units cm^{-4} can be defined as follows

$$dN = n\left(D_p\right)dD_p$$
$$\text{number of particles per } cm^3 \text{ of gas having} \qquad \text{(G.1)}$$
$$\text{diameters in the range } D_p \text{ to } \left(D_p + dD_p\right)$$

The total number of particles pr cm^3, N_t can be stated as follows

$$n = N_t = \int_0^\infty n\left(D_p\right)dD_p = \int_0^\infty dN \qquad \text{(G.2)}$$

The cumulative size function $N(D_p)$ is defined as

$$N\left(D_p\right) = \text{number of particles per } cm^3 \qquad \text{(G.3)}$$
$$\text{having diameter smaller than } D_p$$

Where the function $N(D_p)$ represents the actual particle concentration in the size range 0-D_p and has units of cm^{-3}. By definition $N(D_p)$ is related to $n(D_p)$ by the following integration

$$N\left(D_p\right) = \int_0^{D_p} n\left(D_p^*\right) dD_p^* \tag{G.4}$$

D_p^* is used as integration dummy. The number size distribution function $n(D_p)$ can be written as follows by differentiating Equation (G.4)

$$\begin{gathered} n\left(D_p\right) = \frac{dN}{dD_p} \\ \Updownarrow \\ dN = n\left(D_p\right) dD_p \end{gathered} \tag{G.5}$$

which is the number of particles per unit volume of gas with the particles diameter between D_p up to D_p+dD_p.

A more convenient way to represent the aerosol distribution is as a function of $\ln(D_p)$ instead of D_p. That is expressing the number size distribution function, n, as a function of $\ln D_p$ as follows $n=n(\ln D_p)$ with units cm^{-4}

$$\begin{gathered} n\left(\ln D_p\right) = \frac{dN}{d\left(\ln D_p\right)} \frac{d\left(\ln D_p\right)}{dD_p} \\ \Updownarrow \\ n\left(\ln D_p\right) = \frac{dN}{d\left(\ln D_p\right)} \frac{1}{D_p} \\ \Updownarrow \\ n\left(\ln D_p\right) D_p = \frac{dN}{d\left(\ln D_p\right)} \end{gathered} \tag{G.6}$$

Table G.1 shows an example of the calculation of particle size distribution for an aerosol.

Table G.1: Example of calculation of aerosol particle size distribution.

Particle diameter	Number concentration	Average Particle diameter	Number size distribution	Mass size distribution	Log number size distribution	Log mass size distribution
D_p	dN	D_p	$n(D_p)= dN/d(D_p)$	$m(D_p)$	$n(\ln D_p)\ D_p = dN/d(\ln D_p)$	$m(\ln D_p)\ D_p = dM/d(\ln D_p)$
nm	#/cm^3	nm	#/cm^3 μm^{-1}	#/cm^3 μm^{-1}		
14.1	603.451	14.35	1206.90	3.73281E-09	1.74E04	5.36E-08
14.6	223.603	14.85	447.21	1.53283E-09	6.64E03	2.28E-08
15.1	77.8446	15.4	129.74	4.95961E-10	2.00E03	7.64E-09
15.7	15.3872	16	25.65	1.09945E-10	4.10E02	1.76E-09
16.3	6.53047	16.55	13.06	6.19693E-11	2.16E02	1.03E-09
16.8	2.23615	17.15	3.19	1.68657E-11	5.48E01	2.89E-10
17.5	-	-	-	-	-	-

Appendix H

Characteristic Time for Agglomeration

In order to prevent errors in the SMPS Spectrometer measurements due to agglomeration during the experiments of particle deposition, calculation of the characteristic time for agglomeration, τ, has been carried. This was done to ensure that the changes in particle size distribution measured before and after the three-meter long aerosol deposition pipe was only due to particle deposition and not due to agglomeration of particles which otherwise would give growth in particle sizes.

When the aerosol particles are smaller than a few micrometers in diameter and are under typically atmospheric conditions the dominant mechanism for agglomeration is Brownian motion [Flagan and Seinfeld (1988), p. 332]. For an initially monodisperse population of aerosol particles to agglomerate to one-half the initial number concentration the general dynamic equation for aerosol particles [Flagan and Seinfeld (1988), p. 329] in the absences of evaporation can be solved, which for a constant Brownian agglomeration coefficient, K, gives [Flagan and Seinfeld (1988), p. 338]

$$\frac{dN(t)}{dt} = -\tfrac{1}{2} KN(t)^2 \tag{H.1}$$

The solution to Equation (H.1), for the total initial concentration of aerosol particles, $N(0) = N_0$ is given as [Flagan and Seinfeld (1988), p. 338]

$$N(t) = \frac{N_0}{1 + t/\tau}; \qquad \tau = \frac{2}{KN_0} \tag{H.2}$$

where τ is a characteristic time for coagulation. The coagulation coefficient cannot strictly be independent of time because the average particle size of the aerosol is

increasing as agglomeration proceeds and the population is no longer monodisperse, but the characteristic time for coagulation, τ, still represents a good approximation of the time constant for agglomeration of an aerosol population.

The time for the initial particle number concentration of aerosol particles to decrease one per cent can now simply be found from Equation (H.2) by setting $N(t) = 0.99N_0$. The time for the initial number concentration of aerosol particles to decrease one per cent is given as

$$\begin{aligned} 0.99N_0 &= \frac{N_0}{1+t/\tau} \\ &\Updownarrow \\ t &= \frac{0.01}{0.99}\tau \end{aligned} \tag{H.3}$$

In order to calculate the time for the aerosol particles to decrease to one per cent of the initial total number concentration the Brownian coagulation coefficient, K, has to be determined. The smallest value of the Brownian coagulation coefficient occurs when both particles are of the same size [Flagan and Seinfeld (1988), p. 332]. When the aerosol particles are very large and are in the continuum regime the Knudsen number, $Kn << 1$, and the Brownian coagulation coefficient, K, is independent of particle size, then K can be determined as follows [Flagan and Seinfeld (1988), p. 332]

$$K = \frac{8k_BT}{3\mu} \tag{H.4}$$

where k_B is the Boltzmann constant, T is the temperature and μ is the dynamic viscosity of the fluid. When both particles are very small, of equal size and in the free molecule regime the Knudsen number, $Kn >> 1$, then K is given as follows:

$$K = 4\left(\frac{6k_BT}{\rho_p}\right)^{1/2} D_p^{1/2} \tag{H.5}$$

where ρ_p is the particle density and D_p is the aerosol particle diameter. The Knudsen number can be determined as

$$Kn = \frac{2\lambda}{D_p} \tag{H.6}$$

where λ is the mean free path of the fluid. Table H.1 shows results from the analytic calculations of the Brownian coagulation coefficient, K, and the characteristic time for agglomeration based on one per cent of the initial total concentration to agglomerate.

Table H.1: Brownian coagulation coefficient K and the characteristic time for coagulation as a function of different particle diameters based on an initial particle number concentration, $n_0 = 2 \cdot 10^{12}$ *#/m*^{3}.

Particle diameter D_p [nm]	Knudsen number *Kn*	Coagulation coefficient *K*	Time *T* [s]
3	44.95	7.82E-16	12.92
4	33.71	9.03E-16	11.19
5	26.97	1.01E-15	10.01
6	22.47	1.11E-15	9.13
7	19.26	1.19E-15	8.46
8	16.85	1.28E-15	7.91
9	14.98	1.35E-15	7.96
10	13.48	1.43E-15	7.08
20	6.74	2.02E-15	5.00
30	4.49	2.47E-15	4.08
40	3.37	2.86E-15	3.54
50	2.70	3.19E-15	3.16
60	2.25	3.50E-15	2.89
70	1.93	3.78E-15	2.67
80	1.69	4.04E-15	2.50
90	1.50	4.28E-15	2.36
100	1.35	4.51E-15	2.24
200	0.67	5.97E-16	16.93
300	0.45	5.97E-16	16.93
400	0.34	5.97E-16	16.93
500	0.27	5.97E-16	16.93
600	0.22	5.97E-16	16.93
700	0.19	5.97E-16	16.93
800	0.17	5.97E-16	16.93

The results in Table H.1 are shown for particle diameters between 3-800 nm and are based on an initial particle number concentration, $n_0 = 2 \cdot 10^{12}$ #/m^3. For particles with a diameter up to 0.1 μm which are in the kinetic regime the characteristic time for coagulation is calculated using Equation (H.5) which is dependent on the particle diameter. For particles with a diameter larger than 0.1 μm which are in the continuum regime the characteristic time for coagulation is calculated using Equation (H.4) which is independent on the particle diameter. The residence time in the three-meter long aerosol deposition pipe was about 18 seconds and for a 0.1 μm particle the characteristic time for agglomeration for the

initial particle number concentration of aerosol particles to decrease one per cent was about 2 seconds. These calculations showed that the characteristic time for agglomeration (for a decrease in the initial concentration with one per cent) for e.g. an initial particle number concentration, $n_0 = 2 \cdot 10^{12}$ #/m^3 of monodisperse 100 nm particle in the inlet of the aerosol deposition pipe was about 2 seconds (worst case). The residence time in the three-meter long aerosol deposition pipe was about 18 seconds. So based on a rough approximation the size distribution would decrease 9% due to agglomeration. But this was under the assumption that the size distribution was monodisperse with an initial particle number concentration, $n_0 = 2 \cdot 10^{12}$ #/m^3. In the experiments the maximum total particle number concentration was about $2 \cdot 10^{12}$ #/m^3 for a polydisperse aerosol particle size distribution so the characteristic time for agglomeration would be higher and therefore the influence on the change in the particle size distribution between top and bottom due to agglomeration of particles in the aerosol deposition pipe has been neglected.

Appendix I

Saffman Lift

The following appendix describes the derivation of a coupled differential equation system giving respectively the unsteady and pseudo steady-state trajectory of a single non-diffusive micrometer particle in a fully developed steady-state laminar pipe flow due to Saffman lift.

I.1 Unsteady Particle Motion

Figure I.1 illustrates the forces on a micrometer particle in a fully developed laminar flow. A force balance in the *y*-direction can be stated as follows

$$\begin{gathered} \sum F_y = m_p \frac{dv_{p,y}}{dt} \\ \Updownarrow \\ m_p \frac{dv_{p,y}}{dt} = -F_{drag,y} + F_{Lift} \end{gathered} \tag{I.1}$$

where m_p is the mass of the particle, $v_{p,y}$ is the particle migration velocity in the *y*-direction. A force balance in the *z*-direction, referring to Figure I.1, can be stated as follows

$$\begin{gathered} \sum F_z = m_p \frac{dv_{p,z}}{dt} \\ \Updownarrow \\ m_p \frac{dv_{p,z}}{dt} = mg - F_{drag,z} + F_{buoyancy} \end{gathered} \tag{I.2}$$

where $v_{p,z}$ is the particle migration velocity in the *z*-direction.

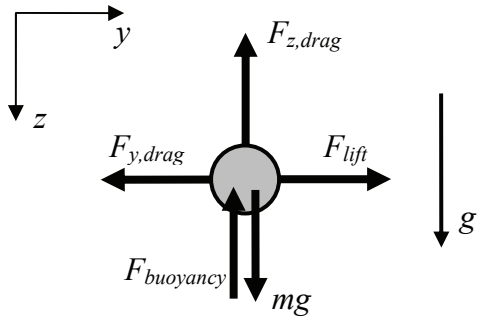

Figure I.1: Force balance on a single micrometer particle.

I.2 Pseudo Steady-State Particle Motion

The system of differential equations for the pseudo steady-state motion of a single particle due to drag, lift and gravity (neglecting buoyancy) in a fully developed steady-state laminar tube flow can be stated from Equation (I.1) and Equation (I.2) by setting the acceleration terms $dv_{p,y}/dt$ and $dv_{p,z}/dt$ equal to zero. Substituting expressions for the drag force given in Equation (2.34) and the Saffman lift force given in Equation (2.13) into Equation (I.1) then gives

$$0 = -\frac{3}{4}\frac{C_D \rho_f v_{p,y}^2}{D_p \rho_p} + \frac{9.69\left|u - v_{p,z}\right|\left(\rho_f \mu_f \left|\frac{du}{dy}\right|\right)^{1/2}}{\pi D_p \rho_p}$$

$$\Updownarrow \qquad \text{(I.3)}$$

$$\frac{3}{4}\frac{C_D \rho_f v_{p,y}^2}{D_p \rho_p} = \frac{9.69\left|u - v_{p,z}\right|\left(\rho_f \mu_f \left|\frac{du}{dy}\right|\right)^{1/2}}{\pi D_p \rho_p}$$

Assuming Stokes flow so that the drag coefficient, C_D, can be expressed as $C_D = 24/\mathrm{Re}_y$ and substituting it into Equation (I.3) together with the velocity gradient for the fully developed axisymmetrical given in Equation (I.5) flow gives

$$\frac{3}{4}\frac{\frac{24}{\mathrm{Re}_y}\rho_f v_{p,y}^2}{D_p \rho_p} = \frac{9.69\left|u - v_{p,z}\right|\left(\rho_f \mu_f 4u_{avg}\frac{y_p}{R^2}\right)^{1/2}}{\pi D_p \rho_p} \qquad \text{(I.4)}$$

The fully developed axisymmetrical flow field and velocity gradient is given as follows

$$u(y) = 2u_{avg}\left(1-\left(\frac{y}{R}\right)^2\right)$$
$$\Downarrow \tag{I.5}$$
$$\frac{du}{dy} = -4u_{avg}\frac{y}{R^2}$$

The particle Reynolds number in the *y*-direction (horizontal direction is) given as

$$\mathrm{Re}_y = \frac{\rho_f v_{p,y} D_p}{\mu_f} \tag{I.6}$$

Substituting the velocity gradient given in Equation (I.5) and the Reynolds number given in Equation (I.6) into Equation (I.4) gives the following equation for the particle migration velocity in the *y*-direction

$$\frac{3}{4}\frac{\dfrac{24}{\dfrac{\rho_f v_{p,y} D_p}{\mu_f}}\rho_f v_{p,y}^2}{D_p\rho_p} = \frac{9.69\left|u-v_{p,z}\right|\left(\rho_f\mu_f 4u_{avg}\dfrac{y_p}{R^2}\right)^{1/2}}{\pi D_p\rho_p}$$
$$\Updownarrow$$
$$\frac{3}{4}\frac{24}{\rho_f v_{p,y} D_p}\mu_f\rho_f v_{p,y}^2 = \frac{9.69\left|u-v_{p,z}\right|\left(\rho_f\mu_f 4u_{avg}\dfrac{y_p}{R^2}\right)^{1/2}}{\pi} \tag{I.7}$$
$$\Updownarrow$$
$$v_{p,y} = \frac{9.69 D_p\left|u-v_{p,z}\right|\left(\rho_f\mu_f 4u_{avg}\dfrac{y_p}{R^2}\right)^{1/2}}{\pi 18\mu_f}$$

Assuming pseudo steady-state conditions so that the particle always is in equilibrium with the fluid and the velocity difference between the velocity field of the fluid and the particle, (u-$v_{p,z}$), is equal to the particle terminal settling velocity, v_t, for Stokes flow, then Equation (I.7) can be stated as follows

$$\frac{dy_p}{dt} = \frac{9.69 D_p v_t\left(\rho_f\mu_f 4u_{avg}\dfrac{y_p}{R^2}\right)^{1/2}}{\pi 18\mu_f} \tag{I.8}$$

where dy_p/dt is the velocity of the particle. The particle terminal settling velocity, v_t, for Stokes flow is given in Equation (2.38). The pseudo steady-state motion of the particle in the z-direction can, by setting the acceleration term to zero in Equation (I.2) and neglecting buoyancy, be stated as

$$\frac{dz_p}{dt} = u + v_t \tag{I.9}$$

The system of differential equations for the pseudo steady-state motion of a single particle due to drag, lift and gravity in a fully developed steady-state laminar pipe flow is now given as Equation (I.10)

$$\frac{dy_p}{dt} = \frac{9.69 D_p v_t \left(\rho_f \mu_f 4 u_{avg} \frac{y_p}{R^2} \right)^{1/2}}{\pi 18 \mu_f}; \qquad \frac{dz_p}{dt} = u + v_t \tag{I.10}$$

I.3 Analytical Solution of Differential Equation System

The system of differential equations for the pseudo steady-state motion of a single particle, as given in Equation (I.10), can be solved by integration based on the limiting trajectory (see Figure I.2). In order to do so the equations are first transformed into dimensionless equations and then they are divided by each other so only one equation is obtained. The equations are transformed as follows

$$\begin{aligned} \xi = \frac{y_p}{R} \Rightarrow \frac{d\xi}{dt} = \frac{d}{dt}\left(\frac{y_p}{R}\right) = \frac{1}{R}\frac{dy_p}{dt} \Leftrightarrow R\frac{d\xi}{dt} = \frac{dy_p}{dt} \\ \eta = \frac{z_p}{L} \Rightarrow \frac{d\eta}{dt} = \frac{d}{dt}\left(\frac{z_p}{L}\right) = \frac{1}{L}\frac{dz_p}{dt} \Leftrightarrow L\frac{d\eta}{dt} = \frac{dz_p}{dt} \end{aligned} \tag{I.11}$$

Substituting the dimensionless coordinates and their differential quotients given in Equation (I.11) into Equation (I.10) gives the following

$$\begin{aligned} R\frac{d\xi}{dt} &= \frac{9.69 D_p v_t \left(\rho_f \mu_f 4 u_{avg} \frac{\xi}{R} \right)^{1/2}}{\pi 18 \mu_f} \\ L\frac{d\eta}{dt} &= u(\xi) + v_t \end{aligned} \tag{I.12}$$

Dividing the differential equations in Equation (I.12) by each other gives the following single differential equation

$$\frac{R}{L}\frac{d\xi}{d\eta}=\frac{9.69D_p v_t\left(\rho_f\mu_f 4u_{avg}\frac{\xi}{R}\right)^{1/2}}{\pi 18\mu_f\left(u(\xi)+v_t\right)} \tag{I.13}$$

Rearranging Equation (I.13) gives

$$\begin{gathered}\frac{R}{L}\pi 18\mu_f\left(u(\xi)+v_t\right)\frac{d\xi}{d\eta}=9.69D_p v_t\left(\frac{\rho_f\mu_f 4u_{avg}}{R}\right)^{1/2}\xi^{1/2}\\ \Updownarrow\\ \left(u(\xi)+v_t\right)\xi^{-1/2}\frac{d\xi}{d\eta}=\frac{9.69D_p v_t}{\pi 18\mu_f}\frac{L}{R}\left(\frac{\rho_f\mu_f 4u_{avg}}{R}\right)^{1/2}\end{gathered} \tag{I.14}$$

Substituting the velocity profile given in Equation (I.5) into Equation (I.14) gives the following

$$\begin{gathered}\left(2u_{avg}\left(1-\xi^2\right)+v_t\right)\xi^{-1/2}\frac{d\xi}{d\eta}=\frac{9.69D_p v_t}{\pi 18\mu_f}\frac{L}{R}\left(\frac{\rho_f\mu_f 4u_{avg}}{R}\right)^{1/2}\\ \Updownarrow\\ \left(\left(1-\xi^2\right)+\frac{1}{2}\frac{v_t}{u_{avg}}\right)\xi^{-1/2}\frac{d\xi}{d\eta}=\frac{9.69D_p v_t}{2u_{avg}\pi 18\mu_f}\frac{L}{R}\left(\frac{\rho_f\mu_f 4u_{avg}}{R}\right)^{1/2}\end{gathered} \tag{I.15}$$

and assuming that the particle terminal settling velocity, $v_t << u_{avg}$ gives the possibility of neglecting the second term in the bracket on the left-hand side of Equation (I.15)

$$\begin{gathered}\left(\left(1-\xi^2\right)+\frac{1}{2}\frac{v_t}{u_{avg}}\right)\xi^{-1/2}\frac{d\xi}{d\eta}=\frac{9.69D_p v_t}{u_{avg}\pi 18\mu_f}\frac{L}{2R}\left(\frac{\rho_f\mu_f 4u_{avg}}{R}\right)^{1/2}\\ \Downarrow\\ \left(1-\xi^2\right)\xi^{-1/2}\frac{d\xi}{d\eta}=\frac{9.69D_p v_t}{u_{avg}\pi 18\mu_f}\frac{L}{D}\left(\frac{\rho_f\mu_f 4u_{avg}}{R}\right)^{1/2}\end{gathered} \tag{I.16}$$

Equation (I.16) can now be integrated in the radial direction from the limiting trajectory, ξ_0, and out to the outer surface of the pipe, ξ=1 and from the inlet, η=0,

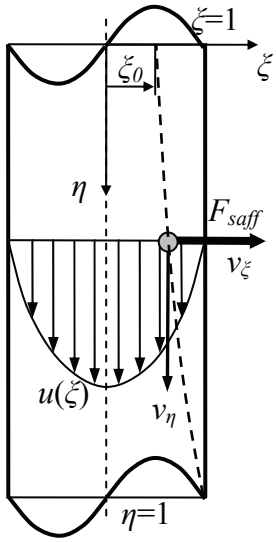

Figure I.2: Schematic illustration of a fully developed axisymmetrical flow with gravity in the positive η-direction (vertical direction). The red dotted line illustrates the limiting trajectory. With the particle velocity faster then the fluid flow the Saffman lift force is in the positive ξ-direction as illustrated.

down the axial length of the pipe until the length, η=1, which is exactly where the limiting trajectory will hit the wall, as shown on Figure I.2.

$$\int_{\xi_0}^{1}\left(\xi^{-1/2}-\xi^{3/2}\right)d\xi=\frac{9.69D_p v_t}{9\pi u_{avg}}\frac{L}{D}\left(\frac{\rho_f\mu_f 4u_{avg}}{4R\mu_f^2}\right)^{1/2}\int_0^1 d\eta$$

$$\Updownarrow \tag{I.17}$$

$$\left[2\xi^{1/2}-\frac{2}{5}\xi^{5/2}\right]_{\xi_0}^{1}=\frac{9.69D_p v_t}{9\pi u_{avg}}\frac{L}{D}\left(2\frac{\rho_f u_{avg}D}{D^2\mu_f}\right)^{1/2}\left[\eta\right]_0^1$$

Substituting the integration boundaries into Equation (I.17) gives

$$2\cdot 1^{1/2}-\frac{2}{5}1^{5/2}-\left(2\xi_0^{1/2}-\frac{2}{5}\xi_0^{5/2}\right)=\frac{6\cdot 1.615D_p v_t}{9\pi u_{avg}}\frac{L}{D}\left(\frac{2}{D^2}\mathrm{Re}_{pipe}\right)^{1/2}(1-0) \tag{I.18}$$

Rearranging Equation (I.18)

$$\frac{2}{5}\left(5-1-5\xi_0^{1/2}+\xi_0^{5/2}\right)=\frac{2\cdot 1.615D_p v_t}{3\pi u_{avg}}\frac{L}{D^2}\sqrt{2}\,\mathrm{Re}_{pipe}^{1/2} \tag{I.19}$$

and reducing Equation (I.19) gives the following expression

$$\frac{2}{5}\left(\xi_0^{5/2} - 5\xi_0^{1/2} + 4\right) = \frac{2 \cdot 1.615 D_p v_t}{3\pi u_{avg}} \frac{L}{D^2} \sqrt{2}\, \mathrm{Re}_{pipe}^{1/2} \tag{I.20}$$

Substituting the expression for the particle terminal settling velocity, v_t for Stokes flow given in Equation (2.38) into Equation (I.17) gives

$$\frac{2}{5}\left(\xi_0^{5/2} - 5\xi_0^{1/2} + 4\right) = \frac{2 \cdot 1.615 D_p}{3\pi u_{avg}} \frac{D_p^2 \rho_p g}{18\mu_f} \frac{L}{D^2} \sqrt{2}\, \mathrm{Re}_{pipe}^{1/2}$$

$$\frac{2}{5}\left(\xi_0^{5/2} - 5\xi_0^{1/2} + 4\right) = \frac{2 \cdot 1.615}{3\pi u_{avg}} \frac{D_p^3 \rho_p g}{18\mu_f} \frac{L}{D^2} \sqrt{2}\, \mathrm{Re}_{pipe}^{1/2} \tag{I.21}$$

$$\frac{2}{5}\left(\xi_0^{5/2} - 5\xi_0^{1/2} + 4\right) = \frac{2 \cdot 1.615}{3\pi u_{avg}} \frac{\left(2R_p\right)^3 \rho_p g}{18\mu_f} \frac{L}{D^2} \sqrt{2}\, \mathrm{Re}_{pipe}^{1/2}$$

Rearranging Equation (I.21) as follows

$$\frac{2}{5}\left(\xi_0^{5/2} - 5\xi_0^{1/2} + 4\right) = \frac{2 \cdot 1.615}{3\pi u_{avg}} \frac{8R_p^3 \rho_p g}{18\rho_f \upsilon_f} \frac{\upsilon_f}{\upsilon_f} \frac{L}{D^2} \sqrt{2}\, \mathrm{Re}_{pipe}^{1/2}$$

$$\Updownarrow$$

$$\frac{2}{5}\left(\xi_0^{5/2} - 5\xi_0^{1/2} + 4\right) = \frac{2 \cdot 1.615}{3\pi} \frac{8}{18} A \frac{\upsilon_f}{u_{avg} D} \frac{L}{D} \sqrt{2}\, \mathrm{Re}_{pipe}^{1/2}$$

$$\Updownarrow$$

$$\frac{1}{5}\left(\xi_0^{5/2} - 5\xi_0^{1/2} + 4\right) = \frac{2 \cdot 1.615}{3\pi} \frac{4}{18} A\, \mathrm{Re}_{pipe}^{-1} \frac{L}{D} \sqrt{2}\, \mathrm{Re}_{pipe}^{1/2} \tag{I.22}$$

$$\Updownarrow$$

$$\frac{\pi}{\sqrt{2}} A^{-1} \mathrm{Re}_{pipe}^{1/2} \frac{D}{L} \frac{3 \cdot 18}{5 \cdot 2}\left(\xi_0^{5/2} - 5\xi_0^{1/2} + 4\right) = 4 \cdot 1.615$$

$$where\ A = \frac{R_p^3 \rho_p g}{\rho_f \upsilon_f^2}$$

Expressing the dimensionless factor, χ as

$$\chi = \frac{L}{D} A \,\mathrm{Re}_{pipe}^{-1/2} \tag{I.23}$$

and substituting it into Equation (I.22) gives an equation for the dimensionless limiting trajectory

$$\begin{gathered} 5.4\frac{\pi}{\sqrt{2}}\chi^{-1}\left(\xi_0^{5/2} - 5\xi_0^{1/2} + 4\right) = 4 \cdot 1.615 \\ \Updownarrow \\ 5.4\frac{\pi}{\sqrt{2}}\chi^{-1}\left(\xi_0^{5/2} - 5\xi_0^{1/2} + 4\right) = K \\ \Updownarrow \\ 11.996\chi^{-1}\left(\xi_0^{5/2} - 5\xi_0^{1/2} + 4\right) = K \end{gathered} \tag{I.24}$$

$$where\ K = 6.46$$

In equation (I.24), K = 6.46 is an integration constant in the expression for the Saffman lift force, given in Equation (2.13), when the force is based on the particle radius. For the force based on particle diameter the constant is 1.615.

Appendix J

UDF for Electrostatic Dispersion

J.1 Monodisperse Euler-UDS

```
/*
This UDF aktivates a
space charge potential equation
and a transport equation for charged particles

2 UDS have to be activated:
UDS0 becomes the space charge potential, none flux function, diffusion coefficient 1
UDS1 transports the particle density distribution , UDS1_flx hooked as flux function and
    diffusion coefficient set to constant value
*/

#include "udf.h"
#include "mem.h"
#include "math.h"
#include "sg.h"
#define i -1                        /*  Number of elementary charges per particle, <0:
    negatively charged, >0:  positively charged */
#define e_0 -1.60219e-19            /* [C] Elementary Charge */
#define eps_0 8.8542e-12            /* [As/Vm] Permitivity */
#define D_p  60.e-9                 /* [m] Particle Diameter */
#define Cc 4.38                 /* Dimensionless */
#define NEG_E0_EPS0 1.80951e-8      /* [[Vm]  e_0 / eps_0  */
#define INT_C0 0
#define INT_C1 1
#define EXT_C0 2

enum UDSI {ElPot, NumberConc, N_REQUIRED_UDS};

DEFINE_EXECUTE_ON_LOADING(load_nms,libudf)
{
    Set_User_Scalar_Name(ElPot, "Electrical Potential [V]");
    Set_User_Scalar_Name(NumberConc, "Particle number conc [#/m3]");
}


/*>>>>>>>>>>>>>>>Flux Function for UDS1 for Particle Density n Distribution
     >>>>>>>>>>>>>>>>>>>>>>>>>>>>>>>>*/
DEFINE_UDS_FLUX(UDS1_flx,f,tf,eqn)
{
  cell_t c0, c1;
  Thread *tc0, *tc1;
  real NV_VEC(A), NV_VEC(E), Z, flrt, rho, visc, cons;

  c0  = F_C0(f,tf);                                          /* C0 cell and thread
```

```
    allways exist */
  tc0 = F_C0_THREAD(f,tf);

  F_AREA(A, f, tf);
  //NV_VS(Ae, =, Ae , /, NV_MAG(Ae));                              /* face area unit
    vector */

  if (!BOUNDARY_FACE_THREAD_P(tf))
   {
      c1  = F_C1(f,tf);                                          /* internal face: C1 cell
    and thread  exist  */
      tc1 = F_C1_THREAD(f,tf);
      NV_VV(E, =, C_UDSI_G(c0,tc0,0) , +, C_UDSI_G(c1,tc1,0));  /* averaged electrical
    field vector as gradient of potential from UDS0*/
      NV_VS(E, =, E, /, 2.);

      rho  = (C_R(c0,tc0) + C_R(c1,tc1)) /2.;                    /* averaged density from
    continuous (carrier)phase*/
      visc = (C_MU_L(c0,tc0) + C_MU_L(c1,tc1)) /2.;              /* averaged viscosity from
    continuous (carrier)phase*/
      cons = (C_UDSI(c0,tc0,1) + C_UDSI(c1,tc1,1)) / 2.;

  }
   else                                                          /* cell is an external one:
     no c1 exists  */
   {
      NV_V(E, =, C_UDSI_G(c0,tc0,0));
      NV_VS(E, =, E, /, 1.);

      rho = C_R(c0,tc0);
      visc = C_MU_L(c0,tc0);
      cons = C_UDSI(c0,tc0,1);
   }

   Z = e_0 * i * Cc / (3 * M_PI *visc * D_p);
   flrt = F_FLUX(f,tf)/rho + NV_DOT(E, A)*Z;

 return  flrt;
}

/*>>>>Source term  in UDS0: Electrostatic Potential due to Space Charges >>>>>>>*/
DEFINE_SOURCE(UDS0_src, c, t, ds, eqn)
{
return i * NEG_E0_EPS0 * C_UDSI(c, t, 1);
}
```

J.2 Polydisperse Euler-UDS

```
/*
This UDF aktivates a
space charge potential equation
and a transport equation for charged particles

2 UDS have to be activated:
UDS0 becomes the space charge potential, none flux function, diffusion coefficient 1
UDS1 tracks the particle density distribution , UDS1_flx hooked as flux function and
    diffusion coefficient set to constant value
*/

#include "udf.h"
#include "mem.h"
#include "math.h"
#include "sg.h"
#define i1 -1.0             /*  Number of elementary charges per particle, <0: negatively
    charged, >0:  positively charged */
#define i2 -1.0
#define i3 -1.0
#define i4 -1.0
#define i5 -1.0
#define i6 -1.0
#define i7 -1.0
#define i8 -1.0
#define i9 -1.0
#define i10 -1.0
#define i11 0.0
#define i12 0.0
#define i13 0.0
#define i14 0.0
#define i15 0.0
#define i16 0.0
#define i17 0.0
#define i18 0.0
#define i19 0.0
#define i20 0.0
#define i21 1.0
#define i22 1.0
#define i23 1.0
#define i24 1.0
#define i25 1.0
#define i26 1.0
#define i27 1.0
#define i28 1.0
#define i29 1.0
#define i30 1.0
#define i31 -2.0
#define i32 -2.0
#define i33 2.0
#define i34 2.0
#define e_0 -1.60219e-19           /* [C] Elementary Charge */
#define eps_0 8.8542e-12           /* [As/Vm] Permitivity */
#define D_p1  5.3e-9               /* [m] Particle Diameter */
#define D_p2  7.6e-9               /* [m] Particle Diameter */
#define D_p3  10.87e-9             /* [m] Particle Diameter */
#define D_p4  15.6e-9              /* [m] Particle Diameter */
#define D_p5  22.35e-9             /* [m] Particle Diameter */
#define D_p6  32.05e-9             /* [m] Particle Diameter */
#define D_p7  45.9e-9              /* [m] Particle Diameter */
#define D_p8  65.8e-9              /* [m] Particle Diameter */
#define D_p9  94.25e-9             /* [m] Particle Diameter */
#define D_p10  137.95e-9           /* [m] Particle Diameter */
#define Cc1 42.7                   /* Dimensionless */
#define Cc2 30.0                   /* Dimensionless */
#define Cc3 21.1                   /* Dimensionless */
#define Cc4 14.9                   /* Dimensionless */
#define Cc5 10.6                   /* Dimensionless */
#define Cc6 7.59                   /* Dimensionless */
#define Cc7 5.50                   /* Dimensionless */
#define Cc8 4.06                   /* Dimensionless */
#define Cc9 3.06                   /* Dimensionless */
#define Cc10 2.36                  /* Dimensionless */
#define NEG_E0_EPS0 1.80951e-8     /* [[Vm]  e_0 / eps_0  */
#define INT_C0_0
```

```
#define INT_C1 1
#define EXT_C0 2


//DEFINE_ADJUST(udm0_init,d)
//{
//  Thread *t;
//  /* Initialises UDM0 every iteration */
//  real sum diss=0.;
//  cell_t c;
//
//  /* loop over all cell threads in the domain */
//  thread_loop_c(t,d)
//  {
//   begin c loop(c,t)
//       C_UDMI(c,t,0) += 0.;
//   end_c_loop(c,t)
//  }
//
//  Message("\n C_UDM0 initialised! \n");
//}

/*>>>>>>>>>>>>>>Flux Function for UDS1 for Particle Density n Distribution
     >>>>>>>>>>>>>>>>>>>>>>>>>>>>>>>>*/
DEFINE_UDS_FLUX(UDS1_flx,f,tf,inum)
{
  cell t c0, c1;
  Thread *tc0, *tc1;
  real NV_VEC(A), NV_VEC(E), Z, flrt, rho, visc, cons;

  c0  = F_C0(f,tf);                                          /* C0 cell and thread
    allways exist */
  tc0 = F_C0_THREAD(f,tf);

  F_AREA(A, f, tf);
  //NV VS(Ae, =, Ae , /, NV_MAG(Ae));                            /* face area unit
    vector */

  if (!BOUNDARY_FACE_THREAD_P(tf))
   {
     c1  = F_C1(f,tf);                                       /* internal face: C1 cell
   and thread  exist  */
     tc1 = F_C1_THREAD(f,tf);
     NV_VV(E, =, C_UDSI_G(c0,tc0,0) , +, C_UDSI_G(c1,tc1,0));  /* averaged electrical
   field vector as gradient of potential from UDS0*/
     NV_VS(E, =, E, /, 2.);

     rho  = (C_R(c0,tc0) + C_R(c1,tc1)) /2.;                 /* averaged density from
   continuous (carrier)  phase*/
     visc = (C_MU_L(c0,tc0) + C_MU_L(c1,tc1)) /2.;           /* averaged viscosity from
   continuous (carrier)  phase*/
     cons = (C_UDSI(c0,tc0,inum) + C_UDSI(c1,tc1,inum)) / 2.;

  }
   else                                                      /* cell is an external one:
     no c1 exists  */
   {
     NV_V(E, =, C_UDSI_G(c0,tc0,0));
     NV_VS(E, =, E, /, 1.);

     rho = C_R(c0,tc0);
     visc = C_MU_L(c0,tc0);
     cons = C_UDSI(c0,tc0,inum);
   }


   if (inum = 1)    Z = e_0 * i1 * Cc1 / (3 * M_PI *visc * D_p1);
   if (inum = 2)    Z = e_0 * i2 * Cc2 / (3 * M_PI *visc * D_p2);
   if (inum = 3)    Z = e_0 * i3 * Cc3 / (3 * M_PI *visc * D_p3);
   if (inum = 4)    Z = e_0 * i4 * Cc4 / (3 * M_PI *visc * D_p4);
   if (inum = 5)    Z = e_0 * i5 * Cc5 / (3 * M_PI *visc * D_p5);
   if (inum = 6)    Z = e_0 * i6 * Cc6 / (3 * M_PI *visc * D_p6);
   if (inum = 7)    Z = e_0 * i7 * Cc7 / (3 * M_PI *visc * D_p7);
   if (inum = 8)    Z = e_0 * i8 * Cc8 / (3 * M_PI *visc * D_p8);
   if (inum = 9)    Z = e_0 * i9 * Cc9 / (3 * M_PI *visc * D_p9);
   if (inum = 10)   Z = e_0 * i10 * Cc10 / (3 * M_PI *visc * D_p10);
   if (inum = 11)   Z = e_0 * i11 * Cc1 / (3 * M_PI *visc * D_p1);
   if (inum = 12)   Z = e_0 * i12 * Cc1 / (3 * M_PI *visc * D_p2);
   if (inum = 13)   Z = e_0 * i13 * Cc3 / (3 * M_PI *visc * D_p3);
```

```
   if (inum = 14)   Z = e_0 * i14 * Cc4 / (3 * M_PI *visc * D_p4);
   if (inum = 15)   Z = e_0 * i15 * Cc5 / (3 * M_PI *visc * D_p5);
   if (inum = 16)   Z = e_0 * i16 * Cc6 / (3 * M_PI *visc * D_p6);
   if (inum = 17)   Z = e_0 * i17 * Cc7 / (3 * M_PI *visc * D_p7);
   if (inum = 18)   Z = e_0 * i18 * Cc8 / (3 * M_PI *visc * D_p8);
   if (inum = 19)   Z = e_0 * i19 * Cc9 / (3 * M_PI *visc * D_p9);
   if (inum = 20)   Z = e_0 * i20 * Cc10 / (3 * M_PI *visc * D_p10);
   if (inum = 21)   Z = e_0 * i21 * Cc1 / (3 * M_PI *visc * D_p1);
   if (inum = 22)   Z = e_0 * i22 * Cc1 / (3 * M_PI *visc * D_p2);
   if (inum = 23)   Z = e_0 * i23 * Cc3 / (3 * M_PI *visc * D_p3);
   if (inum = 24)   Z = e_0 * i24 * Cc4 / (3 * M_PI *visc * D_p4);
   if (inum = 25)   Z = e_0 * i25 * Cc5 / (3 * M_PI *visc * D_p5);
   if (inum = 26)   Z = e_0 * i26 * Cc6 / (3 * M_PI *visc * D_p6);
   if (inum = 27)   Z = e_0 * i27 * Cc7 / (3 * M_PI *visc * D_p7);
   if (inum = 28)   Z = e_0 * i28 * Cc8 / (3 * M_PI *visc * D_p8);
   if (inum = 29)   Z = e_0 * i29 * Cc9 / (3 * M_PI *visc * D_p9);
   if (inum = 30)   Z = e_0 * i30 * Cc10 / (3 * M_PI *visc * D_p10);
   if (inum = 31)   Z = e_0 * i31 * Cc10 / (3 * M_PI *visc * D_p9);
   if (inum = 32)   Z = e_0 * i32 * Cc10 / (3 * M_PI *visc * D_p10);
   if (inum = 33)   Z = e_0 * i33 * Cc10 / (3 * M_PI *visc * D_p9);
   if (inum = 34)   Z = e_0 * i34 * Cc10 / (3 * M_PI *visc * D_p10);
   flrt = F_FLUX(f,tf)/rho + NV_DOT(E, A)*Z;


   C_UDMI(c0,tc0,0) += flrt * cons;                              /*  positive flux is
    outflow for C0 -> positive divergence*/
   if (!BOUNDARY_FACE_THREAD_P(tf))
   {
    C_UDMI(c1,tc1,0) -= flrt * cons;                             /*  positive flux is inflow
      for C1 -> negative divergence*/
   }
 return  flrt;
}

/*>>>>Source term  in UDS0: Electrostatic Potential due to Space Charges >>>>>>>*/
DEFINE_SOURCE(UDS0_src, c, t, ds, eqn)
{
return (i1  * NEG_E0_EPS0 * C_UDSI(c, t, 1)+ \
        i2  * NEG_E0_EPS0 * C_UDSI(c, t, 2)+ \
        i3  * NEG_E0_EPS0 * C_UDSI(c, t, 3)+ \
        i4  * NEG_E0_EPS0 * C_UDSI(c, t, 4)+ \
        i5  * NEG_E0_EPS0 * C_UDSI(c, t, 5)+ \
        i6  * NEG_E0_EPS0 * C_UDSI(c, t, 6)+ \
        i7  * NEG_E0_EPS0 * C_UDSI(c, t, 7)+ \
        i8  * NEG_E0_EPS0 * C_UDSI(c, t, 8)+ \
        i9  * NEG_E0_EPS0 * C_UDSI(c, t, 9)+ \
        i10 * NEG_E0_EPS0 * C_UDSI(c, t, 10)+ \
        i11 * NEG_E0_EPS0 * C_UDSI(c, t, 11)+ \
        i12 * NEG_E0_EPS0 * C_UDSI(c, t, 12)+ \
        i13 * NEG_E0_EPS0 * C_UDSI(c, t, 13)+ \
        i14 * NEG_E0_EPS0 * C_UDSI(c, t, 14)+ \
        i15 * NEG_E0_EPS0 * C_UDSI(c, t, 15)+ \
        i16 * NEG_E0_EPS0 * C_UDSI(c, t, 16)+ \
        i17 * NEG_E0_EPS0 * C_UDSI(c, t, 17)+ \
        i18 * NEG_E0_EPS0 * C_UDSI(c, t, 18)+ \
        i19 * NEG_E0_EPS0 * C_UDSI(c, t, 19)+ \
        i20 * NEG_E0_EPS0 * C_UDSI(c, t, 20)+ \
        i21 * NEG_E0_EPS0 * C_UDSI(c, t, 21)+ \
        i22 * NEG_E0_EPS0 * C_UDSI(c, t, 22)+ \
        i23 * NEG_E0_EPS0 * C_UDSI(c, t, 23)+ \
        i24 * NEG_E0_EPS0 * C_UDSI(c, t, 24)+ \
        i25 * NEG_E0_EPS0 * C_UDSI(c, t, 25)+ \
        i26 * NEG_E0_EPS0 * C_UDSI(c, t, 26)+ \
        i27 * NEG_E0_EPS0 * C_UDSI(c, t, 27)+ \
        i28 * NEG_E0_EPS0 * C_UDSI(c, t, 28)+ \
        i29 * NEG_E0_EPS0 * C_UDSI(c, t, 29)+ \
        i30 * NEG_E0_EPS0 * C_UDSI(c, t, 30)+ \
        i31 * NEG_E0_EPS0 * C_UDSI(c, t, 31)+ \
        i32 * NEG_E0_EPS0 * C_UDSI(c, t, 32)+ \
        i33 * NEG_E0_EPS0 * C_UDSI(c, t, 33)+ \
        i34 * NEG_E0_EPS0 * C_UDSI(c, t, 34));
}
```

J.3 Euler-Lagrange

```
//#include "dpm-euler-elstat0.0.h"
#include "udf.h"
#include "mem.h"
#include "math.h"
#include "sg.h"

#define iq -1.                  /*  Number of elementary charges per ion */
#define e_0 1.60219e-19         /* [C] signless value for Elementary Charge */
#define k_B  1.3807e-23         /* [Ws/K] Boltzmann constant */

#define EPS_0 8.8542e-12        /* [As/Vm] Permitivity */
#define EPS_rel 1.              /* relative Permitivity */


enum UDSI {ElPot, N_REQUIRED_UDS};
enum UDP{Charge, N_REQUIRED_UDP};
enum UDMI {ChrgDens, i_hit, N_REQUIRED_UDM};

static cxboolean ResetUDM0 = TRUE;

static float E_x[3]={1.,0.,0.}, E_y[3]={0.,1.,0.}, E_z[3]={0.,0.,1.};
static float iq_abs=1;
static float iq_sign=-1;

DEFINE_EXECUTE_ON_LOADING(load_nms,libudf)
{
    Set_User_Scalar_Name(ElPot, "Electrical Potential [V]");
    Set_User_Memory_Name(ChrgDens, "Charge density [C/m3]");
    Set_User_Memory_Name(i_hit, "Nr of Part. Hits on Wall [#]");
}

DEFINE_ADJUST(def_adjst,d)
{

    ResetUDM0 = TRUE;
    Message("Reset UDM0 = TRUE \n");
}

DEFINE_DPM_INJECTION_INIT(atInjection,I)
{
real Random_factor, Theta, Injection_Parcel_Area, q_charge;
real Radius_pipe, z_coordinate, u_velocity, v_velocity, w_velocity, particle_temp,
    particle_dia, particle_conc;

Domain *d;
Thread *tc;
cell_t c;
Particle *p;

int counter = 0;
int number_of_injected_parcels = 10000;
int Random_number = 0;

q_charge  = iq * e_0;
//Message("\n q_charge = %d \n", q_charge);
//Message("\n q_charge = \n", q_charge);

Radius_pipe = 0.00298;
z_coordinate = 0.0001;
u_velocity = 0.0;
v_velocity = 0.0;
w_velocity = 0.1651;
particle_temp = 300;
particle_dia = 10e-9;
particle_conc = 1.70E+12;
Random_factor = 0.0;

            if(ResetUDM0)
            {
                 Message("\n C_UDMI (charge density) reset\n");
                        d = Get_Domain(1);
                        thread_loop_c(tc,d)
                        {
                                    begin_c_loop(c,tc)
```

```
                                                C_UDMI(c,tc,ChrgDens) = 0.;
                                                C_UDMI(c,tc,i_hit) = 0.;
                                    end_c_loop(c,tc)
                            }
                            ResetUDM0= FALSE;
                }
/* Creates a stochastic uniform distribution of points */
/* Standard Fluent looping Macro to get particle stream in an Injection */
loop(p,I->p)
{
//Message("\n Loop number %d \n", counter);
    //Injection_Parcel_Area = M_PI * Radius_pipe * Radius_pipe / number_of_injected_parcels
    ;
        if ( counter < number_of_injected_parcels )
        {
            Injection_Parcel_Area = M_PI * Radius_pipe * Radius_pipe /
    number_of_injected_parcels;
            Random number = rand(); /* Gives a random number between 0 and 32767 */
            Random_factor = (1.0 * Random_number) / (1.0 * RAND_MAX); /* Gives a random
    number between 0 and 1 */
            Theta = 2 * M PI * rand() / RAND MAX;
            P_POS(p)[0] = sqrt((1.0 * Random_number) / (1.0 * RAND_MAX)) * Radius_pipe *
    cos(Theta);
            P POS(p)[1] = sqrt((1.0 * Random_number) / (1.0 * RAND_MAX)) * Radius_pipe *
    sin(Theta);
            P_POS(p)[2] = z_coordinate;
            P VEL(p)[0] = u velocity;
            P_VEL(p)[1] = v_velocity;
            P_VEL(p)[2] = w_velocity;
            P DIAM(p) = particle dia;
            P_T(p) = particle_temp;
            P_MASS(p) = P_RHO(p)* M_PI/6.0 * pow( particle_dia, 3.0 );
            P_FLOW_RATE(p) = Injection_Parcel_Area * w_velocity * particle_conc * P_MASS(p)
    ;
            P_USER_REAL(p,Charge) = q_charge;
        }
        else
        {
            p->stream_index = -1;
        }
    counter++;
//  Message("\n Random number %d \n", Random_number);
//  Message("\n RAND_MAX %d \n", RAND_MAX);
//  Message("\n Random factor %e \n", Random_factor);
//  Message("\n Theta %e \n", Theta);
//  Message("\n Injection Parcel Area %e \n", Injection_Parcel_Area);
//  Message("\n Radius of pipe %e \n", Radius_pipe);
//  Message("\n Number of injected parcels %d \n", number_of_injected_parcels);
//  Message("\n Particle diameter %e \n", particle_dia);
//  Message("\n x-coordinate %e \n", P_POS(p)[0]);
//  Message("\n p %d \n", p);
//  Message("\n I %d \n", I);
}
}

/*>>>>>>>>>>>>>>>  UDS0 - Electrostatic Potential equation [V] >>>>>>>>>>>>>>>>>>>>>>>>>>>>>>*
    /
DEFINE_DIFFUSIVITY(UDS0_diff,c,tc,equ)
{
     return EPS 0 * EPS rel;
     /* returns effective diffusion coefficient for Potential equation*/
}

DEFINE_SOURCE(UDS0_src,c,tc,ds,eqn)
/* Returns the charge density [C/m3] calculated in the DEFINE_DPM_SCALAR_UPDATE */
{
    return C_UDMI(c, tc, ChrgDens);
}

 DEFINE_DPM_BC(wall_hit_count,p,tf,f,f_normal,i)
{
    /* particle is in cell c, tc */
    cell_t c0;
    Thread *tc0;
```

```
    c0  = F_C0(f,tf);      /* C0 cell and thread always exist */
    tc0 = F_C0_THREAD(f,tf);

    /* Count number of hits of particles at the wall */
    C_UDMI(c0,tc0,i_hit)+=1;
    //Message ("Particle hit cell %d on wall %d", f, THREAD_ID(tf));
    return PATH_ABORT;
}


/*>>>>>>>>>>>>>>>>>Calculate charge
    density>>>>>>>>>>>>>>>>>>>>>>>>>>>>>>>>>>>>>>>>>>>>>>>>>>>>>>>>>>>>>*/
DEFINE_DPM_SCALAR_UPDATE(DPM_Conc, c, tc, initialize, p)
{
 real q_charge, p_strength, MassDensity, dt_p;

 //q_charge  = iq * e_0;
 q_charge = P_USER_REAL(p,Charge);

// dt_p = P_TIME(p)-P_TIME0(p);

 p_strength = P_FLOW_RATE(p) / P_MASS(p);
 //Message("particle: %d strength: %e P_FLOW: %e P_MASS: %e\n",p, p_strength, P_FLOW_RATE
    (p), P_MASS(p));
 //Message("particle: %d density: %e P_VEL(p)[z]: %e\n",p, P_RHO(p), P_VEL(p)[2]);

 /* Calculate charge density in a cell */
 C_UDMI(c,tc,ChrgDens) += q_charge / C_VOLUME(c, tc) * p_strength * P_DT(p);  /* has to be
    multiplied with */
 //C_UDMI(c,tc,ChrgDens) = q_charge / C_VOLUME(c, tc) * p_strength * dt_p;  /* has to be
    multiplied with */
 //Message("particle: %d Charge density: %e Part time step: %e\n",p, C_UDMI(c,tc,ChrgDens),
     P_DT(p));

 /* Calculate particle mass density */
// MassDensity = C_UDMI(c,tc,ChrgDens) / q_charge * P_MASS(p);
 //Message("particle: %d Particle mass density: %e Particle time step: %e\n",p, MassDensity
    , P_DT(p));
 }

/*>>>>>>>>>>>>>>>  DPM - particle electo static acceleration [V]
     >>>>>>>>>>>>>>>>>>>>>>>>>>>>>>>>*/
DEFINE_DPM_BODY_FORCE(elstat_acc,p,i)
/*Calculates electrostatic acceleration on charged particle.
   Accelleration is charge times electrostatic potential times constant
   force = const*Q_p*grad(V)
*/
{

/*q_charge is the charge carried by a particle, p_strength is the number of real particles
    - counts the particles in a strength
  and add them up to a real number*/
 real q_charge, constant, r_ND, mirror_acc, mass_p, p_strength;
 real NV_VEC(P_ACC_TOT), NV_VEC(A), NV_VEC(F_POS),NV_VEC(R), NV_VEC(R_ND), NV_VEC
    (P_MIRROR_ACC);

  /* particle is in cell c, tc */
 cell_t c;
 face_t f;
 Thread *tc, *tf;
 int n;

 tc = P_CELL_THREAD(p);
 c = P_CELL(p);

 //q_charge  = iq * e_0;
 q_charge = P_USER_REAL(p,Charge);

 p_strength = P_FLOW_RATE(p) / P_MASS(p);
 //Message("particle: %d strength: %e P_FLOW: %e P_MASS: %e\n",p, p_strength, P_FLOW_RATE
    (p), P_MASS(p));
 //Message("particle: %d density: %e P_VEL(p)[z]: %e\n",p, P_RHO(p), P_VEL(p)[2]);
```

```
// Message("\n DPM_body 1");
 NV_V(P_ACC_TOT, =, C_UDSI_G(c, tc, ElPot));            /* E=grad(phi) */
 NV_VS(P_ACC_TOT, =,P_ACC_TOT, *, -1);                  /* -E */
 NV_VS(P_ACC_TOT, =,P_ACC_TOT, *, q_charge);            /* F = qE */
 NV_VS(P_ACC_TOT, =, P_ACC_TOT, /, P_MASS(p));          /* ap = F/Mp; an acceleration has
    to be returned*/

 /* Calculate charge density in a cell */
// C_UDMI(c,tc,ChrgDens) += q_charge / C_VOLUME(c, tc) * p_strength * P_DT(p);  /* has to
    be multiplied with */
 //Message("particle: %d Charge density: %e Part time step: %e\n",p, C_UDMI(c,tc,ChrgDens),
     P_DT(p));

 /* Calculate particle mass density */
// MassDensity = C_UDMI(c,tc,ChrgDens) / q_charge * P_MASS(p);
 //Message("particle: %d Particle mass density: %e Particle time step: %e\n",p, MassDensity
    , P_DT(p));

/* Calculation of Mirror force (Image force) */
//Message("\n DPM_body 2");
//c_face_loop(c,tc,n)   /* loops over all faces of a cell */
// {
//   f = C_FACE(c,tc,n);
//   tf = C_FACE_THREAD(c,tc,n);
//   if (THREAD_TYPE(tf) == THREAD_F_WALL)
//   {
//         F_AREA(A, f, tf);
//         F_CENTROID(F_POS, f, tf);
//       NV_VV(R, =, F_POS, -, P_POS(p));
//       constant = NV_DOT(R, A)/NV_MAG2(A); /* R*A/norm(A)^2 */
//       NV_VS(R_ND, =, A, *, constant); /* Vector in the normal direction to the wall */
//       r_ND = NV_MAG(R_ND); /* Normal particle distance to the wall */
//       mirror_acc = q_charge*q_charge/(16*M_PI*EPS_0*r_ND*r_ND)/P_MASS(p); /*Acceleration
     magnitude towards the wall due to the mirror force */
//       NV_VS(P_MIRROR_ACC, =, R_ND, /,r_ND);
//       NV_VS(P_MIRROR_ACC, =, P_MIRROR_ACC, *,mirror_acc);
//       NV_VV(P_ACC_TOT, =, P_ACC_TOT, +, P_MIRROR_ACC);
//   }
 //Message("\n DPM_body 3");
//}
//Message("particle: %e P_ACC_TOT: %e , %e , %e \n",p, P_ACC_TOT[0], P_ACC_TOT[1],
    P_ACC_TOT[2]);
// Message("particle: %e C_UDSI_G(ElPot): %e , %e , %e \n",p, C_UDSI_G(c, tc, ElPot)[0],
    C_UDSI_G(c, tc, ElPot)[1], C_UDSI_G(c, tc, ElPot)[2]);
 return P_ACC_TOT[i];
}
```

Appendix K

UDF for Particle-Wall Interaction

```
/*******************************************************************************/
/* Electrostatic forces, drag force, Reflect boundary condition for inert      */
/* particles and deposit build-up                                              */
/* Fluent UDF manual page 2-142                                                */
/* Implements drag force                                                       */
/* Haider and Levenspiel (1989)                                                */
/* Implements the critical particle velocity for particle adhesion(bounce)     */
/* Heinl, E & Bohnet, M. (2005), Powder Technology, Vol 159, pp. 95-104        */
/* Löffler, F. & Muhr, W. (1972), Chemie-Ing.-Techn, Vol. 44, No. 8, pp- 510-514 */
/* Calculate the critical growup velocity                                      */
/* Calulate accumulated mass deposition and depositon flux based on moving mesh  */
/* The UDF works for both lamniar and turbulent flow                           */
/* Auther: Michael Lykke Heiredal                                              */
/* date: 11.08.2009                                                            */
/*******************************************************************************/

#include "dpm-euler-elstat-monolith0.0.h"

#define eps_0 8.8542e-12        /* [As/Vm] Permitivity */
//#define TIME_STEP 3600.           /* Pseudo time step in seconds */
static cxboolean ResetUDM0 = TRUE;
static real NV_VEC(P_ACC_TOT);
static int NumberOfTries = 1; /* laminar flow NumberOfTries = 1, turbulent flow
    NumberOfTries = 10 - spec. in Random Walk Model */

enum UDS{ElPot, N_REQUIRED_UDS};
enum UDP{Charge, N_REQUIRED_UDP};
//enum UDMI {ChrgDens, i_hit, N_REQUIRED_UDM};
//enum UDM{GrowupVel, TotalThickness, TotalAccumulatedMass, N_REQUIRED_UDM};
enum UDM{ChrgDens, i_hit, GrowupVel, TotalAccumulatedMass, ParticleDepositionFlux,
    N_REQUIRED_UDM};
//enum UDM{ChrgDens, i_hit, GrowupVel, TotalAccumulatedMass, N_REQUIRED_UDM};

DEFINE_EXECUTE_ON_LOADING(load_udm_name,libudf)
{
    Set_User_Scalar_Name(ElPot, "Electrical Potential [V]");
    Set_User_Memory_Name(ChrgDens, "Charge density [C/m3]");
    Set_User_Memory_Name(i_hit, "Nr of Part. Hits on Wall [#]");
    Set_User_Memory_Name(GrowupVel, "Growup Velocity [m/s]");
    //Set_User_Memory_Name(TotalThickness, "Time integrated Thickness [m]");
    Set_User_Memory_Name(TotalAccumulatedMass, "Time integrated mass [kg]");
    Set_User_Memory_Name(ParticleDepositionFlux, "Particle Dep. Flux [kg/m2-s]");
}


DEFINE_ON_DEMAND(ResetUDM0_TRUE)
{
    ResetUDM0 = TRUE;
    Message ("\n   ResetUDM0 flag set to _TRUE_ at iteration: %d !\n", N_ITER);
}
```

```
DEFINE_ON_DEMAND(ResetUDM0_FALSE)
{
    ResetUDM0 = FALSE;
    Message ("\n   ResetUDM0 flag set to _FALSE_ at iteration: %d !\n", N_ITER);
}

DEFINE_ADJUST(def_adjst,d)
{
  Thread *tc;
  cell_t c;

  //ResetUDM0 = TRUE;


    if(ResetUDM0)
      {
         d = Get_Domain(1);
         thread_loop_c(tc,d)
         {
           begin_c_loop(c,tc)
           C_UDMI(c,tc,GrowupVel) = 0.;
           C_UDMI(c,tc,ChrgDens) = 0.;
           C_UDMI(c,tc,i_hit) = 0.;
           end_c_loop(c,tc)
         }
        Message ("\nADJUST:\n   UDMIs 'GrowupVel', 'ChrgDens' and 'i_hit' reset at
    iteration: %d !\n", N_ITER);
        ResetUDM0 = FALSE;
      }
}

DEFINE_DPM_INJECTION_INIT(atInjection,injection)
{
    Domain *d;
    Thread *tc;
    cell_t c;
    Particle *p, *pointer;

    real Injection_Parcel_Area, Theta, q_charge;
    real particle_dia, particle_conc;
    real Width_channel_x = 0.00819;         /* Width of channel x - used for injection
    surface */
    real Width_channel_y = 0.00459;         /* Width of channel y - used for injection
    surface */
    real z_coordinate = -0.009;             /* z-coordinate for particle release */
    real number_of_parcels;                 /* Number of parcels of particles */
    real u_velocity = 0.0;                  /* Particle velocity in the x-direction */
    real v_velocity = 0.0;                  /* Particle velocity in the y-direction */
    real w_velocity = 4.56;                 /* Particle velocity in the z-direction */
    real particle_temp = 623.15;            /* Particle temperature [K] */
    real Random_factor = 0.0;

    int part_counter = 0;                       /* Counter that counts the number of
    parcels injected */
    //int number_of_injected_parcels = 1000;    /* Number of injected parcels of particles
    */
    //int number_of_particle_sizes = 10;        /* Number of different particle sizes */
    int Random_number = 0;                      /* Number used for stochastic generation of
     injection points */

    q_charge = iq * e_0;                        /* Charge assigned to the injected particle
     q_charge  = iq * e_0 */



    //  if(ResetUDM0)
    //  {
    //     d = Get_Domain(1);
    //     thread_loop_c(tc,d)
    //     {
    //       begin_c_loop(c,tc)
    //       C_UDMI(c,tc,GrowupVel) = 0.;
    //     C_UDMI(c,tc,ChrgDens) = 0.;
    //       C_UDMI(c,tc,i_hit) = 0.;
    //       end_c_loop(c,tc)
    //     }
    //  Message ("\nADJUST:\n   UDMIs 'GrowupVel', 'ChrgDens' and 'i_hit' reset at
    iteration: %d !\n", N_ITER);
    //    ResetUDM0 = FALSE;
```

```
    //  }

    /* Creates a stochastic uniform distribution of points at the injection surface */
    /* Standard Fluent looping Macro to get particle stream in an Injection */
    Message ("\nINJECTION_INIT:\n   Injection started at iteration = %d \n", N_ITER);
    Message ("   Injection-name: %s injection= %d p= %d injection->p= %d\n", injection->
    name, injection, p, injection->p);
    if (injection->p != 0) pointer = injection->p;
    loop(p,pointer)
//  for((p)=(P_INJECTION(p)->p);NULL!=(p);(p)=THREAD_NEXT(p))
    {

        //Injection Parcel Area = Width_channel_x * Width_channel_y /
    number_of_injected_parcels;
        //Random_number = rand(); /* Gives a random number between 0 and 32767 */
        //Random factor = (1.0 * Random_number) / (1.0 * RAND_MAX); /* Gives a random
    number between 0 and 1 */
        P_POS(p)[0] = ((1.0 * rand()) / (1.0 * RAND_MAX)) * Width_channel_x;
        P_POS(p)[1] = ((1.0 * rand()) / (1.0 * RAND_MAX)) * Width_channel_y;
        P_POS(p)[2] = z_coordinate;
        P_VEL(p)[0] = u_velocity;
        P_VEL(p)[1] = v_velocity;
        P_VEL(p)[2] = w_velocity;
        //P_DIAM(p) = particle_dia;
        P_T(p) = particle_temp;
        P_MASS(p) = P_RHO(p)* M_PI/6.0 * pow( P_DIAM(p), 3.0 );
        //P_FLOW_RATE(p) = P_FLOW_RATE(p) / number_of_injected_parcels;  //10*
    Injection_Parcel_Area * w_velocity * particle_conc * P_MASS(p);
        P_USER_REAL(p,Charge) = q_charge;
        part_counter++;
        //Message("particle: %d Particle flow rate: %e\n",p, P_FLOW_RATE(p));
    }
    Message("   Injection stopped at iteration %d with part_counter= %d\n", N_ITER,
    part_counter);
}

DEFINE_DPM_BC(bc_trap,p,tf,f,f_normal,i)
{
  Thread *tc0;
  cell_t c0;
  real alpha;                       /* angle of particle path with face normal */
  real vn=0.;                       /* Normal velocity [m/s] */
  real wp_crit2 = 0.;               /* critical wall particle velocity for adhesion [m/s] *
    /
  real wp_max2 = 0.;                /* maximum particle velocity at wall [m/s] */
  real h_omega = 4.e-19;            /* Liffschitz-van der Waals constant */
  real coeff_e = 1;                 /* coefficient of restitution */
  real z0 = 4.e-15;                 /* the distance at contact [m] */
  real H = 250.e6;                  /* strength of a steel pipe [N/m2] */
  real q_p1 = 0;                    /* particle charge before before wall collision [C] */
  real q_p2 = 0;                    /* particle charge after before wall collision [C] */
  real nor_coeff = 1;               /* normal coefficient of restitution */
  real tan_coeff = 1;               /* tangential coefficient of restitution */
  real PackingLimitFactor = 0.6;    /* Average packing limit factor for spheres */
  real dp;
  real rho_p;
  real NV_VEC(A), NV_VEC(F_POS), NV_VEC(R), NV_VEC(R_ND), NV_VEC(P_VEL_NORMAL), NV_VEC
    (P_VEL_TANGENT);

  real constant, r_ND, p_strength, P_VEL_norm;
  int idim = 3;


  /* Get the particle charge */
  //old_charge = P_USER_REAL(p, Charge);
  //P_USER_REAL(p, Charge)= new_charge;



  /* Check for distance to the wall for the particle */

  F_AREA(A, f, tf); /* return a vector A containing the normal face area vector. Point
    always out */
  F_CENTROID(F_POS, f, tf);
  NV_VV(R, =, F_POS, -, P_POS(p));
  constant = NV_DOT(R, A)/NV_MAG2(A); /* [dotproduct] R*A/norm(A)^2 */
  NV_VS(R_ND, =, A, *, constant); /* Vector in the normal direction to the wall -
    projection of R-vector on A-vector*/
  r_ND = NV_MAG(R_ND); /* Normal particle distance to the wall */
```

```
  /* calcalulate critical particle velocity*/

  dp = P_DIAM(p);       /* particle diameter*/
  rho p = P RHO(p);     /* particle density*/
  p_strength = P_FLOW_RATE(p) / P_INIT_MASS(p); /* particle flow, particles/s */

  wp crit2 = pow(h omega/(coeff e*dp*4*M PI*M PI*z0*z0),2)*3/(4*H*rho p)\
             +3/(2*dp*dp*dp*M_PI*M_PI*M_PI*coeff_e*coeff_e*eps_0*rho_p)*(2*q_p2*q_p2/(2*z0+
    dp)-q_p1*q_p1/r_ND);

  wp max2 = NV MAG2(P VEL(p));
  if (wp_max2 > wp_crit2)
  {
        /* wp max > wp crit the particles will bounce */
        /* Calculate the normal component, rescale its magnitude by the coefficient of
    restitution and substract the change */

        /* Compute normal velocity */
        P_VEL_norm = NV_DOT(P_VEL(p), f_normal);
        NV_VS(P_VEL_NORMAL, =, f_normal, *, P_VEL_norm);

        /* Apply normal coefficient of restitution */
        NV_VS(P_VEL_NORMAL, =, P_VEL_NORMAL, *, nor_coeff);

        /* Calculate tangetial velocity */
        NV_VV(P_VEL_TANGENT, =, P_VEL(p), -, P_VEL_NORMAL);

        /* Apply tangential coefficient of restitution */
        NV_VS(P_VEL_TANGENT, =, P_VEL_TANGENT, *, tan_coeff);

        /* Calculate the reflecting normal component of the velocity */
        NV_VS(P_VEL_NORMAL, =, P_VEL_NORMAL, *, -1);

        /* Calculating the particle velocity after reflection */
        NV_VV(P_VEL(p), =, P_VEL_NORMAL, +, P_VEL_TANGENT);

        return PATH_ACTIVE;

  }
  else
  {
    /* wp_max < wp_crit and particles adhere to the wall */
    /* Abort the trackin because the particle is captured by the wall */
      c0  = F C0(f,tf);         /* C0 cell and thread allways exist */
      tc0 = F_C0_THREAD(f,tf);


      C_UDMI(c0, tc0, GrowupVel) += P_FLOW_RATE(p) / P_RHO(p) / NV_MAG(A) /
    PackingLimitFactor / NumberOfTries; /* Grow up Velocity during CURRENT_TIMESTEP -
    Divivd with 10 due to turbulent spreading */
      C_UDMI(c0, tc0, TotalThickness) += P_FLOW_RATE(p) * CURRENT_TIMESTEP / P_RHO(p) /
    NV_MAG(A) / PackingLimitFactor / NumberOfTries; /* Total Layer thickness*/
      C UDMI(c0, tc0, TotalAccumulatedMass) += P FLOW RATE(p) * CURRENT_TIMESTEP /
    NumberOfTries; /* Total accumulated mass of deposition*/
      C_UDMI(c0, tc0, ParticleDepositionFlux) += P_FLOW_RATE(p) / NV_MAG(A) / NumberOfTries
    ; /* Particle deposition flux - kg/m2 s */
      //Message ("Particle hit cell %d on wall %d", f, THREAD_ID(tf));
      C_UDMI(c0,tc0,i_hit) += 1; /* Count number of hits of particles at the wall */
        //Message("Particle aborted on wall \n");
      return PATH_ABORT;
  }
 }
DEFINE_GRID_MOTION(node_mv, domain, dt, time, dtime)
{
  Thread *tf = DT_THREAD (dt);
  face_t f;
  Node *v;

  real NV_VEC (DISP_VEC);
  int n;

  /* set deforming flag on adjacent cell zone */
  /* SET_DEFORMING_THREAD_FLAG (THREAD_T0 (tf)); test with not activating this because it
    is probably not necessary*/

//  Message ("time = %f", time);
  Message ("\nGRID_MOTION:\n   Begin Grid motion at iteration = %d \n", CURRENT_TIME);
```

```
//  Message ("time = %f", time);
  Message ("\nGRID_MOTION:\n   Begin Grid motion at iteration = %d \n", CURRENT_TIME);

  begin_f_loop (f, tf)  /* Looping over all wall faces ONCE*/
  {
    F_AREA (DISP_VEC, f, tf);
    NV_S(DISP_VEC,/=,NV_MAG(DISP_VEC));
    NV_S(DISP_VEC,/=,F_NNODES(f,tf));
    NV_S(DISP_VEC,*=,-1.); /*reversed, because area vector of a wall is always pointing
    away from the mesh*/
    /*Displacement vector contains now the reversed unit vector of that face devided by the
     number of nodes for that face*/

    NV_S(DISP_VEC, *=, C_UDMI(F_C0(f,tf),F_C0_THREAD(f,tf),GrowupVel));
    NV_S(DISP_VEC,*=, CURRENT_TIMESTEP);
    /* This vector contains the displacement because of layer growup for the face divided
    by the number of nodes of that face*/

    f_node_loop (f, tf, n) /* looping over all nodes of that face*/
    {
        v = F_NODE (f, tf, n);
        NV_V (NODE_COORD (v), +=, DISP_VEC); /* Displacement of every node belonging to
    that face with 1/face_node_number part of the the total face grow up*/
    }
  }
  end_f_loop (f, tf);
/* jens: the following line is very important to reset the UDMs correctly!!! */
  ResetUDM0 = TRUE;
Message ("   End Gridmotion => ResetUDM0 flag set to _TRUE_ at iteration: %d !\n", N_ITER);
/* We only visit every face ONCE but the nodes become moved as many times as there are
    connected faces*/
}

DEFINE_DPM_DRAG(particle_drag_force,Re,p)
{
    real Cc, Kn, drag_force, dp, w;
    real lambda = 1.63E-07;

//  Message("Drag computation\n");
    dp = P_DIAM(p);                         /* Particle diameter*/

    Kn = 2*lambda/dp;                       /* Knudsens number */
    Cc = 1+Kn*(1.257+0.4*exp(-1.1/Kn));     /* cunninghams correctionfactor */

    drag_force = (18 + 3.2508*pow(Re,0.6459) + (7.6518/(1 + 6880.95/Re))*(Re/24))/Cc;
    return(drag_force);
}
/*>>>>>>>>>>>>>>>  UDS0 - Electrostatic Potential equation [V] >>>>>>>>>>>>>>>>>>>>>>>>>>>>>*
    /
DEFINE_DIFFUSIVITY(UDS0_diff,c,tc,equ)
{
     return EPS_0 * EPS_rel;
     /* returns effective diffusion coefficient for Potential equation*/
}

DEFINE_SOURCE(UDS0_src,c,tc,ds,eqn)
/* Returns the charge density [C/m3] calculated in the DEFINE_DPM_SCALAR_UPDATE */
{
    return C_UDMI(c, tc, ChrgDens);
}

/*>>>>>>>>>>>>>>>>>Calculate charge
    density>>>>>>>>>>>>>>>>>>>>>>>>>>>>>>>>>>>>>>>>>>>>>>>>>>>>>>>>>*/
DEFINE_DPM_SCALAR_UPDATE(DPM_Conc, c, tc, initialize, p)
{
 real q_charge, p_strength, MassDensity, dt_p;
// Message("Scalar update\n");
 q_charge  = P_USER_REAL(p,Charge);
 //q_charge  = iq * e_0;

 p_strength = P_FLOW_RATE(p) / P_MASS(p);


 /* Calculate charge density in a cell */
 C_UDMI(c,tc,ChrgDens) += q_charge / C_VOLUME(c, tc) * p_strength * P_DT(p) / NumberOfTries
    ;  /* has to be multiplied with the particle strength and particle timestep*/
 }

/*>>>>>>>>>>>>>>>  DPM - particle electo static acceleration [V]
```

```
/*>>>>>>>>>>>>>>>  DPM - particle electo static acceleration [V]
     >>>>>>>>>>>>>>>>>>>>>>>>>>>>>>>>*/
DEFINE_DPM_BODY_FORCE(elstat_acc,p,i)
/*Calculates electrostatic acceleration on charged particle.
   Acceleration is charge times electrostatic potential times constant
   force = const*Q_p*grad(V)
*/
{

/*q_charge is the charge carried by a particle, p_strength is the number of real particles
    - counts the particles in a strength
  and add them up to a real number*/
 real q_charge, constant, r_ND, mirror_acc, mass_p, p_strength;
 real NV_VEC(A), NV_VEC(F_POS),NV_VEC(R), NV_VEC(R_ND), NV_VEC(P_MIRROR_ACC);

  /* particle is in cell c, tc */
 cell_t c;
 face_t f;
 Thread *tc, *tf;
 int n;

 tc = P_CELL_THREAD(p);
 c = P_CELL(p);

 //q_charge  = iq * e_0;

 if (i == 0)
 {
     q_charge  = P_USER_REAL(p,Charge);

     NV_V(P_ACC_TOT, =, C_UDSI_G(c, tc, ElPot));            /* E=grad(phi) */
//Message("boddy force P_ACC_TOT[%d]= %e \n x= %12.4e, y= %12.4e, z= %12.4e\n",i,P_ACC_TOT
    [i], P_POS(p)[0],P_POS(p)[1],P_POS(p)[2]);
     NV_VS(P_ACC_TOT, =,P_ACC_TOT, *, -1);                  /* -E */
     NV_VS(P_ACC_TOT, =,P_ACC_TOT, *, q_charge);            /* F = qE */
     NV_VS(P_ACC_TOT, =, P_ACC_TOT, /, P_MASS(p));          /* ap = F/Mp; an acceleration
    has to be returned*/

/* Calculation of Mirror force (Image force) */
    c_face_loop(c,tc,n) /* loops over all faces of a cell */
    {
         f = C_FACE(c,tc,n);
         tf = C_FACE_THREAD(c,tc,n);
         if (THREAD_TYPE(tf) == THREAD_F_WALL)
         {
             F_AREA(A, f, tf);
             F_CENTROID(F_POS, f, tf);
             NV_VV(R, =, F_POS, -, P_POS(p));
             constant = NV_DOT(R, A)/NV_MAG2(A); /* R*A/norm(A)^2 */
             NV_VS(R_ND, =, A, *, constant); /* Vector in the normal direction to the wall
    */
             r_ND = NV_MAG(R_ND); /* Normal particle distance to the wall */
             mirror_acc = q_charge*q_charge/(16*M_PI*EPS_0*r_ND*r_ND)/P_MASS(p); /*
    Acceleration magnitude towards the wall due to the mirror force */
             NV_VS(P_MIRROR_ACC, =, R_ND, /,r_ND);
             NV_VS(P_MIRROR_ACC, =, P_MIRROR_ACC, *,mirror_acc);
             NV_VV(P_ACC_TOT, =, P_ACC_TOT, +, P_MIRROR_ACC);
         }
    }
 }

 return P_ACC_TOT[i];
}
```